Cellular and Metabolic Processes in Tumor Growth and Metastasis

-

Recruitment of Myeloid-Derived Suppressor Cells to the Primary and Metastatic Tumor Microenvironment and Multiparametric Metabolic Fingerprinting of Murine Breast Cancer Cells

Dissertation

der Mathematisch-Naturwissenschaftlichen Fakultät

der Eberhard Karls Universität Tübingen

zur Erlangung des Grades eines

Doktors der Naturwissenschaften

(Dr. rer. nat.)

vorgelegt von

Sabrina Helen Linda Hoffmann

aus Nürtingen

Tübingen

2019

Gedruckt mit Genehmigung der Mathematisch-Naturwissenschaftlichen Fakultät der Eberhard Karls Universität Tübingen.

Tag der mündlichen Qualifikation:	16.09.2019
Dekan:	Prof. Dr. Wolfgang Rosenstiel
1. Berichterstatter:	Prof. Dr. Bernd J. Pichler
2. Berichterstatter:	Prof. Dr. Klaus Schulze-Osthoff

FOR MY FAMILY

TABLE OF CONTENTS

LIST OF ABBREVIATIONS

%ID/cm³	Percent injected dose per cubic centimeter
[^{18}F]FAZA	[^{18}F]-fluoroazomycin arabinoside
[^{18}F]FDG	2-deoxy-2-[^{18}F]-fluoro-D-glucose
[^{18}F]FEAU	2-deoxy-2-[^{18}F]-fluoro-5-ethyl-1-β-D-arabinofuranosyl-uracil
[^{18}F]FHBG	9-(4-[^{18}F]-fluoro-3-[hydroxymethyl]butyl)guanine
[^{18}F]FMISO	1*H*-1-(3-[^{18}F]-fluoro-2-hydroxypropyl)-2-nitroimidazole
7-AAD	7-aminoactinomycin D
AKT	Protein kinase B/AKT
ALAT	Alanine aminotransferase
APC	Allophycocyanin
ARG1	Arginase type 1
ATP/ADP/AMP	Adenosine-5'-tri/di/monophosphate
BL	Bioluminescence
BMDC	Bone marrow-derived cell
C57BL/6	Commonly used mouse strain
CCD	Charge-coupled device
CCL	CC chemokine ligands
CD	Cluster of differentiation
CFSE	Carboxyfluorescein succinimidyl ester
Cho	Choline
CM	Conditioned medium
CoA	Coenzyme A
CSC	Cancer stem cell
CTC	Circulating tumor cell
CXCR	CXC chemokine receptors
Cy	Cyanine dye
DC	Dendritic cell
DiD	1,1'-Dioctadecyl-3,3,3',3'-tetramethylindodicarbocyanine perchlorate
DMEM	Dulbecco's Modified Eagle's Medium
DNP	Dynamic nuclear polarization
DOTA	1,4,7,10-Tetraazacyclododecane-1,4,7,10-tetraacetic acid
ECM	Extracellular matrix
EDTA	2,2′,2″,2‴-(Ethane-1,2-diyldinitrilo)tetraacetic acid
EGF/R	Epidermal growth factor/receptor
EMT	Epithelial-to-mesenchymal transition
EPA	Electron paramagnetic agent

ERK	Extracellular signal-regulated kinase
FAD/$FADH_2$	Flavin adenine dinucleotide
FAK	Focal adhesion kinase
FCS	Fetal calve serum
FID	Free induction decay
FITC	Fluorescein isothiocyanate
FOV	Field of view
FSC	Forward scatter
FVB	Commonly used mouse strain
G/M-CSF	Granulocyte/Macrophage colony stimulating factor
GCho	Glycerophosphocholine
GEMM	Genetically engineered mouse model
GFP	Green fluorescent protein
GLUT	Glucose transporter
GM-CSF	Granulocyte-macrophage colony stimulating factor
HIF/-1α	Hypoxia-inducible factor/-subunit 1α
HPLC	High pressure liquid chromatography
HR-MAS	High resolution magic angle spinning
HSV1-tk	Herpes simplex virus-1 thymidine kinase
i.p.	intraperitoneal
i.v.	intravenous
IFN	Interferon
IL	Interleukin
iNOS	Inducible nitric oxide syntase
JAK	Janus kinase
LDH	Lactate dehydrogenase
Lin	Lineage marker
LOR	Line of response
LOX	Lysyl oxidase
LTR	Long terminal repeat
MACS	Magnetic activated cell sorting
MAPK	Mitogen-activated protein kinase
mCh	mCherry
MDSCs	Myeloid-derived suppressor cells
MEK	Mitogen-activated protein kinase kinase
MET	Mesenchymal-to-epithelial transition
MFP	Mammary fat pad

MHC-I/-II	Major histocompatibility complex-I/-II
M-MDSCs	Monocytic myeloid-derived suppressor cells
MMP	Matrix metallopeptidases
MMTV	Mouse mammary tumor virus
MRI	Magnetic resonance imaging
MRS	Magnetic resonance spectroscopy
MSC	Mesenchymal stem cell
NAD^+/NADH	Nicotinamide adenine dinucleotide
$NADP^+$/NADPH	Nicotinamide adenine dinucleotide phosphate
NIR	Near-infrared
NIS	Sodium iodide symporter
NK cell	Natural killer cell
NMR	Nuclear magnetic resonance
NOESY	Nuclear overhauser enhancement spectroscopy
NOTA	1,4,7-Triazacyclononane-1,4,7-triacetic acid
OI	Optical imaging
OSEM	Ordered subset expectation maximization
OT-1	C57BL/6-Tg(TcraTcrb)1100Mjb
OxPhos	Oxidative phosphorylation
PBS	Phosphate buffered saline
PCho	Phosphocholine
PDH	Pyruvate dehydrogenase
PE	Phycoerythrin
PET	Positron emission tomography
PFC	Perfluorocarbon
PFK(2)	Phosphofructokinase (2)
PI3K	Phosphatidylinositol-4,5-bisphosphate 3-kinase
PKC	Protein kinase C
PLCγ	Phosphoinositide phospholipase C γ
PMN-MDSCs	Polymorphonuclear myeloid-derived suppressor cells
ppm	Parts per million
pt	Post adoptive cell transfer
PTEN	Phosphatase and TENsin homologue
PTSM	Pyruvaldehyde-bis(N4-methylthiosemicarbazone)
PVE	Partial volume effect
PyMT	Polyoma virus middle T antigen
qRT-PCR	Quantitative real-time polymerase chain reaction

RAF	Rapidly accelerated fibrosarcoma
RANTES	Regulated on activation, normal T cell expressed and secreted
RARE	Rapid acquisitions with refocused echoes
RAS	Rat sarcoma oncoprotein
RF	Radiofrequency
ROS/RNS	Reactive oxygen species/reactive nitrogen species
RPMI 1640	Roswell Park Memorial Institute 1640
SEM	Standard error of the mean
SLC	Solute carrier
SPIO	Superparamagnetic iron oxide
SREBP	Sterol regulatory element binding proteins
SSC	Sideward scatter
STAT	Signal transducers and activators of transcription
STEAM	Stimulated echo acquisition mode
TAC	Time activity curve
TAM	Tumor-associated macrophage
TCA	Tricarboxylic acid cycle
tCho	Total choline-containing compounds
TCR	T cell receptor
TE	Echo time
TGF-β	Transforming growth factor β
TIMP-1	Tissue inhibitor of metallopeptidase 1
TME	Tumor microenvironment
TNF	Tumor necrosis factor
TR	Repetition time
TSE	Turbo spin echo
UDP	Uridine diphosphate
UDP-GalNAc	UDP-N-acetyl-galactosamine
UDP-GlcNAc	UDP-N-acetyl-glucosamine
VEGF	Vascular endothelial growth factor
VOI	Volume of interest
ZEB1	Zinc finger E-box-binding homeobox 1

LIST OF FIGURES

LIST OF TABLES

ACKNOWLEDGEMENT

Mein Dank gilt zuerst Prof. Dr. Bernd Pichler, der es mir ermöglicht hat, meine Doktorarbeit im Werner Siemens Imaging Center in Tübingen anzufertigen. Außerdem möchte ich ihm für die wissenschaftliche Unterstützung dieser Arbeit, die Möglichkeit der Teilnahme an nationalen und internationalen wissenschaftlichen Kongressen sowie die Ausrichtung der vielen Grill- und Weihnachtsfeiern danken, welche stets zu einer angenehmen Arbeitsatmosphäre beigetragen haben.

Ganz besonders danken möchte ich Dr. Christoph Grießinger für die Bereitstellung dieses außerordentlich interessanten Themas und die exzellente Betreuung auf theoretischer und experimenteller Ebene. Besonders möchte ich mich für sein kontinuierliches, außerordentliches Engagement nach Verlassen des Werner Siemens Imaging Centers bedanken. Vielen Dank für die fortlaufende Unterstützung, die wertvolle Zusammenarbeit, die offenen und angeregten Diskussionen sowie die sorgfältige Korrektur dieser Arbeit.

Mein Dank gilt weiterhin Prof. Dr. Klaus Schulze-Osthoff für die bereitwillige Übernahme des Zweitgutachtens für diese Arbeit.

Außerdem danke ich den Mitarbeitern der Radiopharmazie für die immer zuverlässige Produktion der PET-Tracer, die in dieser Arbeit verwendet wurden.

Mein Dank gilt außerdem meinen externen und internen Kooperationspartnern. Dr. Jaclyn Sceneay, Dr. Christina Wong und Prof. Andreas Möller am Tumour Microenvironment Laboratory in Brisbane, Australien, für die Bereitstellung der untersuchten Brustkrebszelllinien sowie Dr. Marie-Aline Neveu, Dr. Mohamed Jarboui und Dr. Christoph Trautwein am Werner Siemens Imaging Center für ihre Unterstützung der experimentellen Versuche. Außerdem danke ich Birgit Fehrenbacher und Renate Nordin für die Aufbereitung und Bearbeitung der histologischen Proben.
Für ihre tatkräftige Unterstüzung bei der Durchführung der experimentellen Versuche möchte ich mich bei Sandro Aidone, Daniel Bukala, Maren Harant, Natalie Mucha, Linda Schramm und Dr. Andreas Schmid bedanken. Besonders möchte ich mich bei Dorothea Reck für die außerordentlich gute und freundschaftliche Zusammenarbeit während ihrer Masterarbeit am Werner Siemens Imaging Center bedanken. Für die sorgfältigen Korrekturen dieser Arbeit möchte ich mich weiterhin herzlich bei Dr. Florian Maier, Dr. Marie-Aline Neveu und Dr. Mohamed Jarboui bedanken. Mein herzlicher Dank gilt auch allen ehemaligen und aktuellen Mitarbeiter des Werner Siemens Imaging Center für die kollegiale und außerordentlich

hilfsbereite Atmosphäre sowie die gemeinsamen unvergesslichen Erlebnisse auf Konferenzen und Feiern.

Nicht zuletzt möchte ich meinen Eltern Monika und Gert, meinen Großeltern Albert und Marianne, meinen Brüdern Simon und Sascha, sowie meinem Cousin Sebastian für ihre Unterstützung in allen Lebenslagen danken. Vor allem meinem Ehemann Henning danke ich ganz besonders für seine Unterstützung und für seine unendliche Geduld.

1 INTRODUCTION

1.1 Malign tumors, the tumor microenvironment and the metastatic cascade

1.1.1 Malign tumors and the tumor microenvironment

Cancers, solid malign neoplastic cell masses that invade their surroundings and metastasize to distant locations, are a leading cause of disease worldwide. Aside from the exposition to environmental factors causing cancer such as pathogens, exposition to UV- or other highly energetic radiation or carcinogenic compounds, the multi-step transformation of normal tissue cells to malignant cancer cells possess similar molecular, biochemical and cellular traits independent of the cancer type. These common molecular traits have first been described as the hallmarks of cancer in 2000 (Hanahan and Weinberg, 2000). These hallmarks represent mechanistic concepts of tumorigenesis and metastasis of cancer cells (Figure 1). The first three hallmarks of cancer aim to explain the enormous growth rate of cancerous tissue as autonomous proliferation without exogenous stimulation paired with insensitivity to anti-growth signals and resistance to pro-apoptotic signals. The fourth hallmark, limitless replicative potential, is closely related to the first three as it protects cancer cells from telomere shortening and consecutive cellular senescence. Furthermore, the angiogenic switch from vascular quiescence to neoangiogenesis represents the fifth hallmark: tumors induce the formation of new blood vessels to meet their need for oxygen and nutrient supply and sustain proliferation. Tissue invasion and metastasis represent the last of the classical hallmarks of cancer (Hanahan and Weinberg, 2000).

In the recent years, genomic instability and gradual increases in mutational burden have been widely accepted as cause for tumorigenesis. Oncogenic driver mutations and loss of function mutations in tumor suppressor genes result in constitutively active cell signaling pathways for cell survival and proliferation. Genomic instability emerged as enabling characteristic of cancer together with inflammatory responses (Hanahan and Weinberg, 2011). Inflammatory responses may, paradoxically, have tumor-promoting effects by supplying growth and pro-angiogenic factors. Furthermore, the deregulation of cellular energy metabolism and immune evasion emerged as new hallmarks of cancer. Immune evasion refers to a limited recognition of the cancerous cells by the constant anti-tumoral immune surveillance. Thereby the cancerous cell evades eradication leading to the growth of solid tumor masses (Figure 1). Metabolic changes during tumorigenesis will be discussed in further detail in the next section.

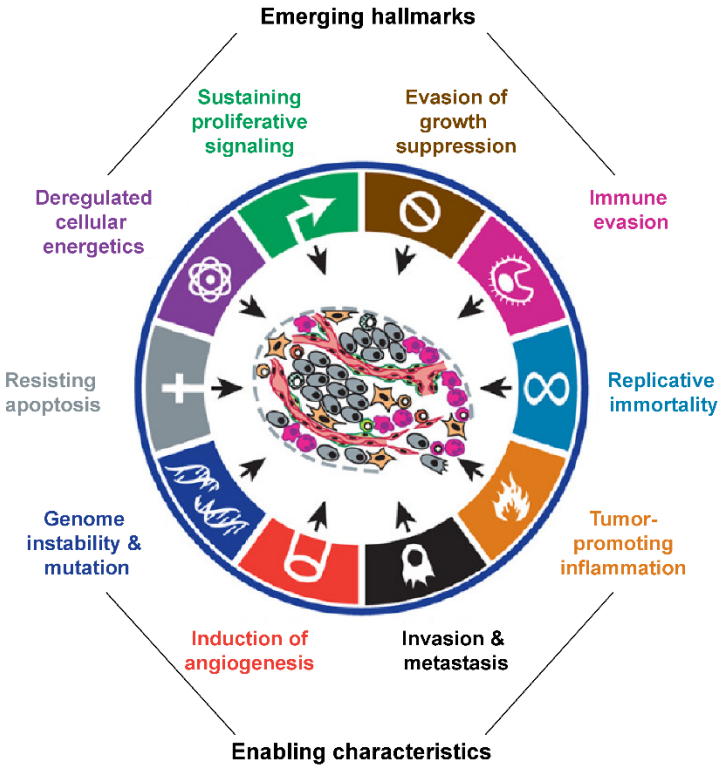

Figure 1: The revisited hallmarks of cancer.
The six acquired capabilities sustained proliferation, evasion of growth suppression, replicative immortality, induction of angiogenesis and invasion and metastasis in concert with the emerging hallmarks and enabling characteristics describe the revisited hallmarks of cancer. Figure modified from Hanahan and Weinberg, 2011.

Malign tumors, however, are not formed by cancer cells alone but represent complex 3-dimensional structures of different cell types, vascular tissue and the surrounding extracellular matrix (ECM) forming the tumor microenvironment (TME) (Hanahan and Weinberg, 2011; Weber and Kuo, 2012). Besides heterogeneous clonal subpopulations of cancer cells, experimental evidence points towards the existence of cancer stem cells (CSCs) in the TME (Figure 2). CSCs were characterized as a low-abundant subclass of neoplastic cells with the ability to give rise to new tumors *in vivo* and as bearing markers of normal stem cells of the cancer-affected tissue. Furthermore, recent research points towards a link between the acquisition of stemness in cancer cells leading to CSC formation and the epithelial-to-mesenchymal transition (EMT) transdifferentiation program (Scheel and Weinberg, 2012). The stromal compartment of tumors encompasses a variety of different cell types including endothelial cells, pericytes, fibroblasts, myofibroblasts and immune cells. Endothelial cells are activated from quiescence during an angiogenic switch to form neovasculature and new lymphatic vessels. Cancer-associated fibroblasts, predominantly found in carcinomas, are tumor-promoting fibroblasts derived, for example, from normal tissue-resident fibroblasts. Inflammatory immune cells of the innate and adaptive immune system, such as dendritic cells (DCs), natural killer (NK) cells, macrophages, neutrophils and cytotoxic T lymphocytes are

present in cancerous lesions to eradicate tumor cells and clear the cellular debris leading to tumor rejection. However, corrupted or alternatively activated immune cell populations promote tumor growth by secretion of growth factors, anti-inflammatory cytokines and matrix-remodeling enzymes (Gabrilovich *et al.*, 2012; Hanahan and Coussens, 2012). Tumor-associated macrophages (TAMs), one prominent example of alternatively activated innate immune cells, are major contributors to tumor neoangiogenesis. The angiopoietin receptor $TIE2^+$ macrophage population is frequently recruited by vascular endothelial cells expressing the TIE2-ligand angiopoietin 2 and align along blood vessels. Here, $TIE2^+$ macrophages stimulate the expression of vascular endothelial growth factor (VEGF) in the vascular endothelial cells and further promote tumor cell escape into the circulation in a paracrine macrophage (M-) colony stimulating factor (CSF)-epidermal growth factor (EGF) loop amongst other methods (Noy and Pollard, 2014). Consequently, determination of the immune cell infiltrates of tumors in cancer patients, often referred to as immunoprofiling or immunoscoring, can be instrumental in prognosis: high densities of tumor-infiltrating lymphocytes are positively associated with longer disease-free survival (Giraldo *et al.*, 2014). Furthermore, current anti-cancer research aims to modulate the TME by depletion of immunosuppressive cell populations and (re-)activation of anti-tumoral cytotoxic T lymphocytes. Dynamic changes in the immune infiltrates in response to this immunotherapy are evaluated to assess treatment response (Fridman *et al.*, 2011; Fridman *et al.*, 2017). Last but not least, bone marrow-derived cells (BMDCs) such as myeloid-derived suppressor cells (MDSCs), not only support tumor growth but actively suppress tumor-directed immune responses.

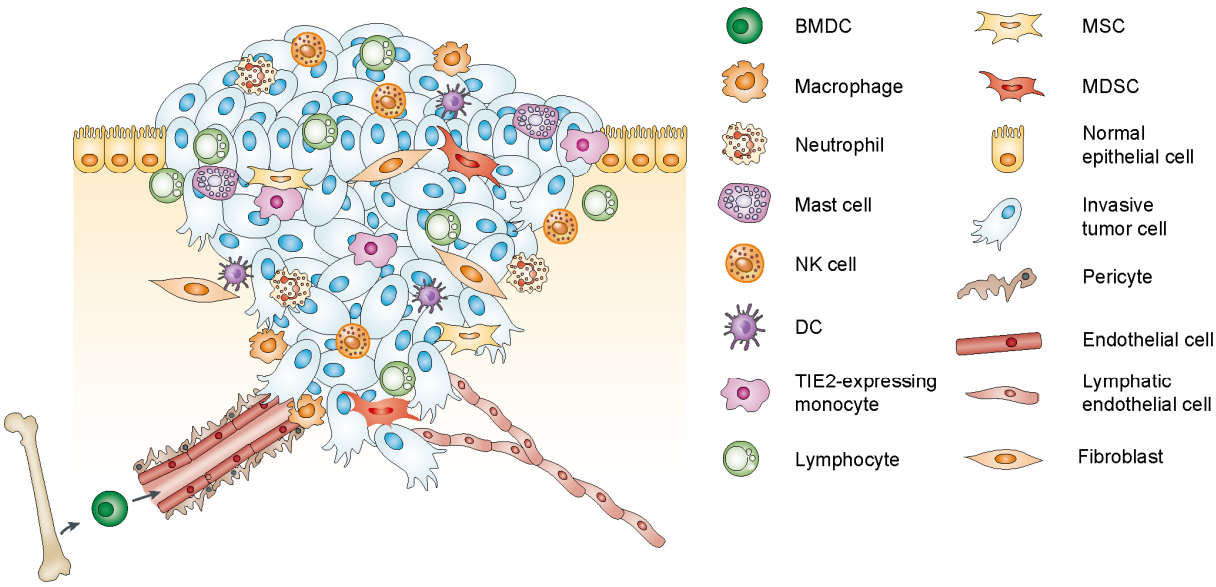

Figure 2: Schematic of the cellular composition of the tumor microenvironment.
The TME is composed of a variety of cells other than tumor cells (light blue) including immune cell infiltrates, fibroblasts, endothelial cells and BMDCs including macrophages, MDSCs, TIE2-expressing monocytes and mesenchymal stem cells (MSCs). Figure adapted from Joyce and Pollard, 2009.

1.1.2 Myeloid-derived suppressor cells

MDSC phenotype in men and mice

In the early 1900s, extramedullary hematopoiesis and neutrophilia were already described as characteristic of tumor progression. The first notion of MDSCs in this context of abnormal myeloid cell differentiation in literature was under the name of null cells or natural suppressor cells: cells lacking common lineage markers (Lin^-) with the ability to suppress lymphocyte activity and proliferation. The nature of these natural suppressor cells, however, remained elusive due to cell heterogeneity and non-consensual investigation (Talmadge and Gabrilovich, 2013). Only in recent years, the term “myeloid-derived suppressor cells” was coined and characterization standards emerged (Bronte *et al.*, 2016; Gabrilovich *et al.*, 2007). Acoording to these standards, murine MDSCs are currently divided into two phenotypically and functionally different subpopulations. Polymorphonuclear (PMN-) MDSCs, which are positive for CD11b and Ly6G and intermediate positive (int) for Ly6C ($CD11b^+/Ly6G^+/Ly6C^{int}$), have granulocyte-like morphology and express high levels of arginase type 1 (ARG1) and myeloperoxidase while $CD11b^+/Ly6^{high}/Ly6G^-$ monocytic (M-) MDSCs have monocyte-like morphology but express low levels of F4/80 and high levels of nitric oxide syntase (iNOS), ARG1 and nicotinamide adenine dinucleotide phosphate (NADPH) oxidase. Further molecular and biochemical characteristics to distinguish MDSCs from neutrophils include genomic, transcriptomic and proteomic profiling (Gabrilovich, 2017). The human PMN-MDSCs counterparts are charcterized as $CD11b^+/CD14^+/CD33^+/HLA\text{-}DR^{-/low}$ and M-MDSCs as $CD11b^+/CD15^+/CD33^+/Lin^-/HLA\text{-}DR^{-/low}$. In contrast to murine MDSCs, a third phenotypically different subtype was found in human cancer patients, $Lin^-/HLA\text{-}DR^-/CD33^+$ early-stage MDSCs lacking the expression of CD14/CD15.

Of note, MDSCs are not only expanded in cancer but also in other chronic inflammatory pathologies such as obesity, in autoimmune diseases such as arthritis (Fujii *et al.*, 2013) and in pregnancy where they sustain maternal-fetal tolerance (Veglia *et al.*, 2018)

MDSC expansion and activation

MDSC subpopulations are highly elevated in tumor-bearing mice and cancer patients. In most types of cancer, PMN-MDSCs are the prevalent MDSC population in spleen and lymph nodes of mice and peripheral blood of cancer patients. The ratio of PMN-MDSCs to M-MDSCs in peripheral blood, however, varies considerably between tumor types and individually in patients.

Tumor-derived signals hijack all differentiation steps of neutrophils - which naturally develop from granulocyte-macrophage progenitors via myeloblasts in sequential steps - resulting in the PMN-MDSC phenotype. The hijacking of the classical differentiation pathway of monocytes

and macrophages from macrophage/DC progenitors results in the M-MDSC phenotype (Figure 3). Interestingly, M-MDSCs can transdifferentiate into PMN-MDSCs and, at the tumor site, mature into TAMs while PMN-MDSCs do not further proliferate or differentiate and have a short lifetime (Youn *et al.*, 2013). Expansion of MDSCs is mediated primarily by granulocyte-macrophage CSF (GM-CSF), M- and granulocyte CSF (G-CSF), FMS-like tyrosine kinase 3 ligand (FLT3L) and VEGF amongst other tumor secreted growth factors. MDSC immunosuppressive activity is likely provoked by many different pro-inflammatory stimuli such as interleukin 6 (IL-6), IL-1β, tumor necrosis factor (TNF) or interferon (IFN)-γ. These cytokines bind to janus kinases (JAK) activating transcription factors of the signal transducers and activators of transcription (STAT) family such as STAT3, STAT5 and STAT6. In detail, STAT3 has been identified as the major STAT family transcription factor in MDSCs and regulates ARG1 production. Effects of STAT3 are mediated via CCAAT-enhancer-binding protein β and downregulation of the negative regulator of the MDSC phenotype interferon regulatory factor 8. Another important transcriptional regulator of MDSC function is hypoxia-inducible factor (HIF) 1α promoting their suppressive activity by upregulation of iNOS and ARG1. The recently elucidated inflammatory factor high mobility group box 1 further contributes to MDSC expansion and immunosuppressive activity (Marvel and Gabrilovich, 2015; Qu *et al.*, 2016; Talmadge and Gabrilovich, 2013).

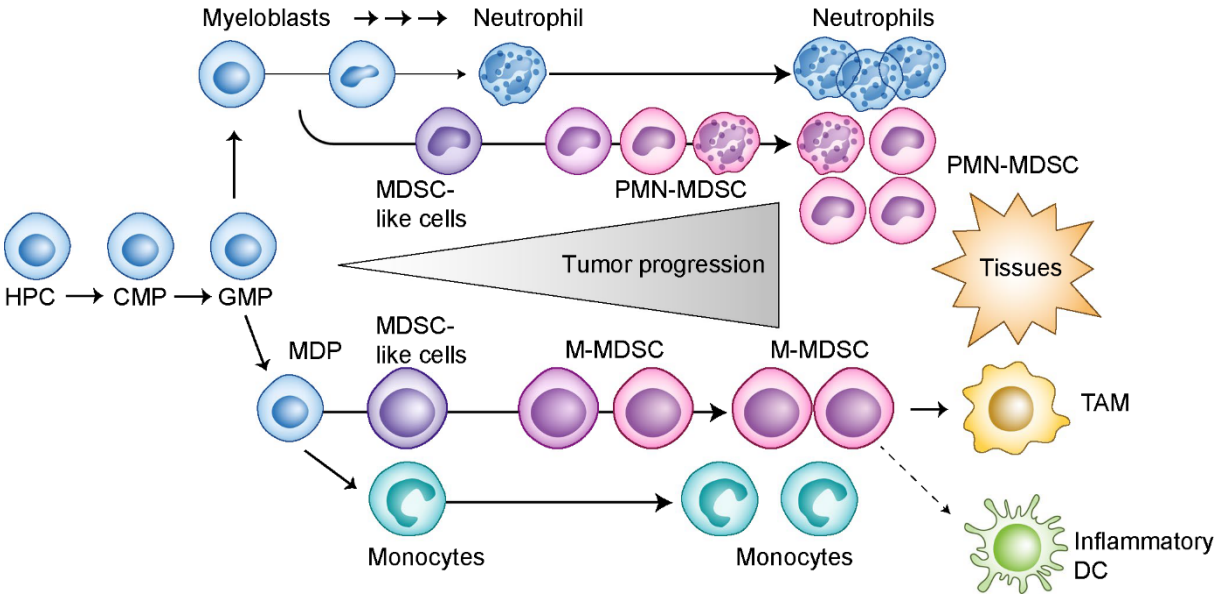

Figure 3: MDSC expansion and activation from hematopoietic progenitor cells.
Hematopoietic progenitor cells (HPCs) give rise to neutrophils and monocytes in the bone marrow via common myeloid progenitors (CMPs) and granulocyte-macrophage progenitors (GMPs). Neutrophil differentiation proceeds via several stages including myeloblasts. Monocyte/macrophage and DC precursors (MDPs) give rise to monocytes. Under pathological conditions such as the presence of tumors, non-immunosuppressive MDSC-like cells, early stages of MDSCs, and immunosuppressive MDSCs expand from immature myeloid cells. In the tumor tissue, M-MDSCs can differentiate into TAMs or inflammatory DCs. Figure adapted from Veglia *et al.*, 2018.

MDSCs as regulators of tumor progression

The major function and defining characteristic of MDSCs is the potent suppression of immune responses. MDSC use a plethora of different, partially redundant mechanisms to suppress immune responses (Figure 4). MDSCs secrete immune modulatory cytokines, chemokines and peptidases. The CC chemokine ligands (CCL) 4 and 5 chemokines attract regulatory T cells (T_{Reg}) to the TME (Figure 4 A). The high metabolic use of L-arginine and L-tryptophan by MDSCs and indoleamine 2,3-dioxygenase (IDO)-mediated sequestration of L-cysteine in the TME limits these metabolites' levels resulting in a proliferative cell cycle arrest of TME-resident T cells (Figure 4 B). Furthermore, L-arginine is metabolized via ARG1 by MDSCs leading to the production of reactive nitrogen species (RNS). Further, reactive oxygen species (ROS), predominantly superoxide, hydrogen peroxide, produced by PMN-MDSCs, and nitric oxide, produced by M-MDSCs through iNOS activity, inhibit T cell functions via nitration or nitrosylation of the T cell receptor (Figure 4 C). Additionally, nitration reduces binding of antigenic peptides to major histocompatibility type II (MHC-II) complexes on tumor cells. ROS and RNS require cell-cell-contact of MDSCs and T cells to exert their function which is commonly provided by antigen-specific interactions. PMN-MDSCs are therefore considered to suppress antigen-dependent immune responses only. The secretion of the a disintegrin and metalloprotease domain (ADAM) metallopeptidase domain 17 (ADAM17) leads to cleavage of the selectin CD62L thereby blocking T cell homing. Transforming growth factor β (TGF-β) modulates NK cell functions and IL-10, via crosstalk with macrophages, inhibits effector T cell functions (Figure 4 D). On the single cell basis, M-MDSCs possess a higher immunosuppressive activity than PMN-MDSCs. Interestingly, both PMN- and M-MDSCs isolated from tumors are more immunosuppressive than their respective counterparts in the secondary lymphoid organs indicating a pronounced effect of the TME on MDSC phenotype (Gabrilovich, 2017; Gabrilovich *et al.*, 2012; Marvel and Gabrilovich, 2015). MDSCs not only hinder tumor rejection by suppressing immune response within the TME but regulate tumor development and promote invasion and metastasis by remodeling the TME, inducing stemness or facilitating EMT in tumors cells and establishing a pre-metastatic niche. MDSCs produce large quantities of ECM-remodeling matrix metallopeptidases (MMPs), the most prominent being MMP9, facilitating tumor cell migration at the invasive margins and secrete the angiogenesis-promoting cytokines VEGF, basic fibroblast growth factor, the VEGF analog Bv8. The involvement of myeloid cells in the induction of EMT and stemness in tumor cells has only recently been described and is still under close investigation (Gabrilovich, 2017; Gabrilovich *et al.*, 2012; Marvel and Gabrilovich, 2015).

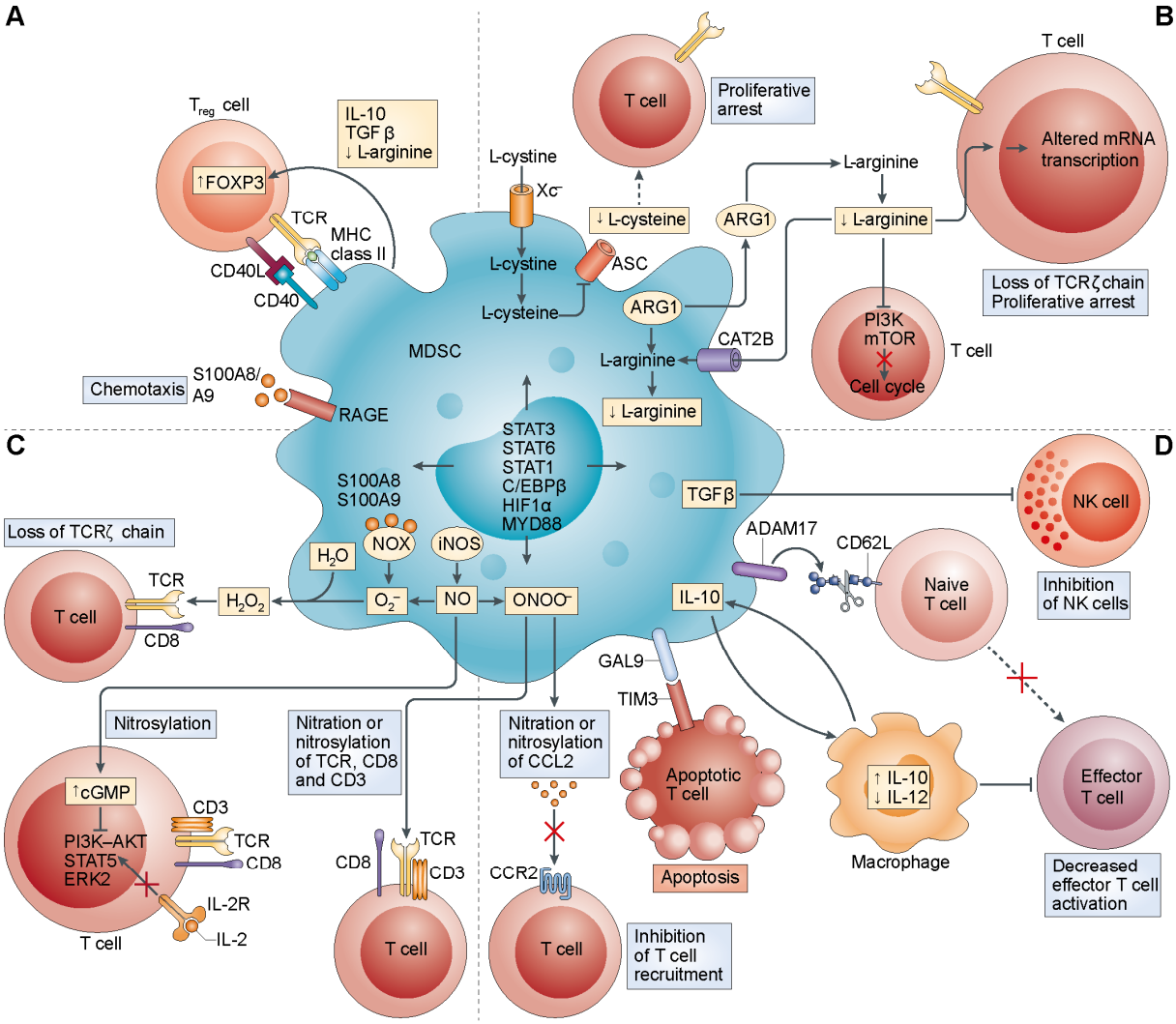

Figure 4: Mechanisms of MDSC-mediated T cell suppression.

MDSCs use a number of different mechanisms to interfere with T cell function including the induction and expansion of T_{reg} cells (**A**), the deprivation of nutrients in the TME (**B**), the release of reactive oxygen and nitrogen species of the NADPH oxidase (NOX) complex resulting in the loss of the TCRζ chain (**C**) and the interference with T cell viability and migration (**D**). ADAM17- ADAM metallopeptidase domain 17, ARG1-arginase type 1, ASC-asc-type amino acid transporter, CAT2B-cationic amino acid transporter 2 isoform 1 (L-arginine transporter), CCL2-CC-chemokine ligand 2, CCR2-CC-chemokine receptor 2, C/EBPβ-CCAAT/enhancer-binding protein-β, ERK2-extracellular signal-regulated kinase 2, FOXP3-forkhead box P3, GAL9-galectin 9, HIF1α-hypoxia-inducible factor 1α, IL-2R-IL-2 receptor, mTOR-mammalian target of rapamycin, MYD88-myeloid differentiation primary-response protein 88; PI3K-phosphoinositide 3-kinase, STAT-signal transducer and activator of transcription, TGFβ-transforming growth factor-β, TIM3-T cell immunoglobulin and mucin domain-containing protein 3, Xc-cystine–glutamate transporter. Figure modified from Gabrilovich *et al.*, 2012.

1.1.3 The pre-metastatic niche and the metastatic cascade

The concept of the pre-metastatic niche was first introduced by Kaplan *et al*. in their hallmark study in 2005 (Kaplan *et al.*, 2005) and is now largely accepted as metastasis-enabling structure in pre-disposed secondary organs. The first notion of organs favorable to metastases, however, was Stephen Paget's frequently cited "seed and soil" hypothesis. In the late 19th century, Paget noted that metastatic tumors were not randomly distributed in breast cancer patients but seemed to follow a pattern: he proposed that the tumor cells, the "seed", selectively colonize secondary organs favorable for metastatic outgrowth, the "soil" (Paget, 1889). In direct challenge of this hypothesis, Ewing described metastasis as the result of physical trapping of disseminated tumor cells in the first encountered capillary bed (Ewing, 1928). After the experimental demonstration of organ-specific metastasis (Fidler and Nicolson, 1976), termed organotropism, interest spiked in the underlying mechanism (Psaila and Lyden, 2009). Pre-metastatic niches in secondary organs are the combined consequence of the action of tumor-derived secreted factors, cytokines and chemokines, and small tumor-shed extracellular vesicles, microvesicles and exosomes (Peinado *et al.*, 2017; Sceneay *et al.*, 2013). Pre-metastatic niche formation in the lungs has been studied intensively as the lungs are frequently affected by metastatic disease of different cancer types and therefore serves as an example for the description of pre-metastatic niche formation in this work (Figure 5).

Vascular leakiness, the loss of vascular integrity leading to elevated permissiveness, is the first in a series of complex molecular and cellular changes in pre-metastatic niche formation enabling circulating tumor cells (CTCs) to extravasate. Leaky vessels permit the pro-tumorigenic and pro-metastatic re-education of stromal cells such as fibroblasts and tissue-resident macrophages by organotropic tumor-shed extracellular vesicles containing DNA, mRNA, micro RNA, metabolites and proteins (Becker *et al.*, 2016; Hoshino *et al.*, 2015). Activated stroma cells induce remodeling of the ECM by, e.g. MMP9- and tissue inhibitor of metallopeptidase 1 (TIMP1)-mediated, enzymatic digestion of ECM components and deposition of fibronectin, an ECM component permissive for the adhesion of BMDCs, versican and periostin. Recruitment of BMDCs in response to tumor-secreted G-CSF is a second important hallmark of pre-metastatic niche formation in the lungs. CCL2 potently attracts monocytes, macrophages, memory T lymphocytes and NK cells to the pre-metastatic niche. Inflammatory responses in the pre-metastatic niche and tumor cell-stromal crosstalk are frequently mediated by the inflammatory proteins S100A8 and S100A9. Moreover, the activation of HIF1 is crucial for pre-metastatic niche formation: the HIF1-target proteins lysyl oxidase (LOX) is one of the main proteins found in the pre-metastatic niche. LOX, S100A8/A9, IL-6 and IL-10 induced by hypoxia have been implicated in the recruitment of MDSCs to the pre-metastatic niche (Peinado *et al.*, 2017; Psaila and Lyden, 2009). In the pre-metastatic niche, MDSC-mediated immune suppression, expression of pro-inflammatory cytokines,

interleukins and stromal-derived factor 1 as well as secretion of MMP9 for ECM remodeling contributes to successful tumor cell colonization of the pre-metastatic niche and outgrowth of micro- to macrometastases.

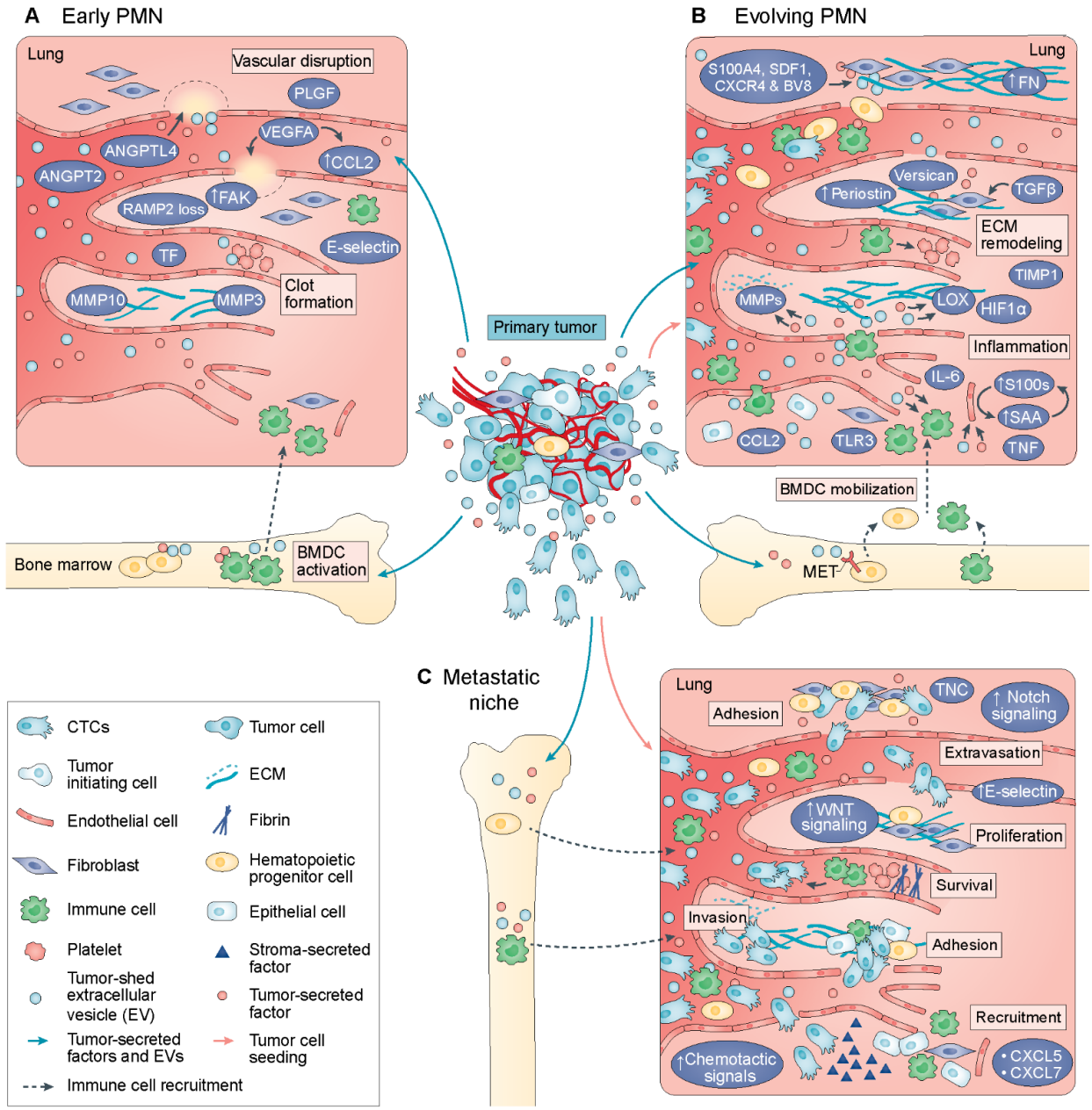

Figure 5: PMN formation in secondary organs.

Permeability of the vasculature permits the initial step of PMN formation (**A**). VEGF-A and angiopoietin-like 4 (ANGPTL4) further enhance permeability while loss of cell-cell-contacts mediated by focal adhesion kinase (FAK) activation enable metastasis. Extracellular vesicles transform stroma cells to secrete chemoattractans and tumor-derived factors, such as CCL2, and recruit BMDC populations. Clot formation, reduced interstitial flow and shear stress arrest CTCs. (**B**) The pre-metastatic niche further evolves: the ECM components fibronectin (FN), periostin or versican are deposited or remodeled aiding tumor cell invasion. Extracellular vesicles (EV) can further determine organotropsim of metastasis. S100A8- and S100A9-mediated inflammation recruits hematopoietic progenitor cells, MDSCs and immune cells. The resulting metastatic niche (**C**) facilitates CTC extravasation and metastatic outgrowth. ANGPT2-angiopoietin 2, CXCL-C-X-C-motif chemokine ligand, CXCR4-C-X-C receptor type 4, PLGF-placenta growth factor, RAMP2-receptor activity-modifying protein 2, SAA-serum amyloid A, TLR3-Toll-like receptor 3, TNC-tenascin C. Figure adapted from Peinado *et al.* 2017.

The TME, pre-metastatic niche and metastasis closely interact. Although a highly inefficient process, metastasis causes approximately 90 % of cancer-related deaths in spite of continuous research and advancing therapeutic options (Quail and Joyce, 2013). Successful metastasis of cancer cells includes invasion in the surrounding tissue, intravasation, survival and adhesion in the circulatory system, extravasation in secondary tissue pre-metastatic niches, colonization of these pre-metastatic niches by formation of micrometastases and outgrowth into metastatic lesions and is summarized as the invasion-metastasis or the metastatic cascade (Figure 6). In the recent years, a few biological principles in metastasis have emerged, particularly in metastasis of the intensively studied cancer type carcinoma, a cancer arising from epithelial cells.

The first steps of carcinoma metastasis, dissemination, is associated with the EMT transdifferentiation program initiated by reactive primary tumor stroma and mediated by EMT master transcription factors SNAIL, SLUG, TWIST or zinc finger E-box-binding homeobox 1 (ZEB1). Carcinoma cells undergoing EMT acquire a more mesenchymal, invasive, metastatic phenotype while frequently retaining some epithelial markers. This phenotypic plasticity and the possibility to undergo the reverse program, termed mesenchymal-epithelial transformation (MET), seems to be crucial for metastatic cancer cells or cell cohorts to invade and colonize secondary tissues. During EMT, epithelial cells lose adherens, tight and gap cell-cell-junctions and movement restrictions conferred by the basement membrane enabling them to escape their cell composite, invade the stromal tissue and intravasate into the circulation. The essential necessity of EMT in global cancer metastasis, however, is still an ongoing debate (Diepenbruck and Christofori, 2016). Immune cells at the primary tumor sites actively contribute to invasion and metastasis: in hypoxic areas TAMs promote tumor angiogenesis and in stromal areas contribute actively to invasion and intravasation (Gabrilovich *et al.*, 2012). Once in blood or lymphatic vessels, CTCs have to resist anoikis, shear stress and NK cell cytotoxicity before platelets form protective structures around the CTCs (Joyce and Pollard, 2009). Furthermore, activated platelets secrete adenosine triphosphate (ATP) or clot both facilitating transendothelial migration of CTCs either through ATP-induced gaps between the endothelial cells or through the lumen of the endothelial cells. In the secondary organ pre-metastatic niche, extravasated tumor cells find a microenvironment favorable for colonization and metastatic outgrowth (Gupta and Massagué, 2006; Lambert *et al.*, 2017).

MDSCs are involved in all steps of the metastatic cascade. At the primary tumor site, as discussed above, MDSCs suppress immune responses against tumor cells and secret hypoxia-induced pro-angiogenic factors that elicit angiogenesis and shape the pre-metastatic niche. Additionally, MDSC-secreted TGF-β has been shown to fuel EMT in carcinoma cells. At the invasive margins, MDSCs secrete MMP9 contributing to ECM remodeling for invasion and intravasation and factors inducing stemness in cancer cells. At the pre-metastatic organs,

MDSCs arrive before the disseminated tumor cells and shape the microenvironment to favor metastatic colonization. Demonstrative of their function, MDSC levels in the peripheral blood of cancer patients correlate negatively with patient survival (Condamine *et al.*, 2015; Quail and Joyce, 2013).

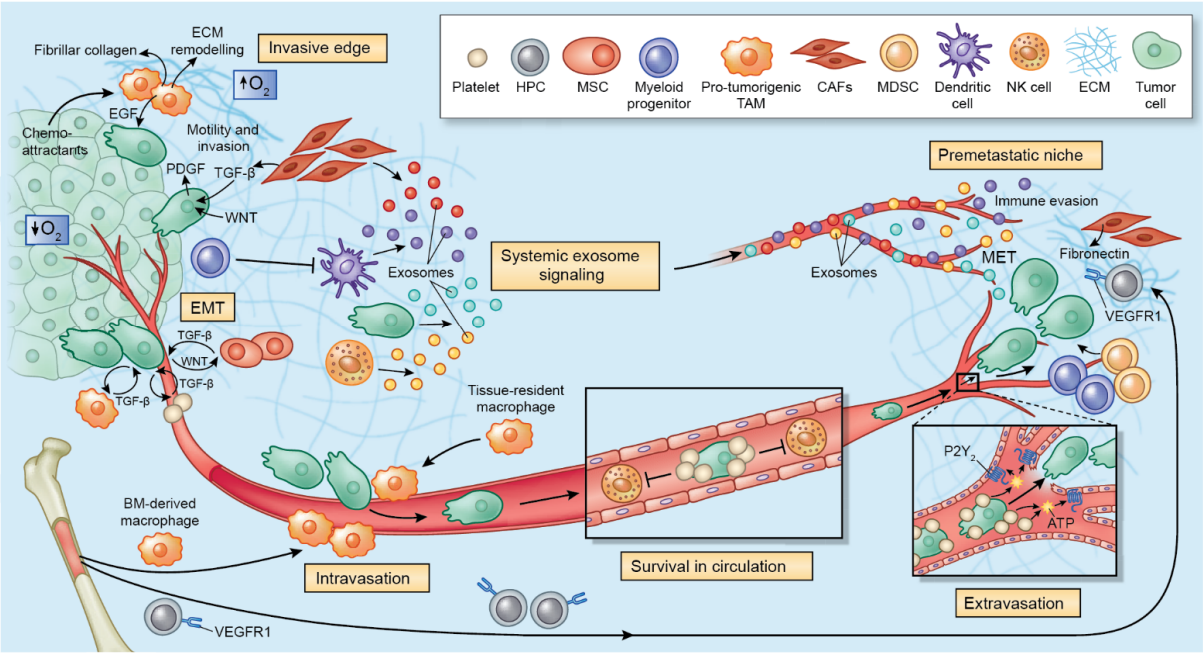

Figure 6: The invasion-metastasis cascade.
Tumor cells with phenotypic plasticity owed to EMT intravasate, survive in the circulation and extravasate at secondary sites with permissive pre-metastatic niches. Macrophages, cancer-associated fibroblasts and MDSCs actively contribute to metastasis at the invasive tumor margins while platelets shield disseminated tumor cells in the circulation from immune recognition and facilitate extravasation. Figure adapted from Quail and Joyce, 2013.

1.2 Metabolism and cancer biology

A complex network of metabolic pathways for anabolism and catabolism of carbohydrates, proteins and lipids is coordinated and reciprocally regulated in mammalian cells. One hallmark of cancer is the reprogramming of cellular metabolism. During cancerogenesis, cancer cells frequently reprogram cellular metabolic pathways to support tumor initiation and progression. This reprogramming of the metabolism often results in the exhibition of a specific metabolic phenotype of the transformed cells in comparison to the adjacent normal tissue cells.

The historically first discovered and in-depth investigated cancer metabolic phenotype is the glycolytic phenotype resulting from the deregulation of the metabolic pathway of D-glucose, glycolysis (Figure 7). Glucose, a monosaccharide and a digestion product of complex carbohydrates, is ubiquitously used in human metabolism.
In the resting physiological state when oxygen is abundant, glucose is imported into the cells by GLUT uniporters through facilitated diffusion, first metabolized to pyruvate via glycolysis and finally oxidized to CO_2 via the citric acid cycle (also called Krebs cycle or tricarboxylic acid cycle, TCA) and oxidative phosphorylation (OxPhos). Oxidative decarboxylation of pyruvate and activation of acetate to acetyl-coenzyme A (CoA) is catalyzed by the pyruvate dehydrogenase complex in the mitochondrial lumen. Acetyl-CoA then enters the TCA for complete oxidation under production of NADH (nicotinamide adenine dinucleotide, NAD; reduced form) and $FADH_2$ (flavin adenine dinucleotide, FAD; reduced form). In OxPhos, the reductive potential of NADH and $FADH_2$ is first converted into an electrochemical gradient over the inner mitochondrial membrane that is the driving force of ATP synthase catalyzing, in a second step, ATP formation. ATP is the common way to provide free energy to allow otherwise thermodynamically unfavorable biochemical reactions. In this fashion, complete oxidation of 1 molecule glucose yields in total up to 38 molecules ATP.
Under anaerobic conditions, cellular glucose metabolism is restricted to anaerobic glycolysis bypassing the TCA and OxPhos. In anaerobic glycolysis or glucose fermentation, pyruvate as metabolic end product is reduced to lactate by lactate dehydrogenases (LDH) to reconstitute the NAD^+ needed to sustain glycolysis. Lactate produced in anaerobic glycolysis is exported from the cells to the liver where glucose is regenerated via gluconeogenesis to avoid lactic metabolic acidosis (Cori cycle). Anaerobic glycolysis is energetically far less efficient than aerobic glycolysis, yielding only 2 molecules ATP per molecule glucose.
Glycolysis is tightly regulated and highly coordinated with other metabolic pathways to meet the need for energy in the form of ATP and glucose-derived biosynthetic building blocks. In the glycolytic cascade, the enzymes hexokinase, phosphofructokinase (PFK) and pyruvate kinase serve as control points for glycolytic flux and are subject to allosteric regulation, covalent modifications conveyed by regulating enzymes and transcriptional control. Hexokinase is

subject to feedback inhibition by glucose-6-phosphate. Pyruvate kinase is allosterically inhibited by ATP and alanine and regulated by phosphorylation in the liver. PFK, the enzyme committing glucose to the glycolytic pathway, is the key regulator of glycolytic flux. PFK is inhibited allosterically by ATP, citrate and H^+ and covalently by phosphorylation and transcription is suppressed by glucagon signaling. Furthermore, fructose-2,6-bisphosphate, a potent activator of PFK, diminishes the inhibitory effect of ATP. The inhibition of glycolysis by respiration under normal oxygen concentrations, largely mediated by allosteric inhibition of PFK by ATP and citrate, is commonly referred to as the Pasteur effect (Berg *et al.*, 2007).

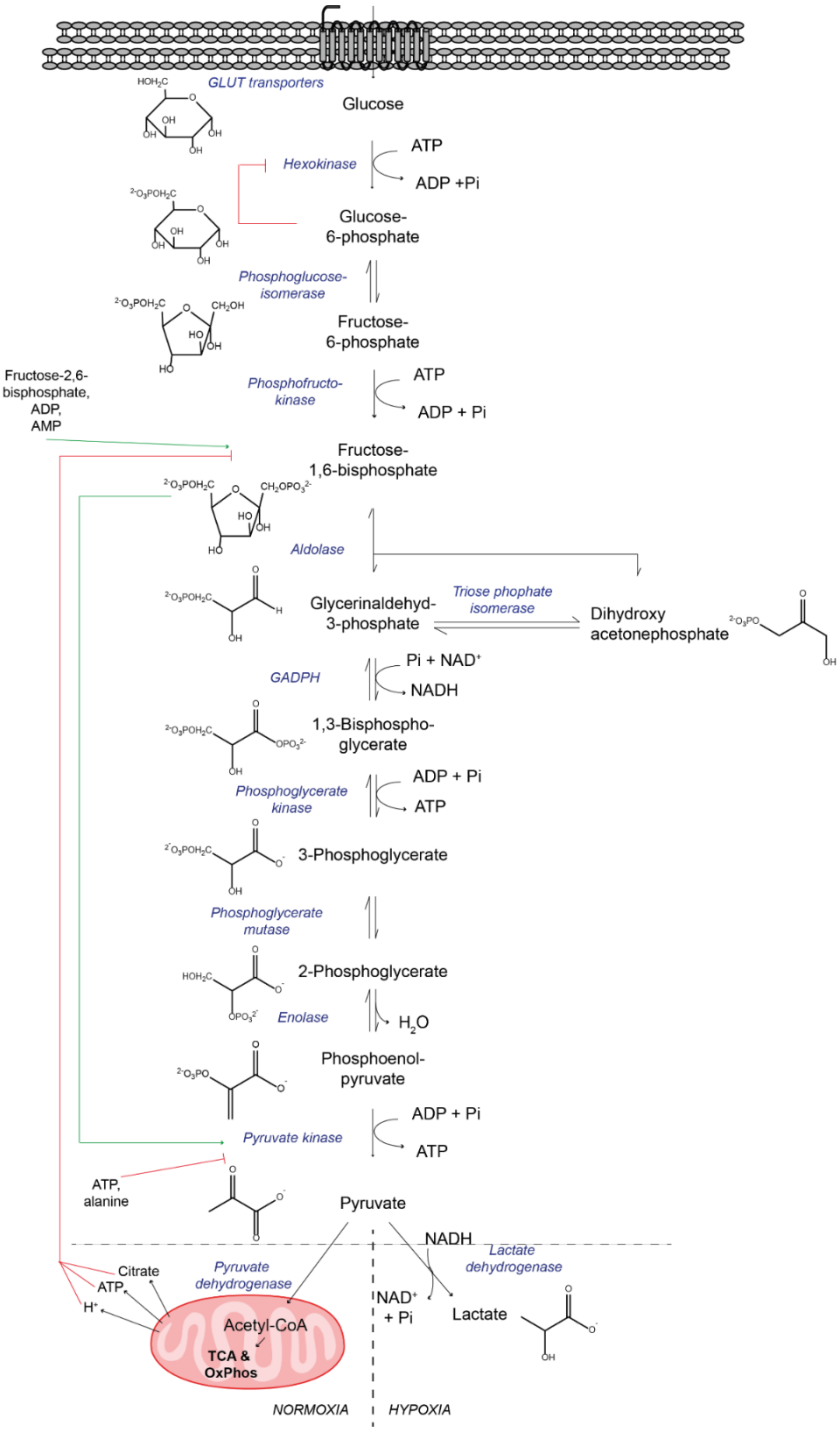

Figure 7: Glycolysis and fate of pyruvate under hypoxic and normoxic conditions.

Glucose is imported into the cells via GLUT transporters and metabolized in the glycolytic enzymatic cascade. Under normoxic conditions, pyruvate is completely oxidized in the mitochondria in the TCA and OxPhos (normoxia, bottom left) while lactic fermentation takes place in oxygen-deficient environments (hypoxia, bottom right). Glycolytic enzymes are printed blue and italic, allosteric regulation of the glycolytic enzymes is indicated as inhibition with red arrows for inhibitory effects and green arrows for stimulatory effects. Figure modified from Berg *et al.*, 2007.

1.2.1 The metabolic switch during tumorigenesis: the Warburg effect

Enhanced glycolysis under normoxic conditions, aerobic glycolysis, was first described as a common metabolic feature of cancer cells by Otto Warburg in the 1920s. Warburg was awarded the Nobel Prize in Physiology or Medicine in 1931 for his observations. The Warburg effect describes enhanced glucose consumption and glycolytic flux decoupled from the TCA and OxPhos in the mitochondria under normoxic conditions. A mitochondrial defect abrogating cellular respiration was originally hypothesized to be the cause for aerobic glycolysis in cancer cells (Warburg, 1956) and remained the central dogma until contradictory evidence emerged. Aerobic glycolysis, however, represents an excellent strategy to produce ATP and glucose-derived carbon building blocks for the synthesis of biomass needed for proliferation while maintaining the cellular redox balance. Indeed, tumor cells rely on glycolysis to supply the biosynthetic pathways essential for proliferation with precursor molecules (Figure 8). The pentose phosphate pathway (PPP), for example, is fueled by the glycolytic intermediate glucose-6-phosphate to produce ribose-5-phosphate, the carbohydrate backbone of all nucleotides, and 5-phosphoribosyl-α-pyrophosphate, one major carbon source in nucleotide synthesis. Additionally, the glycolytic intermediate dihydroxyacetone phosphate is the metabolic precursor of glycerin-3-phosphate, the backbone of glycerophospholipids and an important component in lipid biosynthesis. The glycolytic intermediate 3-phosphoglycerate can enter protein biosynthesis after conversion to serine and further provides the cofactor tetrahydrofolate with one-carbon units for methylation reactions. Transamination of pyruvate via alanine aminotransferase (ALAT) results in alanine production (Lunt and Vander Heiden, 2011). Furthermore, ATP production from glucose via glycolysis is faster than complete oxidation of glucose. The maintenance of the cellular redox balance in the form of NAD^+/NADH and $NADP^+$/NADPH is essential to sustain proliferation. The reduction of pyruvate to lactate is a fast and extremely efficient way to regenerate NAD^+ from NADH to maintain the redox balance. Tumor cells seem to increase lactate production to ensure a fast proliferation capacity. This is further discussed in the literature as a general lack of electron acceptors as a proliferation-limiting factor in cancers. Additionally, in proliferating cells, the amount of glucose taken up cannot be committed to glycolysis for complete oxidation and ATP production since the need for carbon atoms and NADPH for biosynthesis is higher than the need for ATP (Lunt and Vander Heiden, 2011). Indeed, cancer cells have a low NAD^+/NADH ratio which correlates better to their growth rate than the ATP/ADP ratio (Vander Heiden and DeBerardinis, 2017).
Of note, recent evidence suggests an oxidative phenotype in some cancer cells and tumors. Metabolic heterogeneity between tumor cells can promote overall tumor growth: an oxidative population of cancer cells takes up the lactate produced by glycolytic population of cancer cells (Vander Heiden and DeBerardinis, 2017).

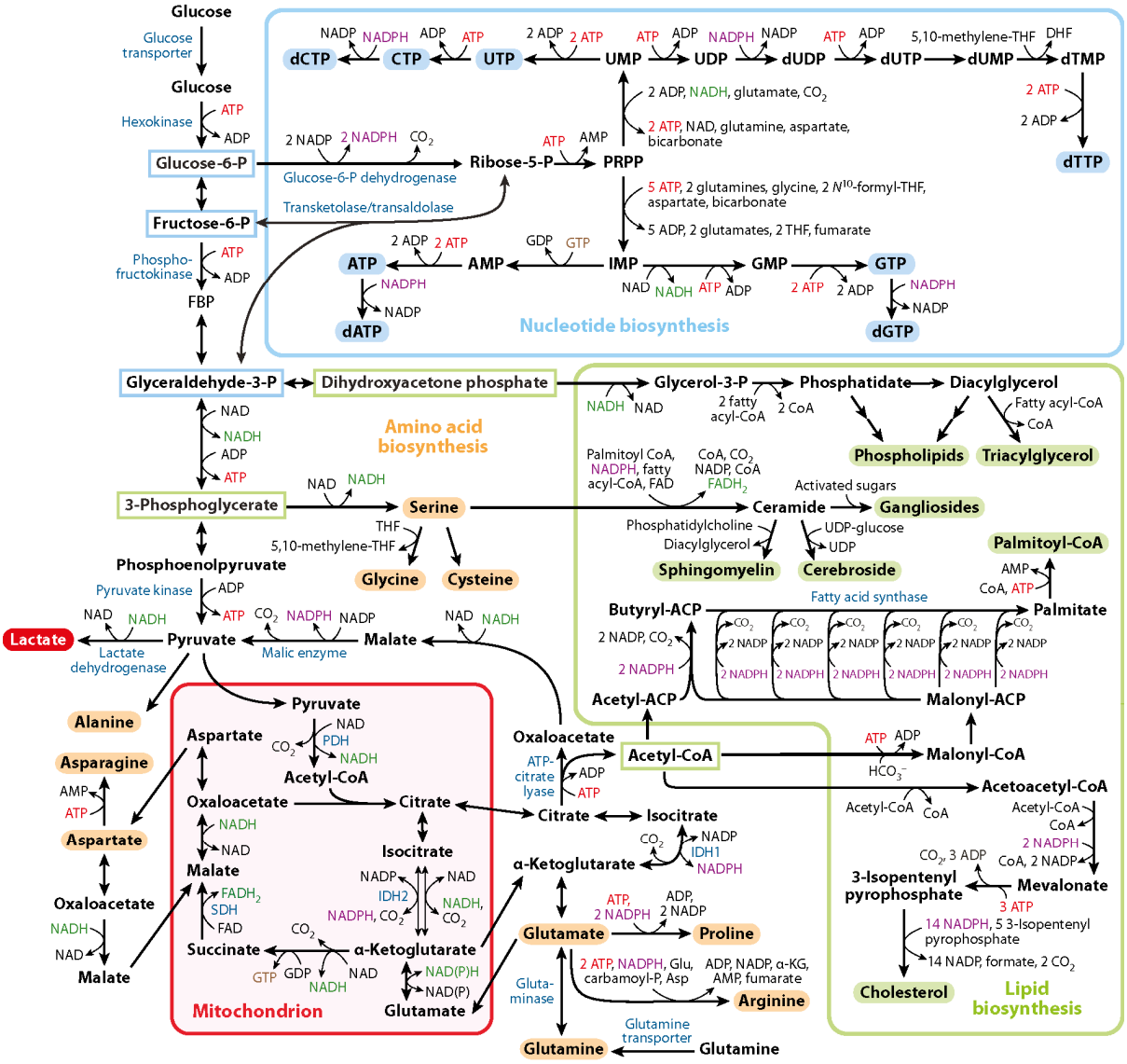

ACP	Acyl carrier protein
ADP	Adenosine diphosphate
Asp	Aspartate
ATP	Adenosine triphosphate
CoA	Coenzyme A
CTP	Cytidine triphosphate
dATP	Deoxyadenosine triphosphate
dCTP	Deoxycytidine triphosphate
dGTP	Deoxyguanosine triphosphate
DHF	Dihydrofolate
dTMP	Deoxythymidine monophosphate
dTTP	Deoxythymidine triphosphate
dUDP	Deoxyuridine diphosphate
dUMP	Deoxyuridine monophosphate
dUTP	Deoxyuridine triphosphate
FAD	Flavin adenine dinucleotide
$FADH_2$	Flavin adenine dinucleotide, reduced
Glu	Glutamate
GMP	Guanosine monophosphate
GTP	Guanosine triphosphate
IDH1	Isocitrate dehydrogenase 1
IDH2	Isocitrate dehydrogenase 2
IMP	Inosine monophosphate
NAD	Nicotinamide adenine dinucleotide
NADH	Nicotinamide adenine dinucleotide, reduced
NADP	Nicotinamide adenine dinucleotide phosphate
NADPH	Nicotinamide adenine dinucleotide phosphate, reduced
P	Phosphate
PDH	Pyruvate dehydrogenase
PRPP	Phosphoribosyl pyrophosphate
SDH	Succinate dehydrogenase
THF	Tetrahydrofolate
UDP	Uridine diphosphate
UMP	Uridine monophosphate
UTP	Uridine triphosphate
α-KG	α-Ketoglutarate

Figure 8: Cellular metabolic pathways and cross-talk points.

Glycolysis (top left), the citric acid cycle (bottom left), the pentose phosphate pathway (not depicted in detail), nucleotide biosynthesis (top right), amino acid biosynthesis (not depicted in detail) and lipid metabolism (bottom right) share common metabolites and are tightly and interdependently regulated. Glutamine metabolism (bottom middle panel) takes an exceptional position in metabolism of some cancer types. Figure modified from Lunt *et al.*, 2011.

1.2.2 Metabolic reprogramming in cancer

Genomic instability and the acquisition of mutations with increases in the mutational burden have been widely accepted as fundamental in tumorigenesis. Interestingly, beside mutations in oncogenes and loss of tumor suppressor genes, somatic mutations in enzymes of metabolic pathways may have a transforming effect on cancer cells (Vander Heiden and DeBerardinis, 2017). Moreover, the signaling pathways that stimulate proliferation often also regulate metabolism giving rise to a metabolic phenotype (Figure 9). Phosphatidylinositol-4,5-bisphosphate 3-kinase (PI3K) is exemplary for the regulation of tumor proliferation and tumor metabolism: PI3K is not only often mutated and hyperactive in cancer cells but also a major regulator of glucose metabolism. PI3K signaling through the protein kinase AKT increases GLUT1 expression and inhibits GLUT1 internalization, maintains hexokinase activation and directly activates PFK leading to a stimulation of glycolysis. Moreover, the PI3K pathway possibly mediates activation of HIF. HIF not only stimulates angiogenesis but also aerobic glycolysis by transcription of glucose transporters and many enzymes of the glycolytic cascade with hypoxia-response elements in their promotor. Elevated levels of pyruvate dehydrogenase kinase phosphorylate and inactive the pyruvate dehydrogenase complex thereby reducing pyruvate flux to the TCA and increasing lactate production. Besides PI3K, oncogenes and loss of tumor suppressor genes commonly found in human cancers such as c-Myc, phosphatase and TENsin homologue (PTEN) and p53 have been associated with the Warburg effect.

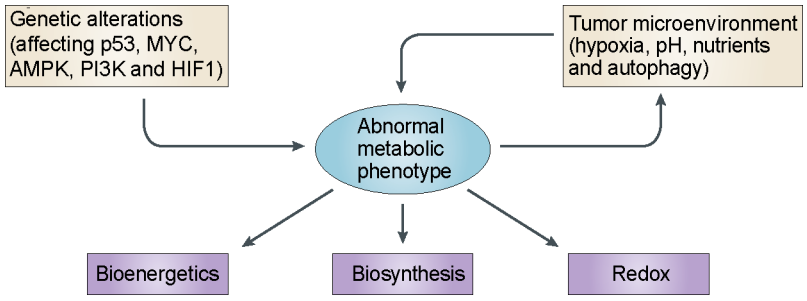

Figure 9: Interplay between genetic and metabolic alternations in cancer.
Genetic alterations may impact cellular metabolic pathway giving rise to metabolic phenotypes that interact closely with the TME. Figure adapted from Cairns *et al.* 2011.

Beside the Warburg effect, a dependence of cancer cells on the amino acid glutamine is frequently observed. Catabolism of glutamine to produce ATP and supply the TCA with anaplerotic carbons for biosynthetic pathways is referred to as glutaminolysis. Glutamine is an abundant nutrient while glutamate is scarce. By deamination of glutamine to glutamate, tumor cells have an advantage compared to normal cells. This reaction is mediated by the mitochondrial enzyme glutaminase and can release ammonia. Glutamine, however, is also an important nitrogen donor for the synthesis of purine and pyrimidine nucleotides. Glutamate can

further be converted to glutathione, a major antioxidant in the cells, or to α-ketoglutarate, an anaplerotic TCR intermediate. Additionally, in the hexosamine biosynthetic pathway, glutamine's amido group is transferred to fructose-6-phosphate to form glucosamine-6-phosphate, a precursor for N-linked and O-linked glycolsylation reactions. This reaction is mediated by glutamine:fructose-6-phosphate amidotransferase (DeBerardinis and Cheng, 2010).

Reprogramming of other metabolic pathways and, consequently, the exhibition of a characteristic metabolic phenotype can further serve as a biomarker for malignant transformation or cancer. The deregulation of the lipid metabolism, for example, encompasses the active upregulation of lipid biosynthesis of the three classical lipids, fatty acids, phospholipids and cholesterol. The phospholipid phosphatidylcholine and its metabolic precursors were intensively investigated in the last years. The cholinic phenotype refers to choline (Cho) and the metabolite phosphocholine (PCho) as biomarker for malignant transformation. Phosphatidylcholine is one of the major components of the lipid bilayer structure of cell membranes. PCho is both a precursor in the biosynthesis pathway and a breakdown product of phosphatidylcholine. Increased PCho and total choline-containing compounds (tCho) levels have been detected in human cancers of different origin. Of note, elevated PCho and tCho levels were observed in breast cancers (Glunde *et al.*, 2011). Enzymes of the choline metabolic pathway are regulated by different oncogenic signaling pathways. The RAS pathway, for example, activates mitogen-activated protein kinases (MAPK) which in turn modulates expression of sterol regulatory element binding proteins that induce expression of enzymes in the choline metabolic pathway. Furthermore, evidence points towards PI3K-AKT signaling affecting the activation of choline kinase (Glunde *et al.*, 2011).

Additionally to phosphatidylcholine, the family of sphingolipids and sphingolipid metabolism have recently been recognized for an involvement in malignant transformation, cancer-relevant cell proliferation, apoptosis and angiogenesis pathways. The sphingolipid family encompasses ceramide, sphingosine, sphingomyelin and sphingosine-1-phosphate, lipids that are metabolically interconvertible with ceramide as the central hub. Elevated levels of sphingosine kinase 1 were found in biopsies of breast cancer patients and, interestingly, evidence suggests a mediatory function of sphingosine kinases between estrogens and growth factor signaling in breast cancer (Furuya *et al.*, 2011).

1.2.3 Metabolic changes as drivers for tumor metastasis

Although therapeutic options for cancer improved considerably over the last decades, metastatic disease remaines the main cause for cancer-related deaths. The relation of metabolism and metastasis, however, is still the subject of ongoing intensive biomedical research.

At the primary tumor site, increased lactate generation and excretion of high levels of lactate as an effect of aerobic glycolysis conditions the TME. Both lactate and the excreted protons acidify the extracellular pH giving tumor cells adapted to the extracellular acidosis a survival advantage over non-transformed cells. Additionally, experimental evidence suggests a metabolic interplay between glycolytic tumor cells and tumor cells with oxidative metabolism: lactate secreted by the glycolytic populations is actively imported for energy generation in the oxidative population. In this fashion, tumor cells have another survival advantage compared to normal resident tissue cells. Besides, acidosis can be mutagenic possibly by inhibition of DNA repair mechanisms. Furthermore, lactate excretion might promote invasion by facilitating degradation of the ECM. In summary, the glycolytic phenotype creates a tumor-favorable microenvironment and is correlated with poor outcome in cancer patients (Gatenby and Gillies, 2004; Lunt and Vander Heiden, 2011).

At both primary and pre-metastatic sites, the niches for cancer cells are preconditioned: the microRNA miRNA-122 has been reported to downregulate expression of GLUT-1 and the pyruvate kinases isozymes in normal resident cells. This increases glucose abundance for disseminated cancer cells and provokes a glycolytic phenotype in the metastatic lesions. The glycolytic phenotype in metastatic lesions has been a central dogma inherited from countless patient studies (Gillies *et al.*, 2008). Recent evidence, however, points towards metabolic heterogeneity of metastatic cells. The metabolic program of cancer cells colonizing different secondary organs seems different and dynamic within both the TME and secondary organs. Although a few recent studies provided insight into the metabolic heterogeneity of tumor cells during tumor formation and metastasis, the underlying mechanistic connections between the metabolic behavior of the tumor cells during each step of metastasis, and the signaling pathways that mediate metastatic growth, however, remain elusive (Pascual *et al.*, 2018).

1.3 Preclinical tumor, pre-metastatic niche and tumor metastasis models

1.3.1 Polyoma virus middle T-derived mammary carcinoma model

Breast cancer is the single most common cancer in women with an estimated incidence of 404,900 in 2018 in Europe alone. Breast cancer is also estimated to be the second most frequent cause of cancer-related death (Ferlay *et al.*, 2018). Hereditary breast cancer caused by somatic mutations in cancer-related genes makes up between 5-10 % of all cases. Dependent on staging of the disease and the molecular phenotype, therapy options include the surgical clearance of the cancerous lesion, localized radiation therapy and systemic chemotherapy, hormone therapy or targeted therapy with monoclonal antibodies. Breast cancer management is currently oriented towards personalized care (McDonald *et al.*, 2016; Warrier *et al.*, 2016).

The widely studied genetically engineered mouse strain B6.FVB-Tg(MMTV-PyVT)634Mul/LellJ served as basis for the allograft mouse mammary carcinoma model used in this work. B6.FVB-Tg(MMTV-PyVT)634Mul/LellJ mice are transgenic for the expression of the polyoma virus middle T antigen (PyMT) under the transcriptional control of the mouse mammary tumor virus (MMTV) long terminal repeat (LTR) promotor. PyMT expression is restricted to the mammary epithelium with low to undetectable expression in other tissue (Guy *et al.*, 1992). Tumor formation in the MMTV-PyMT mouse model progresses from first hyperplasia and adenomas via early carcinomas to invasive carcinomas in a step-wise manner resembling human disease progression. Polyclonal tumors arise as early as 7-8 weeks of age in all mammary fat pads in both males and females and mice frequently develop lung metastases at a later stage (Maglione *et al.*, 2001). Additionally to the stage-wise progression resembling human disease, biomarker expression is similar to human breast cancers including loss of expression of estrogen and progesterone receptors (Lin *et al.*, 2003). The potent tumorigenic capacity of the PyMT oncoprotein is caused by the capacity to activate critical signaling kinases of the Src family, the PI3K subunit p85, phosphoinositide phospholipase C (PLC) γ and 14-3-3 adaptor proteins (Marcotte and Muller, 2008; Raptis *et al.*, 1991). These signaling pathways are also involved in human disease (Verbeek *et al.*, 1996; Wood *et al.*, 2007).

Based on the classical MMTV-PyMT mouse model, a transplantable murine breast cancer model was used in this thesis (Sceneay *et al.*, 2018; Wong *et al.*, 2012). The orthotopic injection of the MMTV-PyMT-derived established cell line S2WTP3 results in the rapid growth of allograft tumors. Tumor nodules are palpable after 7 days and allografts reach end stage in approximately 3-4 weeks after tumor induction. In comparison to the MMTV-PyMT mouse model, this transplantable tumor model was chosen due to the restriction of tumor growth to

the injection site, the rapid growth of homogenous tumors while reducing overall tumor burden and abolishing the need for elaborate breeding of the B6.FVB-Tg(MMTV-PyVT)634Mul/LellJ mice. In the second MMTV-PyMT-derived murine breast cancer model, the orthotopic injection of the established cell line ML1B1B1 results in the rapid, aggressive growth of breast cancer tumors that reach end stage in 10-14 days after induction.

1.3.2 B16 melanoma model

Melanoma, skin cancer caused by degeneration and pathological proliferation of epidermal melanocytes, is the sixth most frequent cancer in males and the seventh most frequent cancer in females with approximately 120,500 expected new incident cases in 2018 in Europe alone (Ferlay *et al.*, 2018). Melanoma patients benefit from surgical removal of the cancerous lesions, however, relapse and metastatic disease require systemic treatment. Management of melanoma metastatic disease experienced a paradigm shift in the recent decade towards immunotherapy with monoclonal antibodies and adjuvant therapeutics (Corrie *et al.*, 2014; Rotte *et al.*, 2015).

The B16 melanoma cell lines were established for cell culture from a spontaneously arising melanoma in a wild-type C57BL/6 mouse. The B16 daughter cell lines were derived from the parental B16 cell line by *in vivo* selection for the ability to form lung metastases after intravenous (*i.v.*) injection. Accordingly, the B16-F10 melanoma cell line was established in cell culture after 10 cycles of *i.v.* injections and cell isolation from metastatic foci (Fidler, 1973). Consequently, the B16 melanoma model represents a syngeneic, transplantable tumor model. *In vivo,* the B16 cell lines grow to end stage within 14 days after intracutaneous or subcutaneous injection (Overwijk and Restifo, 2001). Although B16-F10 melanomas are considered poorly immunogenic, these tumors secrete cytokines and chemokines responsible for the recruitment of immune cells and, indeed, exhibit immune cell infiltrates rendering the mouse model suitable for cell trafficking studies (Lechner *et al.*, 2013; Romano *et al.*, 2018).

1.3.3 Preclinical pre-metastatic niche models

Pre-metastatic niche formation in secondary organs is dependent on a multitude of factors including the secretion of inflammatory cytokines, chemokines, growth factors and extracellular vesicles by the primary tumor, recruitment of BMDCs and immune cells and the remodeling of the local organ microenvironment. Therefore, experimental modeling of this complex procedure *in vivo* to study pre-metastatic niche formation and elucidate key factors is challenging.

Repeated application of cytokines, chemokines and growth factors represents one way to model the pre-metastatic niche *in vivo*. Kaplan *et al.* first described experimental pre-metastatic niche formation *in vivo* by application of tumor cell-conditioned media (CM). Detection of VEGF receptor (VEGFR) positive bone marrow-derived hematopoietic progenitor cells in the lungs implicated pre-metastatic niche formation (Kaplan *et al.*, 2005). Tumor cell CM essentially represents an uncharacterized cocktail of cytokines, chemokines and growth factors. VEGF has been implicated as one crucial factor in pre-metastatic niche formation, especially in the formation of a lymph node pre-metastatic niche (Sleeman, 2015). Repeated *i.v.* injections of purified recombinant VEGF-C led to the formation of a lung pre-metastatic niche in wild-type BALB/c mice (Scherer and Sleeman, 2017). Further, transgenic mice overexpressing VEGF-C specifically in the skin exhibited increased lymph node-lymphangiogenesis promoting chemically induced skin cancer metastasis to the sentinel lymph node (LN) and the lungs (Hirakawa *et al.*, 2007).

Tumor-derived exosomes elicit an organ-specific pre-metastatic niche and contribute to cancer-type dependent organotropism in metastasis (Becker *et al.*, 2016; Weidle *et al.*, 2017). Application of murine B16-F10 melanoma-derived exosomes into the footpads of albino C57BL/6 mice led to exosome trafficking to the draining LN in this model, followed by enhanced melanoma cell migration to the sites of exosome migration (Hood *et al.*, 2011). Likewise, fluorescently-tagged breast cancer-derived exosomes could be followed to the lungs of BALB/c mice conditioning a favorable microenvironment for metastasis (Wen *et al.*, 2016). Engineered niche-mimicking biomaterials represent a more sophisticated yet experimentally challenging way to model the pre-metastatic niche *in vivo*. Further, these scaffolds pose excellent tools to study the contribution of individual secreted factors to cell recruitment and formation of the pre-metastatic niche (Aguado *et al.*, 2017*)*. Interestingly, the combined use of exosomes embedded in a 3D scaffold resulted in a potent artificial pre-metastatic niche that modulated peritoneal metastasis in a preclinical setting (de la Fuente *et al., 2015)*.

1.3.4 Preclinical metastasis models

Genetically engineered mouse models (GEMMs) or transplantable models including spontaneous and experimental models of metastasis represent the two main available mouse models for metastasis.

GEMMs, such as the before mentioned MMTV-PyMT mouse strain, develop tumors *de novo* with varying rates of metastasis formation. Due to the *de novo* tumor formation in a natural microenvironment in an immunocompetent host, GEMMs have the potential to mimic all stages of the metastatic cascade closely. Although GEMM were designed to resemble human pathological characteristics of the respective disease including tumor heterogeneity, the

genetic background is restricted. While not all animals develop metastatic disease, much less so synchronously, the long latency of metastatic disease requires the resection of the primary tumors. Additionally, metastatic tropism can deviate from the clinical situation (Gómez-Cuadrado *et al.*, 2017; Khanna and Hunter, 2005; Saxena and Christofori, 2013).

Spontaneously metastasizing allograft transplantation models represent an alternative to model the entire metastatic cascade *in vivo*. Orthotopic transplantation, if experimentally possible, allows for interactions of the tumor cells with the tissue of origin. Metastatic disease then follows primary tumor growth. As discussed for GEMMs, a long latency period of metastatic disease commonly requires the removal of the primary tumor which is usually only possible for mammary tumors and melanoma (Gómez-Cuadrado *et al.*, 2017; Khanna and Hunter, 2005; Saxena and Christofori, 2013). Due to its frequent and rather fast metastatic spread to the lungs, the syngeneic allograft 4T1 breast cancer model has often been used for non-invasive imaging of immune cell migration (Makela and Foster, 2018; Makela *et al.*, 2017) or of the distribution of the cancer cells *in vivo* (Danhier *et al.*, 2015).

In all experimental metastasis models, cancer cells are introduced directly into the vasculature by either intraportal, intracarotid, intracardiac or *i.v.* injection into the lateral tail vein. Consequently, experimental metastasis models are not suitable to model the first steps of the metastatic cascade but model homing of the cancer cells to the secondary organs. Once in the circulation, the cancer cells need to successfully arrest, extravasate and colonize the recipient tissue to form macrometastases. In this process, the site of injection defines the site of colonization: injection into the lateral tail vein leads to formation of lung metastases, intraperitoneal injection restrict metastases to the peritoneum while intracardiac injections allow wider dissemination of cancers cells and metastases formation in the brain and bone (Gómez-Cuadrado *et al.*, 2017). MDSC tracking with optical imaging in a metastatic breast cancer induced by intracardiac injection was recently described (Sceneay *et al.*, 2018).

1.4 Non-invasive imaging and spectroscopic modalities

The following part introduces the non-invasive imaging modalities used in this work, namely positron emission tomography (PET) and optical imaging (OI) as well as the imaging techniques based on the phenomenon of nuclear magnetic resonance (NMR), nuclear magnetic resonance imaging, ^{1}H NMR spectroscopy and dynamic nuclear polarization (DNP) for hyperpolarized ^{13}C MR spectroscopy.

1.4.1 Positron emission tomography

Positron emission tomography (PET) was developed by Michael E. Phelps and Michel Ter-Pogossian in 1975 (Ter-Pogossian *et al.*, 1975) and has advanced to routine use in nuclear medical diagnostics of malignancies. PET as a method is based on the detection of 511 keV annihilation photons arising from the β^+-decay of applied radioactive molecules. The detection and location of these photons, computed reconstruction into images and consideration of the biochemical properties of the applied radioactive molecule provide insight into functional or metabolic states. The main advantage of PET is the supreme sensitivity in a picomolar range (Cherry, 2001). Therefore, the amount of the radioactive material needed for a confident detection rate has a negligible effect on the examined biological system. This is also referred to as the tracer principle for which Georg de Hevesy was attributed the Nobel Prize in Medicine in 1943. The basic principle of PET is further discussed in detail in the following section.

Nuclides with excess protons or neutrons are prone to radioactive decay to achieve a more stable configuration. Nuclei high in protons can reach a more stable configuration by positron emission, or β^+-decay, and electron capture. Thereby, a proton (p) is converted to a neutron (n) under emission of a positron (β^+), the antiparticle to the electron, and an electron-neutrino (ν_e):

$$ {}^{1}_{1}p^{+} \rightarrow {}^{1}_{0}n + {}^{0}_{1}\beta^{+} + \nu_e \qquad \textbf{Equation 1} $$

The emitted positron resulting from the decay has an initial energy that can assume values up to a maximum energy E_{max} where E_{max} is determined by the differences in the atomic mass between the decaying atom and its daughter atom. The ejected positron travels through the tissue environment, a distance only up to a few millimeters, termed positron range, and thereby loses kinetic energy. The positron range contributes to the limits of spatial resolution in PET, referred to as blurring (Moses, 2011). Due to the electron richness of the surrounding tissue, however, the positron has a rather short lifetime. When the positron's kinetic energy is essentially lost, it combines with an electron to either annihilate directly or, in few cases only, to first form a short-lived intermediate, the positronium. This intermediate state can best be described in analogy to the hydrogen atom: the positron substitutes the proton as the nucleus.

In the following annihilation reaction, the remaining mass of the positron and electron are released in the form of two 511 keV annihilation photons. The two 511 keV annihilation photons are emitted simultaneously in an angle of 180° to one another on a line of response (LOR) to conserve both energy and momentum. A non-zero momentum at the time of annihilation results in photon non-collinearity, a deviation in the angle 180° ± θ with θ 0-0.5° (Figure 10). The physical constraints for the emittance of the annihilation photons are the basis for PET image reconstruction: the signal emitted is recorded along the LOR by the PET detector blocks and thus the location of the annihilation event can be computed (Baley, 2005; Cherry and Dahlbom, 2006).

Further, nuclei high in protons can decay by electron capture: the nucleus converts a proton into a neutron by capturing an orbital electron and releasing a neutrino. This decreases the nuclei's atomic number by one. Although decay by positron emission is predominant, positron emission and electron capture compete with one another. Since positron emission is the basis of PET imaging, radionuclides with high fractions of positron emission, given as the β^+ branching fraction, are the preferred radionuclides of choice. The radioisotope ^{64}Cu used in this work, however, decays by 17.86 % by β^+ decay to ^{64}Ni, 39.0 % by β^- decay to ^{64}Zn, 43.08 % by electron capture to ^{64}Ni and 0.48 % internal conversion (Holland *et al.*, 2009).

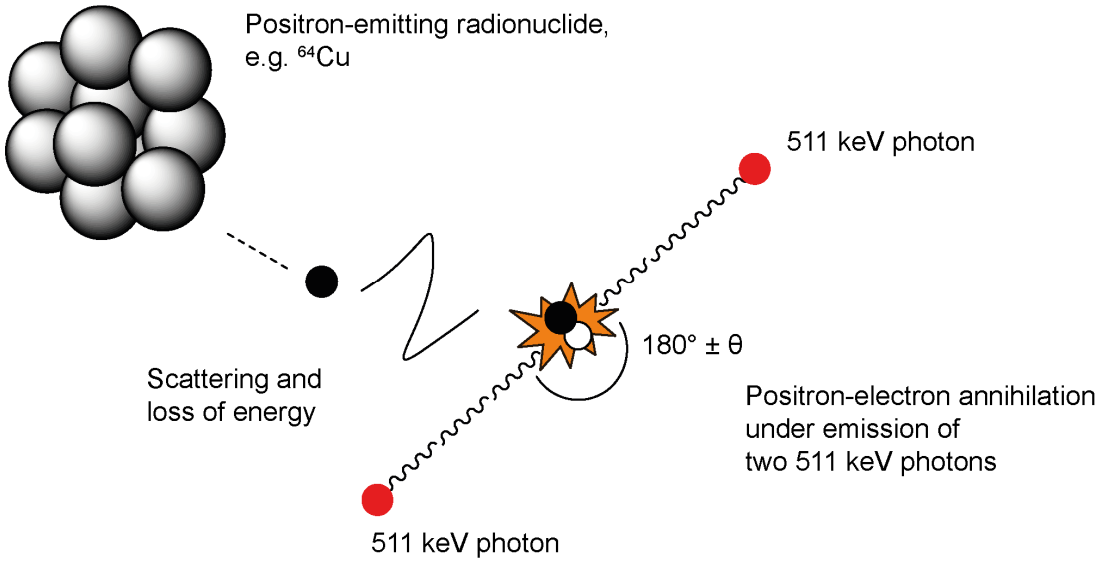

Figure 10: Positron emission, positron-electron annihilation and emission of two 511 keV photons.
Figure modified from Cherry, 2001.

Most systems in preclinical imaging operate with detector blocks arranged in a ring-shape around the object of interest. The detector blocks consist of scintillator crystals such as bismuth germanate (BGO) or cerium-doped lutetium oxyorthosilicate (LSO:Ce). The scintillator crystals detect and stop the highly energetic 511 keV photons and convert them into low-power optical photons. The light emitted by the scintillator crystals is then further converted into an electrical

signal using photomultiplier tubes. When two 511 keV photons are detected by two opposite detector blocks in a tight timing window (dependent on the instrument used), the two photons are registered as coincidence event. The single crystals in the detector blocks, however, may exhibit differences in their sensitivity profiles. These differences are corrected for by normalization with phantoms of known activity and shape. Additionally, during the conversion of 511 keV photons into optical photons of lower power and the material-specific scintillation decay time, no further coincidence event can be detected; this is referred to as dead time of the detector. Dead time of the detector and following electronics is commonly mathematically corrected for based on the determined difference between measured and true count rate.

Ideally, coincidence events are only recorded from 511 keV photons emitted in an angle of 180° on a LOR that further did not have any other interactions with matter than the annihilation, termed true coincidences (Figure 11). However, the positron can experience scattering via inelastic or elastic collisions. Elastic scattering of the positron at atomic electrons or nuclei results in deflection, energy and momentum are conserved. Inelastic scattering, however, often results in the emission of bremsstrahlung radiation. Compton scattering, as an example of inelastic scattering, refers to the interaction of a 511 keV photon with a loosely bound orbital electron. As a result, the 511 keV photon deviates from its original path and the orbital electron is ejected as Compton recoil electron. Furthermore, the deviation of the 511 keV photon from the LOR and detection in the scanner as scatter events results in background in the image. Additionally, two annihilation events taking place at the same time with loss of one 511 keV photon each can lead to random coincidences when, by chance, two opposite detector blocks simultaneously record the remaining 511 keV photons (Figure 11). As scatter and random coincidences result in diffuse background and reduced contrast in the reconstructed PET image and errors in absolute quantification, scatter correction and random correction algorithms are commonly employed.

Besides scattering, the 511 keV photon can lose energy or the energy of the 511 keV photon can be completely absorbed by the surrounding matter so that 511 keV photon cannot be detected leading to signal loss in PET data acquisition. This absorbance of 511 keV photons and, further, the scattering of the photons, is also commonly referred to as attenuation. Photon attenuation reduces image quality and leads to errors in quantitative data evaluation when not corrected for. As photon attenuation is dependent on the material or tissue composition of the object in the FOV and its thickness, attenuation maps for attenuation correction can be computed from computed tomography images when available or from the attenuation of the γ-quant emitter ^{57}Co when rotating the emitting source around the object in the FOV as acquired in a transmission scan (Zanzonico, 2004).

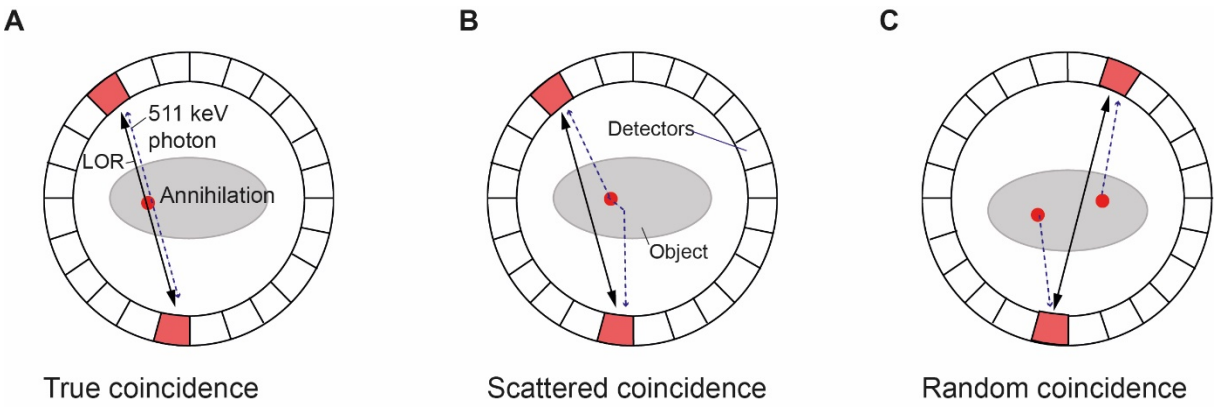

Figure 11: Different types of coincidence events.
Different types of coincidences that can be detected by the PET system. Ideally, only true coincidences (**A**) are detected by opposing detector blocks (highlighted in light red). In case of scattering of one or both annihilation photons, scattered coincidences (**B**) are recorded leading to the calculation of a wrong LOR. Random coincidences (**C**) can be detected when two 511 keV photons derived from two separate annihilation reactions are randomly registered by opposing detector blocks as coincidence, also leading to the calculation of a wrong LOR. Figure modified after Cherry and Dahlbom, 2006.

The detected coincidence events are recorded in conjunction with further information about the energy of the detected photons in list mode files according to the time of detection. In the next step, the recorded events are sorted into a sinogram file, essentially a 2-dimensional matrix file, that accounts for the location of the coincidence event in the scanner and the angle of detection. In this process, time resolution is conserved which allows for different image reconstruction strategies. On the one hand, time resolution can be neglected by summarizing all recorded events over time while, on the other hand, a time-resolved image can be created by subdividing the acquisition time into parts, frames, and attributing the distribution of the radioactivity to a certain time frame. In this fashion, time activity curves can be created (Baley, 2005; Cherry and Dahlbom, 2006).

Image reconstruction from acquired PET data is either performed with analytical or iterative reconstruction algorithms, such as the iterative ordered subset expectation maximization (OSEM) algorithm used in this work. As for all iterative reconstruction algorithms, the final image is computed in various iterations from an initial estimation of the distribution of the radioactivity. From the initial estimation, the projection data resulting in this initially estimated image is calculated by forward projection. The set of projections of the initial estimation is then compared to the actually recorded projection and the initial estimation is adjusted. By repetition of this process, the projections converge and the final image is obtained. The OSEM algorithm uses only a subset of the projection angles in one iteration.

The main goal of PET analysis is the accurate quantification of accumulated radioactivity in different structures of interest. If the structures of interest are relatively small compared to the resolution of the PET scanner, around one third of the scanner's resolution, partial volume effects (PVE) can affect quantification results. The images are essentially reconstructed from a matrix of voxels and the respective mean values of activity in the voxels. In case of a localized

high activity value surrounded by very low to no activity, the mean value does not represent the actual distribution of activity in this voxel and leads to underestimation of the actual activity. In addition, a spill-out effect into surrounding structures, for example, results in an underestimation of the actual activity in the examined structure and an overestimation in the surroundings. Further, the method used for correction can influence data analysis (Baley, 2005; Cherry and Dahlbom, 2006; Mannheim *et al.*, 2017).

1.4.1.1 PET tracers

For the application of PET in clinical and preclinical diagnostic questions, a PET compatible radioactive molecule, termed tracer, has to be applied. As mentioned before, due to the supreme sensitivity of the PET system, the tracer amount needed for confident detection does not perturb the examined biological system. A selection of commonly used clinical and preclinical PET tracers sorted by radioisotope are given in Table 1. The archetypical and still most frequently used PET tracer for the diagnosis of oncologic malignancies is the glucose analogue 2-deoxy-2-[^{18}F]fluoroglucose ([^{18}F]FDG). In normal energy homeostasis, in a state of rest, all organs and tissues rely on glucose as metabolic fuel for energy production (refer to section 1.2 for details). Glucose, and [^{18}F]FDG, are taken up into the cells mainly via uniporters of the GLUT transporter family. In the cells, [^{18}F]FDG undergoes phosphorylation to 2-deoxy-2-[^{18}F]fluoroglucose-6-phosphate by the first enzyme of the glycolytic cascade, hexokinase, under ATP consumption. The resulting phorphorylated reaction product is trapped in the cells since it cannot be exported due to the electric charge or metabolized further in the glycolytic cascade. Glycolytic tumors subject to the Warburg effect meet their energy needs by increased consumption of glucose, leading to an enhanced [^{18}F]FDG uptake and the visualization of the malignancy in a PET scan (Lewis *et al.*, 2015a; Zhu and Shim, 2011).

In the preclinical setting, in the recent years, a renewed interest in antibodies, antibody fragments or sophisticated engineered antibodies fragments such as minibodies, diabodies, nanobodies or engineered peptides for the detection of malignancies or immune cell infiltrates, commonly referred to as immunoPET, was omnipresent (Knowles and Wu, 2012; Wu and Olafsen, 2008). This interest might have spiked due to the clinical approval of various monoclonal humanized antibodies (biologicals) for the treatment of several diseases including, for example, the anti-TNF antibody adalimumab (Humira®, AbbVie Ltd.) and the anti-CD20 antibody rituximab (Rituxan®, Genentech) for inflammatory diseases and rheumatoid arthritis. In molecular imaging or theranostic approaches, therapeutically approved antibodies can be radiolabeled for detection, clinical staging and subsequent radioimmunotherapy of malignancies (Gaykema *et al.*, 2013; Muylle *et al.*, 2015).

Table 1: Commonly used positron emitters, half-life, maximum positron energy and range and examples for clinically and preclinically used PET tracers.
Merged from Cherry and Dahlbom, 2006; Conti and Eriksson, 2016; Zhu and Shim, 2011.

Positron emitting radionuclide	Half-life $t_{1/2}$	Maximum positron energy E_{max} (MeV)	β^+ branching fraction	Tracer example
^{11}C	20.4 min	0.96	1.00	[^{11}C]choline, [^{11}C]methionine
^{68}Ga	68.3 min	1.89	0.89	[^{68}Ga]PSMA, [^{68}Ga]NODAGA-RGD
^{18}F	109.8 min	0.64	0.97	[^{18}F]FDG, [^{18}F]FMISO
^{64}Cu	12.7 h	0.65	0.29	^{64}Cu-labeled antibodies, engineered fragments
^{89}Zr	78.4 h	0.89	0.22	^{89}Zr-labeled antibodies, engineered fragments

1.4.2 Optical Imaging

Optical imaging (OI) relies on the detection of visible light, light of the near-infrared (NIR) part of the electromagnetic spectrum and bioluminescence. *In vivo* OI methods include planar OI, fluorescence molecular tomography, bioluminescence tomography and optical coherence tomography. The following section focuses on planar OI in the visible and NIR part of the spectrum as employed in this work and bioluminescence OI.

Planar OI relies on the presence of a fluorescent dye, fluorochrome or fluorescent protein in the examined specimen, either introduced by genetic modification or simple direct labeling. In principle, the fluorochrome is excited with light matching its absorption peak. A photon with distinct energy is absorbed and excites an orbital electron in the fluorochrome from ground state to a metastable excited state. The electron in the metastable excited state loses energy mainly by vibrational relaxation until it reaches the first electronically excited state. From the

ground state of the first excited state, according to spin multiplicity laws in quantum physics, the transition to ground state is coupled to the emission of a photon of a higher wavelength (Jablonski, 1933). The difference in the wavelength of absorbance and emittance is referred to as Stokes shift. The emitted photon is then detected by a charge-coupled device (CCD) camera. The CCD camera's sensitivity is improved by cooling to up to -100 °C to reduce dark current and thermal noise. CCD cameras can reach quantum efficiencies of up to 95 %. Owing to the nature of this technique, the signal intensity is directly proportional to the exposure time (Zelmer and Ward, 2013).

Major issues in OI include light absorption, tissue autofluorescence and a limited penetration depth. Light absorption in tissue is mainly caused by oxy- and deoxyhemoglobin at wavelengths under 650 nm. Water resonance starts at around 900 nm (Figure 12). Therefore, wavelengths between 650-900 nm are considered optimal for OI and frequently referred to as OI window (Kobayashi *et al.*, 2010; Smith *et al.*, 2009). Light is not only absorbed in organic tissue but also scattered. Although scattering begins in superficial tissue layers, most scatter events occur in forward direction (Ntziachristos, 2006). Absorbance and scattering result in a limited penetration depth that averages up to approximately 4 mm for wavelengths under 650 nm. In the NIR range between 650-900 nm, tissue autofluorescence is practically negligible since endogenous fluorochromes do not absorb light of these wavelengths and penetration depths of up to 2.5 cm can be reached (Ntziachristos, 2006). Fluorescent proteins for *in vivo* applications include the green fluorescent protein (GFP), the orange-red fluorescent protein DsRed as well as genetically engineered variants with shorter maturation times (mFruits such as mCherry or DsRed-Express) and NIR-shifted fluorescent proteins. Fluorescent dyes of different classes suitable for *in vivo* OI include rhodamine and oxazines dyes (Alexa dyes, rhodamine B, Texas Red) and the cyanine dyes Cy3, Cy5 and Cy5.5 (Nolting *et al.*, 2011).

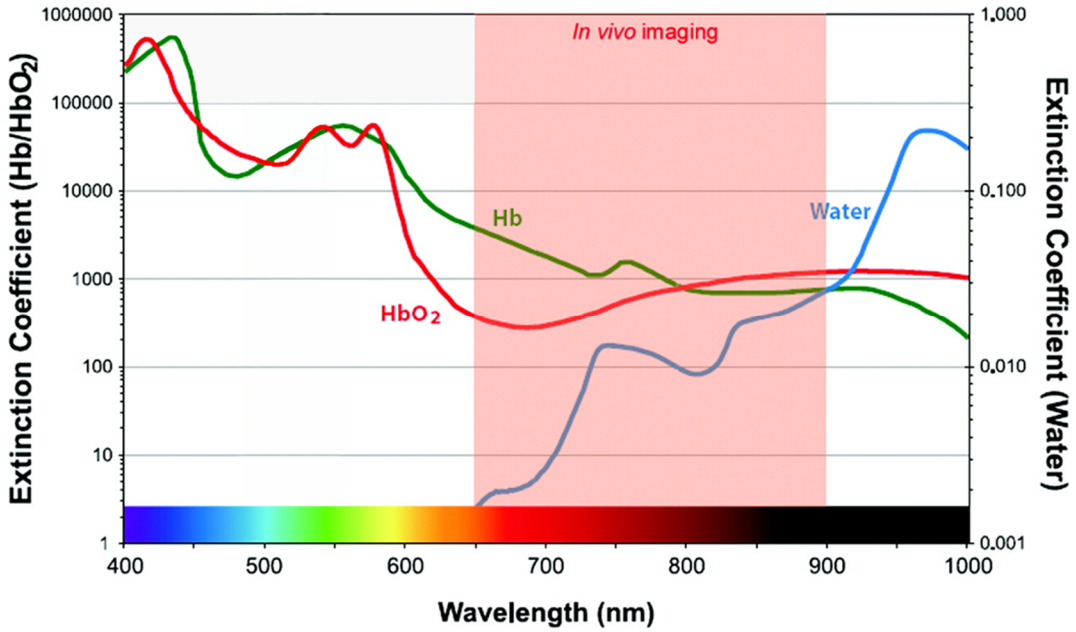

Figure 12: Plot of the extinction coefficient values of water, oxy- and deoxyhemoglobin in the visible and NIR range of the spectrum.
The extinction coefficient as measure for light attenuation per mole of chemical species serves as a indication for the light absorbed by oxy- and deoxyhemoglobin as well as water in the visible and NIR part of the spectrum. Accordingly, the *in vivo* optical imaging window ranging from 650-900 nm is hightlighted in red. Figure adapted from Kobayashi *et al.* 2010.

Bioluminescence (BL) OI relies on the production of photons in a biochemical reaction or, in a wider sense, a chemical reaction, termed chemiluminescence. The most frequently used light producing biochemical reaction was first found in the common eastern firefly *Photinus pyralis*: the firefly enzyme luciferase catalyzes the oxidative decarboxylation of D-luciferin to oxyluciferin under ATP consumption with divalent magnesium ions as cofactor. The reaction intermediate, a circular α-peroxyketone, decarboxylates to the more stable reaction product oxyluciferin that remains in an electronically excited state. A few nanoseconds after the decarboxylation, oxyluciferin returns to ground state by emitting a photon of a characteristic wavelength. For the firefly D-luciferin-luciferase system, light emitted by this reaction has a wavelength of 560 nm. The wavelength of the emitted photon changes from biological system to biological system. The red-shift of the firefly luciferase compared to *Renilla* luciferase isolated from sea pansy *Renilla reniformis* producing blue light of 480 nm renders it more suitable for *in vivo* imaging (Ntziachristos *et al.*, 2005). In comparison to planar fluorescence OI, one major advantage of BL OI is the practically non-existing background leading to improved sensitivity and signal-to-noise ratios. For BL OI, however, reporter genes such as the firefly luciferase have to be introduced into either cells of interest or mice as reporter for the specific biological question. Frequently, these systems are used as reporters for gene expression. The generation of genetically modified animal models, however, is time-consuming. Moreover, absolute quantification proves difficult due to absorbance, scattering and attenuation in the tissue that cannot be corrected for. On the other hand, however, planar

fluorescence OI and BL OI are cost-effective molecular imaging methods, suitable for high-throughput measurements and longitudinal *in vivo* imaging studies without the need for ionizing radiation.

1.4.3 Nuclear magnetic resonance spectroscopy and imaging

The magnetic characteristics of atomic nuclei were first described in 1938 by Isidor Rabi who was awarded the Nobel Prize in Physics in 1944 for his discovery. Nuclear magnetic resonance (NMR) in liquids and solids, the principle of modern NMR imaging, was first discovered independently by Felix Bloch and Edward Purcell who shared the Nobel Prize in Physics in 1952 for the discovery. The foundation for modern NMR imaging as it is performed today was laid by Paul Lauterbur and Peter Mansfield who described, independently, the use of magnetic field gradients for spatial localization of NMR signals. This discovery was honored in 2003 with the Nobel Prize in Physiology or Medicine (Ai *et al.*, 2012).
NMR spectroscopy and NMR imaging, hereafter referred to as magnetic resonance imaging (MRI), use the same natural quantum mechanical phenomenon, the spin angular momentum of nuclei, and its possibility to enter into resonance in a magnetic field. Therefore, underlying theory for spectroscopic and imaging methods will be presented in the same section.

In quantum mechanics, the spin angular momentum, or spin, describes a property of protons, neutrons, electrons and whole nuclei that, in a simplified analogy, can be thought of as a precession movement around the nuclei's own axis. The spin of nuclei, examined in NMR, is dependent on the number of protons and neutron and quantized to discreet integer and half-integer values denoted by the spin quantum number I with I= 0, ½ or 1 and so forth while nuclei with I=0 are inept for NMR. Due to its natural abundance, ^{1}H, with the quantum number ½ and the two possible spin states m_i=½ (spin-up) and m_i=-½ (spin-down), is the most prominent nucleus for clinical MRI and magnetic resonance spectroscopy (MRS).
In the absence of an external magnetic field B_0, the spin states are degenerate. If an external magnetic field B_0 is applied, the interaction between the magnetic field B_0 and the nuclear magnetic moment μ_M leads to an alignment of the spin either parallel or antiparallel to the external magnetic field B_0. The energy difference of the separation of the spin states is given as

$$\boldsymbol{\Delta E = \frac{h}{2\pi}\gamma B_0} \qquad \textbf{Equation 2}$$

This is also defining their resonance frequency v_0, the Lamor frequency, as

$$\boldsymbol{v_0 = \frac{\gamma}{2\pi}B_0} \qquad \textbf{Equation 3}$$

The spin distribution follows a Boltzmann distribution with a higher amount of spins in ground state N_0 as compared to the excited state N_1

$$\frac{N_1}{N_0} = e^{\frac{-\gamma h B_0}{2\pi k T}}$$ **Equation 4**

with k the Boltzmann constant and T the absolute temperature in Kelvin (Atkins, 2008) yielding a netto magnetization M_0 along the external magnetic field (Figure 13).

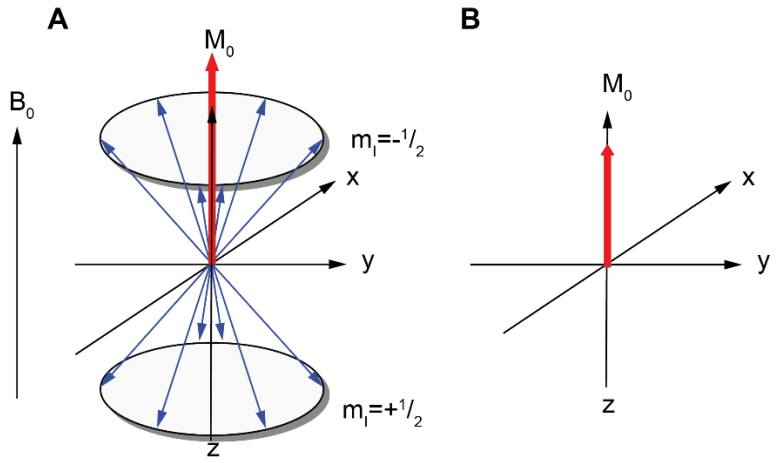

Figure 13: Schematic of MR net magnetization.
The interaction between the magnetic field B_0 and the nuclear magnetic moment μ_M leads to a separation of the spin states into a ground state N_0 and an excited state N_1 and distribution of the spins (represented as blue arrows) following Boltzmann distribution (**A**). The sum of the precession of the spins leads to an observable net magnetization (red arrow). This is simplified in (**B**).

If energy as described by the Lamor frequency is applied to the spin system, e.g. in the form of a radiofrequency (RF) pulse, the absorption of energy leads to the crossing of spins from ground state to excited state and further, the flip of the net magnetization M_0 in x- or y-direction (Figure 14 A). The resulting angle between the net magnetization vector M_0 and the magnetic field vector B_0 is referred to as flip angle. The net magnetization vector M_0 further returns to equilibrium magnetization (Figure 14 B) and the absorbed energy is released, referred to as relaxation, inducing a signal in the receiver coil, termed free induction decay (FID). The relaxation process is characterized by two mechanisms: energy can either be released longitudinally or transversally. Longitudinal relaxation, or spin-lattice relaxation, refers to the transfer of energy to the surrounding matter while transversal relaxation or spin-spin relaxation refers to the transfer of energy between spins. In accordance, the time a spin system needs to relaxate back to ground state in exponential manner is given as T1 relaxation time for spin-lattice relaxation or T2 relaxation time for spin-spin relaxation. Differences in tissue proton density and the relaxation times of tissue are the basis for contrast in MR imaging (Mlynárik, 2017).

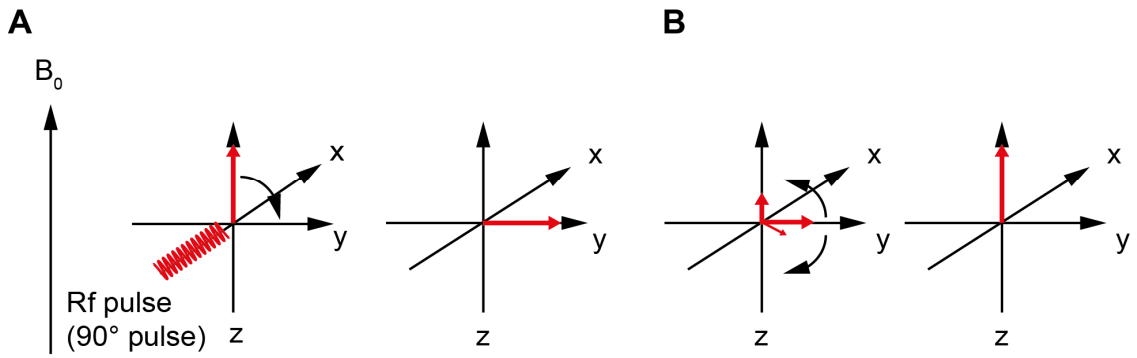

Figure 14: Flip of the net magnetization vector M_0 and relaxation.
The net magnetization M_0 flips in y-direction in the transverse plane when the spin system is excited with a 90° RF pulse, meeting the resonance condition given as Lamor frequency (**A**). Relaxation (**B**) of the net magnetization vector M_0 is another characteristic of a specified spin system relevant for medical applications.

1.4.3.1 Magnetic resonance imaging

Due to its high natural abundance, the ^1H nucleus spin system is ideal for morphological, anatomical MR imaging. More sophisticated applications include, for example, functional MR imaging of tissue oxygenation and blood flow or perfusion. MR images yield a high soft-tissue contrast, however, sensitivity ranging between 10^{-3}-10^{-5} M is orders of magnitude lower than in PET images (Kircher and Willmann, 2012).

MR images are acquired and computed from pulse sequences, the two principle sequence types being spin echo and gradient echo. In gradient echo sequences, the echo is generated from one RF pulse followed by refocusing of dephased spins using the gradient fields. Therefore, as only one RF pulse is applied, acquisition of gradient echo sequences can be very rapid. Spin echo sequences use two RF pulses to generate the echo: the second RF pulse serves to refocus dephased spins that have been affected by e.g. magnetic field inhomogeneities or distortions for image acquisition. The pulse sequences are further characterized by their echo time (TE) and their repetition time (TR) that are employed to control contrast and weighting of the images. TE refers to the time between the center of the excitation RF pulse and the center of the echo, TR to the time between two repetitions of a series of pulses and echos.

For anatomical MR images, fast or turbo spin echo (TSE), commercial adaptions of the rapid acquisitions with refocused echoes (RARE) technique are commonly used (Hennig *et al.*, 1986). A series of 180°-refocusing pulses with different phase-encoding gradients are applied after the RF pulse. In this way, multiple data points can be collected within one repetition cycle which significantly reduces the time needed for acquisition. For spatial localization of the signal, additional gradient magnetic fields are applied for slice selection, frequency and phase encoding. For this purpose, the gradient coils in the x, y and z direction alter the magnetic field strength of the main magnetic field B_0 in a linear fashion so that the exact precession frequency

along the generated gradient axis can be calculated. The acquired phase- and frequency information, which is stored in so called k-space, is then further processed into images with Fourier transformation. In the resulting anatomical images, for example, differences in T1 and T2 relaxation times and overall water content yield organ- and structure-resolving contrast.

1.4.3.2 Magnetic resonance spectroscopy

While MRI produces anatomical or functional images from bulk magnetic properties of tissues such as T1 and T2, magnetic resonance spectroscopy (MRS) elucidates the chemical composition of a volume of interest. The interaction of atoms in their chemical composite and their interaction with the magnetic field B_0 are the basis for NMR spectroscopic analysis.
The movement of the negatively charged electrons around the nucleus induce a magnetic field opposed to the main magnetic field B_0 reducing the effective magnetic field to B_{eff}

$$\boldsymbol{B_{eff} = B_0 - \sigma B_0} \qquad \textbf{Equation 5}$$

with σ as shielding constant characterized by the electron density and distribution in the examined nucleus. With the alteration of B_0 to B_{eff}, the Lamor frequency v_0 changes. As a result, chemically different nuclei give rise to discrete signals in the resonance spectrum. This is further characterized by the chemical shift δ as independent reference

$$\boldsymbol{\delta_i = \frac{v_i - v_{Standard}}{v_0}} \qquad \textbf{Equation 6}$$

with v_i as resonance frequency of the examined nucleus, $v_{Standard}$ as resonance frequency of a standard solution usually set to zero and v_0 as measurement frequency, δ is given in parts per million (ppm). Tetramethylsilane, for example, is a common reference substance for *in vitro* ^{1}H NMR spectroscopy (Mlynárik, 2017). The basic approach to NMR is a single pulse experiment, yieliding non-localiced information on the target compounds. However, the spins of nuclei interact either via scalar spin-spin coupling via shared bonds as well as coupling via two or more chemical bonds. These interactions result in complex line splitting of the resonance signals into multiplets. Although line splitting is essential for precise identification of each chemical compound, signal overlap in complex biological samples complicates accurate identification. Accordingly, more sophisticated approaches include more complex pulse programs such as J-resolved spectroscopy (JRES), nuclear overhauser enhancement spectroscopy (NOESY) or 2- or more dimensional NMR spectroscopy to deal with the complexity of biological samples (Bingol and Bruschweiler, 2014; Marchand *et al.*, 2017).

In vivo, the ^{1}H MRS signal is dominated by the naturally abundant water signal. Accordingly, water suppression techniques are employed to detect small molecule metabolites in the millimolar range. Comparable to *in vitro* NMR spectroscopy, the metabolites are identified by their chemical shift δ. However, the number of metabolites that can be detected in *in vivo* ^{1}H

MRS is rather limited with about 20 metabolites described under ideal conditions (Hajek and Dezortova, 2008). In clinical MRS, metabolites with a molecular weight under 2 kDa such as N-acetly-aspartate, creatine and choline and their respective phosphorylated counterparts phosphocreatine and phosphocholine are of major interest due to their characteristic increase in cancerous lesions of the brain and breast, for example (Glunde *et al.*, 2011; Hajek and Dezortova, 2008).

For ^{1}H spectroscopy *in vivo*, the point resolved spectroscopy, referred to as PRESS, or stimulated echo acquisition mode (STEAM) spectroscopic techniques are common. The STEAM method uses three slice-selective 90° pulses. The ^{1}H signal is derived from protons in the intersecting plane constructing the spectroscopic voxel that has been excited by all three RF pulses. In STEAM spectroscopy, the first two RF pulses are applied with a delay of TE/2. The stimulated echo is then recorded TE/2 after the third RF pulse is applied. In the time between the second and third RF pulse, denoted mixing time, the magnetization is stored along the z-axis and does not undergo T2 decay (Klose, 2008). Although STEAM is limited to half the signal of compared to the point resolved spectroscopy method resulting in inferior signal-to-noise ratios, it has several advantages: detection of metabolites with short T2 is feasible due to the possibility to shorten TE to very small values, the sharp slice profile results in well-defined imaging voxels and the higher bandwidth results in less chemical shift displacement artifacts (Moonen *et al.*, 1989).

1.4.3.3 Dynamic nuclear polarization for ^{13}C-MRS

Besides MRI and MRS of ^{1}H with its superior natural abundance for anatomic imaging and fair sensitivity for the detection of high abundance metabolites, non-invasive ^{13}C-MRS has become increasingly important over the last decade. ^{13}C, the only stable isotope of ^{12}C with a natural abundance of only approximately 1.1 % (Comment and Merritt, 2014), is the isotope of choice for labeling tracer molecules for ^{13}C-MRS. With only approximately one fourth of the gyromagnetic ratio of ^{1}H, sensitivity is a major issue for ^{13}C-MRS (Ardenkjaer-Larsen, 2016). In 2003, the introduction of dissolution dynamic nuclear polarization (DNP) for ^{13}C-labeled small metabolites enabled their use to study their uptake, metabolic use and conversion in the preclinical and clinical setting. Polarization describes the difference between spin-up and spin-down spins of spin systems with I=½ in an external magnetic field. Hyperpolarization, accordingly, refers to a spin system in which polarization deviates significantly from thermal equilibrium. Dissolution DNP provides enhancement of sensitivity by enhancement of the polarization of a metabolic probe. Accordingly, an increase of sensitivity and signal-to-noise ratio by more than 10^{4}-fold and a reduction of acquisition times is achieved (Ardenkjaer-Larsen *et al.*, 2003). Protocols for *in vitro* or *in vivo* ^{13}C-MRS include, beside single-shot spectroscopy

with dynamic repetitions, further sophisticated pulse programs that are required for spectroscopic imaging in order to achieve proper image and time resolution within the lifetime hyperpolarization (Brindle *et al.*, 2011).

Hyperpolarization of nuclear spins via dissolution DNP is achieved by transfer of the strong electron spin in the solid state at low temperature and in a high magnetic field. To use the electrons' polarization, the ^{13}C-labeled tracer is mixed with a free radical, nitroxide or trityl radicals, and rapidly frozen to from a non-crystalline amorphous solid to ensure homogeneous distribution of the free radical. At low temperatures near absolute zero and in high magnetic field strength, the electron spins practically completely polarize and their polarization is transferred to the nuclear spins by microwave irradiation at the electron resonance frequency. The nuclear spin populations redistribute slowly to enhanced polarization in the solid state over 1-2 h depending on the ^{13}C-labeled molecule. Addition of trivalent Gadolinium ions (Gd^{3+}) shortens the electron spin longitudinal relaxation time and thereby improves DNP enhancement. The hyperpolarized amorphous solid is rapidly dissoluted to room temperature with minimal loss of polarization in a pressurized buffer solution superheated to 180 °C. These steps require high solubility of the hyperpolarized ^{13}C-labeled molecule compound to ensure dissolution in the buffer. The dissoluted hyperpolarized ^{13}C-labeled molecule can then be used for spectroscopic imaging either *in vitro* or *in vivo*. However, the imaging window is limited from 10-30 sec to 1 min *in vivo* since polarization is lost quickly and the application of radiofrequency pulses to perform MR measurements accelerates the polarization decay. Due to this short polarization life-time *in vivo*, the hyperpolarized ^{13}C-labeled molecule's rapid transport over the plasma membrane as well as following rapid metabolic reactions are essential for successful imaging (Ardenkjaer-Larsen, 2016; Brindle, 2015).

The most prominent and most widely used hyperpolarized ^{13}C-labeled metabolite and metabolic substrate and the first to be translated to clinical use is [1-^{13}C]pyruvate. The hyperpolarized [1-^{13}C]pyruvate is injected *i.v.* into the circulation and taken up into the cells via monocarboxylate transporters. During and after injection, the hyperpolarized [1-^{13}C]pyruvate is detected at approximately 171 ppm. In the cells, metabolism of [1-^{13}C]pyruvate to [1-^{13}C]alanine via the ALAT or to [1-^{13}C]lactate via LDH can be followed by the appearance of peaks at approximately 183 ppm for [1-^{13}C]lactate and at approximately 176 ppm for [1-^{13}C]alanine. Furthermore, hydratation of [1-^{13}C]pyruvate to [1-^{13}C]pyruvate hydrate is observable as a peak appearing at 179 ppm. Oxidative decarboxylation of [1-^{13}C]pyruvate to acetyl-CoA via the pyruvate dehydrogenase enzyme complex releases [^{13}C]CO_2 that, after hydration, can be detected as hydrogencarbonate at 161 ppm (Figure 15).

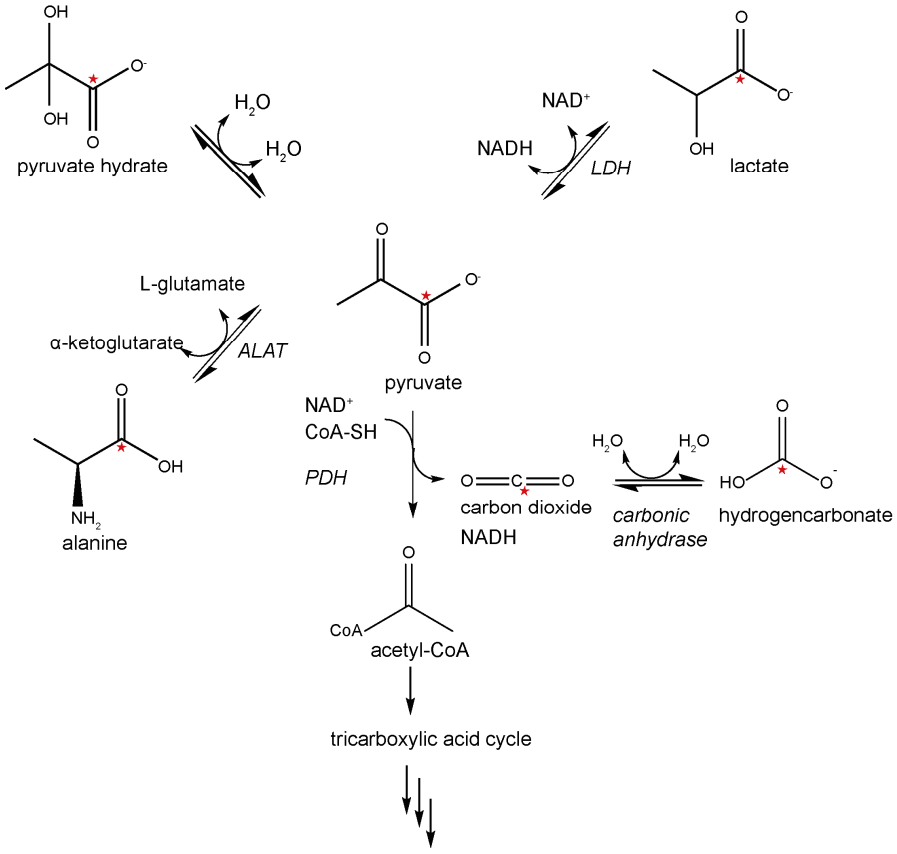

Figure 15: [1-^{13}C]pyruvate transformation and metabolism *in vivo*.
Schematic of the fate of [1-^{13}C]pyruvate *in vivo*. ^{13}C-labeling is indicated by a red asterisk, enzymes are printed in italic; PDH-pyruvate dehydrogenase complex.

DNP-enhanced MRS with [1-^{13}C]pyruvate has proven to be a sensitive tool for clinical detection of prostate and breast cancer lesions. The grade of prostate tumors has been shown to parallel the degree of transformation of [1-^{13}C]pyruvate into [1-^{13}C]lactate with more aggressive tumors showing higher ^{13}C-lactate labeling. Further, early response to drug treatment could be successfully detected by a decline of lactate labeling after [1-^{13}C]pyruvate injection (Brindle, 2015; Day *et al.*, 2007).

In comparison to PET imaging, DNP-enhanced MRS with ^{13}C-labeled metabolites has one tremendous advantage: the metabolic flux and fate of the ^{13}C-labeled metabolite can be detected in real-time and a time-resolved manner indicating the metabolic state of a tissue or lesion while PET imaging is limited to tracer distribution and uptake reflecting steady state metabolism. Moreover, although not comparible to PET in sensitivity using much higher amounts of metabolic tracers, DNP-enhanced NMR spectroscopy uses non-radioactive compounds as tracers reducing exposition to radiation and facilitating repeated measurements and treatment monitoring. Nevertheless, the infrastructure needed is expensive. Due to the low natural abundance of ^{13}C of only approximately 1.1 %, expected background signals are infinitesimal.

1.4.4 Cell labeling techniques for non-invasive imaging

For non-invasive imaging studies, the cells of interest need to bear a compatible label for detection by the respective imaging modality. In principle, two major approaches to label cells for *in vivo* non-invasive imaging are distinguished: direct and indirect cell labeling (Figure 16). Direct labeling (Figure 16 A) refers to the direct incubation of isolated primary or cultivated cells with the labeling agent in the presence of an uptake mediator if needed while indirect labeling (Figure 16 B) involves genetic modification of the cells of interest either *in vitro* or *in vivo* to express an imaging-compatible reporter that can then be detected with its substrate.

Depending on the labeling agent and the cells of interest, direct labeling is achieved with basic and straightforward procedures. In case of passive uptake of the label, simple incubation may already result in successful labeling. Phagocytic cells take up labeling agents actively without the need for further transduction. Another frequently used option is the facilitation of the label uptake with chemical transduction agents or by exploiting endogenous cellular transporters. The main advantage of direct cell labeling is its simplicity and the transferability of existing protocols to different cells types of interest. Disadvantages include the possible loss of the labeling agent resulting in background in the images and the dilution of the cells' signal after cell division *in vivo*. Terminally differentiated cells that do not undergo further division *in vivo* such as DCs and macrophages are therefore preferable for this labeling technique. Furthermore, the observation time is usually limited by physical and chemical properties of the label itself and its stability in the cells. Direct cell labeling does not permit repeated imaging exceeding the label's biological half-life time. This problem, however, can be overcome by using injectable labels individually adapted to target a specific cell type of interest, also referred to as *in situ* labeling. Nevertheless, the possibility to visualize cell activation, proliferation or death is not given.

Indirect cell labeling, on the other hand, requires labor-intensive genetic modification of cells either *in vitro* or *in vivo* or the use of transgenic organisms. However, the introduction of reporter genes permits repeated examinations of the distribution of the cells and cell progeny during a prolonged observation time. Additionally, restriction of reporter gene expression with a specific promoter enables the visualization of cell activation (Akins and Dubey, 2008; Kircher *et al.*, 2011; Ottobrini *et al.*, 2011).

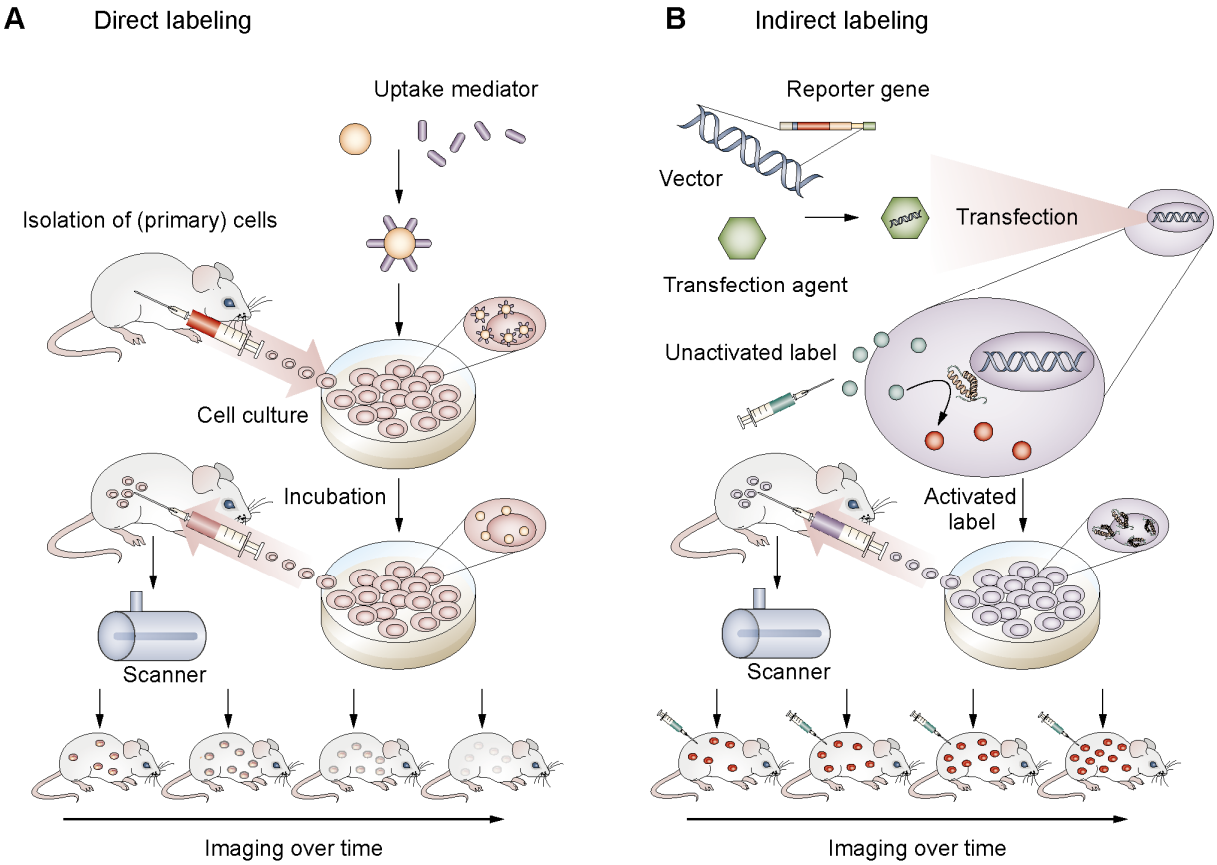

Figure 16: Principles of cell labeling for non-invasive imaging.
In principle, direct cell labeling techniques (**A**) and indrect cell labeling techniques (**B**) represent the two major approaches for cell labeling for the non-invasive imaging modalities. Figure modified from Kirchner *et al.*, 2011.

Different labeling agents and protocols for direct and indirect cell labeling adapted to the respective imaging have been described in literature. Briefly, direct cell labeling agents for MRI rely on the modification of the T1 or T2 relaxation times. Paramagnetic contrast agents containing Gd^{3+}-formulations yield positive contrast in conventional T1-weighted ^{1}H imaging sequences while superparamagnetic iron oxide (SPIO) formulations yield negative contrast in T2-weighted ^{1}H imaging sequences by virtue of their strongly magnetic iron oxide core. Different biocompatible SPIO formulations are available for *in vitro* cell labeling and MR imaging of adoptively transferred cells including ultra-small SPIOs. ^{19}F-perfluorocarbon (PFC) emulsions serve as probes for cell labeling for ^{19}F-MRI. Comparable to ^{1}H-MRI, ^{19}F-MRI detects the ^{19}F nuclei distribution *in vivo*. Due to the extremely low abundance of ^{19}F *in vivo*, the ^{19}F signal is directly proportional to the adoptively transferred ^{19}F-PFC labeled cells. *In situ* labeling of phagocytic cells is feasible with both SPIOs and ^{19}F-PFC emulsions. Biodistribution of the ^{19}F-PFC emulsion can be verified *ex vivo* using conventional NMR spectroscopy comparable to γ-counting for *in vivo* PET imaging (Ahrens and Bulte, 2013; Bulte and Kraitchman, 2004; Srinivas *et al.*, 2010).

Cell labeling techniques for OI and PET as used in this work are presented in detail in the following subsections.

1.4.4.1 Cell labeling for optical imaging

Relying on the emission of light in the visible and NIR part of the electromagnetic spectrum, direct cell labeling for fluorescence OI involves the introduction of fluorescent dyes into the cells. Formulations of the fluorescent dyes include lipophilic formulations of rhodamine, oxazines or cyanine dyes that insert into the membrane lipid bilayer (Sutton *et al.*, 2008) and extraordinarily bright classical or functionalized quantum dots introduced into the cytoplasm (Li and Zhu, 2013; Wegner and Hildebrandt, 2015). Fluorescent proteins such as GFP, tdTomato or mFruits serve as reporter genes for tumor cells (Sceneay *et al.*, 2018; Yang *et al.*, 2000) or immune cell populations in transgenic animals such as neutrophils (Hasenberg *et al.*, 2015), T lymphoid cells (Singbartl *et al.*, 2001) or B cells (Fuxa and Busslinger, 2007).

For BL OI, the most frequently described reporter gene is the enzyme luciferase (refer to section 1.4.2). Gene introduction is achieved by simple transfection, viral transduction, electroporation of the cells or genome-editing techniques such as the CRISPR-CAS system. The use of response elements and specific promoters enables, for example, visualization of cell activation in the context of inflammation, in detail NF-kB activation in transgenic mice (Carlsen *et al.*, 2002) or TCR-dependent activated T cells (Ponomarev *et al.*, 2001). Interestingly, both *Renilla* and firefly luciferase have been used successfully in parallel in living mice (Bhaumik and Gambhir, 2002).

1.4.4.2 Cell labeling for PET imaging

Both direct and indirect cell labeling methods for non-invasive PET imaging of cell migration and homing dynamics *in vivo* have been described in the literature.

Direct cell labeling for PET imaging can be readily performed with various unspecific agents *in vitro* for adoptive cell transfer. [^{18}F]FDG, commonly used for the detection of cancers subject to the Warburg effect and taken up into the cells by GLUT transporters, has been used for clinical imaging of T lymphocytes (Malviya *et al.*, 2014). Adonai *et al*. evaluated and compared [^{64}Cu]pyruvaldehyde-bis(N4-methylthiosemicarbazone) ([^{64}Cu]PTSM) and [^{18}F]FDG as labeling agents for cell tracking by PET. The lipophilic [^{64}Cu]PTSM complex passively diffuses over the cell membrane where reduction of Cu^{2+} to Cu^{1+} and association with macromolecules traps the copper ions in the cells while, as described above, [^{18}F]FDG is taken up into the cells via specialized transporters (Adonai *et al.*, 2002). Human DCs (Prince *et al.*, 2008) and rhesus monkey hematopoietic and mesenchymal stem cells (Huang *et al.*, 2008) were labeled with

[^{64}Cu]PTSM for non-invasive cell tracking. Further, *in vivo* cell tracking in an inflammatory model elucidated the spatial and temporal distribution and homing to lymphatic tissues of [^{64}Cu]PTSM-labeled T cells specific to the inflammation-eliciting antigen (Griessinger *et al.*, 2014). The use of a monoclonal antibody to target the TCR of T cells specific to the inflammation-eliciting antigen represented an elegant advancement of this technique with higher specificity, stability and less detrimental effects on the cells (Griessinger *et al.*, 2015).

Radioactively modified monoclonal antibodies or engineered antibody fragments are the most often used imaging tracers for direct *in situ* labeling and monitoring of endogenous immune cells in cancer, referred to as immunoPET (Freise and Wu, 2015; Wu, 2014; Wu and Olafsen, 2008). ImmunoPET is a highly versatile tool for the assessment of the migration and recruitment of tumor-infiltrating lymphocytes in syngenic tumor models (Beckford Vera *et al.*, 2018), CD4$^+$ T cells (Freise *et al.*, 2017) or CD8$^+$ T cells in context of immunotherapy treatment responses (Seo *et al.*, 2018; Tavare *et al.*, 2016), CD4$^+$ and CD8$^+$ T cells in the context of stem cell transplantation (Tavare *et al.*, 2015).

The most frequently used reporter genes for PET imaging are variations of the herpes simplex virus-1 thymidine kinase (HSV1-tk). These viral variants of thymidine kinases differ from the human enzyme in substrate specificity thereby enabling specific targeting of the engineered enzymes with nucleoside analog tracers *in vivo* (Figure 17). The radioactive tracers such as 2'-deoxy-2'-[^{18}F]-fluoro-5-ethyl-1-β-D-arabinofuranosyl-uracil ([^{18}F]FEAU) or 9-(4-[^{18}F]-fluoro-3-[hydroxymethyl]butyl)guanine ([^{18}F]FHBG) bind specifically to the viral variant expressed in the cells of interest (Najjar *et al.*, 2009; Thunemann *et al.*, 2017). In clinical translation of this approach, genetically engineered, tumor-targeting CAR T cells expressing HSV1-tk have already been successfully tracked to brain lesions in glioma patients with [^{18}F]FHBG by PET (Keu *et al.*, 2017). The sodium iodide symporter (NIS) represents a second common PET reporter imaging system (Figure 17). Physiological NIS expression is restricted to the thyroidal tissue with low expression levels in the salivary glands, stomach, intestines and the lactating breast resulting in low background in other tissues. NIS activity can be visualized with the radioactive iodide nuclide ^{124}I or iodide analogue ^{18}F derivatives such as ^{18}F-labeled hexafluorophosphate or tetrafluoroborate (Penheiter *et al.*, 2012). The radioactive label is then trapped in the cells. With this technique, first attempts have been made to track CSCs in ischemic mouse hindlimbs (Park *et al.*, 2016b). Clinical use of the SLCA5A gene encoding the NIS is a vivid field of investigation (Ravera *et al.*, 2017).

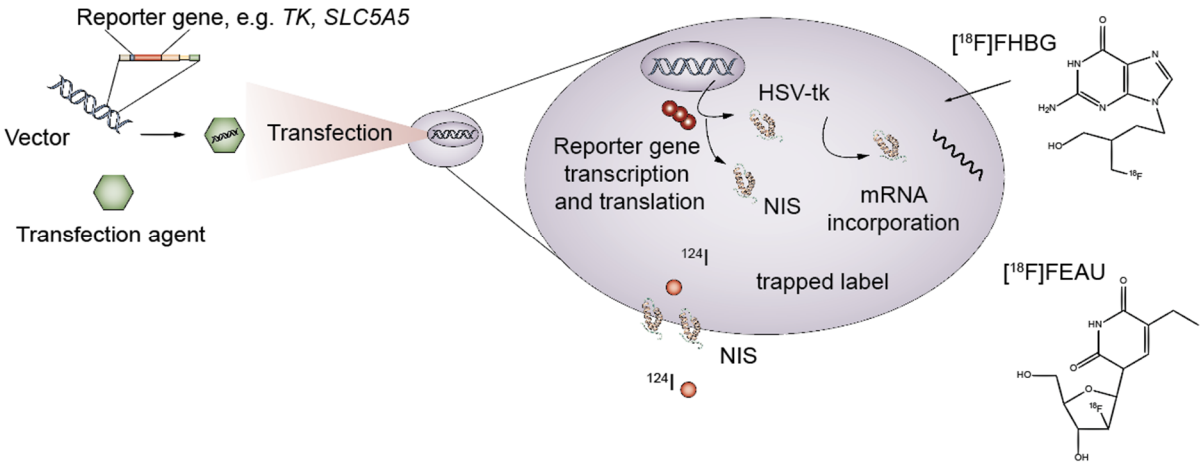

Figure 17: Principle of PET reporter gene imaging with HSV-tk and NIS.
The reporter gene for HSV-tk or NIS, for example, is introduced into the biological system via transfection resulting in the expression of the reporter protein. Figure modified from Kirchner *et al.*, 2011.

For multimodal imaging combining both OI and PET, Ray *et al.* developed a triple fusion gene cassette containing the sequences for the reporter genes HSV-tk, red fluorescent protein and luciferase and successfully applied this approach to image the distribution of human melanoma cells in mice (Ray *et al.*, 2004; Ray *et al.*, 2007).

2 AIM OF THIS WORK

Cancer and particularly metastatic disease represent one of the major health issue worldwide with metastasis causing approximately 90 % of all cancer-related deaths. Cancer-provoked abnormal myelopoiesis results in, amongst others, expansion and activation of immunosuppressive MDSCs. MDSCs are key players in tumor progression in the primary TME, pre-metastatic niche formation in secondary organs and metastasis. Since peripheral MDSC levels were correlated with disease progression and survival in cancer patients in the last decades, MDSCs moved closer into the focus of cancer research. MDSC migration in tumor-bearing mice, however, has not yet been extensively studied.

Deregulation of cellular metabolism was further recognized as hallmark of cancer. Metabolic reprogramming in cancer cells and established tumors results in the exhibition of a metabolic phenotype with the glycolytic phenotype being the historically most prominent example. A metabolic phenotype, however, is not necessarily static. Cancer cells becoming metastatic may exhibit high degrees of metabolic flexibility and undergo a metabolic switch during metastasis.

In the last decades, non-invasive imaging approaches have proven valuable for not only the characterization of tumor metabolism *in vivo* but also for the elucidation of cellular migration and dynamics of immune or stem cells.

The primary objective of this work was the investigation of MDSC migration *in vivo* with the following questions and milestones:

- Is the *in vivo* tumor homing of M-MDSCs comparable to the previously examined recruitment of PMN-MDSCs to the primary breast cancer TME (Sceneay *et al.*, 2018)? Hence, *in vitro* expanded M-MDSCs and PMN-MDSCs were labeled with a fluorescent dye and adoptively transferred into primary breast cancer-bearing mice for a preliminary OI imaging study.

- Is it possible to transfer a previously published antibody-mediated radiolabeling approach to the murine MDSC subpopulations PMN- and M-MDSCs by use of CD11b as antigen? Herein, the applicability of this approach to murine MDSC subpopulations was determined by characterization of the fate and stability of this radiolabel in PMN- and M-MDSCs and its effects on cell viability and the induction of apoptosis and DNA-double strand breaks.

- Can differential MDSC migration and tumor homing be visualized by PET imaging with the envisioned radiolabeling approach? To elucidate this question, radiolabeled PMN-

or M-MDSCs were adoptively transferred to primary breast cancer- and primary melanoma-bearing mice and breast cancer- and melanoma metastasis-bearing mice, respectively, and homing to the primary tumors and metastatic lesions was quantified.

- Does tracking of radiolabeled MDSCs permit the *in vivo* visualization of the pre-metastatic niche? Hence, two experimental approaches to induce a lung pre-metastatic niche *in vivo* were evaluated and employed for *in vivo* MDSCs cell tracking studies.

The secondary objective of this work was the multiparametric metabolic profiling of two MMTV-PyMT-derived cell lines, the parental cell line S2WTP3 and the S2WTP3-derived, more aggressive and potentially metastatic cell line ML1B1B1, for metabolic markers and underlying causes for their differential degree in aggressiveness. A special focus was placed on glucose metabolism in this part.

- Did a metabolic switch affecting glucose metabolism occur in the metastatic cell line ML1B1B1 in comparison to S2WTP3? *In vitro* and *in vivo* [^{18}F]FDG uptake was therefore assessed to elucidate differences in the glucose metabolism in S2WTP3 and ML1B1B1 cells and cell-derived allograft tumors.

- Are there other metabolic markers for the more aggressive phenotype of the metastatic MMTV-PyMT-derived cell line ML1B1B1 in comparison to its parental, less aggressive cell line S2WTP3? As elevated levels of phosphocholine and total choline-containing metabolites is frequently observed in breast cancer, ^{1}H *in vivo* spectroscopy and *ex vivo* ^{1}H NMR spectroscopy was performed to examine changes in choline metabolism in ML1B1B1 in comparison to S2WTP3 cells.

- How does the metabolic phenotype of ML1B1B1 cells correlate with enhanced metastatic potential in comparison to S2WTP3 cells and what are the molecular drivers of the more aggressive phenotype of ML1B1B1 cells in comparison with S2WTP3 cells? To investigate any correlations between the metabolic phenotype and the enhanced metastatic potential, the proteome of ML1B1B1 cells was compared to S2WTP3 cells in an untargeted approach. To confirm the results of proteomic analysis, metabolomic analysis of cell extracts was performed.

3 MATERIAL AND METHODS

3.1 Experimental animals and animal models

3.1.1 Mouse strains

Female, 8-12 week old C57BL/6 mice (Charles River, Sulzfeld, Germany) were used as bone marrow donors for MDSC differentiation and as experimental animals in cell tracking experiments and experiments on tumor metabolism. The T cell receptor transgenic mouse line C57BL/6-Tg(TcraTcrb)1100Mjb (OT-1) recognizing the ovalbumin amino acid sequence SIINFEKL (residues 257-264) in a MHC-I restricted manner was used as donor mouse line for the isolation of $CD8^+$ T cells for immunosuppression assays. OT-1 mice were bred in the service facility for transgenic animals FORS/HI of the University of Tübingen. All animal experiments were in concordance with German federal regulations on the use and care of experimental animals, in consultation with the animal welfare officer of the University Tübingen and approved by the Regional Commission Tübingen (R10/12, R10/14 and R9/15).

3.1.2 Husbandry conditions

All experimental animals were housed in groups of maximum five animals in type IV Makrelen individually ventilated cages (IVC, Tecniplast, Hohenpeißenberg, Germany) with bedding, nesting material and wooden enrichment according to German federal regulations. Animals had access to standard pellet rodent food (Ssniff, Soest, Germany) and tap water *ad libitum* and were kept at 22 °C and 50 % humidity at a standardized 12 h day and night rhythm.

3.1.3 Experimental animal models

All experimental animal models used descended from the C57BL/6 strain to eliminate possible variation caused by differences in the genetic background. Female C57BL/6 mice (Charles River) between 8-12 weeks of ages were used as experimental animals.

3.1.3.1 Polyoma virus middle T-derived primary mammary carcinoma model

The B6.FVB-Tg(MMTV-PyVT)634Mul/LellJ (MMTV-PyMT) mouse strain is transgenic for the MMTV-LTR sequence encoding the PyMT antigen specifically introduced into the mammary glandular tissue. This mouse strain develops early onset, multifocal tumors in all mammary glands that metastasize to the lungs between 20-24 weeks of age (Lin *et al.*, 2003).

The murine breast cancer cell lines S2WTP3 and ML1B1B1 were generated by Dr. Christina Wong and Dr. Jaclyn Sceneay and were used for cell tracking and metabolic experiments as fast-growing, transplantable breast cancer model (for details on the cell lines, refer to section 3.2.1).

S2WTP3 and ML1B1B1 cells were thawed freshly, passaged at least twice before inoculation and used until passage 20 for *in vivo* experiments. For primary tumor inoculation, S2WTP3 or ML1B1B1 cells were trypsinated according to protocol (described in section 3.2.1), washed twice with phosphate buffered saline (PBS, Gibco by Thermo Fisher Scientific, Waltham, Massachusetts, USA) and counted in 0.125 % trypan blue (Gibco by Thermo Fisher Scientific). The cell suspension was adjusted to a concentration of $20x10^7$ cells/mL PBS and kept on ice until injection. For tumor inoculation, experimental animals were anaesthetized with 2 % isoflurane (CP Pharma, Burgdorf, Germany) in oxygen (Linde AG, Pullach, Germany) in a heated anesthesia box; anesthesia was maintained with 1.5 % isoflurane in oxygen. When proper anesthesia depth was reached as assessed by non-responsiveness to triggers of the pedal withdrawal reflex in the hind limbs, experimental animals were transferred to a pad-covered heating mat and ointment was applied to the eyes. The animals were positioned on their right side and the groin area was disinfected with disinfectant (Dr. Schumacher, Malsfeld, Germany). Then, the cell suspension was resuspended, drawn into a 1 mL insulin syringe without needle (BD Biosciences, Franklin Lakes, New Jersey, USA) and the syringe was equipped with a 25G cannula (BD Biosciences). After location of the left fourth mammary fat pad (MFP) by palpation, 25 µL of the cell suspension corresponding to either $0.5x10^6$ S2WTP3 cells or $0.5x10^6$ ML1B1B1 cells, respectively, was injected into the fourth MFP. Experimental animals were kept on the heated pad for recovery from anesthesia. For cell tracking experiments, S2WTP3 tumors were allowed to grow for 19 days. Tumor growth was assessed with calipers and the animals' weight was monitored once a week. ML1B1B1 tumors were allowed to grow for 7 days before *in vivo* PET measurements. Tumor growth was assessed with calipers and the animals' weight was monitored once a week.

3.1.3.2 B16-F10 melanoma model

B16-F10-Red-FLuc cells (Perkin Elmer, Waltham, Massachusetts, USA) were thawed freshly for every *in vivo* experiment and passaged twice before usage. B16-F10-Red-FLuc cells were utilized until passage 20. For primary B16-F10 melanoma induction, B16-F10-Red-FLuc cells were trypsinated according to protocol, washed twice with PBS and counted in 0.125 % trypan blue (for details, refer to section 3.2.2). The concentration of the cell suspension was adjusted to $1x10^7$ cells/mL PBS and cells were placed on ice until further use. Experimental animals to be inoculated were anaesthetized with 2 % isoflurane in oxygen. When proper anesthetic

depth was reached as assessed by lack of the pedal withdrawal reflex under appropriate stimulus, the experimental animals were transferred to a pad-covered heating mat where anesthesia was maintained at 1.5 % isoflurane in oxygen. The right subscapular area was shaved to allow access to the skin for an *intracutaneous* injection. Then, the B16-F10-Red-FLuc melanoma cells were drawn into a 0.5 mL insulin syringe (BD Biosciences). The skin of the subscapular area was folded into a skin fold in flat tipped tweezers to ensure an *intracutaneous* injection of the B16-F10-Red-FLuc melanoma cells. For injection of $0.25x10^6$ B16-F10-Red-FLuc melanoma cells, the tip of the cannula of the insulin syringe only was inserted into the molded skin fold and 25 µL of the cell suspension were injected. After injection, the animals were allowed to wake up in their home cage. Tumor growth was measured with calipers and animal weight was surveilled at least once a week and primary B16-F10 melanoma were allowed to grow for 12 days before adoptive cell transfer for cell tracking experiments.

3.1.3.3 Metastatic mammary carcinoma and metastatic melanoma model

As an experimental metastasis model, the left ventricular *intracardiac* injection technique was chosen to induce distant PyMT-derived breast cancer or B16-F10-derived melanoma metastases. Utilizing this technique enhances the chance to induce metastases in the bone and brain of experimental animals (Simmons *et al.*, 2015). For induction of breast cancer metastases, the cell line S2WTP3 expressing the reporter enzyme luciferase (Luc) and the fluorescent protein mCherry (mCh; S2WTP3-Luc-mCh, for details, refer to section 3.2.1) or the B16-F10-Red-FLuc melanoma cell line was used to enable surveillance of metastatic growth by bioluminescence OI.

S2WTP3-Luc-mCh or B16-F10-Red-FLuc were thawed freshly and passaged at least twice before inoculation (for details, refer to sections 3.2.1 and 3.2.2). For inoculation of breast cancer metastases, $0.25x10^6$ S2WTP3-Luc-mCh cells/100 µL PBS and for inoculation of melanoma metastases, $0.1x10^6$ B16-F10-Red-FLuc cells/100 µL were prepared and kept on ice until injection. For metastases induction, experimental animals were anaesthetized with 1.5 % isoflurane in oxygen in a heated anesthesia box. Proper anesthesia depth was probed by triggering the pedal withdrawal reflex in the hind limbs. Then, experimental animals were transferred to a pad-covered heating mat, ointment was applied to the eyes and the animals received a subcutaneous injection of Rimadyl® (Pfizer, New York City, New York, USA). The respective cell suspension was resuspended, drawn into a 1 mL insulin syringe without needle and the syringe was equipped with a 30G needle (BD Biosciences). Shortly before injection, the animals were turned into a dorsal position and the thorax was disinfected with disinfectant. The cannula was slowly inserted in the intercostal space between the fifth and sixth rip to allow

for the injection of the cell suspension into the left ventricle. The right placement of the canula was confirmed by blood flowing into the canula in the rhythm of the animal's heartbeat. After correct placement of the canula, 100 µL of either the S2WTP3-Luc-mCh or the B16-F10-Red-FLuc cell suspension were injected slowly. Directly after injection, the animal was turned into prone position to wake up and kept on the heated pad to check for any signs of stroke such as paralysis of a limb or hemiplegia.

Breast cancer metastases were allowed to grow for 19 days before adoptive cell transfer for tracking experiments. Animal weight and behavior was monitored three times in week 1 of metastatic growth and daily in week 2 and 3. Metastatic burden was assessed by bioluminescence OI on day 17 after inoculation, two days before the adoptive cell transfer for cell tracking experiments.

B16-F10-Red-FLuc metastases were allowed to grow for 11 days before cell tracking experiments. Animal weight and behavior was monitored at least three times per week in week 1, then daily. Metastatic growth was assessed via *in vivo* bioluminescence OI two days before the cell tracking experiments.

3.1.3.4 Pre-metastatic niche induction with tumor-cell conditioned media

For the experimental induction of pre-metastatic niche formation in secondary organs, tumor cells were used to condition DMEM without phenol red (Gibco by Thermo Fisher Scientific) with soluble tumor-derived factors. To generate tumor cell CM, $0.2x10^6$ S2WTP3 cells or $0.15x10^6$ B16-F10-Red-FLuc cells were seeded into 6-well plates (Greiner Bio-One, Kremsmünster, Austria) and grown overnight to 80 % confluence. When cells reached 80 % confluence, the regular growth medium was removed, cell layers were washed twice with PBS to remove traces of fetal calve serum (FCS, Merk Millipore, Billerica, Massachusetts, USA) and phenol red, and covered with 2 mL of serum-free DMEM without phenol red. The medium was conditioned overnight for 18 h in a standard humidified incubator at 37 °C and 7.5 % CO_2. The DMEM without phenol red was pooled into a 50 mL screw-cap tube (Greiner BioOne). The medium was centrifuged at 400 g for 5 min to remove cells and cell debris and sterile filtered through a 0.22 µm syringe-compatible filter (Merck Millipore). Aliquots of 2 mL CM were prepared aseptically in 2 mL cryogenic screw-cap tubes (Nalgene by Thermo Fisher Scientific) and stored at -80 °C until use.

To induce pre-metastatic niche formation in secondary organs, experimental animals were injected *intraperitoneally* (*i.p.*) with 300 µL S2WTP3- or B16-F10-Red-FLuc CM daily for 9 days. Therefore, 300 µL of the respective CM were drawn into a 1 mL insulin syringe. The experimental animal was physically immobilized and the cannula was inserted *i.p.* along the diagonal between the fourth and fifth nipple to avoid injection into the intestine or bladder.

3.1.3.5 Pre-metastatic niche induction with recombinant VEGF-C

The recombinant VEGF-C used in this experiment was generously provided by the group of Prof. Jonathan Sleeman at the Karlsruhe Institute of Technology and Institute of Toxicology and Genetics in Eggenstein-Leopoldshafen, Germany via communication with Dr. Wilko Thiele and Sandra Scherer.

To induce pre-metastatic niche formation in the lungs, experimental animals received *i.v.* injections of 70 µg recombinant VEGF-C on five consecutive days. Murine serum albumin served as control. For all *i.v.* injections, self-made catheters were constructed from the needle of a 20G cannula (BD Biosciences), medical tubing (High-Med-PE Mikrotubing, Reichelt Chemietechnik GmbH + Co., Heidelberg, Germany) and a 0.5 mL insulin syringe filled with heparinized (Medunasal Heparin 500 IU, Sintetica GmbH, Aschaffenburg, Germany) saline solution (Fresenius Kabi AG, Bad Homburg von der Höhe, Germany) for flushing of the tubing and aspiration. Experimental animals were anesthetized with 2 % isoflurane in oxygen in a temperature controlled anesthesia box. Anesthetized animals were transferred to a pad-covered heating mat after reaching proper anesthesia depth and anesthesia was maintained with 1.5 % isoflurane in oxygen. To facilitate catheterization and to provoke vasodilatation of the tail vein, the tail of the experimental animal was submerged in warm water. Then, the self-made catheter was inserted into the tail vein, correct placement was indicated by unrestricted blood flow into the catheter upon aspiration. The recombinant VEGF-C or murine serum albumin was injected slowly and the catheter was flushed with 50 µL of the heparinized saline solution. After the injection, the cannula was removed, pressure was applied onto the tail vein to stop bleeding and the animal was transferred back to its cage.

3.2 Cell culture

Established murine cell lines were, if not indicated otherwise, cultured in standard T175 cm^2 cell culture flasks (Sarstedt, Nümbrecht, Germany) in a humidified incubator at 37 °C and 7.5 % CO_2 (Linde AG). FCS used for cell culture was heat-inactivated at 57 °C for 30 min.

3.2.1 Polyoma virus middle T-derived murine mammary carcinoma cell lines

The murine mammary carcinoma cell line S2WTP3 was established from wild-type B6.FVB-Tg(MMTV-PyVT)634Mul/LellJ (MMTV-PyMT) mice at the Peter MacCallum Cancer Center (Melbourne, Australia) by Dr. Christina Wong (Wong *et al.*, 2012). The established cell line S2WTP3 was further modified to express the reporter enzyme Luc and the fluorescent protein mCh (denoted S2WTP3-Luc-mCh) for imaging studies by Dr. Jaclyn Sceneay.

The murine mammary carcinoma cell line ML1B1B1 was established at the Tumour Microenvironment Laboratory, QIMR Berghofer Medical Research Institute (Brisbane,

Australia) from spontaneously formed bone metastases after S2WTP3-mCh inoculation in the 4th MFP of female C57BL/6 mice and bone metastases after *intracardiac* injection. Briefly, cancerous cells were isolated from bone metastases by sorting for mCh-positive populations and established in culture as cell line ML1. To enrich for metastatic cells, ML1 tumor cells were injected *intracardically*, bone metastases were isolated and established in culture as cell line ML1B1B1. PyMT-derived carcinoma cell lines were maintained in Dulbecco's Modified Eagle's Medium (DMEM, Merck Millipore) supplemented with 10 % FCS, 10 mM HEPES (Merck Millipore), 1 mM sodium pyruvate (Merck Millipore), 1 % MEM amino acids (Merck Millipore), 100 U/mL penicillin and 100 µg/mL streptomycin (Merck Millipore) and 0.05 mM 2-β-mercaptoethanol (Sigma-Aldrich, St. Louis, Missouri, USA). PyMT-derived carcinoma cells were passaged into new cell culture flasks when reaching 70-80 % confluence. Growth media was removed, cells were washed with PBS and incubated with 0.05 %/0.02 % trypsin-EDTA solution (Merck Millipore) for 5 min in an incubator. Digestion was stopped by adding complete growth medium. The resulting cell suspension was centrifuged for 5 min at 400 g, the cell pellet was resuspended in growth medium and diluted into new cell culture flasks.

3.2.2 B16-melanoma cell lines

The murine melanoma cell line B16-F0 was obtained from Dr. Stefanie Maurer, Internal Medicine II, University Hospital Tübingen. The murine melanoma cell line B16-F10 was purchased from ATCC. B16-F0 and B16-F10 cells were maintained in DMEM supplemented with 10 % FCS, 10 mM HEPES, 1 mM sodium pyruvate, 1 % MEM amino acids, 100 U/mL penicillin and 100 µg/mL streptomycin and 0.05 mM 2-β-mercaptoethanol and split into new flasks when reaching 70-80 % confluence according to need.

The Luc-transgenic murine melanoma cell line B16-F10-Red-FLuc was purchased from Perkin Elmer and maintained in Roswell Park Memorial Institute 1640 (RPMI 1640; Merck Millipore) medium supplemented with 10 % FCS according to the manufacturer's instructions. B16-F10-Red-FLuc cells were split into new cell culture flasks when reaching 70-80 % confluence according to need. For subculture of B16 cell lines, the growth medium was removed, the cells were washed with PBS and incubated with 0.05 %/0.02 % trypsin-EDTA for 5 min in an incubator. Trypic digestion was stopped by addition of growth medium and the resulting cell suspension was centrifuged at 400 g for 5 min. The cell pellet was resuspended in new medium and diluted into new cell culture flasks.

3.2.3 *In vitro* culture of MDSCs

In vitro expansion of MDSCs was performed as previously published (Sceneay *et al.*, 2018) with a protocol modified from Marigo *et al*. (Marigo *et al.*, 2010).

3.2.3.1 Isolation of murine bone marrow cells

Female 8-16 week old C57BL/6 mice were sacrificed by CO_2 asphyxiation and disinfected in 70 % ethanol (SAV Liquid Production GmbH, Flintsbach am Inn, Germany) for 2 min. Femurae and tibiae were cut adjacent to the hip and knee joint and the knee and the subtalar joint, respectively. Excess tissue and muscle was scraped away with a blade 16 scalpel (B-Braun, Melsungen, Germany). Bones were stored in DMEM medium on ice before being flushed from both sides with DMEM medium with a 25G cannula (BD Biosciences). Bone marrow cells were collected in 50 mL screw cap tubes (Greiner Bio-One, Kremsmünster, Austria) and spun down for 5 min at 400 g. Erythrocytes were lysed by addition of 0.5 mL ACK lysis buffer (Lonza, Basel, Switzerland) per donor animal to the cell pellet and incubation for 4 min at room temperature. Lysis was stopped by adding twice the volume of PBS.

3.2.3.2 Differentiation of murine bone marrow cells to MDSCs and magnetic cell sorting

Freshly isolated bone marrow cells were suspended in RPMI 1640 growth medium supplemented with 10 % FCS, 10 mM HEPES, 1 mM sodium pyruvate, 1 % MEM amino acids, 100 U/mL penicillin and 100 µg/mL streptomycin and 0.05 mM 2-β-mercaptoethanol (full RPMI growth medium) and dispensed into 6 cm sterile petri dishes (Greiner Bio-One) to allow differentiated cells to adhere to the dishes overnight. On the following day, bone marrow-derived cells were collected, suspended at approximately $1x10^6$ cells/mL in full RPMI growth medium supplemented with 40 ng/mL GM-CSF and 40 ng/mL IL-6 (Peprotech, Hamburg, Germany), transferred to 10 cm sterile suspension cell culture dishes (Sarstedt) and cultivated for 5 days. GM-CSF and IL-6 were added every other day at a final concentration of 40 ng/mL, medium was exchanged when necessary. On day 6 of cultivation, suspension cells were collected into 50 mL screw cap tubes (Greiner Bio-One), counted and pooled. PMN- and M-MDSCs were separated using the myeloid-derived suppressor cell isolation kit (Miltenyi Biosciences, Bergisch Gladbach, Germany) for murine samples according to the manufacturer's instructions. Briefly, cells were suspended in 350 µL PBS + 1 % FCS (MACS buffer) per 10^8 cells. Unspecific antibody binding was blocked by adding 50 µL FcR Blocking Reagent per 10^8 cells and incubating for 10 min at 4 °C. Then, 100 µL Anti-Ly6G-Biotin was added and incubated for 10 min at 4 °C to bind to $Ly6G^+$ cells. Cells were washed in 50 mL MACS buffer, spun down at 400 g for 5 min and suspended in 800 µL MACS buffer per

10^8 cells. Then, the cell suspension was incubated with 200 µL Anti-Biotin-MicroBeads for 15 min at 4 °C to allow for magnetic labeling of $Ly6G^+$ cells. After washing in 50 mL MACS buffer, cells were suspended in 500 µL MACS buffer per 10^8 cells and pipetted onto a magnetic cell separation column mounted in the QuadroMACS® Separator (Miltenyi Biosciences) and pre-rinsed with 3 mL MACS buffer. After the cell suspension cleared completely from the reservoir, the column was rinsed three times with 3 mL buffer while the column flow-through was collected for further processing. Magnetically labeled $Ly6G^+$ cells were eluted from the column by placing it onto a 50 mL screw cap tube and pressing 5 mL MACS buffer through the column with the column plunger. To further isolate $Ly6C^+$ cells, the column flow through was adjusted to a concentration of 10^8 cells/400 µL and incubated with 100 µL Anti-Gr-1-Biotin per 10^8 cells for 10 min at 4 °C. Cells were washed in 50 mL MACS buffer, spun at 400 g for 5 min and suspended in 900 µL MACS buffer per 10^8 cells. For magnetic labeling of the $Ly6C^+$ cell fraction, 100 µL Streptavidin MicroBeads were added and incubated with the cell suspension for 15 min at 4 °C. After washing in 50 mL MACS buffer, the concentration was adjusted to 10^8 cells/500 µL buffer and the cell suspension was pipetted onto a pre-rinsed magnetic cell separation column mounted in the QuadroMACS® Separator. The magnetic cell separation column was washed three times with 3 mL MACS buffer once the fluid had cleared from the column reservoir. Magnetically labeled $Ly6C^+$ cells were eluted from the column with 5 mL MACS buffer after removing the column from the magnetic field and placing it onto a 50 mL screw cap tube. A schematic drawing of MDSC expansion and magnetic cell separation is given in Figure 18.

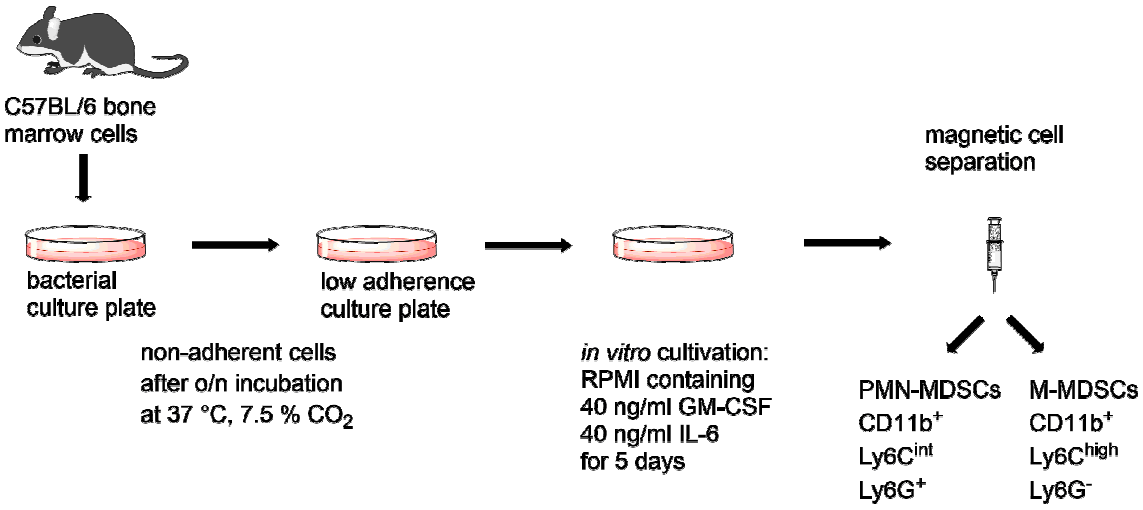

Figure 18: Schematic of MDSC generation and magnetic cell sorting into subpopulations.
Bone marrow cells were isolated from C57BL/6 donor mice and plated on bacterial cell culture plates overnight (o/n). The next day, BMDCs were transferred to low adherence culture plates and cultivated in RPMI medium supplemented with 40 ng/mL GM-CSF and IL-6 for 5 days. On day 6 of cultivation, the subpopulations were isolated by magnetic cell sorting.

3.2.4 Isolation of murine C57BL/6-Tg(TcraTcrb)1100Mjb (OT-1) CD8$^+$ T cells

The homozygous C57BL/6-Tg(TcraTcrb)1100Mjb mouse line contains transgenic inserts for mouse Tcra-V2 and Tcrb-V5 genes resulting in a transgenic T cell receptor designed to recognize ovalbumin residues 257-264 (SIINFEKL) in a MHC-I restricted manner. For the isolation of OT-1 CD8$^+$ T cells, donor animals were sacrificed by CO_2 asphyxiation and disinfected in 70 % ethanol for 2 min. Donor animals were fixed onto a styrofoam block to facilitate a median incision and the separation of the skin from the peritoneum. The extraperitoneal cervical, axial, brachial and inguinal LNs were located, removed with blunt forceps and stored in a petri dish containing MACS buffer. The spleen was aseptically removed from the peritoneum and stored with the lymph nodes. To receive a single cell suspension, lymph nodes and the spleen were ground through a sterile 70 µm cell strainer (Falcon by Thermo Fisher Scientific) with the plunger of a sterile syringe into a 50 mL screw-cap tube. The 70 µm cell strainer was washed twice with 10 mL MACS buffer in total and the resulting cell suspension was centrifuged at 400 g for 5 min. Erythrocyte lysis was performed by resuspending the cell pellet in 3 mL ACK lysis buffer per donor animal and incubation for 4 min at room temperature. Lysis was stopped by adding twice the volume of PBS and the cell suspension was passed through a 40 µm cell strainer (Falcon by Thermo Fisher Scientific) into a new 50 mL screw cap tube. The cell suspension was adjusted to 10 mL of volume in MACS buffer and cell yield was determined by counting live cells in 0.125 % trypan blue in PBS. For the untouched isolation of CD8$^+$ T cells, the CD8a$^+$ T Cell Isolation Kit, mouse (Miltenyi Biosciences) was used according to the manufacturer's instructions. Briefly, cells were centrifuged and the suspension volume was adjusted to 10^7 cells in 40 µL MACS buffer. To label non-CD8$^+$ cells magnetically, 10 µL Biotin-Antibody Cocktail per 10^7 cells were added and incubated with the cell suspension for 5 min at 4 °C. Then, 30 µL MACS buffer and 20 µL Anti-Biotin MicroBeads per 10^7 total cells were added, mixed well and incubated at 4 °C for 10 min. The cell suspension was pipetted onto a pre-rinsed magnetical cell separation column mounted in the QuadroMACS® Separator and the unlabeled CD8$^+$ cells in the column flowthrough were collected. The column was rinsed with 3 mL MACS buffer and non-CD8$^+$ cells, denoted APCs, were eluted with 5 mL MACS buffer into a separate 50 mL screw cap tube by firmly pressing the plunger into the column. Yield of CD8$^+$ T cells and non-CD8$^+$ cells was determined by cell counting in 0.125 % trypan blue.

3.2.5 Cultivation of M1/70 hybridoma cells for anti-CD11b antibody production

The hybridoma cell line M1/70 produces a rat anti-mouse anti-CD11b monoclonal antibody (mAb; isotype IgG_{2b}) and was purchased from ATCC. For maintenance, M1/70 cells were cultivated in DMEM supplemented with 10 % FCS, 10 mM HEPES, 1 mM sodium pyruvate,

1 % MEM amino acids, 100 U/mL penicillin and 100 µg/mL streptomycin and 0.05 mM 2-β-mercaptoethanol at 37 °C in a humidified incubator. For antibody production and purification, M1/70 cells were cultivated in high density in DMEM supplemented with 10 mM HEPES, 1 mM sodium pyruvate and 1 % MEM amino acids for 5 days.

3.3 Tracer synthesis

3.3.1 ^{64}Cu synthesis and quality control

^{64}Cu synthesis was performed mainly by Walter Ehrlichmann and Ender Özdemir in the Department of Preclinical Imaging and Radiopharmacy, University of Tübingen.

The radioisotope ^{64}Cu was produced via the ^{64}Ni(p,n)^{64}Cu nuclear reaction with a PETtrace cyclotron (General Electric Medical Systems, GEMS, Uppsala, Sweden) as previously described (Hoffmann *et al.*, 2017). Briefly, ^{64}Ni (approx. 30 mg) was electroplated on a platinum/iridium plate (90/10; Ögussa, Wien, Austria) as holder and irradiated with 30 µA for 1-6 h with a proton beam of 12.4 MeV. Then, the platinum/iridium holder was heated to 100 °C in a dedicated polyetheretherketone (PEEK; WKL, Elztal, Germany) chamber and ^{64}Cu/^{64}Ni was dissolved in 2 mL of concentrated HCl (Merck Millipore) for 20 min. The HCl was evaporated using a stream of argon (Linde). The reaction chamber was flushed with 3 mL of 4 % 0.2 M HCl and 96 % methanol (Merck Millipore) and this solution was transferred further to an ion exchange column (AG1x8, BioRad, Hercules, California, USA) preconditioned with 4 % 0.2 M HCl in methanol for at least 15 min. The ion exchange column was washed with 4 % 0.2 M HCl in methanol. Then, ^{64}Cu was eluted from the column with 70 % 1.3 M HCl/30 % isopropanol (v/v; Merck Millipore) into a collection vial and the solvent was evaporated in a stream of argon. Finally, the ^{64}Cu was taken up in approximately 200 µL of 0.1 M HCl. The resulting [^{64}Cu]$CuCl_2$ was buffered to pH 5-6 with 0.5 M ammonium acetate (pH 5; Sigma-Aldrich).

3.3.2 [^{18}F]FDG synthesis

[^{18}F]FDG synthesis was performed by the staff of the Radiopharmacy of the Department of Preclinical Imaging and Radiopharmacy, University of Tübingen.

^{18}F was produced at the PETtrace cyclotron (General Electric Medical Systems) via the ^{18}O(p,n)^{18}F nuclear reaction with 16.5 MeV protones as [^{18}F]flouride using [^{18}O]H_2O (Rotem, Leipzig, Germany) as target material. [^{18}F]FDG was then synthesized in a TRACERlab MX_{FDG} synthesizer (GE Healthcare, Chicago, Illinois, USA) with mannose triflate (ABX, Radeberg, Germany) as precursor according to a protocol provided by GE Healthcare. Quality control of

[^{18}F]FDG was performed according to the guidelines of the European Pharmacopoiea (Council of Europe, 2017).

3.4 Radioactive cell labeling with the [^{64}Cu]NOTA-anti-CD11b monoclonal antibody

3.4.1 Anti-CD11b mAb production and purification

The rat anti-mouse anti-CD11b mAb producing hybridoma cell line M1/70 (ATCC) was cultivated in ISF-1 medium (Biochrom by Merck Millipore) supplemented with 100 U/mL penicillin and 100 µg/mL streptomycin in either standard cell culture flasks or in the miniPERM® HDC 50 bioreactor (Sarstedt). In standard cell culture flasks, M1/70 hybridoma cells were left to grow for 5 days until a high cellular density was reached. Then, the anti-CD11b mAb-containing medium was collected from the flasks by centrifugation and kept under sterile conditions until further processing.

For antibody production in the bioreactor, the nutrient module of the reactor was sterilized in 70 % ethanol for 2-3 days. Then, M1/70 hybridoma cells were adjusted to a concentration of 1-5x10^6 per mL ISF-1 medium and approximately 45 mL of the cell suspension was filled into the sterile production unit of the bioreactor. The nutrient module was filled with prewarmed ISF-1 medium and the bioreactor was placed on a roller shaker (Sarstedt) in a standard humidified incubator at 37 °C with 7.5 % CO_2 for the rotating cultivation of hybridoma cells in high density and small volumes. Excess pressure in the bioreactor was released aseptically after 1 h in the incubator. To harvest the mAb-containing medium, approximately 35 mL of the cell suspension was removed from the production module with a Luer-Lock connector syringe (BD Biosciences) once a week. The cell suspension was then centrifuged at 400 g for 5 min, the cell pellet was discarded while the supernatant was kept under sterile conditions for further purification.

The collected cell culture or bioreactor supernatants were centrifuged at 4000 g for 30 min to remove cellular debris. The resulting supernatant was sterile filtered with Stericup® Filter Units (Merck Millipore) and diluted with PBS in a 1:1 ratio. Purification of the rat anti-mouse anti-CD11b mAb was achieved via affinity chromatography utilizing HiTrap® Protein G High Performance columns (GE Healthcare) with 1 mL bed volume. Liquid flow with a flow rate of 1 mL/min was managed with a P-1 peristaltic pump (GE Healthcare). First, the affinity chromatography column was washed with 10 mL PBS. Then, the diluted anti-CD11b mAb solution was pumped onto the column. After washing with 20 mL PBS, the anti-CD11b mAb was eluted from the Protein G column with 10 mL 0.1 M glycine-HCl pH 2.5 elution buffer (glycine: Sigma Aldrich, HCl: Carl Roth GmbH & Co KG, Karlsruhe, Germany). The first 0.8 mL

fraction was discarded due to the dead volume of the tubing. Then, 8-10 elution fractions of alternating volumes of 1.5 mL and 1 mL were collected directly into 1 mL reaction cups (Eppendorf) prefilled with 100 µL Tris/HCl buffer (Tris: Sigma Aldrich, HCl: Carl Roth) to neutralize the pH. For storage, the affinity column was rinsed with 10 mL PBS and 10 mL 20 % ethanol. PD-10 desalting columns (GE Healthcare) were utilized for desalting and removal of trace and low-molecular weight contaminants from the anti-CD11b mAb solution according to the manufacturer's instructions. Briefly, PD-10 columns were equilibrated with PBS, 2.5 mL anti-CD11b mAb solution was applied on the column and washed through it by addition of 3.5 mL PBS. PD-10 columns were rinsed with 10 mL PBS and stored in 20 % ethanol at 4 °C. The anti-CD11b mAb solution was sterile filtered through a 0.22 µm syringe-compatible filter (Merck Millipore) and stored at 4 °C until further use.

3.4.2 Chelator conjugation and radioactive labeling with ^{64}Cu

Chelator conjugation of the anti-CD11b mAb was performed by Dr. Andreas Maurer and Natalie Mucha at the Department of Preclinical Imaging and Radiopharmacy, University of Tübingen.

The concentration of the anti-CD11b mAb was determined by UV/Vis spectroscopy using the NanoDrop1000 photometer (Thermo Fisher Scientific). The protein concentration was adjusted to 8 mg/mL in PBS by centrifugation using 100 kDa Amicon Ultra-15 Centrifugal Filter Units (Merck Millipore). The anti-CD11b mAb solution was washed first with 0.5 M EDTA (pH 7; Carl Roth GmbH + Co. KG) and then three times in sterile 0.1 M HEPES buffer (pH 7.5; Sigma Aldrich) treated with 1.2 g of Chelex 100 (Sigma Aldrich) to eliminate trace metal contaminations. The chelator 1,4,7-triazacyclononane-N,N',N''-triacetic acid (NOTA), in the chemical formulation of an activated NOTA-N-hydroxysuccinimide ester (NOTA-NHS; Macrocyclics), was solved in Rotipuran Ultrapure water (Carl Roth GmbH + Co. KG) at a concentration of 10 mg/mL and the displacement reaction between the mAb and the NOTA-NHS ester was performed in a 55-fold molar excess over night at 4 °C. The NOTA-anti-CD11b mAb was washed 7 times in sterile 0.25 M sodium acetate (pH 6; Sigma-Aldrich) treated with 1.2 g of Chelex 100 and concentrated to 2-6 mg/mL using 100 kDa Amicon Ultra-15 Centrifugal Filter Units. The NOTA-conjugated anti-CD11b mAb (NOTA-anti-CD11b) was stored at 4 °C until radiolabeling.

For ^{64}Cu radiolabeling, the NOTA-anti-CD11b-mAb was incubated with [^{64}Cu]$CuCl_2$ in a 2:1 ratio MBq:µg protein for 60 min at 42 °C. Afterwards, radiochemical purity of the [^{64}Cu]NOTA-anti-CD11b mAb was assessed by instant thin layer chromatography on silica gel with 0.1 M citrate as running buffer, the instant thin layer chromatography-silica gel was analyzed on the Cyclone Plus PhosphorImager (Perkin Elmer). Radiochemical purity ranged between 75-90 %.

3.4.3 MDSC labeling with [^{64}Cu]NOTA-anti-CD11b mAb

Directly after magnetic cell separation, freshly isolated PMN- and M-MDSCs were suspended in complete RPMI 1640 growth medium (as described in 3.2.3) supplemented with 40 ng/mL GM-CSF and IL-6 (Peprotech) at 2x10^6 cells/mL. Then, 500 µL of the cell suspension corresponding to 10^6 PMN- or M-MDSCs, respectively, were plated in low adherence 48-well plates (Sarstedt). 0.74 MBq [^{64}Cu]NOTA-anti-CD11b mAb corresponding to on average 1.6 µg of mAb in 20 µL PBS were added to each well and the labeling reaction was performed at 37 °C for 30 min. After radiolabeling (Figure 19), MDSCs were washed twice in PBS and cell yield was determined by cell counting in 0.125 % trypan blue.

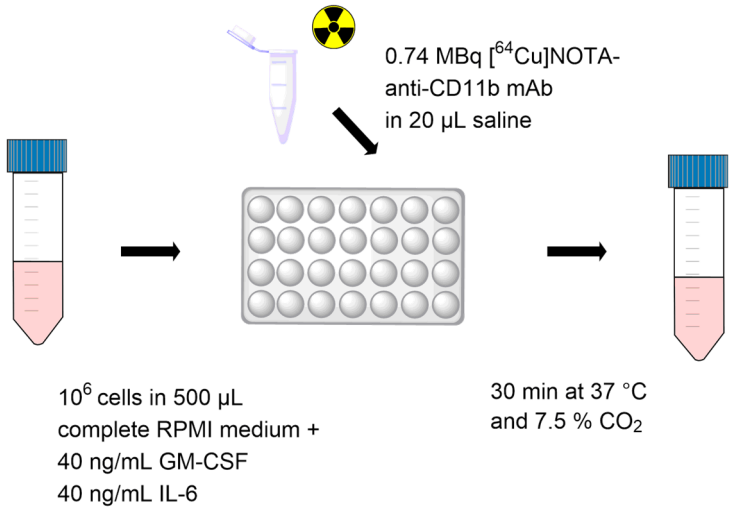

Figure 19: Schematic of MDSC radiolabeling with 0.74 MBq [^{64}Cu]NOTA-anti-CD11b mAb.
10^6 PMN- or M-MDSCs in 500 µL complete RPMI medium supplemented with 40 ng/mL GM-CSF and IL-6 were dispensed in a low-adherence 48-well plate and 0.74 MBq [^{64}Cu]NOTA-anti-CD11b mAb in 20 µL saline were added. The cells were labeled with the radioactive antibody for 30 min at 37 °C and 7.5 % CO_2. After labeling, the MDSC subpopulations were harvested and washed twice in PBS.

3.4.4 MDSC labeling for fluorescence optical imaging

Labeling of MDSCs for fluorescence OI with the fluorescent dye Cy5 derivate 1,1'-dioctadecyl-3,3,3',3'-tetramethylindodicarbocyanine perchlorate (DiD) was performed with the Vybrant™ DiD Cell-Labeling Solution (Thermo Fisher Scientific). For DiD-labeling, MDSCs were suspended in serum-free RPMI 1640 medium without supplements at a density of 1x10^6 cells/mL in a 50 mL screw-cap tube. Then, 5 µL of the DiD cell-labeling solution per mL of cell suspension were added and incubated for 2 min at 37 °C. The screw-cap tube was centrifuged at 400 g for 5 min, the supernatant was removed. The cell pellet was washed twice in PBS and cell count was determined for adoptive cell transfer.

3.5 Evaluation of possible detrimental effects of the [^{64}Cu]NOTA-anti-CD11b mAb-labeling MDSCs

3.5.1 Uptake of radioactivity and labeling stability

To determine uptake and efflux of the [^{64}Cu]NOTA-anti-CD11b mAb in PMN- and M-MDSCs, 10^5 [^{64}Cu]NOTA-anti-CD11b mAb-labeled PMN- and M-MDSCs were dispensed into γ-counting tubes (Sarstedt) in 1 mL complete RPMI 1640 medium. The radioactive uptake in MDSCs was determined directly after radiolabeling in a γ-counter (Perkin Elmer). To determine the efflux of the [^{64}Cu]NOTA-anti-CD11b mAb, the supernatant medium of each tube was transferred into a new γ-counting tube and the cells were washed with new medium that was than transferred to another new γ-counting tube as wash fraction. 1 mL new medium was added to the cells. The supernatant, the wash fraction and the cells were measured in a γ-counter (Perkin Elmer). This precedure was repeated at 5, 24 and 48 h post radiolabeling. The stability of radioactivity was calculated as percent of initial uptake measured directly after radiolabeling.

3.5.2 Determination of cell viability after [^{64}Cu]NOTA-anti-CD11b mAb-labeling

Viability of PMN- and M-MDSCs after radiolabeling with [^{64}Cu]NOTA-anti-CD11b mAb and apoptosis induction was assessed by 7-aminoactinomycin D (7-AAD) and PE Annexin V staining at 3 and 48 h post radiolabeling utilizing the phycoerythrin (PE) Annexin V Apoptosis Detection Kit I (BD Biosciences) according to the manufacturer's instruction. Briefly, radiolabeled MDSCs and unlabeled control MDSCs were washed in PBS and suspended in 100 µL of the provided binding buffer. Then, 5 µL of PE Annexin V and 5 µL 7-AAD were added and incubated for 15 min at room temperature in the dark. For analysis, 400 µL of the binding buffer were added. Samples were analyzed on a BD LSR II flow cytometer (BD Biosciences). Data analysis was performed using the Flow Jo software Version 10 (Tree Star, Inc., Ashland, Oregon, USA).

3.5.3 Immunosuppression assay for determination of MDSC functionality

One key function of MDSCs is the potent immunosuppression of both innate and adaptive immune responses. Therefore, the capacity of naïve *in vitro* expanded, anti-CD11b mAb-labeled and [^{64}Cu]NOTA-anti-CD11b mAb-labeled PMN- and M-MDSCs to suppress T cell proliferation was evaluated in a carboxyfluorescein succinimidyl ester (CFSE)-dilution assay. For the CFSE staining of OT-1 $CD8^+$ T cells, carboxy-fluorescein diacetate succinimidyl ester (Vybrant® CFDA SE Cell Tracer Kit, Life Technologies by Thermo Fisher Scientific) was used.

OT-1 $CD8^+$ T cells were isolated from the spleen and extraperitoneal LNs of OT-1 mice (as described in 3.2.4). For labeling with carboxy-fluorescein diacetate succinimidyl ester, freshly isolated OT-1 $CD8^+$ T cells were suspended at 10^7 cells/mL in PBS. OT-1 $CD8^+$ T cells were mixed with an equivalent volume of 2.5 µM carboxy-fluorescein diacetate succinimidyl ester staining solution prepared freshly in PBS and incubated in a 37 °C water bath in the dark for 10 min. Then, 5 mL of DMEM medium supplemented with 10 % FCS was added and incubated with the cells for 20 min in the 37 °C water bath. CFSE-stained OT-1 $CD8^+$ T cells were washed in warm DMEM medium supplemented with 10 % FCS twice and cell yield was determined by counting in 0.125 % trypan blue. The concentration of the CFSE-labeled OT-1 $CD8^+$ T cells was adjusted to $2x10^6$ cells/mL in complete DMEM medium.

MDSCs were expanded and subpopulations were isolated as described in 3.2.3.2. PMN- and M-MDSCs were labeled with 1.6 µg anti-CD11b or 0.74 MBq [^{64}Cu]NOTA-anti-CD11b mAb as described in 3.4.3. Then, naïve PMN-MDSCs, anti-CD11b mAb-labeled PMN-MDSCs or ^{64}Cu-NOTA-anti-CD11b mAb-labeled PMN-MDSCs were mixed with CFSE-labeled OT-1 $CD8^+$ T cells in the wells of a 96-well plate in different MDSCs:T cell ratios. The number of CFSE-labeled OT-1 $CD8^+$ T cells were kept constant at 10^5 T cells per well. The same serial dilution was done with naïve M-MDSCs, anti-CD11b mAb-labeled M-MDSCs and [^{64}Cu]NOTA-anti-CD11b mAb-labeled M-MDSCs and CFSE-labeled OT-1 $CD8^+$ T cells. CFSE-labeled OT-1 $CD8^+$ T cells without MDSCs served as control for non-suppressed T cell proliferation. T cell proliferation was stimulated with 250 U/mL IL-2 (Novartis, Basel, Switzerland), 8 µg/mL SIINFEKL peptide (EMC Microcollections, Tübingen, Germany), $2x10^5$ APCs and 2 µL of the prepared magnetic-bead-coupled anti-CD3 and anti-CD28 mAb of the T Cell Activation and Expansion Kit (Miltenyi Biosciences); OT-1 T cells were allowed to proliferate for 72 h. After the incubation time, the cells were centrifuged in the 96-well plate at 400 g for 5 min, washed twice with 200 µL of 1 % MACS buffer and centrifuged again at 400 g for 5 min. Then, $CD8^+$ T cells were stained with 50 µL of a 1:300 dilution of PE-Cy7-anti-CD8 antibody for flow cytometry for 30 min at 4 °C. Each well was then filled up with 150 µL MACS buffer and centrifuged in the 96-well plate at 400 g for 5 min. The cells were then washed twice in 200 µL MACS buffer. The resulting cell pellet was resuspended in 80 µL MACS buffer for analysis. Flow cytometric analysis was performed on the BD LSRFortessa (BD Biosciences). The percentage of proliferated T cells for each condition was assessed according to CFSE-dilution in comparison to $CD8^+$ T cells without MDSCs using the FlowJo software.

3.6 PET data acquisition

3.6.1 PET data acquisition for cell tracking experiments

PET data acquisition for cell tracking experiments was performed on three dedicated small animal PET scanners (Inveon microPET; Siemens Healthineers, Knoxville, Tennessee, USA; Figure 20 A) with a FOV of 12.7 cm in axial direction and 10 cm in transaxial direction and a spatial resolution of approximately 1.4 mm in the center of the FOV. The energy window was set to 350-650 keV with the photopeak at 511 keV and the coincidence window set to 3.432 ns. For PET data acquisition, the experimental animal was anesthetized at least 10 min before the start of the PET scan in a temperature-controlled anesthesia box with 2 % isoflurane in oxygen. When the animal reached appropriate anesthetic depth, ointment (Corneregel, Dr. Mann Pharma GmbH, Berlin, Germany) was applied to the eyes before the animal was transferred to an animal bed (Bruker, Billerica, Massachusetts, USA) that had been positioned on the PET scanner. Anesthesia was maintained with 1.5 % isoflurane in oxygen. To facilitate image fusion with the anatomical MR scans, 10 µL glass micropipettes (Hirschmann Laborgeräte, Eberstadt, Germany) were filled with 0.37 MBq/mL radioactive ^{64}Cu-NOTA-anti-CD11b mAb solution and mounted on the left and right rim inside the animal bed (Figure 20 B, C). The mouse was fixed on the bed with cotton swabs and adhesive tape (3M, Maplewood, Minnesota, USA). The PET scanners' laser cross-hair was angled to the center body mass of the mouse and the animal bed was translocated into the center FOV of the PET scanner via the control software Inveon Acquisition Workplace (Siemens Heathineers). Consecutively, a 20 min static emission PET scan was started. For anatomical reference, a standard MR image was acquired as described in 3.7.1.

After data acquisition, the list mode file was histogrammed and the resulting sinogram file was reconstructed into an image file using the iterative OSEM2D algorithm (matrix size 128x128, pixel size 0.79x0.79 mm^2). Attenuation correction was not performed. Data analysis was performed in Inveon Research Workplace Software (Version 1.5.0.28; Siemens Healthineers). The reconstructed PET images were fused with the respective anatomical MR images with the help of the glass micropipettes and normalized according to the injected amount of radioactivity. Furthermore, the scans were decay corrected to the injection time. Volumes of interest (VOI) were drawn on the normalized PET image to quantify cellular uptake in tumor tissue and metastases. VOIs on the possible homing tissues of MDSCs lung, liver and spleen and the muscle as control tissue were drawn on the MR images only to avoid researcher bias. From the obtained mean uptake values (Bq/mL), the percent of the injected dose per cubic centimeter (%ID/cm^3) was calculated.

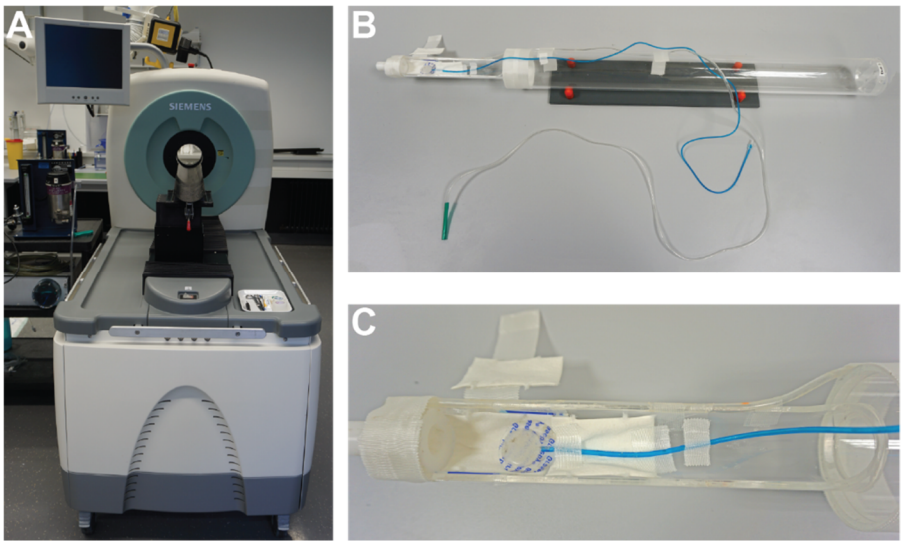

Figure 20: Experimental setup for PET data acquisition for cell tracking studies.
Representative image of one small-animal dedicated Inveon microPET scanner (**A**) and the animal bed (**B**) used for cell tracking studies with a close up (**C**) on the trigger pad for respiratory gating and the glass micropipettes (filled with blue dye for visualization) used as marker for PET and MR image fusion.

3.6.2 PET data acquisition for metabolic fingerprinting of the cells lines S2WTP3 and ML1B1B1

PET data acquisition for experiments on the glucose metabolism of the primary PyMT breast cancer tumors S2WTP3 and ML1B1B1 was performed on a MR-compatible PET insert (Bruker) for simultaneous PET/MR acquisitions (Figure 21). The FOV of the PET insert spans 7.1 cm in axial direction and 7.2 cm in transaxial direction with a spatial resolution of 1.4-1.6 mm. The energy window was set to 350-650 keV, the photopeak to 511 keV.

For simultaneous PET/MR data acquisition, a 7 T, 300 MHz small animal MR scanner (Bruker) equipped with a preclinical PET insert was utilized. Experimental animals were anesthetized with 2 % isoflurane in oxygen in a heated anesthesia box. Once the animal reached proper anesthetic depth, the animal was transferred to a pad-covered heating mat where anesthesia was maintained at 1.5 % isoflurane in oxygen. A self-made catheter was inserted into and stabilized in the tail vein with tissue adhesive. Then, the animal was transferred onto an animal bed equipped with a heating mat to avoid a drop in body temperature and fixed on the bed with cotton swabs and adhesive tape. The ^{1}H MR volume coil (inner diameter: 40 mm) was placed onto the bed to ensure close proximity to the animal. After mounting the MR coil onto the animal bed, the latter was placed into the center of the FOV of the preclinical PET insert positioned in the center of the magnet of the 7 T MR scanner. Then, the animal was injected with 13 ± 1 MBq [^{18}F]FDG in a maximum volume of 100 µL while a 70 min dynamic emission PET scan was started simultaneously. To ensure complete tracer injection, the catheter was flushed with 50 µL heparinized saline solution. During the dynamic PET scan, anatomical MR images and ^{1}H spectroscopy were acquired (for details, refer to sections 3.7.1 and 3.7.2). Data

analysis was performed in Inveon Research Workplace (Siemens Healthineers). The reconstructed PET images were fused with the respective anatomical MR images and normalized according to the injected amount of radioactivity. VOIs were drawn on the tumor and the muscle as control tissue and the tracer uptake (in %ID/cm³) was calculated as mentioned above.

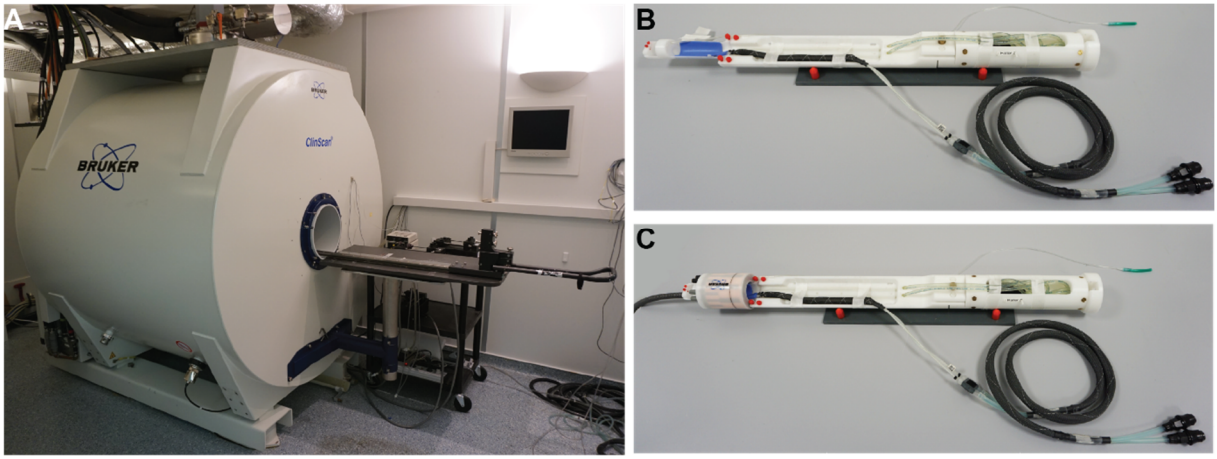

Figure 21: Experimental setup for simultaneous PET/MRI acquisitions.
Representative image of the 7 T 300 MHz small animal MR scanner (**A**) equipped with the preclinical PET insert (not visible). The animal bed with the heating mat (**B**) was mounted with the ^{1}H resonance volume coil (**C**).

3.7 Nuclear magnetic resonance spectroscopy and imaging

For anatomical reference for PET scans, MR imaging was performed on either a 7 T BioSpec 70/30 small animal MR scanner (Bruker) or a 7 T, 300 MHz small animal MR scanner (Bruker; Figure 21 A) operated under Paravision (Version 6.01; Bruker). For whole-body anatomical MR images, a ^{1}H resonance volume coil (inner diameter: 86 mm) was used. A ^{1}H resonance volume coil was utilized for both acquisition of anatomical MR images and ^{1}H *in vivo* spectroscopy (inner diameter: 40 mm).

^{13}C-MRS with DNP-hyperpolarized [^{13}C]pyruvate was performed with a ^{1}H/^{13}C dual tune surface coil with an inner diameter of 20 mm.

Ex vivo NMR spectroscopy was performed on the Avance III NMR spectrometer (^{1}H resonance frequency 600 MHz, 14.1 T; Bruker; Figure 24) and a 5 mm TXI ^{1}H/^{13}C RT probe. Spectra of tissue samples were acquired using the high resolution magic angle spinning (HR-MAS) technique with the TXI HR-MAS probe (Bruker).

3.7.1 *In vivo* acquisition of anatomical magnetic resonance images

Whole-body MR images for anatomical reference for cell tracking experiments were usually acquired before the PET scans. Therefore, animals were anesthetized with 2 % isoflurane in oxygen in a heated anesthesia box. When reaching proper anesthetic depth, the mouse was transferred onto an animal bed and fixed with cotton swabs and adhesive tape. During MR imaging, anesthesia was maintained at 1.5 % isoflurane in oxygen. The animal was then placed into the center of the ^{1}H resonance volume coil (inner diameter: 86 mm), correct placement was checked by acquiring a FLASH localizer scan (TE 2.67 ms, TR 100 ms). Then, a T2-weighted TurboRARE protocol (TE 90.51 ms, TR 1800 ms, FOV 76.8x34.8x22.8 mm, image size 256x116x76, slice thickness 0.3 mm) with fat suppression was acquired for anatomical reference. Acquisition of the T2-weighted TurboRARE protocol was gated according to the respiration of the animal surveilled with the trigger pad (Figure 20 C) to minimize motion artefacts caused by respiration. After MR image acquisition, the animal bed was transferred to the PET scanner without moving the animal to ensure proper co-registration of the MR and PET images.

Anatomical reference images for the examination of the [^{18}F]FDG uptake in the PyMT-derived S2WTP3 and ML1B1B1 allograft tumors were acquired during the 70 min dynamic PET scan with the ^{1}H resonance volume coil (inner diameter: 40 mm) and the T2-weighted TurboRARE protocol with the same acquisition parameters as just described on the 7 T, 300 MHz small animal MR scanner.

3.7.2 *In vivo* ^{1}H magnetic resonance spectroscopy

Single voxel *in vivo* ^{1}H-MRS on murine breast cancer allograft tumors was performed with the ^{1}H resonance volume coil (inner diameter: 40 mm) during the 70 min dynamic PET scan. For spectroscopy, a water-suppressed STEAM protocol (TE 3 ms, TR 1800 ms, voxel size 3x3x3 mm^{3}, 256 averages) was employed. As a reference, the same protocol was acquired without water suppression. Briefly, the spectroscopic voxel was positioned in the center of the tumors with the help of a previously acquired anatomical MR scan. For shimming, first a B_0 map was acquired, then shims were adjusted using a localized Mapshim sequence. Automatic quantification of *in vivo* ^{1}H spectra was performed with LCModel (version 6.1-1L; Inverse Problems) using the settings for breast tissue to quantify total choline and lipid peaks (Provencher, 1993).

3.7.3 DNP-hyperpolarized ^{13}C-pyruvate magnetic resonance spectroscopy

Hyperpolarized [^{13}C]pyruvate MRS acquisition was performed with and data analysis was performed by Dr. Marie-Aline Neveu, Werner Siemens Imaging Center.

Hyperpolarization of [^{13}C]pyruvic acid was performed with the SPINlab system (GE Healthcare) operating at 5 T and 0.85 K (Figure 22 A). The SPINlab system employs an elaborate fluid path system consisting of a 2 mL sample vial, a dynamic seal that allows for movement in the system under vacuum, transfer tubing for inlet and outlet of the dissolution medium, a valve that opens inlet and outlet simultaneously and the dissolution syringe that holds the dissolution medium. In this fashion, the [^{13}C]pyruvic acid sample can be kept sterile throughout the polarization, dissolution and, optionally, quality control processes for clinical use while the transfer tubing system and dissolution syringe can be reused (Ardenkjaer-Larsen *et al.*, 2011; Malinowski *et al.*, 2016). For the *in vitro* use, though, the hyperpolarized [^{13}C]pyruvate was not kept under sterile conditions.

A pre-prepared mixture of 15 mM electron paramagnetic agent (EPA) radical sodium salt (GE Healthcare) in [1-^{13}C]pyruvic acid (1-^{13}C, 99 %, Cortecnet, Voisins-le-Bretonneux, France) was prepared and stored at -20 °C until use. 27 µL of the EPA radical and [^{13}C]pyruvic acid solution were then mixed with 1 µL 50 mM Gadolinium chelate, in the dedicated sample vial. The syringe was filled with 14 mL dissolution medium (0.1 g/L Na_2EDTA in pure water, Sigma-Aldrich). The fluid path was then assembled. A tubing was mounted onto the cup according to the manufacturer's instructions, hermetically sealed with a UV-sensitive polymer clue and connected to the syringe part via the transfer tubing. The quality of the sealing of the fluid path was checked by applying pressure while dipping the cup into liquid nitrogen (Linde). Leaking of the cup or tubing connections in any way could be ruled out in this fashion. The fluid path was then allowed to equilibrate to room temperature again before it was loaded into the SPINlab system. The sample was then hyperpolarized for 60 to 90 min.

During [^{13}C]pyruvic acid polarization, cell suspensions were prepared. S2WTP3, ML1B1B1, B16-F0 or B16-F10 cells were washed with pre-warmed PBS and incubated with 0.05 %/0.02 % trypsin-EDTA for 5 min in an incubator. When the cells had detached from the flask, trypsination was stopped by adding the respective growth medium and the cell suspension was collected. The cells were centrifuged at 400 g for 5 min, washed in 10 mL PBS and counted in an appropriate dilution in 0.125 % trypan blue. Triplicates of $5x10^7$ cells were then suspended in 6 mL DMEM medium without pyruvate and pipetted into a cell culture dish with 6 cm diameter. For hyperpolarized [^{13}C]pyruvate injection, medical tubing was connected to the lid of the cell culture dish to allow the injection of the hyperpolarized tracer during the acquisition (dead volume of 200 µL). The cell culture dish was then fixed on the dual tuned ^{1}H/^{13}C surface coil (Figure 22 B) and centered into the magnet of the BioSpec 70/30 7 T MR tomograph. Correct placement of the coil and cell culture dish was verified by acquisition of a

FLASH localizer sequence (TE 2.7 ms, TR 25 ms). For shimming, first a B_0 map was acquired before a localized shim sequence was run on the cell culture dish.

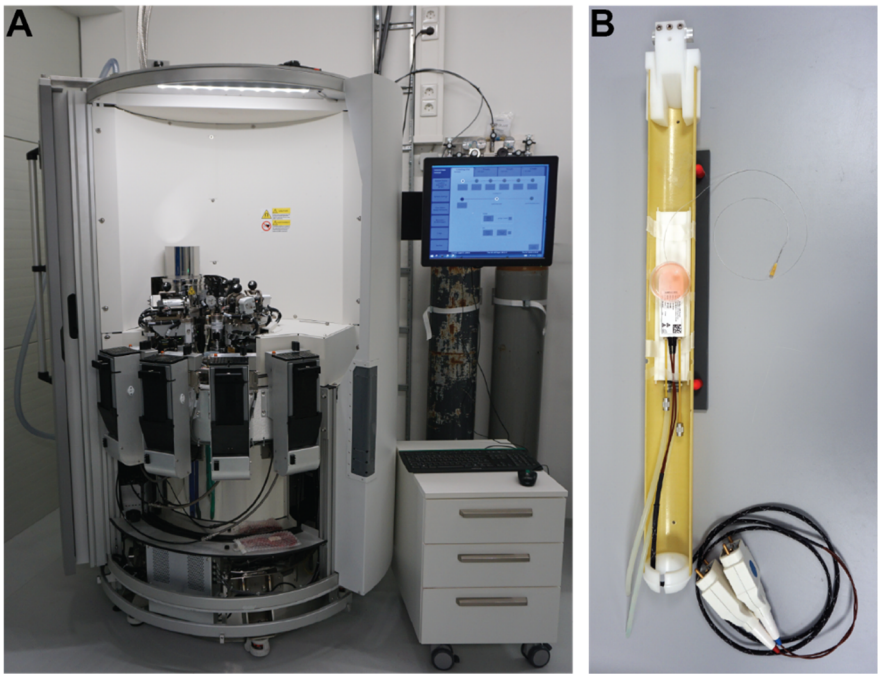

Figure 22: The SPINlab system and experimental setup for *in vitro* ^{13}C spectroscopy.
The SPINlab system (**A**) for DNP-hyperpolarization of [1-^{13}C]pyruvic acid and the experimental setup for *in vitro* ^{13}C spectroscopy (**B**) on cell suspension. The dual tuned ^{1}H/^{13}C resonance coil was fixed in a dedicated holder in the bed and the cell culture dish on the resonance coil with adhesive tape.

Shortly before dissolution of the hyperpolarzied [1-^{13}C]pyruvic acid, the acquisition of the ^{13}C resonance spectrum was started with the following parameters: TR 1000 ms, flip angle 5°, bandwidth 3019.32 Hz (40 ppm) centered at 175 ppm, 2048 points, 512 repetitions. With the described sequence, the signal of the hyperpolarized [^{13}C]compounds is acquired every second. In this fashion, the influx of hyperpolarized [1-^{13}C]pyruvate and its metabolic transformation into [1-^{13}C]alanine and [1-^{13}C]lactate can be followed over time until hyperpolarization is completely decayed. When the acquisition of the sequence was started, the hyperpolarized [1-^{13}C]pyruvic acid was dissoluted into an appropriate receiver syringe prefilled with 0.4 mL dissolution medium and 0.4 mL neutralization medium (0.1 g/L Na_2EDTA, 0.4 M Tris and 0.72 M NaOH in pure water) ensuring immediate neutralization of the hyperpolarized compound after dissolution. Immediately after the hyperpolarized [1-^{13}C]pyruvic acid was dissoluted into the receiver syringe, 2 mL of the solution were drawn into a syringe and injected into the cell culture dish via the medical tubing. Successful hyperpolarized [1-^{13}C]pyruvate injection was verified by real-time change in the FID. A schematic overview of the experimental setup and data procession is given in Figure 23.

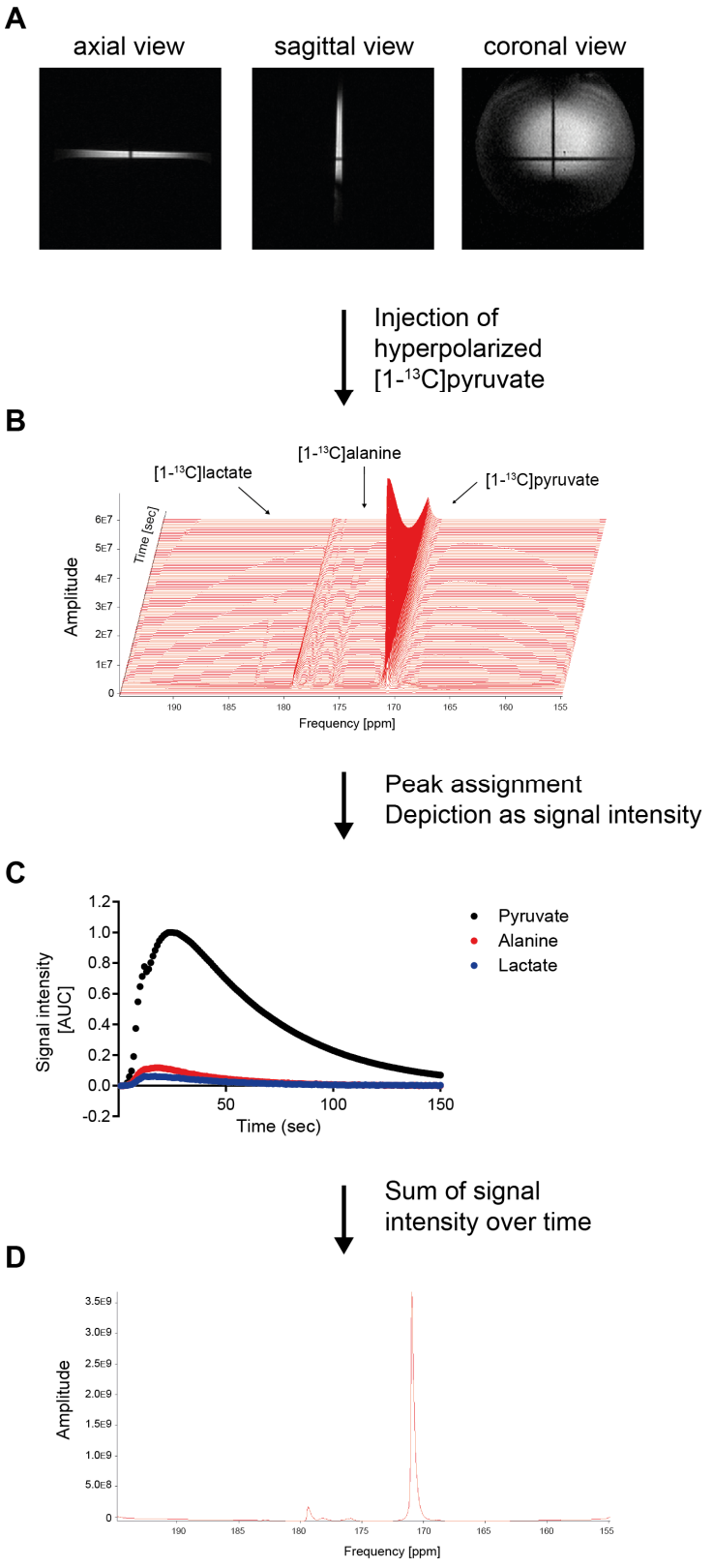

Figure 23: Schematic of the experimental setup for measuring metabolism of the hyperpolarized [1-^{13}C]pyruvate *in vitro*.

(**A**) Correct placement of the cell suspension-containing petri dish and (**B**) a typical [1-^{13}C]pyruvate spectra time series with assigned peaks displayed on the ppm. Spectra procession includes the illustration of the data as signal intensity over time (**C**) and summation of the signal for each metabolite (**D**) for each time point.

Spectra preprocessing and correction were performed with jMRUI (MRUI Consortium): acquired spectra were depicted on the ppm scale, spectra without signal before [1-^{13}C]pyruvate injection were not included in the analysis. Phase correction and noise reduction in the form of apodization were performed. Then, peaks were assigned for each metabolite of interest, in this case [1-^{13}C]pyruvate, [1-^{13}C]alanine and [1-^{13}C]lactate, and data was exported for further analysis in MATLAB (MathWorks, Natick, Massachusetts, USA). In MATLAB, data was converted into signal intensity for each point on each individual spectrum. Signal intensity over time for each metabolite was corrected for baseline and normalized to the cell number in 10^6 cells. Then, metabolite intensity over time was normalized to the maximum [1-^{13}C]pyruvate peak signal. Signal intensity time curves were generated for the injected [1-^{13}C]pyruvate and its metabolites [1-^{13}C]alanine and [1-^{13}C]lactate. For maximum intensity analysis, the area under the curve (AUC) was calculated for each metabolite as sum of the metabolite intensity over the whole time line. Results were then depicted as ratios to the injected [1-^{13}C]pyruvate as reference in Prism Version 7 (GraphPad Software, La Jolla, California, USA).

3.7.4 Sample preparation and NMR spectroscopy for metabolomics

Cell extraction, spectra acquisition and primary data analysis were performed by Dr. Christoph Trautwein, Werner Siemens Imaging Center, University of Tübingen.

The S2WTP3 and ML1B1B1 cell lines were cultured as described (section 3.2.1). For metabolomics, 5 technical replicates of $3x10^7$ cells each were prepared in 1.5 mL reaction cups. Cellular metabolism was quenched by addition of 500 µL methanol (LS-MS grade, Sigma-Aldrich). Samples were stored at -80 °C until further procession.

Extraction of polar, water-soluble metabolites was achieved using an ultrasonic homogenizer (Covaris, Woburn, Massachusetts, USA) and a two phase liquid-liquid methyl tert-butyl ether:methanol/H_2O extraction protocol. The methanol-quenched cell suspension was transferred into a system-compatible 1 mL glass tube and 500 µL methyl tert-butyl ether were added. Extraction was performed in the Covaris S220X (Covaris) with two 5 min consecutive programs at a temperature maximum of 8 °C. The resulting extracts were transferred into 2 mL reaction cups and 500 µL H_2O were added to induce phase separation. The samples were spun down at 3000 g for 10 min and the methyl tert-butyl ether phase and methanol/H_2O phase were separated. Then, 750 µL of the polar methanol/H_2O were transferred into 1.5 mL reaction cups and evaporated to dryness overnight (Concentrator 5301, Eppendorf). The remaining metabolites were resuspended in 600 µL D_2O with 100 µM TSP and transferred into 5 mm NMR tubes. For all replicates, ^{1}H NOESY spectra (size of FID: 65536, 4 dummy scans, 256 repetitions, 20 ppm spectral width, 277 K, 30 min acquisition time) and ^{1}H JRES spectra (size of FID: 8192/40, 16 dummy scans, 16 repetitions, 16.7/0.13 ppm spectral width, 277 K, 30 min

acquisition time) were acquired on the Avance III NMR spectrometer (^{1}H resonance frequency 600 MHz, 14.1 T; Bruker; Figure 24). Due to baseline shifts in the ^{1}H NOESY spectra, the positive projections of the 2D ^{1}H JRES spectra were used for assignment of metabolite resonance with Chenomx (Chenomx Inc., Edmonton, Alberta, Canada) and further chemometric statistical analysis (pareto scaling, fold change threshold >2.0, p value threshold <0.05 false discovery rate adjusted).

Figure 24: The Avance III NMR spectrometer.
The NMR spectrometer is equipped with an auto sampler for the 5 mm TXI ^{1}H/^{13}C RT probe.

3.7.5 HR-MAS ^{1}H NMR spectroscopy

Tissue samples from S2WTP3 and ML1B1B1 allografts that were instantly snap-frozen in liquid nitrogen after removal were prepared for HR-MAS ^{1}H NMR spectroscopy at -25 °C. Between 10 to 12 mg of the tissue samples were transferred into the NMR rotor inserts with biopsy

punchs and covered with 15 µL 100 % D_2O. The rotor inserts were sealed with a screw-cap and stored at -80 °C until the measurement in the NMR spectrometer (Figure 24).

For acquisition of the ^1H resonance spectrum, the insert containing the tissue sample was inserted into a rotor. The rotor was then inserted into the HR-MAS probe and spun at 5000 Hz. The combination of 90 % H_2O + 10 % D_2O was chosen as lock signal for shimming and the temperature was locked at 4 °C. A water-suppressed ^1H NOESY spectrum was then recorded with the following parameters: size of FID: 97596, 4 dummy scans, 32 repetitions, 29.88 ppm spectral width, 5 min acquisition time.

3.8 Optical imaging

Optical fluorescence and bioluminescence images were acquired on the IVIS Spectrum (Perkin Elmer; Figure 25). The IVIS Spectrum *in vivo* imaging system is equipped with a CCD camera with 13.5 micron pixels and a resolution of 2048x2048. The CCD camera is thermoelectrically cooled to -90 °C to ensure low dark current and low noise. Furthermore, the IVIS Spectrum has 10 30 nm bandwidth excitation and 18 20 nm bandwidth emission filters to enable spectral scanning from the blue to the near-infra red part of the visual light spectrum. For animal care and maintenance, anesthesia in-lets and out-lets are built in as is a heated stage to ensure preservation of the body temperature.

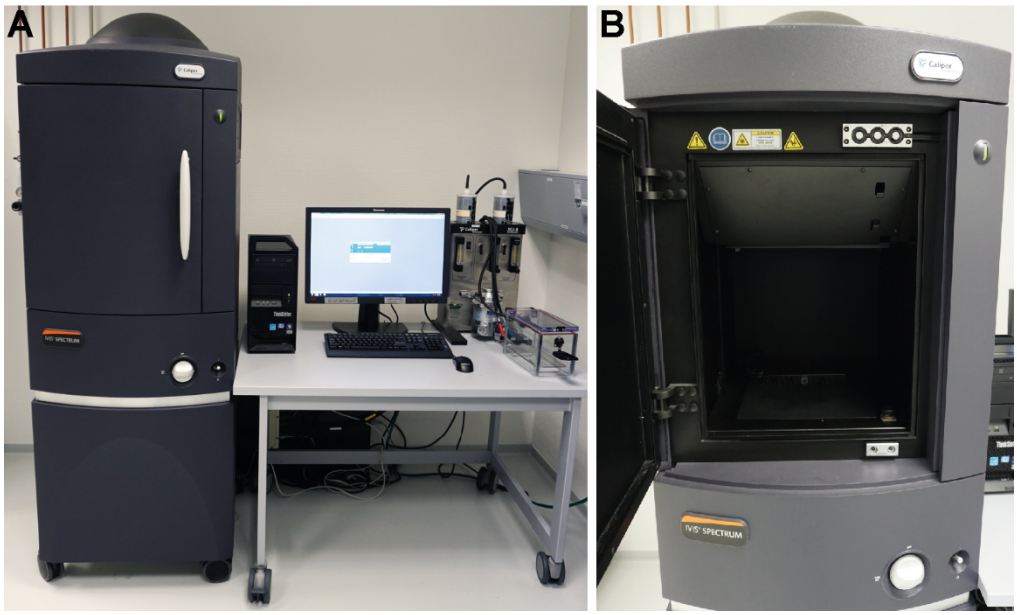

Figure 25: The IVIS Spectrum OI system.
The IVIS Spectrum (**A**) has an in-built anesthesia unit on a heated, movable stage (**B**).

3.8.1 *In vivo* image acquisition

For all *in vivo* OI acquisitions, the chest and the abdomen of the experimental mice had to be shaved and depilated to minimize signal absorption and scattering by the fur. For shaving, experimental mice were anesthetized in a heat-controlled anesthesia box with 1.5 % isoflurane in oxygen and transferred to a pad-covered heating mat for shaving with an electrical razor. The remaining fur was removed with a depilatory cream (Veet, Reckitt Benckiser, Heidelberg, Germany): the depilatory cream was applied in a thin layer, left on the shaved skin for about 2 min and removed with wet cotton swabs. Due to the possibility of an artifact signal in fluorescence and bioluminscence OI stemming from the depilatory cream, experimental animals were measured only at least one day after fur removal.

For fluorescence OI, animals were anesthetized with 2 % isoflurane in oxygen. When sufficient anesthetic depth for imaging was reached, the animals were transferred to the IVIS Spectrum. Fluorescence images to depict DiD-labeled MDSCs (described in section 3.10.1) were acquired using the filter set for DiD with the excitation/emission filter pair 640/680 nm in reflective illumination mode. Binning was set to 8, the lens aperture to f-stop 2. Fluorescence images were recorded in a 14x14 cm FOV with exposure time of 1-2 sec.

For bioluminescence OI to visualize tumor metastases (as described in sections 3.10.3 and 3.10.5), animals were anesthetized with 2 % isoflurane in oxygen. When proper anesthetic depth was reached, experimental animals were *i.p.* injected with 200 µL Luciferin (XenoLight, D-Luciferin – K^+ salt, Perkin Elmer) in a final dose of 150 mg/kg bodyweight. Luciferin was allowed to circulate for 2 min before bioluminescence images were acquired. Bioluminescence images were recorded with open emission filter, medium binning and f-stop 1 in a 14x14 cm FOV. Images were acquired as image sequences with exposure times of 10, 30, 60 and 120 sec.

3.8.2 *Ex vivo* image acquisition

For *ex vivo* fluorescence image acquisition, the experimental animal was killed by cervical dislocation in deep anaesthesia, fixed onto a subereous plate and sprayed with PBS to minimalize involontary distribution of fur. A medial incision was made to separate the skin from the peritoneum and the organs of interest were harvested and placed onto non-fluorescent and non-reflective black paper. Fluorescence images were acquired as described above.

When *ex vivo* bioluminescence images were acquired, blood sampling was performed directly after the *in vivo* bioluminescence image acquistion and the experimental animal was *i.p.* injected with 100 µL Luciferin at a concentration of 150 mg/mL. The Luciferin was allowed to distribute for 10-20 secs before the experimental animal, still deep in anesthesia, was sacrificed by cervical dislocation. A medial incision was made to separate the skin from the

peritoneum. The heart, lungs, liver, spleen, stomach and intestines, kidneys with adrenal glands, femurae and tibiae connected via the knee joint, the ovaries, muscle and the ribcage were harvested and placed onto non-fluorescent and non-reflective black paper. Bioluminescence images were then recorded as described before.

3.9 *In vitro* experiments

3.9.1 Proteomics

For the analysis of the proteome of the PyMT-derived cell lines S2WTP3 and ML1B1B1, 5 biological replicates were generated from one single flask of each cell line. Briefly, S2WTP3 and ML1B1B1 were trypsinated according to protocol (as described in 3.2.1) and cell yield was assessed. Then, 10^6 cell were plated on 10 cm cell culture plates and left to grow for 2 days. When the cells reached 80 % confluence, the cells were washed with ice-cold PBS, scraped from the plates and transferred into 1.5 mL reaction cups. The suspension was spun down and the weight of the cell pellet was determined. The cell pellet was stored at -80 °C until lysis.

Further procession of the samples was performed by the staff of the Proteome Centrum Tübingen, data analysis was performed by Dr. Mohamed Ali Jarboui, Werner Siemens Imaging Center, University of Tübingen.

Cell lysis was performed in lysis buffer containing 1 % NP-40, 20 mM Tris/HCl pH 7.5, 150 mM NaCl, 1 mM $MgCl_2$ supplemented with protease inhibitor tablets (F. Hoffmann-La Roche Ldt., Basel, Switzerland) and 2 mM sodium orthovanadate, 10 mM sodium fluoride and 10 mM β-glycerophosphate to inhibit phosphatases (all Sigma-Aldrich). The total protein content was then measured using the BCA protein assay (Pierce by Thermo Fisher Scientific) according to the manufacturer's instructions. The same amount of total protein from each replicate was digested with the proteolytic enzyme trypsin using 5 g/mL modified sequencing-grade trypsin (Promega, Madison, Wisconsin, USA) for 1 h at 37 °C. The resulting peptides were alkylated for 30 minutes in the dark at room temperature with 5 mg/mL iodoacetamide. Samples were desalted using C18 Stage Tips and analyzed by mass spectrometry.

Tryptic digests were analyzed on an LTQ Orbitrap Q-exactive mass spectrometer coupled to an Ultimate3000 RSLC system (Thermo Fisher Scientific). Tryptic peptides were automatically loaded onto a nanotrap column in 98 % buffer C (0.1 % trifluoroacetic acid in HPLC-grade water) and 2 % buffer B (80 % acetonitrile and 0.08 % formic acid in HPLC-grade water). The peptides were then eluted and separated on an analytical C18 LC column (Acclaim PepMap RSLC C18, particle size 2 µm, pore size 100 Å; Dionex, 75 µm i.d. × 25 cm) by a linear gradient from 2 % to 30 % of buffer B in buffer A (2 % acetonitrile and 0.1 % formic acid in HPLC-grade water) at a flow rate of 300 nL/min over 180 min.

The resulting mass spectra were analyzed using the MaxQuant software suite (Tyanova *et al.*, 2016a) with an in-built Andromeda search engine to identify the proteins from the Uniprot mouse database (Uniprot Consortium, 2017). The following MaxQuant parameters were used: trypsin was selected as enzyme for digestion with two missed cleavages per peptide allowed; fixed amino acids modification was carboamidomethylation of cysteines; variable amino acids modifications were oxidation in methionine, deamidation of asparagine and glutamine, and acetylation in protein N-terminus; first search 20 ppm and main search 7 ppm with fragment ion mass tolerance set to 0.5 Da; 0.01 False Discovery Rate for both peptide and protein level. To perform label free protein quantification, the LFQ MaxQuant algorithm was used with the following criteria: a minimum of one unique peptide with a minimum length of six amino acids, and a minimum ratio count of two. In summary, 5 biological replicates from each cell lines were used to identify differentially expressed proteins. Data were integrated and analyzed using the Perseus statistical analysis platform (Tyanova *et al.*, 2016b) specifically designed to analyze MaxQuant output files. Differentially expressed proteins were only considered significant if the following conditions were fulfilled: pairwise p-values <0.05, number of unique peptides detected and used in quantification per protein equal to or more than 1 for protein analysis and with a minimum of ratios count equal or more than 2 per unique peptide.

3.9.2 Quantitative real-time polymerase chain reaction for gene expression profiling

Transcriptomic analysis of the expression levels genes of interest was performed by quantitative real-time polymerase chain reaction (qRT-PCR). Standard crossing point (C_t) analysis according to the $\Delta\Delta C_t$ method (Livak and Schmittgen, 2001) was chosen for analysis and results were expressed as relative fold gene expression level according to

$$2^{-\Delta\Delta C_t} = 2^{-\,(\boldsymbol{C_t}(\boldsymbol{target\ gene})-\boldsymbol{C_t}(\boldsymbol{reference\ gene}))_{\boldsymbol{treatment}}-(\boldsymbol{C_t}(\boldsymbol{target\ gene})-\boldsymbol{C_t}(\boldsymbol{reference\ gene}))_{\boldsymbol{control}}}$$

Equation 7

Primer design for all qRT-PCR experiments was performed using the National Center for Biotechnology Information (NCBI) Primer-BLAST tool (U.S. National Library of Medicine, Bethesda, MD, USA) against the Refseq mRNA database for *Mus musculus*. Primers were requested to span an exon-exon junction to ensure specificity to the mRNA level, the product size range was set between 100-280 base pairs and melting temperature to 60.0 ± 3.0 °C. All resulting primers were rechecked for specificity by using the regular NCBI BLAST algorithm and tested for self-annealing and formation of secondary structures.

RNA isolation was achieved with the peqGOLD Total RNA Kit (PEQLAB Biotechnologie GmbH, Erlangen, Germany) according to the manufacturer's instructions. Additionally, genomic DNA was digested on column with the peqGOLD DNase I digest kit (PEQLAB

Biotechnologie GmbH) according to the manufacturer's instructions. Then, the obtained RNA was unspecifically transcribed into cDNA using oligo(dT) primers with the Superscript II Reverse Transcriptase (Invitrogen by Thermo Fisher Scientific).
For qRT-PCR analysis in the LightCycler Real Time PCR System (Hoffmann-La Roche LTD), 1-2 ng cDNA were mixed with 1 pmol of the indicated primers, 5 µL of the SYBR Green Master Mix (Applied Biosystems by Thermo Fisher Scientific) and the reaction volume was adjusted to 10 µL with the PCR-grade water supplied. The following program was run in the thermocycler: 95°C, 900 sec as heat activation step, then 95 °C, 15 sec; 62 °C, 45 sec and 72 °C, 30 sec for amplification. Amplification quality was controlled by melting curve analysis from 62 °C to 95 °C with a slope of 0.1 °C/sec.

3.9.2.1 Transcriptomic profiling of *in vitro* expanded MDSCs in comparison to MDSCs isolated from tumor-bearing animals

Immunosuppression is the one key feature distinguishing MDSCs from other tumor-associated myeloid cells. Therefore, transcriptomic profiles of *in vivo* tumor-expanded MDSCs were compared with transcriptomic profiles of *in vitro* expanded MDSC subpopulations by qRT-PCR.

For RNA isolation, MDSCs were expanded *in vitro* and isolated as described in section 3.2.3. For comparison with MDSCs naturally occurring in tumor-bearing animals, female C57BL/6 were inoculated with $0.5x10^6$ S2WTP3 into the left 4th MFP. At day 21 of the tumor growth period, experimental animals were sacrificed by cervical dislocation under deep anesthesia and the spleen, lungs and tumors were isolated. Tumors, lungs and spleens were processed into single cell suspensions as described in section 3.11.2.2 and PMN- and M-MDSCs were isolated by magnetic cell separation as described in section 3.2.3.2.
10^7 *in vitro* generated PMN- and M-MDSCs and entire PMN- and M-MDSCs subpopulations from the tumor, lung and spleen were homogenized in 500 µL lysis buffer for RNA isolation and reverse transcription as described above.
For analysis, the glycolytic enzyme fructose-bisphosphate aldolase was chosen as reference gene and MDSCs isolated from the spleen of naïve C57BL/6 mice were chosen as control for *in vitro* expanded MDSCs and MDSCs from tumor-bearing animals. The following primers (Eurofins Scientific SE, Luxemburg) were used for analysis:

S100A8 (*S100a8*)
Forward: 5´-TGAGCAACCTCATTGATGTCTACC-3´
Reverse: 5'-ATGCCACACCCACTTTTATCACC-3´

S100A9 (*S100a9*)

Forward: 5´-GAAGAAAGAGAAGAGAAATGAAGCC-3´

Reverse: 5'- CTTTGCCATCAGCATCATACACTCC -3´

Nitric oxide synthase 2 (*Nos2*)

Forward: 5'-GTCAACTGCAAGAGAACGGAG-3'

Reverse: 5'-TGAGAACAGCACAAGGGGTTT-3'

Nitric oxide synthase 3 (*Nos3*)

Forward: 5'-CTCCAGCACCGGAGCCTA-3'

Reverse: 5'-TACAGGGCCCATCCTGCT-3'

Arginase, type 1 (*Arg1*)

Forward: 5'-ACAAGACAGGGCTCCTTTCAG-3'

Reverse: 5'-GGCTTATGGTTACCCTCCCG-3'

Arginase type 2 (*Arg2*)

Forward: 5'-AATCCCCTCCCTGCCAATCA-3'

Reverse: 5'-CACTCCTAGCTTCTTCTGTCCC-3'

Fructose-bisphosphate aldolase (*Aldoa*)

Forward: 5′-TGGGCCTTGACTTTCTCCTAT-3′

Reverse: 5′-TGTTGATGGAGCAGCCTTAGT-3′

3.9.2.2 Transcriptomic profiling of the PyMT-derived cell lines S2WTP3 and ML1B1B1

Gene expression analysis on the PyMT-derived cell lines S2WTP3 and ML1B1B1 was performed on genes for key metabolic enzymes and proteins involved in invasion and EMT.

RNA was isolated from 10^7 S2WTP3 and ML1B1B1 cells and cDNA produced as described above. For comparative analysis of the fold changes in gene expression between the cell lines S2WTP3 and ML1B1B1, β-actin was used as references gene and the cell line S2WTP3 as control for ML1B1B1.

Primer sequences for the metabolic enzymes glycerin-3-phosphat dehydrogenase, fatty acid synthase, pyruvate dehydrogenase, acetyl-CoA-carboxylase as well as enzymes and proteins involved in EMT matrix metalloproteinase 9, vimentin, cadherin-1, cadherin-2 were designed as described. Primers for the glucose transporter GLUT-1 and β-actin were already established and at hand. The following primers were used for analysis:

Fatty acid synthase (*Fasn*)

Forward: 5'-CTGACTCGGCTACTGACACG-3′

Reverse: 5′-GTAGTAGGCAGCCAGGTTCG-3′

Pyruvate dehydrogenase E1 α1 (*Pdha1*)

Forward: 5'-GTTTTGGGCGTGGCTTCG-3′

Reverse: 5′-CCGATGAAGGTCACATTTCTTAATC-3′

Acetyl-Coenzyme A carboxylase α (*Acaca*)

Forward: 5'-TGGGGGCATCCAGATTATGC-3′

Reverse: 5′-CCTTTCTGGGTTGGGTGAGG-3′

Glucose transporter 1 (*Slc2a1*)

Forward: 5'-CCTATGGCCAAGGACACACT-3′

Reverse: 5′-CTGGTCTCAGGCAAGGAAAG-3′

Glycerin-3-phosphat dehydrogenase (*GAPDH*)

Forward: 5'-CCCTTAAGAGGGATGCTGCC-3‘

Reverse: 5′-TACGGCCAAATCCGTTCACA-3’

Fructose-bisphosphate aldolase (*Aldoa*)

Forward: 5′-TGGGCCTTGACTTTCTCCTAT-3′

Reverse: 5′-TGTTGATGGAGCAGCCTTAGT-3′

Focal adhesion kinase (*Fak*)

Forward: 5′-GCGATTCCTGAAACCTGATGTG-3’

Reverse: 5′-GGCACAGATACCCACCTTGA-3’

Matrix metallopeptidase 9 (*Mmp9*)

Forward: 5'-TGAATCAGCTGGCTTTTGTG-3′

Reverse: 5′-GTGGATAGCTCGGTGGTGTT-3′

Vimentin (*Vim*)

Forward: 5'-CCGCTTTGCCAACTACATCG-3′

Reverse: 5′-CCTGCAATTTCTCTCGCAGC-3′

Cadherin 1 (*Cdh1*),

Forward: 5'-CCTACACCATCGTCAGCCAG-3′

Reverse: 5′-GACCCTGATACGTGCTTGGG-3′

Cadherin 2 (*Cdh2*)

Forward: 5'-AGCCCCTTCTCAATGTGAAATTC-3′

Reverse: 5′-CTCCCGGCTCAGGTTTACAG-3′

β-actin (*Actb*)

Forward: 5'-GGCCAGGTCATCACTATTGG-3′

Reverse: 5′-CGGATGTCAACGTCACACTT-3′

3.9.3 *In vitro* [^{18}F]FDG uptake of PyMT-derived cell lines S2WTP3 and ML1B1B1

To estimate glucose uptake and consumption in the PyMT-derived cell lines S2WTP3 and ML1B1B1 *in vitro*, the cells were trypsinated according to the standard protocol, washed twice in PBS and counted in 0.125 % trypan blue. The S2WTP3 and ML1B1B1 cells were then suspended in DMEM medium containing 5 mM glucose as surrogate for the physiological state. Then, 10^6 cells were dispensed into 5 mL polystyrene tubes (Sarstedt) suitable for analysis in the automated Wizard^2 γ-counter (Perkin Elmer) and 3 MBq [^{18}F]FDG diluted in a volume of 20 µL PBS were added. The cells were incubated with [^{18}F]FDG for 60 min at 37 °C and 7.5 % CO_2 in a humidified incubator. Afterwards, the cells were washed twice in PBS and spun down at 400 g for 5 min for analysis in the γ-counter. Controls without cells for non-specific tracer binding to the polystyrene tube were processed accordingly, while control tubes for initially applied tracer amount were not washed. For comparison, the same experiment was performed with B16-F0 and B16-F10 murine melanoma cells. A schematic overview of the experimental procedure is given in Figure 26.

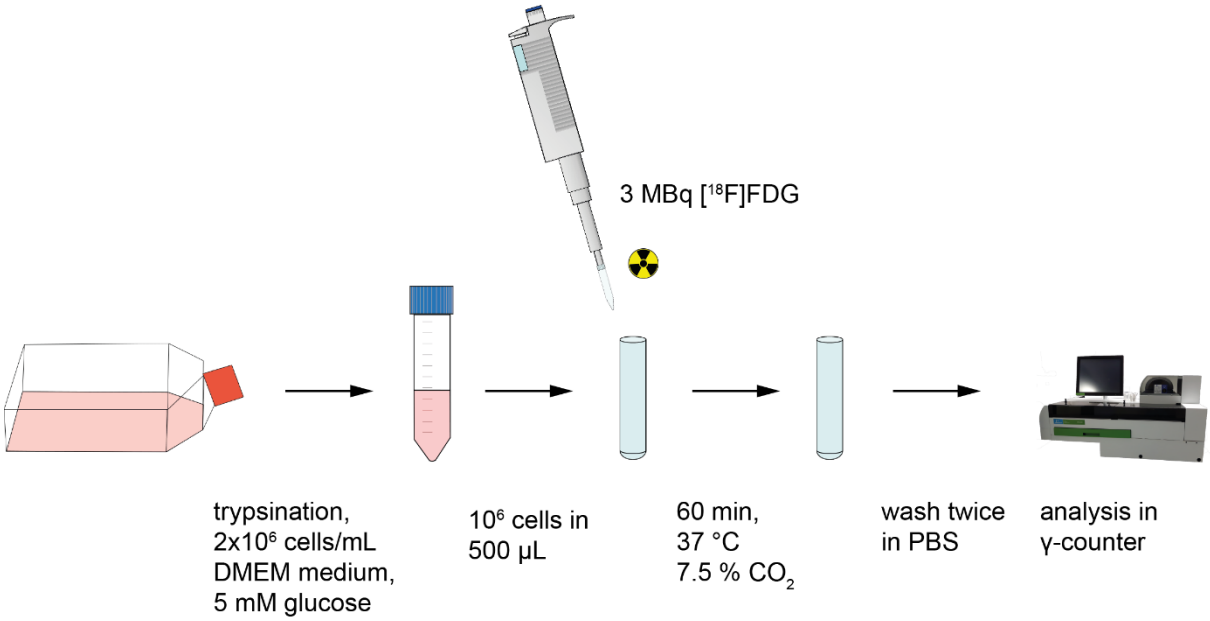

Figure 26: Schematic presentation of the *in vitro* [^{18}F]FDG uptake study.
The cell lines were trypsinated according to protocol and 10^6 cells in 500 µL medium with 5 mM glucose were dispensed into polystyrene tubes. Then, 3 MBq [^{18}F]FDG were added and incubated with the cells for 1 h at 37 °C. Following the incubation time, the cells were washed twice in PBS and the cell pellets measured in the γ-counter.

3.9.4 Colony-formation assay with PyMT-derived cell lines S2WTP3 and ML1B1B1

The colony formation assay or clonogenic assay is an *in vitro* assay to determine survival of single cells and their ability to grow without cell-cell contacts and undergo unlimited cell division to produce new colonies of at least 50 cells. This assay is also the method of choice to determine cell reproductive death after treatment with a certain agent or, frequently in radiation biology, dosages of radioactivity (Crowley *et al.*, 2016; Franken *et al.*, 2006).

To assess the capability of single S2WTP3 and ML1B1B1 cells to grow without cell-cell contacts and form colonies, S2WTP3 and ML1B1B1 cells were trypsinated according to protocol and counted in 0.125 % trypan blue. Then, 1000 cells were seeded into 12.5 cm² cell culture dishes in complete DMEM growth medium. The cells were left to grow colonies for 7 days at 37 °C and 7.5 % CO_2 in a humidified incubator. The assay was stopped before the more aggressively growing cell line could overgrow the culture dish. For analysis, the cells were washed twice in ice-cold PBS, fixed and stained in 0.1 % crystal violet dye in 20 % methanol (both Sigma-Aldrich) for 10 min and washed several times with tap water to remove background dye. For comparison, the same experiment was performed with B16-F0 and B16-F10 cells. Then, the culture plates were scanned with a photo scanner and the colonies were counted in ImageJ (Schneider *et al.*, 2012).

3.10 *In vivo* experiments

3.10.1 Depiction of the *in vivo* migration of MDSCs in the PyMT primary tumor model by OI

The *in vivo* migration and tumor homing of PMN- and M-MDSCs were examined in the PyMT primary tumor model by OI (Figure 27). Experimental animals were inoculated with $5x10^5$ S2WTP3 PyMT breast cancer cells in the left 4^{th} MFP. Tumors were allowed to grow for 19 days before adoptive cell transfer. During this period, experimental animals were monitored every second day to ensure their well-being and tumor size was assessed at least weekly. On day 6 before the scheduled adoptive cell transfer, bone marrow cells from donor mice were isolated, expanded and differentiated to MDSCs as described in section 3.2.3. Then, MDSCs were isolated and separated into subpopulations by magnetic cell sorting. MDSC labeling with the DiD dye compound was performed as described in section 3.4.4. The DiD-labeled PMN- and M-MDSCs (DiD-PMN- and DiD-M-MDSCs) were kept in the incubator for further 10 min to allow for recovery. Then, DiD-PMN- and DiD-M-MDSCs were suspended in saline for adoptive transfer into S2WTP3-tumor-bearing mice (n=4). Tumor-bearing littermates without adoptive cell transfer served as controls (n=3). Fluorescent OI was performed at 48, 72 and 96 h post adoptive cell transfer.

In addition, the confocal laser endomicroscopy system Cellvizio Lab (Mauna Kea Technologies, Paris, France) was tested at 72 h post adoptive transfer for one animal per group. To enhance tissue contrast for fluorescence endomicroscopy, the animal was *i.v.* injected with 200 µL FITC-Dextran (average molecular weight 3000-5000; Sigma-Aldrich) to non-specifically stain the microvasculature directly before image acquisition with the Cellvizio Lab system (probe: PF-2254, FOV: 590x592 µm, axial resolution 54 µm, lateral resolution 3.9 µm, laser wavelength 488 nm and 660 nm).

At 96 h post adoptive cell transfer, *in vivo* and *ex vivo* fluorescence OI was performed and the tumors, spleens and lungs were processed for flow cytometric analysis (see section 3.11.2.2) of the fate of DiD-PMN- and DiD-M-MDSCs in the TME.

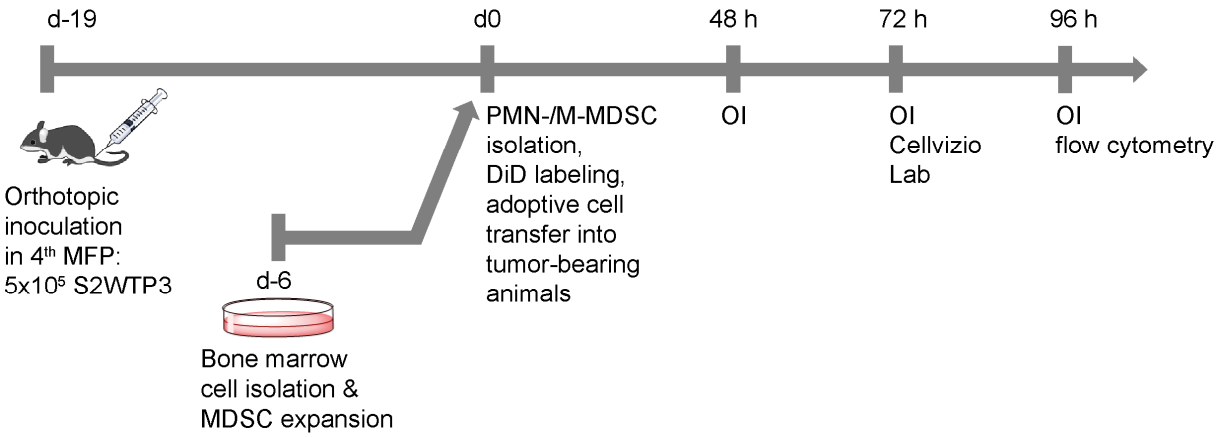

Figure 27: Schematic diagram of MDSC cell tracking in the S2WTP3 PyMT primary breast cancer tumor model.

Breast cancer tumors were inoculated 19 days, bone marrow cells were isolated and expanded to MDSCs 6 days before the scheduled MDSC transfer. For the adoptive MDSC transfer, MDSCs were isolated via magnetic cell separation, labeled with DiD and *i.v.* injected into tumor-bearing animals. OI was performed at 48, 72 and 96 h post adoptive MDSC transfer with additional imaging with Cellvizio Lab at 72 h post adoptive MDSC transfer. After the last imaging time point, the organs were harvested for flow cytometry.

3.10.2 Depiction of the *in vivo* migration of MDSCs in the PyMT primary tumor model by PET

To elucidate migration dynamics in the PyMT primary tumor model (Figure 28), experimental animals were injected orthotopically with $5x10^5$ S2WTP3 cells in 25 µL in the left 4th MFP (as described in 3.1.3) 19 days before the scheduled adoptive transfer of either [^{64}Cu]NOTA-anti-CD11b mAb-labeled PMN- or M-MDSCs. Bone marrow cells were isolated from donor mice and expanded to MDSCs (as described in 3.2.3). At day 6 of cell cultivation, PMN- and M-MDSC subpolutations were isolated via magnetic cell sorting (as described in section 3.2.3.2) and labeled with 0.74 MBq [^{64}Cu]NOTA-anti-CD11b mAb (as described in section 3.4.3). Then, either $2x10^6$ [^{64}Cu]NOTA-anti-CD11b-PMN or [^{64}Cu]NOTA-anti-CD11b-M-MDSCs were *i.v.* injected into S2WTP3 tumor-bearing mice. Static 20 min PET scans and T2-weighted anatomical MR images were acquired at 3, 24 and 48 h post adoptive cell transer (pt). Experimental animals were sacrificed after the last imaging time point and their organs harvested for *ex vivo* biodistribution analysis (section 3.11.1).

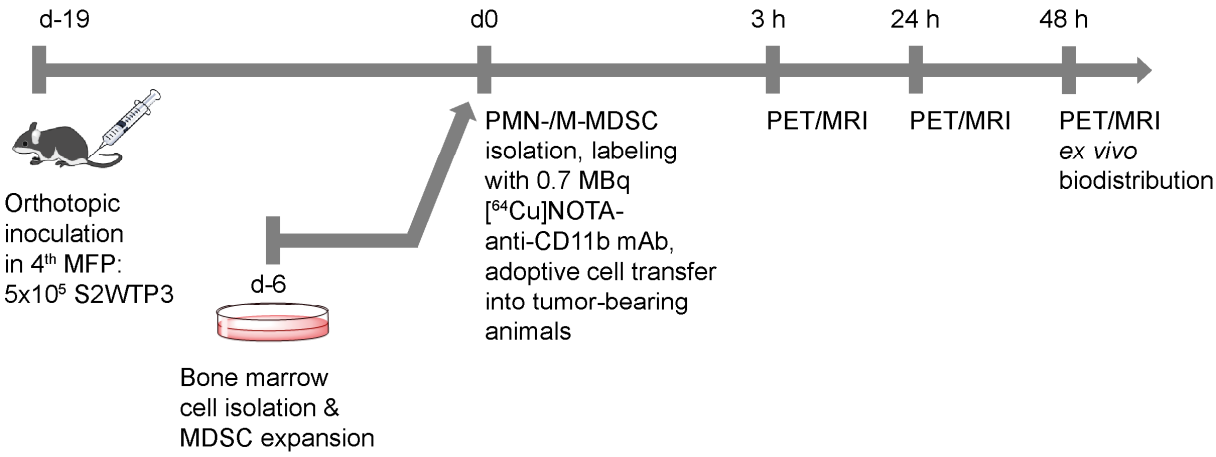

Figure 28: Schematic diagram of [^{64}Cu]NOTA-anti-CD11b mAb-labeled MDSC cell tracking in the S2WTP3 PyMT primary breast cancer tumor model by PET.
S2WTP3 primary breast cancer tumors were inoculated 19 days before adoptive MDSCs transfer, bone marrow cells were isolated and differentiated to MDSCs 6 days before. Then, PMN- and M-MDSCs were isolated via magnetic cell sorting, labeled with 0.74 MBq [^{64}Cu]NOTA-anti-CD11b mAb and *i.v.* injected into the tumor-bearing animals. PET and MR imaging was performed at 3, 24 and 48 h pt. Additionally, organs were harvested for *ex vivo* biodistribution after the last imaging time point.

3.10.3 Depiction of the *in vivo* migration of MDSCs in the PyMT metastasis model by PET

To elucidate differences in MDSC migration dynamics between the primary and metastatic TME, PyMT breast cancer metastases were induced in experimental animals by tumor cell injection into the left ventricle (Figure 29). Mice were injected with 2.5x10^5 S2WTP3-Luc-mCh cells in 100 µL saline 19 days before the scheduled adoptive transfer of either [^{64}Cu]NOTA-anti-CD11b mAb-labeled PMN- or M-MDSCs. Bone marrow cells were isolated from donor mice, expanded to MDSCs and PMN- and M-MDSC subpolutations were isolated via magnetic cell sorting (as described in section 3.2.3.2). Metastases-bearing animals for cell tracking experiments were identified by *in vivo* bioluminescent OI (as described in section 3.8.1). MDSC subpopulations were labeled with 0.74 MBq [^{64}Cu]NOTA-anti-CD11b mAb (as described in 3.4.3). Then, either 2x10^6 [^{64}Cu]NOTA-anti-CD11b-PMN or [^{64}Cu]NOTA-anti-CD11b-M-MDSCs were *i.v.* injected into S2WTP3-Luc-mCh metastases-bearing mice. Static 20 min PET scans and T2-weighted anatomical MR images were acquired at 3, 24 and 48 h pt. Experimental animals were sacrificed after the last imaging time point and organs were harvested for *ex vivo* biodistribution analysis (as described in section 3.11.1).

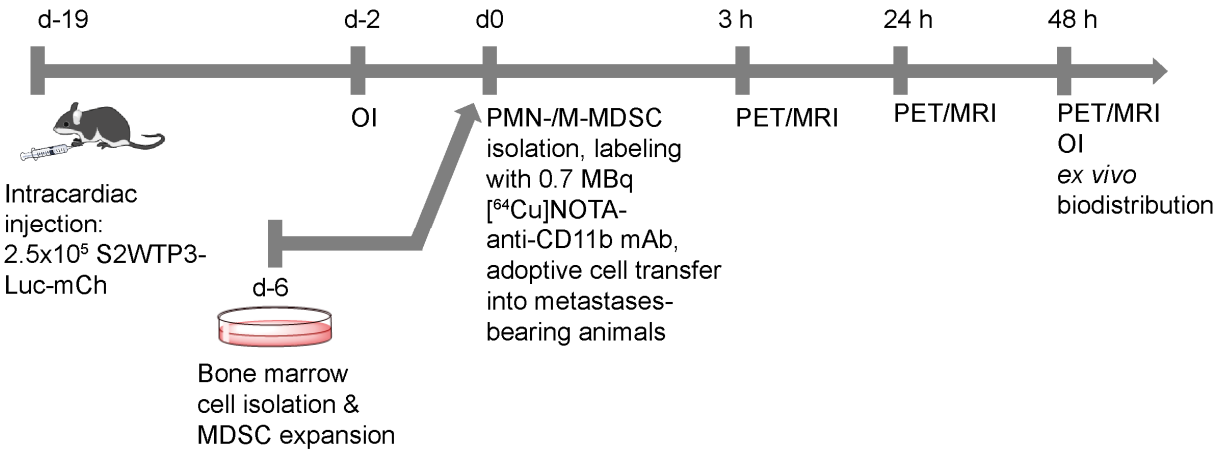

Figure 29: Schematic diagram of [^{64}Cu]NOTA-anti-CD11b mAb-labeled MDSC cell tracking in the S2WTP3-Luc-mCh metastatic breast cancer model by PET.
[^{64}Cu]NOTA-anti-CD11b mAb-labeled PMN- and M-MDSCs were adoptively transferred into S2WTP3-Luc-mCh breast cancer metastases-bearing mice 19 days after inoculation. PET and MR imaging was performed at 3, 24 and 48 h post adoptive cell transfer. Additional bioluminescence OI scans were acquired 48 h pt to separate metastatic tissue from healthy tissue for *ex vivo* biodistribution.

3.10.4 Depiction of the *in vivo* migration of MDSCs in the B16 primary tumor model by PET

To visualize migration dynamics and homing to the primary B16-F10 melanoma (Figure 30), experimental mice were intracutaneously injected with 2.5x10^5 B16-F10-Red-FLuc cells in 25 µL just over the right scapula 12 days before the scheduled adoptive transfer of either [^{64}Cu]NOTA-anti-CD11b mAb-labeled PMN- or M-MDSCs. For MDSC expansion, bone marrow cells were isolated from donor mice (as described in section 3.2.3). At day 6 of MDSC cultivation, PMN- and M-MDSC subpolutations were isolated via magnetic cell sorting (as described in 3.2.3.2) and labeled with 0.74 MBq [^{64}Cu]NOTA-anti-CD11b mAb (as described in section 3.4.3). Then, either 2x10^6 [^{64}Cu]NOTA-anti-CD11b-PMN or [^{64}Cu]NOTA-anti-CD11b-M-MDSCs were *i.v.* injected into B16-F10-Red-FLuc melanoma-bearing mice. Static 20 min PET scans and T2-weighted anatomical MR images were acquired at 3, 24 and 48 h pt. Experimental animals were sacrificed after the last imaging time point and their organs subjected to *ex vivo* biodistribution analysis (as described in section 3.11.1).

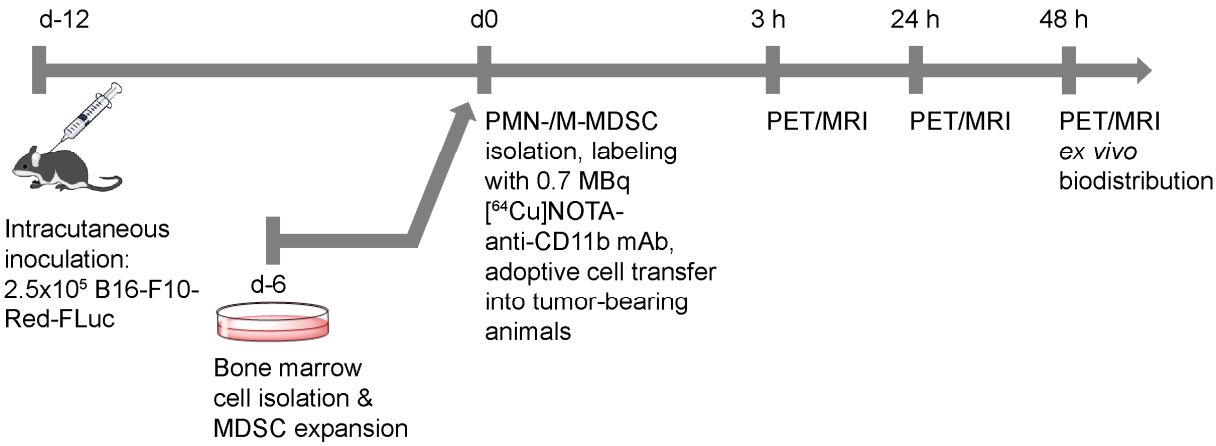

Figure 30: Schematic diagram of [^{64}Cu]NOTA-anti-CD11b mAb-labeled MDSC cell tracking in the B16-F10 primary melanoma model by PET.
[^{64}Cu]NOTA-anti-CD11b mAb-labeled PMN- and M-MDSCs were *i.v.* injected into primary B16-F10-Red-Fluc melanoma bearing animals 12 days post inoculation. PET/MR imaging was performed at 3, 24 and 48 h pt with additional *ex vivo* biodistribution at 48 h post pt.

3.10.5 Depiction of the *in vivo* migration of MDSCs in the B16 metastasis model by PET

To elucidate differences in MDSC migration to the primary and metastatic TME, B16-F10 melanoma metastases were induced in experimental animals by intracardial injection of 1x10^5 B16-F10-Red-FLuc melanoma cells into the left ventricle 12 days before the scheduled adoptive transfer of either [^{64}Cu]NOTA-anti-CD11b mAb-labeled PMN- or M-MDSCs (Figure 31). Bone marrow cells were isolated, expanded to MDSCs and MDSC subpolutations were isolated via magnetic cell sorting (as described in section 3.2.3). B16-F10 metastases-bearing animals were identified by *in vivo* bioluminescence OI (as described in section 3.8.1). MDSC subpopulations were labeled with 0.74 MBq [^{64}Cu]NOTA-anti-CD11b mAb (as described in 3.4.3) and either 2x10^6 [^{64}Cu]NOTA-anti-CD11b-PMN or [^{64}Cu]NOTA-anti-CD11b-M-MDSCs were *i.v.* injected into B16-F10 metastases-bearing mice. Static 20 min PET scans and T2-weighted anatomical MR images were acquired at 3, 24 and 48 h pt. Additionally, at 48 h post cell injection, *in vivo* and *ex vivo* bioluminescent OI (as described in 3.8.1) was performed to, to the extent possible, separate healthy from tumor tissue. Healthy and metastatic tissue was then subjected to *ex vivo* biodistribution analysis (as described in section 3.11.1).

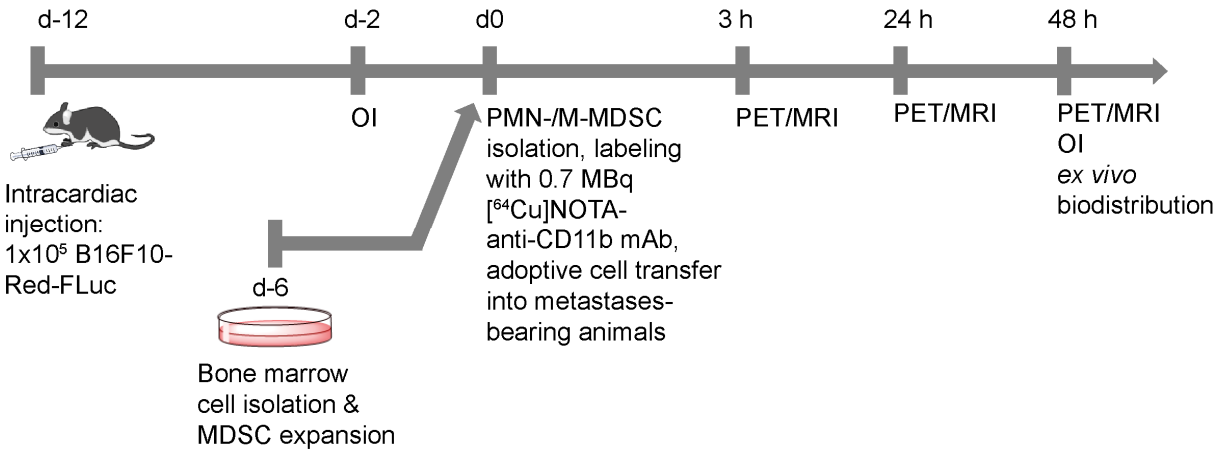

Figure 31: Schematic diagram of cell tracking of [^{64}Cu]NOTA-anti-CD11b mAb-labeled MDSC in the B16-F10-Red-FLuc melanoma metastasis model by PET.
[^{64}Cu]NOTA-anti-CD11b mAb-labeled PMN- and M-MDSCs were *i.v.* injected into B16-F10 melanoma metastases-bearing animals 12 days post inoculation. PET/MR imaging was performed at 3, 24 and 48 h pt with additional *in vivo* and *ex vivo* bioluminescence OI to facilitate separate biodistribution analysis of metastatic and healthy tissue at 48 h pt.

3.10.6 [^{64}Cu]$CuCl_2$-controls for the primary tumor models

As control for the *in vivo* MDSC tracking experiments, the distribution of [^{64}Cu]$CuCl_2$ was imaged in S2WTP3 breast cancer allograft-bearing mice (n=3), B10-F10-Red-FLuc melanoma-bearing mice (n=3) and naïve controls (n=3). S2WTP3 breast cancer induction was performed (as described in section 3.1.3.1). 19 days before the injection of [^{64}Cu]$CuCl_2$, B16-F10-Red-FLuc melanoma induction was performed (as described in section 3.1.3.2) 12 days before the injection of [^{64}Cu]$CuCl_2$. On day 0, S2WTP3 breast cancer allograft-bearing mice, B16-F10-Red-FLuc melanoma allograft-bearing mice and naïve controls were *i.v.* injected with 0.37±0.05 MBq [^{64}Cu]$CuCl_2$. At 3, 24 and 48 h post injection, static 20 min emission PET scans and T2-weighted anatomical MR images were acquired. At 48 h post injection, after the last MR image acquisition, experimental animals were sacrificed and organs were harvested and subjected to *ex vivo* biodistribution analysis as described in section 3.11.1. A schematic summary of the experiment is given in Figure 32.

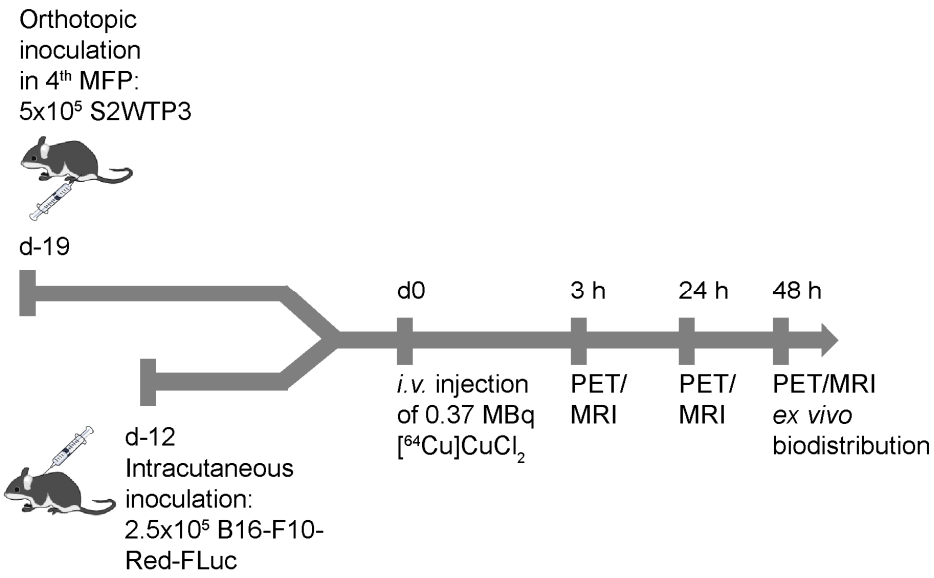

Figure 32: Experimental setup for imaging the distribution of [^{64}Cu]$CuCl_2$ in S2WTP3 breast cancer- and B16-F10-Red-FLuc melanoma-bearing mice and naïve littermates as control for MDSC cell tracking experiments.
The biodistribution of [^{64}Cu]$CuCl_2$ was visualized in S2WTP3 breast tumor- and B16-F10 melanoma-bearing mice and control littermates at 3, 24 and 48 h post injection by PET and MRI with additional *ex vivo* biodistribution at 48 h post injection.

3.10.7 [^{18}F]FDG uptake studies to assess changes in glucose metabolism

To examine possible changes in glucose metabolism, the *in vivo* [^{18}F]FDG uptake of S2WTP3 tumor allografts and ML1B1B1 tumor allografts was determined (Figure 33). To induce tumor cell allografts, mice were orthotopically injected with either 5x10^5 S2WTP3 (n=5) or 2.5x10^5 ML1B1B1 (n=5) breast cancer cells into the left 4th MFP. Mice bearing ML1B1B1 tumors were subjected to 70 min dynamic PET scans on day 7 post tumor cell inoculation while imaging was performed on day 14 post induction for S2WTP3 allograft-bearing mice. All experimental animals were fasted for 6 hours before [^{18}F]FDG injection. For the 70 min dynamic PET scan, animals received an *i.v.* bolus injection of 13 ± 1 MBq [^{18}F]FDG (as described in 3.6.2). During the dynamic PET scan, anatomical MR images (as described in 3.7.1) and ^{1}H spectroscopy (as described in 3.7.2) were acquired. At endstage of tumor growth, experimental animals were sacrificed via cervical dislocation in deep anesthesia, tumor allografts were harvested and snap-frozen for ^{1}H HR-MAS NMR spectroscopy (as described in 3.7.5).

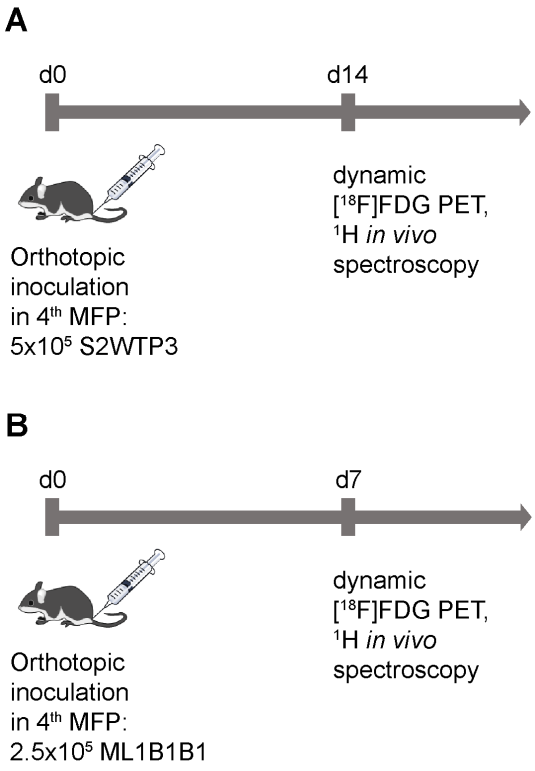

Figure 33: Schematic diagram of the [^{18}F]FDG uptake study in the S2WTP3 and ML1B1B1 PyMT-derived primary breast cancer tumor models by PET and MRI.
In vivo [^{18}F]FDG uptake was assessed in S2WTP3 primary breast tumors (**A**) on day 14 and in ML1B1B1 primary breast tumors (**B**) on day 7 after inoculation by PET. During the 70 min dynamic PET scan, anatomical MR images and *in vivo* ^{1}H spectra were acquired. At endstage, tumor tissued was harvested and snap frozen for ^{1}H HR-MAS NMR.

3.11 *Ex vivo* examinations

3.11.1 Biodistribution studies by γ-counting

Ex vivo biodistribution analysis was performed at the last imaging time point, following the last PET scan, to validate data obtained from *in vivo* PET scans. Retro-orbital blood was sampled from every animal with 10 µL glass micropipettes under anesthesia after the preceding PET scan. The animal was then sacrificed via cervical dislocation.

For the primary tumor models, the tumor, lungs, liver, spleen, kidneys, the left femur and tibia and muscle tissue were harvested and stored in formalin in 5 mL polystyrene tubes.

For the metastatic tumor models, as far as technically possible, the cancerous tissue was separated from the healthy organ according to the tissue margins indicated by *ex vivo* bioluminescence OI. In this way, metastases were separated from the heart, lungs, liver, spleen, kidneys, adrenal glands, ovaries, femurae and tibiae and the muscle and stored in separate 5 mL polystyrene tubes. The weight of the 5 mL polystyrene tubes was determined

before and after addition of the organ of interest to obtain its weight. A standard solution with a known amount of radioactivity was prepared as reference: 1.85 MBq [^{64}Cu]NOTA-anti-CD11b mAb solution was added to a 50 mL graduated measuring glass filled with tap water and quadruplets of 0.1, 0.5 and 1 mL of this standard solution corresponding to 3.7, 18.5 and 37 kBq, respectively, were pipetted into 5 mL polystyrene tubes. The tubes containing the standard solution and the organs were measured in the Wizard^2 automated γ-counter (Perkin Elmer) at an energy window of 350 to 650 keV. The resulting decay corrected counts per minute were then first normalized to the injected dose with the help of the standard solution and to the respective weight of the organ to obtain the injected dose per gram of tissue (%ID/g).

3.11.2 Flow cytometry

3.11.2.1 Principle

Flow cytometry is a high-throughput, multiparametric analytical method for single cell or particle suspensions that allows permits in-depth characterization of cell populations by passing single cells in sheath fluid through laser-beams in a highly precise glass cuvette and detecting the resulting optical signals. Basic cell characteristics, such as the size and granularity, are analyzed by determination of the light refraction in a 180° angle (forward scatter, FSC) and in a 90° angle to the cell (sideward scatter, SSC), respectively. More complex characteristics can be elucidated by labeling cells with fluorescent dye-conjugated antibodies recognizing, for example, cell surface antigens, receptors or intracellular transcription factors. The fluorescent dyes bound to the cells are excited by laser light of different frequencies (commonly 405 nm, 488 nm and 640 nm) and detection of the emitted fluorescence signal is achieved by complex filters arrays with narrow bandwidth. Remaining spectral overlap of the fluorescence signals is electronically compensated for with the operating system. The detected signal is enhanced with photomultiplier tubes and converted into an electrical signal for recording. The use of multiple antibodies conjugated with different fluorescent dyes in antibody cocktails permits in-depth characterization of cell populations.

3.11.2.2 Tissue processing to generate single cell suspensions for flow cytometry

Since flow cytometric analyses are performed on single cell suspensions, the isolated organs were processed to isolate immune cell infiltrates and free single cells of connective tissue. Tumor samples and lungs were cut into small pieces (approximately 1.5-2 mm in height and width) and digested with 2 mg/mL Collagenase Type IV (Sigma Aldrich) in DMEM supplemented with 5 % FCS and 10 mM HEPES buffer for 40 min at 37 °C. The resulting

tissue digest was macerated and washed first through a 70 µm cell strainer and then through a 40 µm cell strainer. Remaining erythrocytes were lysed with 3 mL ACK lysing buffer for 4 min at room temperature. Lysis was stopped by adding 6 mL PBS, cells were spun down and resuspended in 3 mL unsterile PBS + 1 % FCS (FACS buffer). The single cell suspension was then pipetted into a 5 mL polystyrene tube with 40 µm cell strainer snap cap (Corning, Corning, New York, USA), centrifuged again and resuspended in 300-400 µL FACS buffer.

Spleens were macerated first through 70 µm cell strainer and then through a 40 µm cell strainer in FACS buffer. Erythrocytes were lysed with 1.5 mL ACK lysis buffer for 4 min at room temperature and lysis was stopped by adding 3 mL PBS. The splenocyte suspension was further filtered by pipetting into a 5 mL polystyrene tube with 40 µm cell strainer snap cap. The resulting single cell suspension was centrifuged again and resuspended in 300-400 µL FACS buffer. The volume of the buffer was adjusted to the number of antibody cocktails in the respective experiment.

For staining with the antibody cocktails, 100 µL of the single cell suspensions were pipetted into a U-bottom 96-well plate and centrifuged for 5 min at 400 g. The supernatant was discarded and the cell pellet was resuspended in 50 µL of the respective antibody cocktail. Antibody staining was performed for 30 min at 4 °C. After the incubation period, 150 µL FACS buffer were added, the plate was centrifuged and the supernatant discarded. The cells were further washed twice in 150 µL FACS buffer and taken up in 400 µL FACS buffer.

3.11.2.3 Flow cytometric analyses

The different flow cytometry-based experiments performed in this work are described in detail in the following section.

3.11.2.3.1.1 CD11b expression after pre-labeling with the anti-CD11b mAb

Labeling of MDSCs with [^{64}Cu]NOTA-anti-CD11b mAb reduces the availability of free CD11b at least transiently and might therefore restrict cell migration. To assess the extent of the blocking of available CD11b molecules, PMN- and M-MDSCs were labeled with 1.6 µg anti-CD11b mAb as a surrogate for [^{64}Cu]NOTA-anti-CD11b mAb according to protocol. Then, at 3, 24 and 48 h post pre-labeling, PMN- and M-MDSCs were stained with a Cy5-conjugated anti-CD11b mAb (self-made with Lightning-Link Rapid Cy5 kit, Innova Biosciences, Cambridge, United Kingdom) in a 1:200 dilution in FACS buffer for 30 min at 4 °C. Cells were washed twice and analyzed on the LSR II flow cytometer (BD Biosciences). At all time points, naïve PMN- and M-MDSCs served as a control for the CD11b expression level.

3.11.2.3.1.2 Apoptosis induction in MDSCs after radiolabeling with [^{64}Cu]NOTA-anti-CD11b mAb

Since antibody labeling and radiation emitted by the isotope ^{64}Cu can induce apoptosis and cell death, [^{64}Cu]NOTA-anti-CD11b mAb-labeled PMN- and M-MDSCs were stained with PE-Annexin V and 7-Aminoactinomycin (7-AAD; PE Annexin V Apoptosis Detection Kit, BD Biosciences) to reveal apoptotic and dead cells at 3 and 48 h post radiolabeling. According to the manufacturer's instructions, the cells were washed twice with PBS and suspended in the supplied binding buffer. Then, triplicates of the cells were stained with 5 µL PE-Annexin V and 5 µL 7-AAD for 15 min at room temperature in the dark. After staining, 400 µL of the binding buffer were added and analysis of the cells was performed within the hour on the LSR II flow cytometer (BD Biosciences). Naïve PMN- and M-MDSCs served as control at all time points.

3.11.2.3.1.3 Location of DiD-MDSCs after adoptive transfer in S2WTP3 tumor-bearing mice

Possible homing sites of adoptively transferred DiD-MDSCs in tumor-bearing animals (n=3 for DiD-PMN-MDSCs and DiD-M-MDSCs, respectively) could include, beside the tumor, the lungs and spleen. Therefore, these organs were further processed to single cell suspensions after *ex vivo* OI measurements (as described above). Adoptively transferred DiD-PMN- and DiD-M-MDSCs were identified according to their staining with the fluorescent DiD (excitation maximum at 644 nm, emission maximum at 665 nm) that can be detected by flow cytometry in the Allophycocyanin (APC; excitation maximum at 652 nm, emission maximum at 656 nm) channel. Due to the fluorescent label of the DiD-MDSCs and the settings of the LSR II flow cytometer, the fluorescent dyes for further staining were restricted to fluoresceinisothiocyanat (FITC), PE and the coumarin dyes V450 and V500. Furthermore, tumor, lung and spleen samples were stained with the antibody cocktails given in Table 2 to detect possible changes in the immune cell profile (T cells detected as $CD3^+/CD4^+/CD8^+$ and NK cells detected as $CD3^-/NK1.1^+$) and to detect if the adoptively transferred MDSC subpopulations might have undergone further differentiation to DCs (identified as $CD11c^+/CD11b^+$) or macrophages (identified as $CD11b^+/F4/80^+$). Untreated tumor-bearing animals (n=3) served as control. A Fc blocking reagent (purified anti-mouse CD16/32 antibody, Biolegend, San Diego, California, USA) was added to all antibody cocktails to block unspecific binding of the Fc-part of the antibody to Fc receptors on, e.g., macrophages.

Table 2: Antibody cocktails for the flow cytometric analysis of immune cell infiltrates in the tumor, lung and spleen after adoptive transfer of DiD-MDSCs.

Cocktail 1			
Fluorchrome	**Antigen**	**Dilution**	**Clone&Supplier**
V450	Ly6C	1:300	AL-21, BD Biosciences
V500	CD45.2	1:300	104, BD Biosciences
FITC	CD11b	1:300	M1/70, BD Biosciences
PE	Ly6G	1:300	1A8, BD Biosciences
Cocktail 2			
Fluorchrome	**Antigen**	**Dilution**	**Clone&Supplier**
V450	CD3	1:300	500A2, BD Biosciences
V500	CD45.2	1:300	104, BD Biosciences
FITC	CD8	1:300	53-6.7, BD Biosciences
PE	CD4	1:300	GK1.5, BD Biosciences
Cocktail 3			
Fluorchrome	**Antigen**	**Dilution**	**Clone&Supplier**
V450	CD3	1:300	500A2, BD Biosciences
V500	CD45.2	1:300	104, BD Biosciences
PE	NK1.1	1:300	PK136, BD Biosciences
Cocktail 4			
Fluorchrome	**Antigen**	**Dilution**	**Clone&Supplier**
V450	CD11c	1:300	HL3, BD Biosciences
V500	CD45.2	1:300	104, BD Biosciences
FITC	CD11b	1:300	M1/70, BD Biosciences
PE	F4/80	1:300	BM8, Biolegend

The gating scheme for the identification of immune cell popuations is given in Figure 34. Each cell population identified by the given markers was further examined for staining with DiD.

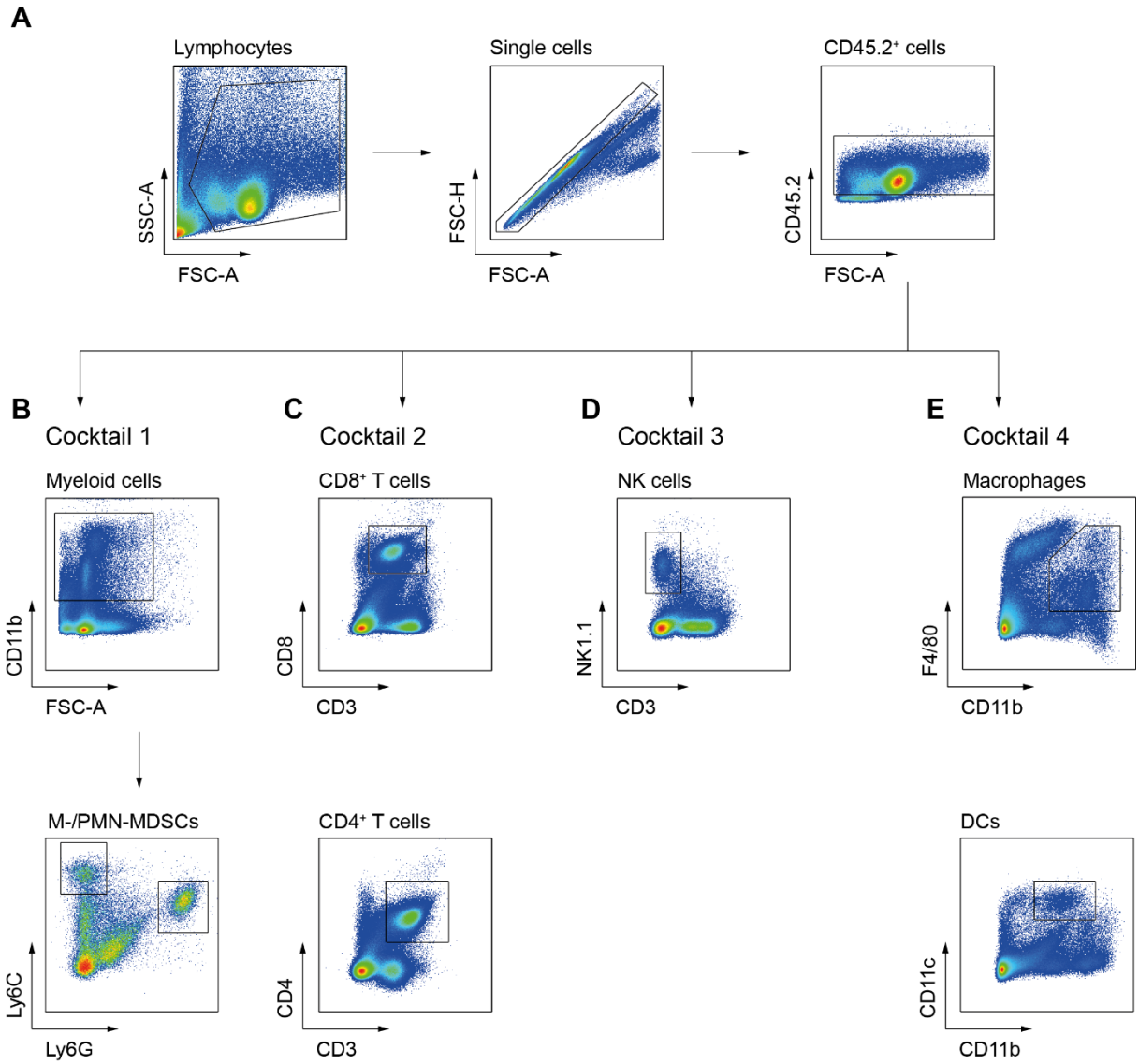

Figure 34: Gating strategy for flow cytometric analysis of immune cell populations after adoptive transfer of DiD-MDSCs.

(**A**) Separation of cellular debris and selection of lymphocytes based on size and granularity in FSC-A plotted against SSC-A. Then, single cells and doublets were separated by plotting FSC-A against FSC-H and hematopoietic cells were selected according to expression of CD45.2. Staining with (**B**) antibody cocktail 1 allowed for identification of $CD11b^+/Ly6C^{high}/Ly6G^-$ M-MDSCs and $CD11b^+/Ly6C^{int}/Ly6G^+$ PMN-MDSCs, (**C**) antibody cocktail 2 for $CD3^+/CD4^+$ and $CD3^+/CD8^+$ T cells, (**D**) antibody cocktail 3 for $CD3^-/NK1.1^+$ NK cells and (**E**) antibody cocktail 4 for $CD11b^+/F4/80^+$ macrophages and $CD11b^+/CD11c^+$ DCs.

3.11.2.3.1.4 Pre-metastatic niche induction with tumor cell CM

Detection of the induction of a lung pre-metastatic niche with tumor cell CM was performed by flow cytometric analysis of the lungs. Therefore, the lungs of S2WTP3 CM-treated animals (n=4), B16F10 CM-treated animals (n=4) and untreated controls (n=4) were isolated and processed as described in section 3.11.2.2. Furthermore, the spleens were isolated and processed in the same fashion to serve as control tissue. The generated single cell

suspensions were stained with the antibody cocktails detailed in Table 3. Cocktail 1 was employed to characterize the PMN- and M-MDSC populations in the lungs and spleen while changes in the abundance of T cells and NK cells could be surveyed with cocktail 2. Additionally, the activation status of T cells and NKs cells was measured as expression of the early activation marker CD69 (eBioscience by Thermo Fisher Scientific).

Table 3: Antibody cocktails for the flow cytometric analysis of pre-metastatic niche induction in mice treated with tumor cell CM.

Cocktail 1			
Fluorchrome	**Antigen**	**Dilution**	**Clone&Supplier**
V450	CXCR4	1:300	2B11, eBioscience
V500	CD45.2	1:300	104, BD Biosciences
FITC	CD244	1:300	244F4, eBioscience
PE	Ly6G	1:300	1A8, BD Biosciences
7-AAD	Viability	1:20	BD Biosciences
APC	Ly6C	1:300	HK1.4, Biolegend
PE-Cy7	CD115	1:300	AFS98, eBioscience
APC-eFlour780	CD11b	1:300	M1/70
Cocktail 2			
Fluorchrome	**Antigen**	**Dilution**	**Clone&Supplier**
V450	CD3	1:300	500A2, BD Biosciences
V500	CD45.2	1:300	104, BD Biosciences
FITC	CD8	1:300	53-6.7, BD Biosciences
7-AAD	Viability	1:20	BD Biosciences
APC	NK1.1	1:300	PK136, Miltenyi
PE-Cy7	CD69	1:300	H1.2F3, eBioscience
APC-eFlour780	CD4	1:300	GK1.5, eBioscience

The gating strategy to identify PMN- and M-MDSCs as well as T cell and NK cell inflitrates in the lungs of CM-treated animals is given in Figure 35 as a schematic.

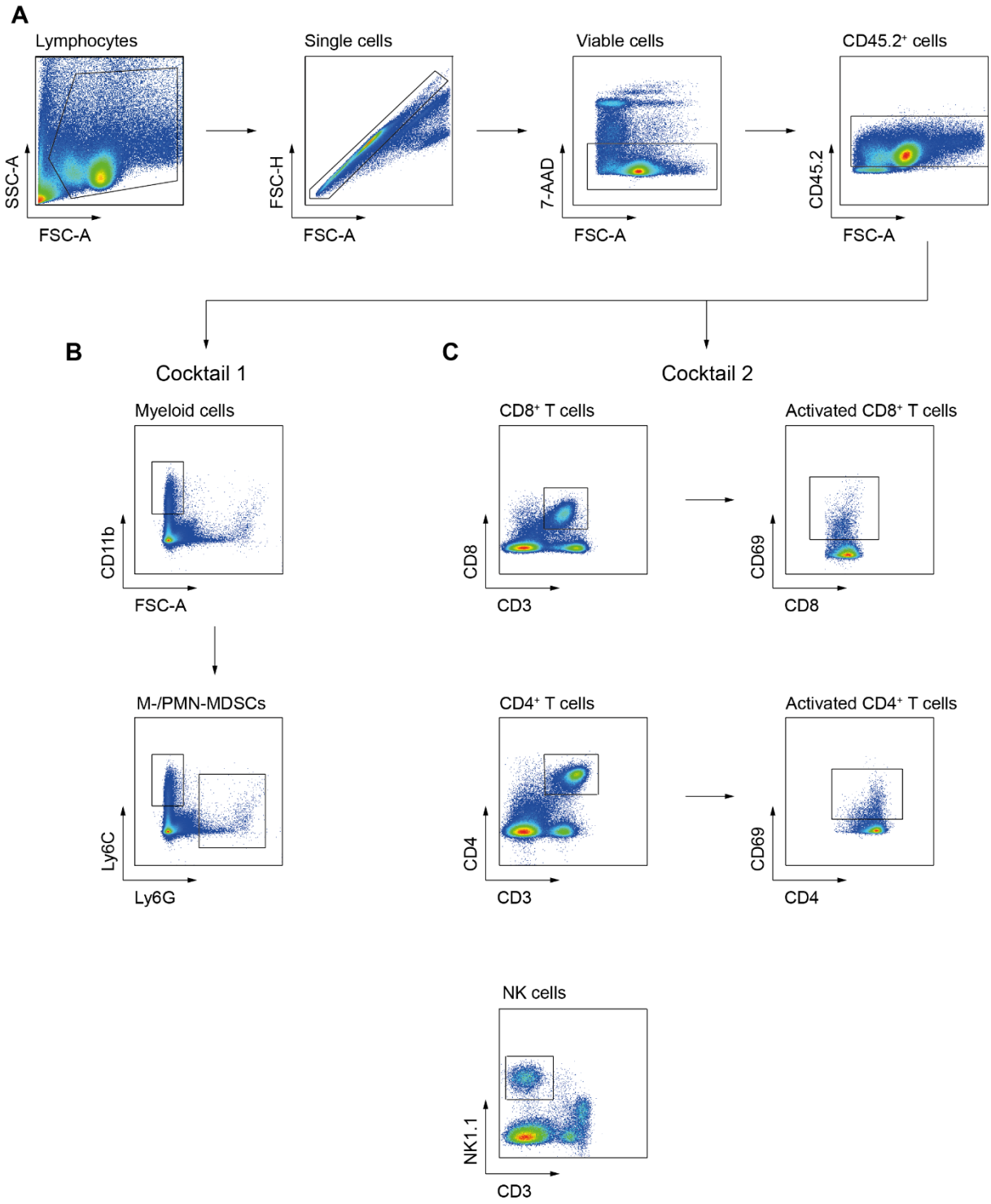

Figure 35: Exemplary gating strategy for the flow cytometric analysis of immune cell populations in the lungs of experimental animals after treatment with tumor cell CM.

(**A**) Separation of cellular debris and selection of lymphocytes based on size and granularity in FSC-A plotted against SSC-A and exclusion of doublets by plotting FSC-A against FSC-H. Viable cells did not stain positive for 7-AAD. From viable cells, hematopoietic cells were selected according to expression of CD45.2. Staining with (**B**) antibody cocktail 1 allowed for identification of $CD11b^+/Ly6C^{high}/Ly6G^-$ M-MDSCs and $CD11b^+/Ly6C^{int}/Ly6G^+$ PMN-MDSCs and (**C**) antibody cocktail 2 for $CD3^+/CD4^+$ and $CD3^+/CD8^+$ T cells as well as activated $CD3^+/CD4^+/CD69^+$ and $CD3^+/CD8^+/CD69^+$ T cells.

3.11.3 Histology

Immunofluorescence stainings and microscopy were performed by Renate Nordin and Birgit Fehrenbacher of the electron microscopy laboratory of the Department of Dermatology, University Tübingen.

3.11.3.1 Fluorescence microscopy to visualize Cy3-anti-CD11b mAb internalization in MDSCs

Internalization of the [^{64}Cu]NOTA-anti-CD11b mAb enhances the stability of the radiolabel in the cells (Griessinger *et al.*, 2015). To visualize internalization of the anti-CD11b mAb in PMN- and M-MDSCs, the anti-mouse anti-CD11b mAb was conjugated with the fluorescent dye Cy3 (Lightning-Link Rapid Cy3 kit, Innova Biosciences) according to the manufacturer's instructions as a surrogate for the [^{64}Cu]NOTA-anti-CD11b mAb. PMN- and M-MDSCs were labeled with the Cy3-anti-CD11b mAb as described in 3.4.3. Cy3-anti-CD11b mAb-labeled PMN- and M-MDSCs were then suspended in complete RPMI 1640 medium supplemented with 40 ng/mL GM-CSF and IL-6 and plated in 10 cm sterile suspension cell culture dishes. Unlabeled PMN- and M-MDSCs were used as control. Cell samples were removed at 3, 24 and 48 h post labeling, washed once in PBS and resuspended in 10-20 µL 2 % formalin. For analysis directly after preparation, the samples were pipetted onto a glass slide, covered with a cover slip and examined with the LSM 800 confocal microscope (Zeiss, Oberkochen, Germany) operated under the Zen software (Version 2.3, Zeiss).

3.11.3.2 Immunofluorescence staining for phosphorylated H2AX histones as indicator for DNA damage

Staining for phosphorylated H2AX histones was performed as indication for DNA-double strand breaks in [^{64}Cu]NOTA-anti-CD11b mAb-labeled PMN- and M-MDSCs and naïve PMN-MDSCs and M-MDSCs as control. PMN- and M-MDSCs were labeled with [^{64}Cu]NOTA-anti-CD11b mAb as described in 3.4.3. Then, [^{64}Cu]NOTA-anti-CD11b mAb-labeled PMN- and M-MDSCs were suspended in complete RPMI 1640 supplemented with 40 ng/mL GM-CSF and IL-6 and plated in 10 cm sterile suspension cell culture dishes. At 3, 24 and 48 h post radiolabeling, cell samples were fixed 2 % formalin for 10 min, washed twice in ultrapure water and suspended in 30 µL ultrapure water. Then, the cells were pipetted onto microscope slides with a black epoxy resin color mask (Paul Marienfeld GmbH Co. KG, Lauda-Königshofen, Germany) and heat-fixation onto microscopy slides was performed for 10 min at 60 °C. Cell samples were permeabilized with 0.3 % Triton X-100 in 10 % donkey serum (Sigma-Aldrich) for 30 min. After washing, microscopy slides were incubated in anti-phosphorylated H2AX antibody (1:200, Abcam, Cambridge, United Kingdom) for 1 h, washed and stained with

donkey anti-rabbit F(ab')2-Cy3 (1:500 in PBS/BSA/Tween, Dianova, Hamburg, Germany) and donkey anti-rat F(ab')2-Alexa 488 (1:500 in PBS/BSA/Tween, Dianova) for 1 h. Staining with DAPI (1:10000 in PBS/BSA/Tween, Sigma-Aldrich) was used for the visualization of cell nuclei. All images were acquired on the LSM 800 (Zeiss) operated under the Zen software (Version 2.3).

3.11.3.3 Immunofluorescence staining to detect adoptively transferred MDSCs

For immunofluorescence staining, tissue samples of S2WTP3- and B16-F10-Red-FLuc-tumor-bearing animals were collected and fixed in 4.5 % buffered formalin solution (SAV Liquid Production) for 72 h.

For antigen recovery, paraffin-embedded tissue sections were deparaffinized, rehydrated, and incubated in citrate buffer pH 6.0 for 2 min in a pressure cooker. Glass slides were cooled in deionized water for 10 min at room temperature. After washing, tissue sections were blocked in a 1:20 dilution of donkey serum for 30 min and incubated with rabbit anti-Ki-67 (1:100 in PBS/BSA/Tween, Abcam) for 1 h at room temperature to assess cell proliferation. Secondary antibody staining was performed with anti-rabbit Alexa 647 (1:500 in PBS/BSA/Tween, Dianova) and anti-rat-Cy3 (1:500 in PBS/BSA/Tween, Dianova) for 1 h at room temperature. The cell nucleus was then stained with YO-PRO nuclear dye (1:2000 in PBS, Molecular Probes by Thermo Fisher Scientific). The tissue sections were embedded in Mowiol (Thermo Fisher Scientific) and fluorescence images were acquired on the LSM 800 confocal microscope operated under the Zen software (Version 2.3).

3.12 Statistics

The results of *in vitro* experiments, *in vivo* PET imaging data as well as *ex vivo* analysis were depicted as mean ± standard error of the mean (SEM). Statistical analysis of *in vivo* PET imaging data was performed with the two-tailed Student's t-test (under the assumption of same variances) separately for each time point. Multi-group comparisons with respective control groups were performed using the Tukey-Kramer method or Dunnett's Multiple Comparison test. P values < 0.05 were considered significant. Statistical analysis was performed with the JMP software (SAS Institute, Cary, North Carolina). The statistical test used for each experiment is indicated the respective figure legend. All other results were subjected to descriptive statistics.

Statistical analysis of metabolomics and proteomics was performed by Dr. Christoph Trautwein and Dr. Mohamed Ali Jarboui, Werner Siemens Imaging Center at the University of Tübingen as described in the respective sections 3.7.4 and 3.9.1, respectively.

3.13 Software

Proprietary software for data acquisition and analysis is given in the respective chapter of this section. Further, if not otherwise stated, graphs and figures were generated with ChemBioDraw (Version 13.0, Perkin Elmer), GraphPad Prism 7 (Version 7, GraphPad Software, LLC, San Diego, California, USA) and Adobe Illustrator (Version CS6, Adobe Systems Software Ireland Limited, Dublin, Ireland).

4 RESULTS

In the part “MDSC tracking with non-invasive imaging modalities”, the PyMT-derived breast cancer cell line S2WTP3 was used for the induction of primary breast cancer tumors and breast cancer metastases. Accordingly, the S2WTP3 tumors and metastases were referred to as PyMT breast cancer and PyMT breast cancer metastases in part 1. Primary and metastatic melanoma growth for cell tracking experiments was induced with the B16-F10-Red-FLuc melanoma cell line.

In the part “Metabolic fingerprinting for markers for differential metastatic potency – Examination of the PyMT-derived cell lines S2WTP3 and ML1B1B1” the PyMT-derived cell lines S2WTP3 and ML1B1B1 were compared. The melanoma cell lines B16-F0 and B16-F10 served for comparison wherever technically feasible.

4.1 MDSC tracking with non-invasive imaging modalities

For all MDSC cell tracking experiments, regardless of the non-invasive imaging modality used, MDSCs were expanded *in vitro* from bone marrow progenitor cells. PMN- and M-MDSCs were isolated by magnetic cell separation and directly labeled for the respective imaging modality.

4.1.1 Characterization of *in vitro* differentiated bone marrow-derived MDSCs

As MDSCs are immature myeloid cells, no cell lines were available for cell tracking studies. Therefore, MDSCs were expanded from bone marrow precursor cells with GM-CSF and IL-6 (Marigo *et al.*, 2010). Immunosuppression is considered a key defining function of PMN- and M-MDSCs and serves to identify $CD11b^{+}/Ly6C^{int}/Ly6G^{+}$ myeloid cells as PMN- and $CD11b^{+}/Ly6C^{high}/Ly6G^{-}$ myeloid cells as M-MDSCs, respectively. The immunosuppressive activity of the bone-marrow-derived $CD11b^{+}/Ly6C^{int}/Ly6G^{+}$ and $CD11b^{+}/Ly6C^{high}/Ly6G^{-}$ myeloid cells was measured as capacity to suppress antigen-independent (Figure 36 A) and antigen-induced (Figure 36 B) T cell proliferation.

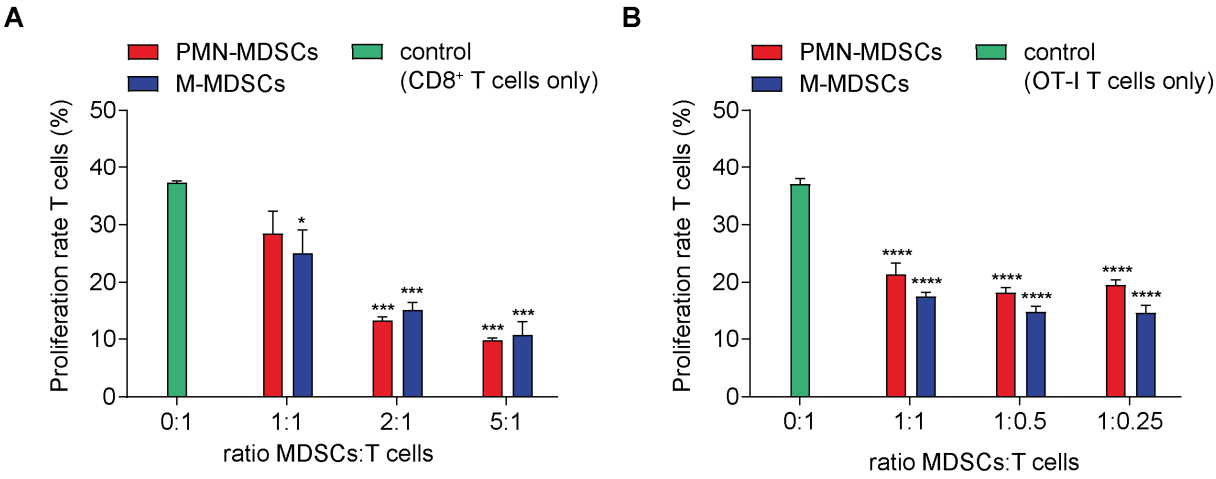

Figure 36: Immunsuppressive activity of bone marrow-derived PMN- and M-MDSCs.
Bone marrow-derived, *in vitro* differentiated PMN- and M-MDSCs demonstrated immunosuppressive activity against non-specifically induced (anti-CD3/CD28 stimulation) and antigen-induced proliferation of CFSE-labeled $CD8^+$ T cells (**A**) and CFSE-labeled OT-1 $CD8^+$ T cells (**B**), respectively (mean ± SEM in percent of all T cells, n=3 for all conditions, statistics: Dunnett's Multiple Comparison Test with control as reference, *p<0.05, ***p<0.001, ****p<0.0001).

Both $CD11b^+/Ly6C^{int}/Ly6G^+$ and $CD11b^+/Ly6C^{high}/Ly6G^-$ bone marrow-derived myeloid cells exhibited T cell proliferation-inhibiting functions (Figure 36) and were therefore referred to as PMN- and M-MDSCs, respectively.

PMN-MDSCs reduced unspecifically induced $CD8^+$ T cell proliferation (Figure 36 A) significantly in a 2:1 (13.23 ± 0.84 % vs. 37.67 ± 0.30 % in the control, p<0.001) and 5:1 (9.84 ± 0.36 % vs. 37.67 ± 0.30 % in the control, p<0.001) PMN-MDSCs:T cell ratio in comparison to the control. Moreover, PMN-MDSCs reduced antigen-dependent $CD8^+$ T cell proliferation of OT-1 T cells (Figure 36 B) in a 1:1 (21.41 ± 1.89 % vs. 37.07 ± 0.95 % in the control, p<0.0001), 1:0.5 (18.20 ± 0.85 % vs. 37.07 ± 0.95 % in the control, p<0.0001) and 1:0.25 (19.53 ± 0.86 % vs. 37.07 ± 0.95 % in the control, p<0.0001) PMN-MDSCs:T cell ratio in comparison to the respective control.

M-MDSCs inhibited unspecifically induced $CD8^+$ T cell proliferation (Figure 36 A) significantly in M-MDSC:T cell ratios of 1:1 (25.07 ± 4.08 % vs. 37.67 ± 0.30 % in the control, p<0.05), 2:1 (15.23 ± 1.35 % vs. 37.67 ± 0.30 % in the control, p<0.001) and 5:1 (10.77 ± 2.27 % vs. 37.67 ± 0.30 % in the control, p<0.001). Further, antigen-dependent $CD8^+$ T cell proliferation of OT-1 T cells (Figure 36 B) was significantly reduced in M-MDSCs:T cell ratios of 1:1 (17.55 ± 0.72 % vs. 37.07 ± 0.95 % in the control, p<0.0001), 1:0.5 (14.86 ± 0.97 % vs. 37.07 ± 0.95 % in the control, p<0.0001) and 1:0.25 (14.67 ± 1.34 % vs. 37.07 ± 0.95 % in the control, p<0.0001) in comparison to control OT-1 T cells.

Transcription of genes encoding the proteins S100A8 (gene: *S100A8*) and S100A9 (gene: *S100A9*) and arginase type 1 (gene: *Arg1*) as well as arginase type 2 (ARG2, gene: *Arg2*), responsible for MDSC immunosuppressive function, was profiled using qRT-PCR. The

expression profile of *in vitro* expanded MDSCs were compared to MDSCs isolated from tumor (tumor-MDSCs), spleen (spleen-MDSCs) and lungs (lung-MDSCs) of PyMT tumor-bearing mice (Sceneay *et al.*, 2018) to assess their adequacy for MDSC cell tracking studies.

In vitro expanded PMN-MDSCs (*in vitro* PMN-MDSCs in Figure 37) expressed significantly higher levels of mRNA for the inflammatory protein S100A8 than tumor- (mean fold change 2.1675 + 0.1917 in *in vitro* PMN-MDSCs vs. 0.0075 + 0.0007 in tumor-PMN-MDSCs, $p<0.0001$) and spleen-PMN-MDSCs (mean fold change 2.1675 + 0.1917 in *in vitro* PMN-MDSCs vs. 1.0817 + 0.0572 in spleen-PMN-MDSCs, $p<0.001$) isolated from tumor-bearing animals. No significant difference was detected compared to lung-PMN-MDSCs isolated from tumor-bearing animals. Compared to *in vitro* PMN-MDSCs, S100A9 mRNA was expressed to a higher degree in lung-PMN-MDSCs (mean fold change 2.1534 + 0.2188 in lung-PMN-MDSCs vs. 1.2728 + 0.2048 in *in vitro* PMN-MDSCs, $p<0.05$) and to a lower degree in tumor- (mean fold change 0.0085 + 0.0011 in tumor-PMN-MDSCs vs. 1.2728 + 0.2048 in *in vitro* PMN-MDSCs, $p<0.0001$). No significant difference was detected in comparison to spleen-PMN-MDSCs. The mRNA for the enzyme ARG1 was expressed to a higher degree in tumor- (mean fold change 141.3701 + 17.9599 in tumor-PMN-MDSCs vs. 22.3159 + 0.6143 in *in vitro* PMN-MDSCs, $p<0.0001$) and to a lower degree in lung- (mean fold change 3.8371 + 1.0128 in lung-PMN-MDSCs vs. 22.3159 + 0.6143 in *in vitro* PMN-MDSCs, $p<0.05$) and spleen-PMN-MDSCs (mean fold change 1.2687 + 0.6578 in spleen-PMN-MDSCs vs. 22.3159 + 0.6143 in *in vitro* PMN-MDSCs, $p<0.001$) compared to *in vitro* PMN-MDSCs. The opposite was the case for the enzyme ARG2, mRNA was expressed to a higher degree in lung- (mean fold change 16.1486 + 0.9799 in lung-PMN-MDSCs vs. 1.3597 + 0.1526 in *in vitro* PMN-MDSCs, $p<0.0001$) and spleen-PMN-MDSCs (mean fold change 1.8747 + 0.0495 in spleen-PMN-MDSCs vs. 1.360 + 0.153 in *in vitro* PMN-MDSCs., $p<0.05$) and to a lower degree in tumor-PMN-MDSCs (mean fold change 0.0823 + 0.0086 in tumor-PMN-MDSCs vs. 1.3597 + 0.1526 in *in vitro* PMN-MDSCs, $p<0.0001$) of tumor-bearing mice compared to *in vitro* PMN-MDSCs.

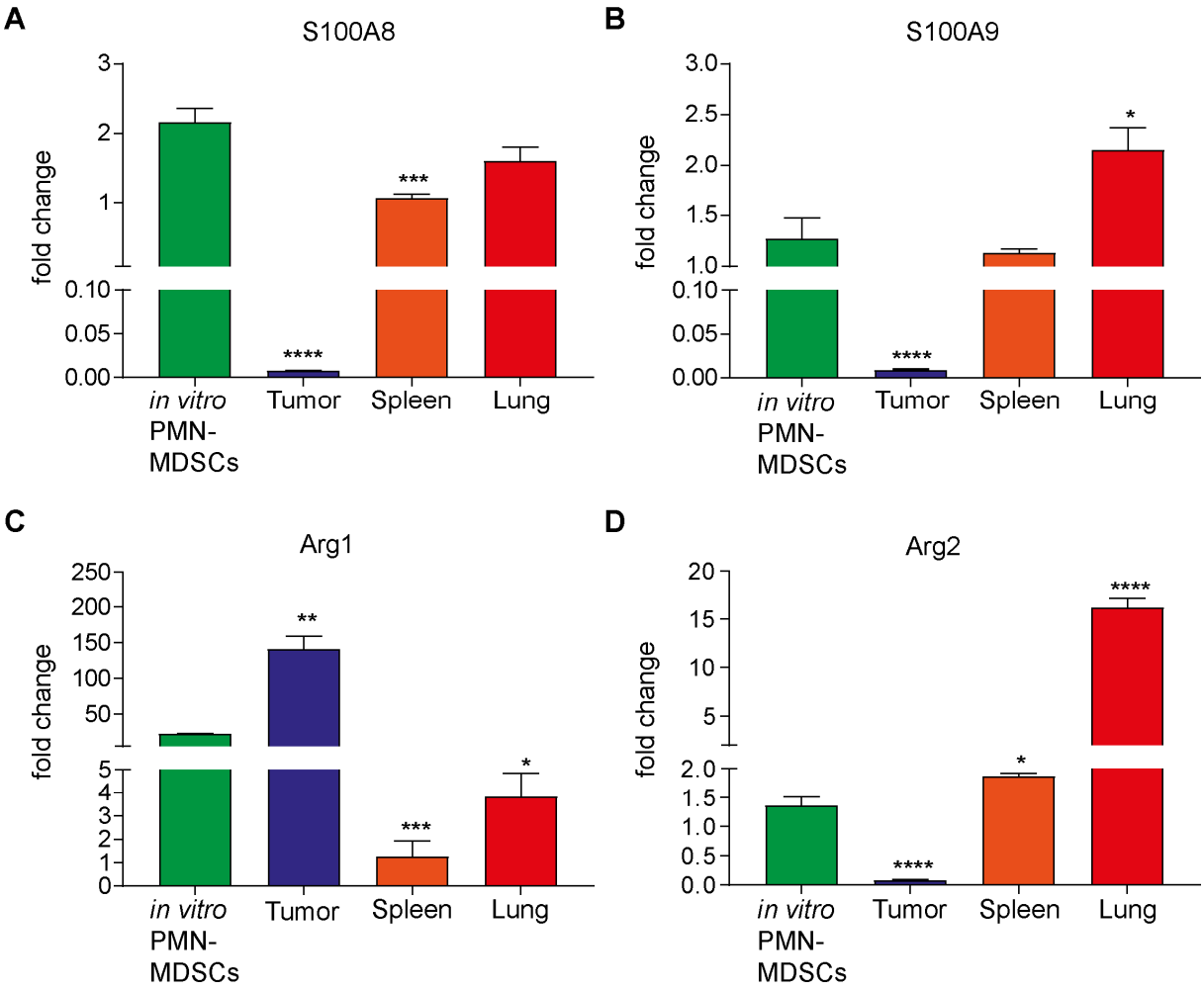

Figure 37: Gene expression profiling of enzymes important for PMN-MDSC function.
Differences in the gene expression levels for (**A**) *S100A8*- and (**B**) *A9* as well as (**C**) *Arg1* and (**D**) *Arg2* were detected between *in vitro* expanded PMN-MDSCs (green), PMN-MDSCs isolated from the PyMT tumor (blue), spleen (orange) and the lungs (red) of PyMT tumor-bearing animals (mean fold change + error calculated with the $\Delta\Delta C_t$ method in the indicated PMN-MDSC population normalized to PMN-MDSCs isolated from the spleen of naïve mice, aldolase served as references gene, n=3 for all conditions, statistics: Tukey Kramer HSD, *p<0.05, ***p<0.001, ****p<0.0001).

S100A8 mRNA expression (mean fold change 0.0027 + 0.0003 in tumor-M-MDSCs vs. 1.0847 + 0.2399 in *in vitro* M-MDSCs, p<0.0001) and *S100A9* mRNA expression (mean fold change 0.0026 + 0.0002 in tumor-M-MDSCs vs. 0.6067 + 0.1611 in *in vitro* M-MDSCs, p<0.0001) were significantly lower in tumor-M-MDSCs compared to *in vitro* M-MDSCs. *S100A9* mRNA expression was significantly higher in lung- (mean fold change 3.0951 + 0.7344 in lung-M-MDSCs vs. 0.6067 + 0.1611 in *in vitro* M-MDSCs, p<0.001) and spleen-M-MDSCs (mean fold change 1.4948 + 0.0256 in spleen-M-MDSCs vs. 0.6067 + 0.1611 in *in vitro* M-MDSCs, p<0.05) compared to *in vitro* M-MDSCs (Figure 38). Similar to *in vitro* PMN-MDSCs, *Arg1* expression was significantly higher in tumor-M-MDSCs (mean fold change 871.0832 + 66.3553 in tumor-M-MDSCs vs. 18.2101 + 4.1713 in *in vitro* M-MDSCs, p<0.001) than in *in vitro* M-MDSCs, while expression in spleen-M-MDSCs was lower (mean fold change 1.0767 + 0.2973 in spleen-M-MDSCs vs. 18.2101 + 4.1713 in *in vitro* M-MDSCs, p<0.05). In lung-M-

MDSCs, no *Arg1* expression was detectable. Again, the opposite was the case for the *Arg2* mRNA expression, it was expressed to a higher degree in the lung-M-MDSCs (mean fold change 2.3729 + 1.2050 in lung-M-MDSCs vs. 0.4313 + 0.0520 in *in vitro* M-MDSCs, p<0.0001) and spleen-M-MDSCs, and to a lower degree in PyMT tumor-M-MDSCs (mean fold change 0.0102 + 0.0002 in tumor-M-MDSCs vs. 0.4313 + 0.0520 in *in vitro* M-MDSCs, p<0.0001) of tumor-bearing mice compared to *in vitro* M-MDSCs.

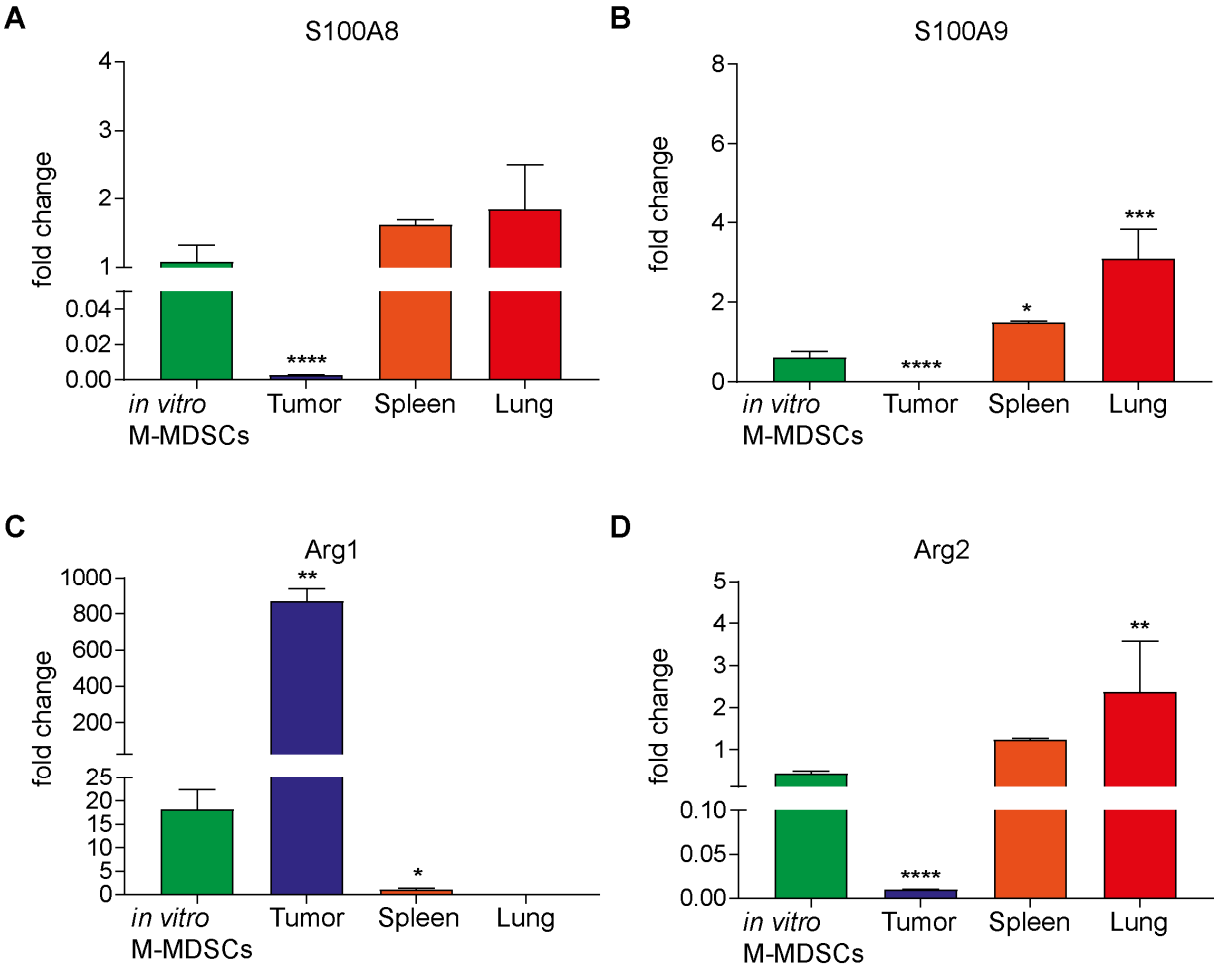

Figure 38: Gene expression profiling of enzymes important for M-MDSC function.
Differences in the gene expression levels for (**A**) *S100A8*- and (**B**) *A9* as well as (**C**) *Arg1* and (**D**) *Arg2* mRNA were detected between *in vitro* expanded M-MDSCs (green), M-MDSCs isolated from the tumor (blue), spleen (orange) and the lungs (red) of S2WTP3 tumor-bearing animals (mean fold change + error calculated according to the ΔΔCt method in the indicated M-MDSC population normalized to M-MDSCs isolated from the spleen of naïve controls, aldolase served as reference gene, n=3 for all conditions, statistics: Tukey Kramer HSD, *p<0.05, **p<0.01, ***p<0.001, ****p<0.0001).

4.1.2 MDSC tracking with optical imaging

To investigate the distribution of PMN- and M-MDSCs in S2WTP3 PyMT breast tumor-bearing mice (in section 4.1 referred to as PyMT tumor) with OI, either $2x10^6$ DiD-labeled PMN- (DiD-PMN-MDSCs) or DiD-labeled M-MDSCs (DiD-M-MDSCs) were *i.v.* injected directly after labeling with DiD and *in vivo* planar fluorescence OI was performed at 48, 72 and 96 h post adoptive cell transfer (pt). With this experimental setup, the recruitment of *in vitro* expanded PMN- and M-MDSCs to the primary TME was examined descriptively since absolute quantification of planar fluorescence OI is challenging due to scattering and absorption of light in tissue.

At 48 h pt, both DiD-PMN- and DiD-M-MDSCs could be detected in the area in and around the liver of PyMT tumor-bearing animals (Figure 39 A). The liver signal in the DiD-PMN-MDSC group, however, had a higher intensity than in the DiD-M-MDSC group indicating a higher fraction of DiD-PMN-MDSCs in the liver. Furthermore, a fluorescent signal was detected in the spleen. In the respective control group, PyMT tumor-bearing animals that had not received an adoptive cell transfer, the fluorescent signal was restricted to the intestine representing the normal background signal in this area derived from fluorescent ingredients of the animals' diet. Tumor homing of both DiD-PMN- and DiD-M-MDSCs was already detected at 48 h pt, with a higher signal in the DiD-PMN-MDSC group in the PyMT tumor. Compared to 48 h pt, at 72 h pt, the fluorescent signal in the liver in both treatment groups, DiD-PMN- and DiD-M-MDSCs, was reduced while tumor homing of DiD-PMN- and -M-MDSCs was still detectable (Figure 39 B).

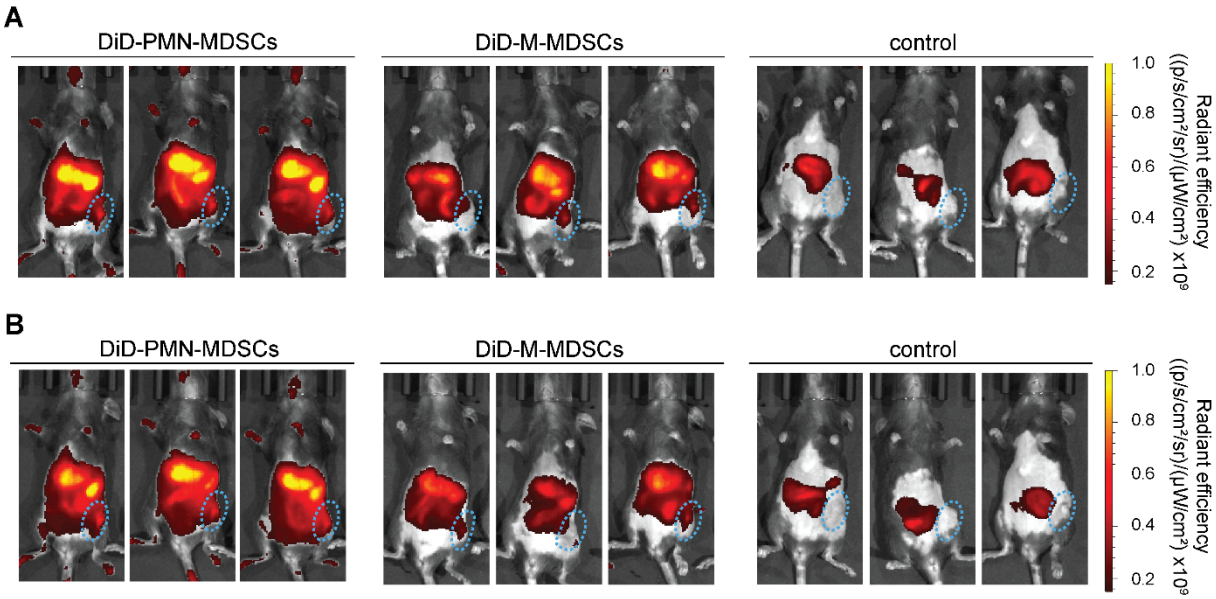

Figure 39: *In vivo* fluorescence OI of PyMT breast tumor-bearing animals injected with DiD-PMN- or DiD-M-MDSCs and PyMT breast tumor-bearing littermates as controls.
Exemplary *in vivo* fluorescence OI images of PyMT breast cancer tumor-bearing mice at 48 h (**A**) and 72 h (**B**) pt showed migration of DiD-PMN-MDSCs (left panel) and DiD-M-MDSCs (middle panel) to the liver, spleen and primary tumor (blue dashed elipse). PyMT breast cancer tumor-bearing mice without adoptive cell transfer served as control for the expected background signal in the gut area in fluorescence OI (color scale in radiant efficiency, n=3 in all groups).

Additionally to *in vivo* OI, *in vivo* and *ex vivo* confocal laser endomicroscopy was performed on one animal per group. Therefore, the animals were *i.v.* injected with 200 µL FITC-Dextran under 1.5 % isoflurane anesthesia to enhance tissue contrast by staining of the microvasculature (Figure 40, green structures) directly before *in vivo* image acquisition. Fluorescence images of the tumors could be acquired both *in vivo* and *ex vivo* while the animals had to be sacrificed to record images of the lungs, liver, spleen, bone marrow and muscle.

DiD-PMN-MDSCs (Figure 40, left panel, yellow arrows) and DiD-M-MDSC (Figure 40, middle panel, yellow arrows) were detected in the tumor, lung, liver, spleen and bone marrow of the tumor-bearing animals while recording an image of DiD-M-MDSCs in the lung and bone marrow was experimentally challenging. Concordant to the expectations, no signal of DiD-labeled MDSCs was found in the muscle of the tumor-bearing animals and in all examined organs of the control animal. Hence, confocal laser microscopy with the Cellvizio Lab system confirmed the *in vivo* OI data.

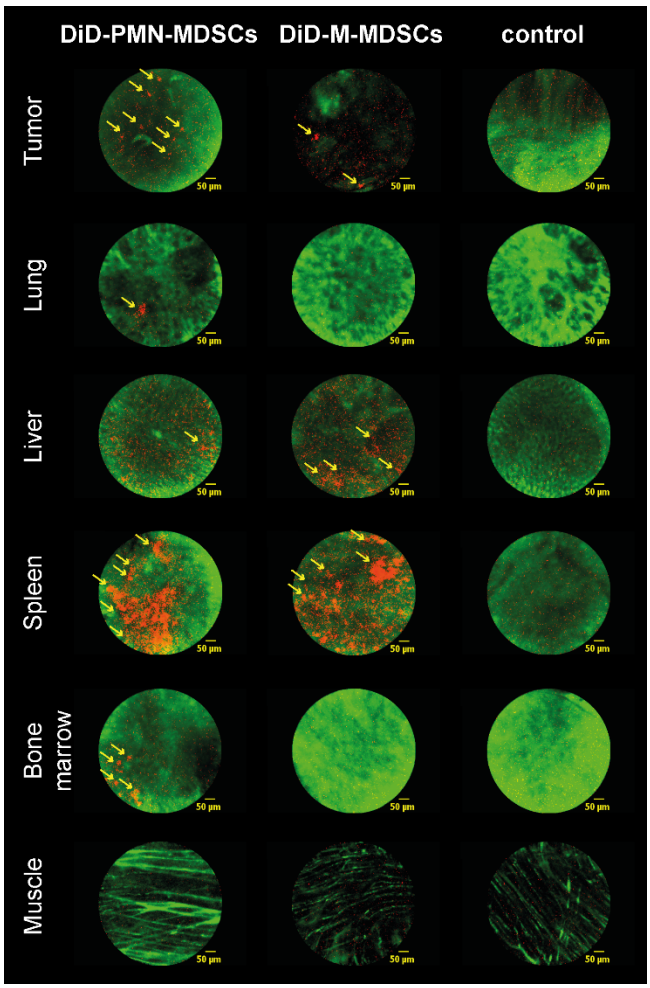

Figure 40: *Ex vivo* confocal laser endomicroscopy with the Cellvizio Lab system.
Exemplary *ex vivo* fluorescence images acquired with the Cellvizio Lab system revealed migration of DiD-MDSCs (red; yellow arrows) to the tumor, lung, liver, spleen and bone marrow of PyMT tumor-bearing mice that had received an adoptive transfer of DiD-PMN- (left panel) or DiD-M-MDSCs (middle panel). Tumor-bearing animals without DiD-MDSC-transfer served as control (right panel). Image contrast was enhanced by non-specific staining of the blood microvasculature with FITC-Dextran (green; n=1 per group).

At 96 h pt, the experimental animals were sacrificed via cervical dislocation in deep anesthesia. The organs were removed and placed onto non-reflecting black paper for *ex vivo* biodistribution analysis (Figure 41). The *ex vivo* biodistribution analysis confirmed migration of both DiD-PMN- and DiD-M-MDSCs to the PyMT breast cancer tumor, liver and spleen of tumor-bearing mice. Additionally, a fluorescence signal indicated PMN-and M-MDSC migration to the lungs. As expected, in the tumor-bearing controls that did not receive an adoptive MDSC transfer, fluorescence signals were only detected in the intestine.

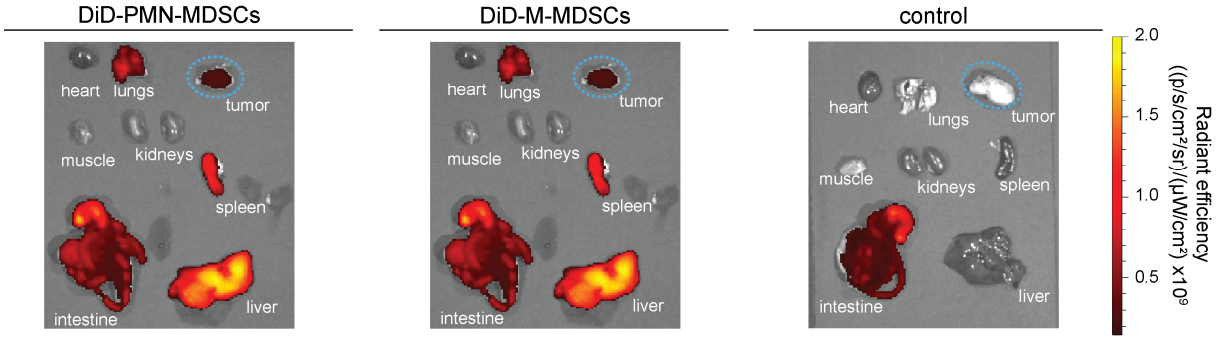

Figure 41: Representative *ex vivo* fluorescence OI images of PyMT breast tumor-bearing animals injected with DiD-PMN- or DiD-M-MDSCs and controls.
Exemplary *ex vivo* fluorescence OI images of organs of PyMT breast cancer tumor-bearing mice at 96 h pt confirmed migration of DiD-PMN-MDSCs (left panel) and DiD-M-MDSCs (middle panel) to the primary tumor (blue dashed ellipse), the liver and the spleen, and eluciated cell migration to the lungs. Mice that had not received an adoptive cell transfer (right panel) served as control for the expected background signal in fluorescence OI (color scale in radiant efficiency, n=3 in all groups).

The comparative quantification of the fluorescence signal in the isolated organs in the *ex vivo* biodistribution (Figure 42) revealed significantly higher fluorescence signals (in radiant efficiency, RE) in PyMT tumors in the DiD-PMN-MDSC group ($1.05x10^8 \pm 2.30x10^8$ RE vs. $1.03x10^7 \pm 5.83x10^6$ RE in control, $p<0.01$) and DiD-M-MDSC group ($1.05x10^8 \pm 6.12x10^6$ RE vs. $1.03x10^7 \pm 5.83x10^6$ RE in control, $p<0.01$) in comparison to the control group. The fluorescence signal in the heart was significantly higher in both the DiD-PMN-MDSC group ($6.17x10^6 \pm 1.13x10^6$ RE vs. $1.93x10^4 \pm 3.33x10^5$ RE in control, $p<0.05$) and DiD-M-MDSCs group ($2.97x10^6 \pm 4.69x10^5$ RE vs. $1.93x10^4 \pm 3.33x10^5$ RE in control, $p<0.01$) in comparison to the control group. Interestingly, a significantly higher fluorescence signal was detected in the lungs of animals from the DiD-PMN-MDSCs in comparison to the DiD-M-MDSC group ($2.36x10^8 \pm 5.45x10^7$ RE vs. $8.36x10^7 \pm 3.58x10^6$ RE in the DiD-M-MDSC group, $p<0.05$) and the control group ($2.36x10^8 \pm 5.45x10^7$ RE vs. $3.08x10^6 \pm 2.58x10^5$ RE in the control group, $p<0.01$). In comparison to the control group that had not received an adoptive cell transfer, a significantly higher fluorescence signal was found in the liver of the animals in the DiD-PMN- ($9.16x10^8 \pm 2.65x10^7$ RE vs. $1.24x10^7 \pm 4.28x10^5$ RE in the control group, $p<0.0001$) and DiD-M-MDSC group ($7.36x10^8 \pm 5.08x10^7$ RE vs. $1.24x10^7 \pm 4.28x10^5$ RE in the control group, $p<0.0001$). Furthermore, the fluorescence signal in the spleen was significantly higher in the DiD-PMN- ($4.43x10^8 \pm 6.12x10^7$ RE vs. $-1.00x10^6 \pm 1.33x10^6$ RE in the control group, $p<0.01$) and DiD-M-MDSC ($4.90x10^8 \pm 8.63x10^7$ RE vs. $-1.00x10^6 \pm 1.33x10^6$ RE in the control group, $p<0.01$) group compared to the control group. The fluorescence signal in the kidneys ($2.89x10^7 \pm 4.65x10^6$ RE vs. $9.69x10^6 \pm 1.27x10^6$ RE in the control group, $p<0.05$) and the muscle ($9.79x10^6 \pm 3.53x10^6$ RE vs. $-6.04x10^5 \pm 1.61x10^6$ RE in the control group, $p<0.05$) of the DiD-M-MDSCs group was significantly higher than in the control group. In the DiD-PMN-MDSC group, in comparison to the control group, a significantly higher fluorescence signal was detected in the intestine ($4.43x10^8 \pm 1.17x10^7$ RE vs. $3.09x10^8 \pm 7.45x10^6$ RE in the control

group, p<0.05). The fluorescence signal in the intestine of mice from the control group is derived from fluorescent components of the animals' diet.

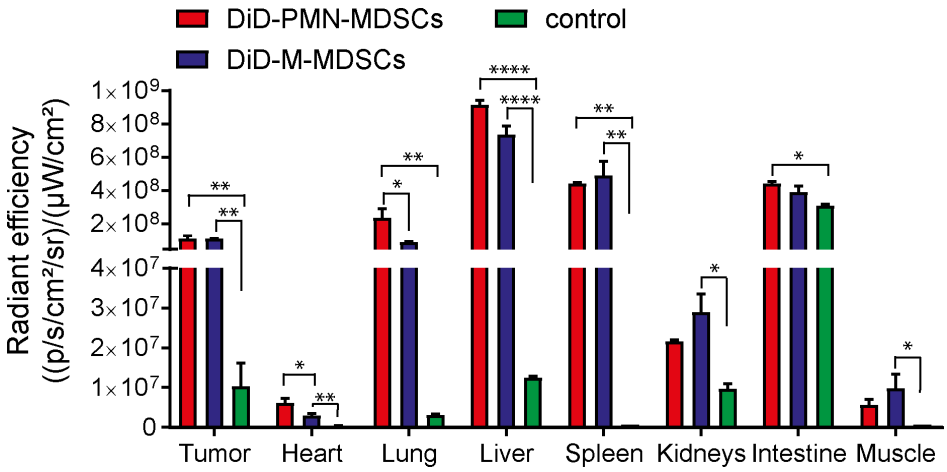

Figure 42: Quantification of the *ex vivo* biodistribution of DiD-labeled MDSCs.
For comparative quantification, ROIs were drawn around the organs, quantified and corrected for background (mean ± SEM in radiant efficiency, n=3, statistics: Tukey Kramer HSD Test).

The organs isolated for *ex vivo* biodistribution were further processed for flow cytometric analysis to validate the *in vivo* and *ex vivo* OI data and to examine the fate of the DiD-MDSCs in the tumor, lung and spleen (Figure 43).

Concordantly to the *in vivo* and *ex vivo* OI data, flow cytometric analysis confirmed migration of DiD-PMN- and DiD-M-MDSCs to the PyMT primary breast tumor. Furthermore, $CD11b^+/F4/80^+$ macrophages and $CD11b^+/CD11c^+$ DCs were found in the PyMT tumor (Figure 43 A), lungs (Figure 43 B) and spleen (Figure 43 C) of animals that had received an adoptive transfer of DiD-PMN-MDSCs (Figure 43, red bars) or DiD-M-MDSCs (Figure 43, blue bars). The fractions of DiD-positive $CD11b^+/F4/80^+$ macrophages and $CD11b^+/CD11c^+$ DCs indicate possible differentiation of PMN-MDSCs and M-MDSCs in the TME. Autofluorescence from tumor cells and possibly other cells, however, could explain the DiD-positive cell populations detected in the control group, PyMT tumor-bearing animals that did not receive an adoptive transfer of DiD-labeled MDSCs.

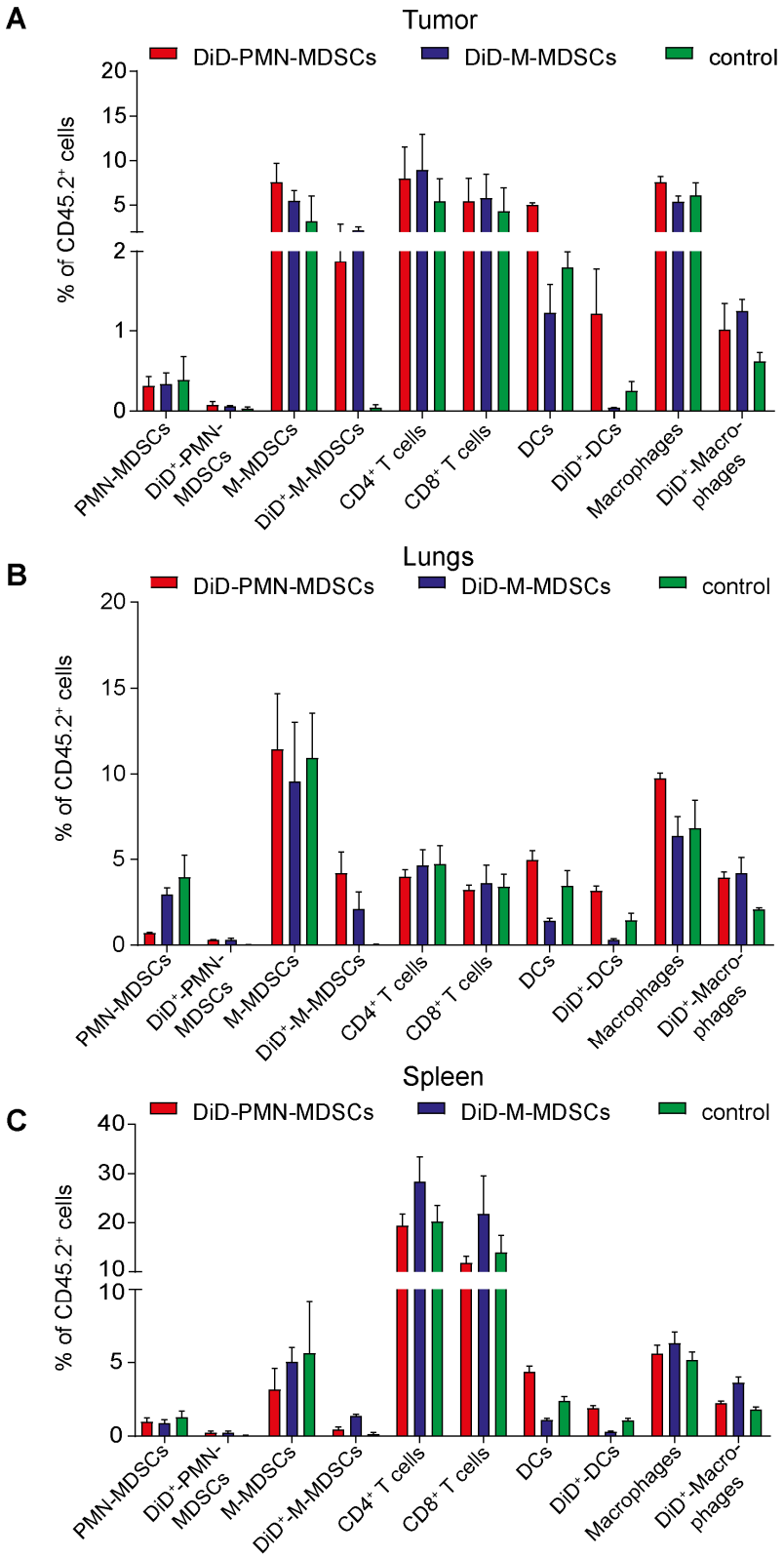

Figure 43: Flow cytometric analysis of PyMT breast tumor-bearing animals injected with DiD-PMN- or DiD-M-MDSCs and controls.

Single cell suspensions were prepared from tumors (**A**), lungs (**B**) and spleen (**C**) of PyMT tumor-bearing animals and subsequently subjected to flow cytometric analysis to confirm tumor homing of DiD-PMN- and DiD-M-MDSCs. Additional cell populations were examined for transfer of the dye DiD (mean ± SEM in percent of $CD45.2^+$ cells, n=3).

4.1.3 MDSC tracking with PET

Due to quantification limitations of planar fluorescence OI, the main aim of this work was to perform PET imaging of adoptively transferred MDSCs. Besides enabling 3-dimensional imaging, PET as a technique stands out due to its prime sensitivity for the detection of low tracer concentrations and, thus, theoretically also of low cell numbers. Therefore, a radiolabeling approach for murine MDSCs was established and evaluated for further cell tracking experiments.

4.1.3.1 Characterization of the effects of [^{64}Cu]NOTA-anti-CD11b mAb-labeling on MDSCs

Due to being pathologically activated immature cells of the myeloid compartment, MDSCs do not express a cell specific surface marker. Therefore, the pan-myeloid cell marker CD11b, also known as integrin α_M, was selected as target for MDSC radiolabeling. The *in vitro* evaluation of the applicability of the [^{64}Cu]NOTA-anti-CD11b mAb as radiolabel for PMN- and M-MDSCs is described in the following.

The integrin CD11b is involved in cell migration, so prolonged blocking of CD11b might affect cell migration. To assess the amount of accessible CD11b-binding sites, the fluorescent dye Cy5 was conjugated to the anti-CD11b mAb (same clone as used for radiolabeling) and both PMN- and M-MDSCs were stained with Cy5-anti-CD11b mAb at 3, 24 and 48 h after initial 30 min pre-labeling with 1.6 µg anti-CD11b mAb. Thereby, the amount of anti-CD11b mAb conformed to the average amount of [^{64}Cu]NOTA-anti-CD11b mAb used for radiolabeling.
Available CD11b-binding sites on both PMN- (Figure 44 A) and M-MDSCs (Figure 44 B) were reduced at 3 h post anti-CD11b mAb pre-labeling compared to unlabeled controls (48.63 ± 2.16 % for pre-labeled PMN-MDSCs vs. 63.40 ± 1.28 % for unlabeled PMN-MDSCs, $p<0.01$, and 37.67 ± 2.65 % for pre-labeled M-MDSCs vs. 51.43 ± 1.74 % for unlabeled M-MDSCs, $p<0.01$). CD11b re-expression was induced after pre-labeling and completed 24 h hereafter (79.13 ± 2.44 % vs. 79.90 ± 4.64 % for PMN-MDSCs and 71.10 ± 0.42 % vs. 61.80 ± 1.78 % for M-MDSCs). Moreover, pre-labeled M-MDSCs have upregulated CD11b expression 24 h post pre-labeling (71.67 ± 0.42 % vs. 61.80 ± 1.78 % on unlabeled controls). Comparable to 24 h post pre-labeling, there was no significant reduction of CD11b expression in pre-labeled MDSC samples compared to unlabeled controls at 48 h post pre-labeling (97.97 ± 0.09 % vs. 97.13 ± 0.41 % for PMN-MDSCs and 96.73 ± 0.24 % vs. 93.93 ± 1.00 % for M-MDSCs). Additionally, overall CD11b expression increased over 48 h in both pre-labeled and control MDSC samples.

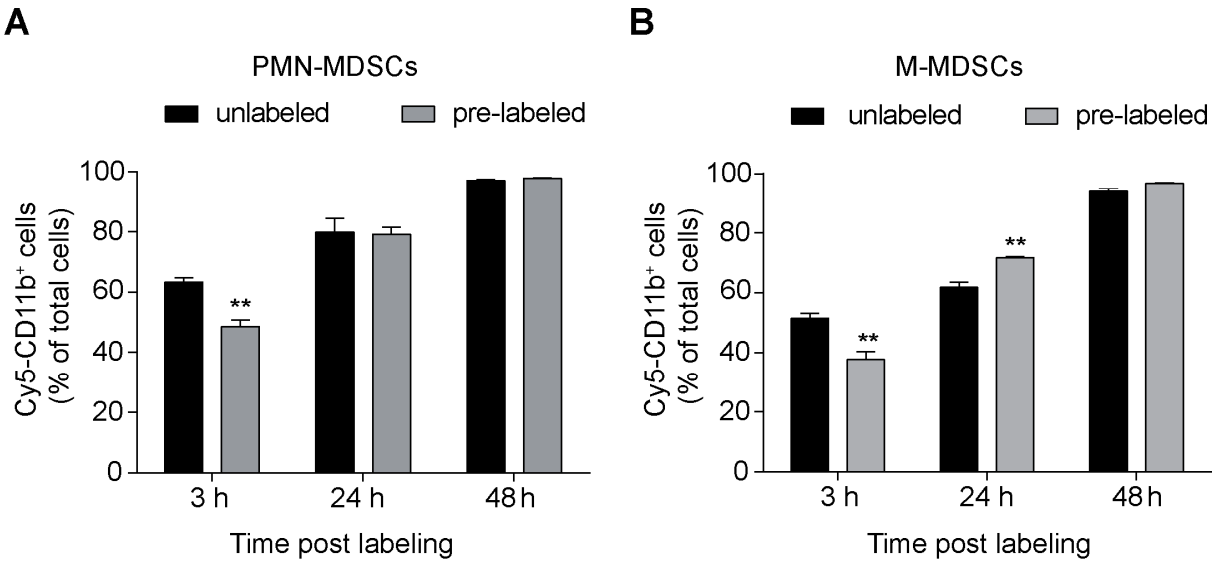

Figure 44: CD11b re-expression after anti-CD11b mAb labeling.
Flow cytometric quantification of CD11b expression by staining PMN-MDSCs (**A**) and M-MDSCs (**B**) with Cy5-anti-CD11b mAb 3, 24 and 48 h after pre-labeling with 1.6 µg anti-CD11b mAb revealed a reduced CD11b availability at 3 h post pre-labeling and CD11b re-expression after 24 h (values are given as mean percent of total PMN-MDSCs ± SEM and total M-MDSCs ± SEM, n=3, statistics: Student's t-test with **p<0.01).

Engagement of membrane-bound receptors, such as integrins, often leads to internalization and recycling of the receptor. The fluorescent dye Cy3 was conjugated to the anti-CD11b mAb to examine, with confocal microscopy, if the antibody-receptor-complex was internalized. The dye Cy3 was used as the confocal microscope could not detect the dye Cy5. Comparability of the Cy3-anti-CD11b and the Cy5-anti-CD11b mAbs was assumed since the dyes Cy3 and Cy5 chemically only differ by one ethylene group in the linker. Using confocal microscopy, the internalization of the Cy3-anti-CD11b-mAb-CD11b-complex was verified and the process was completed as early as 3 h post labeling in both PMN- (Figure 45 A) and M-MDSCs (Figure 45 B). The internalized Cy3-anti-CD11b-mAb-CD11b-complex remained stable in the cells over 48 h (Figure 45).

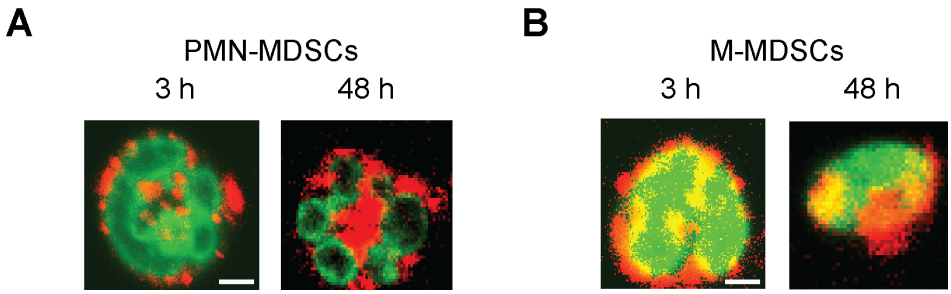

Figure 45: Internalization of the anti-CD11b-mAb-CD11b complex.
Confocal microscopy of PMN- (**A**) and M-MDSCs (**B**) 3 and 48 h after labeling with 1.6 µg Cy3-anti-CD11b mAb proved internalization of the CD11b-antibody complex within 3 h and retention in the cells over 48 h (green – YO-PRO nuclear dye, red – Cy3-anti-CD11b, scale bar 1 µm).

The internalization of the anti-CD11b-mAb-CD11b-complex indicated the adequacy for translation of the anti-CD11b mAb for radiolabeling of MDSCs. Therefore, the anti-CD11b mAb was modified with the chelator NOTA and labeled with ^{64}Cu to examine effects of the [^{64}Cu]NOTA-anti-CD11b mAb radiolabel on PMN- and M-MDSCs.

To assess the stability of the [^{64}Cu]NOTA-anti-CD11b mAb in PMN- and M-MDSCs, either 1x10^{6} PMN- or M-MDSCs were radiolabeled with 0.74 MBq [^{64}Cu]NOTA-anti-CD11b mAb (corresponding to 1.6 µg mAb) for 30 min at 37 °C. Radiolabeled [^{64}Cu]NOTA-anti-CD11b-PMN- and -M-MDSCs (hereafter referred to as [^{64}Cu]PMN- and [^{64}Cu]M-MDSCs, respectively) were centrifuged and suspended in fresh medium before the initial uptake value was assessed by γ-counting (Figure 46). The initially measured uptake values were set to 100 % and the percentage of remaining radioactivity in the cells over the course of 48 h was calculated as percentage of the initial uptake.

At 5 h post radiolabeling, 86.17 ± 0.03 % of initially measured radioactivity was retained in [^{64}Cu]PMN-MDSCs and 84.12 ± 0.02 % in [^{64}Cu]M-MDSCs indicating a high stability over the first 5 hours. At 24 h post radiolabeling, retained radioactivity decreased significantly to 53.23 ± 0.01 % for [^{64}Cu]PMN- and 51.81 ± 0.02 % for [^{64}Cu]M-MDSCs. Intracellular radioactivity was further decreased at 48 h post initial radiolabeling to 37.89 ± 0.01 % of initially measured radioactivity in [^{64}Cu]PMN-MDSCs and 35.43 ± 0.02 % in [^{64}Cu]M-MDSCs.

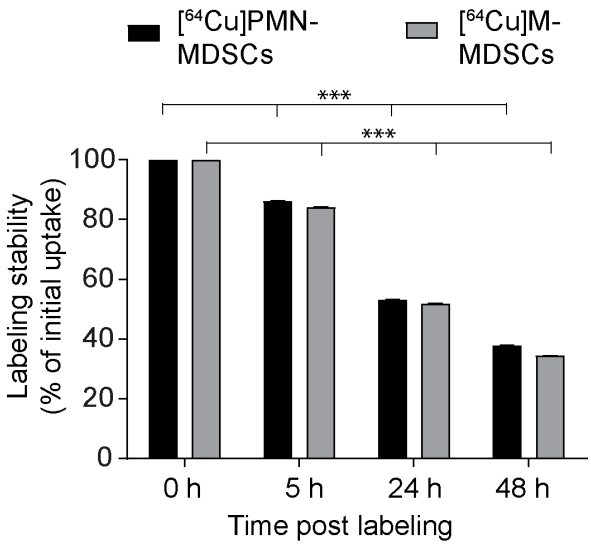

Figure 46: Stability of MDSC radiolabeling with [^{64}Cu]NOTA-anti-CD11b mAb.
In vitro evaluation of [^{64}Cu]NOTA-anti-CD11b mAb-labeling stability in PMN-MDSCs and M-MDSCs 5, 24 and 48 h after radiolabeling measured by γ-counting measured stability of the radiolabel. Data was normalized to the initial uptake at 0 h, respectively (mean ± SEM in percent, n=9, statistics: Dunnett's Multiple Comparison Test with 0 h as control, ***p<0.001).

Cell labeling with a radioactive mAb might compromise cell viability and induce apoptosis, amongst others as a result of DNA double strand breaks. Therefore, viability of and apoptosis induction in [^{64}Cu]PMN- and [^{64}Cu]M-MDSC was assessed by staining with 7-AAD and fluorescently labeled Annexin V while DNA double strand breaks were assessed by immunofluorescence staining for phosphorylated H2AX.

A non-significant decrease of viability in [^{64}Cu]PMN-MDSCs and [^{64}Cu]M-MDSCs after radiolabeling was detected by 7-AAD staining (Figure 47 A). An increase in phosphatidylserine exposition on the cell membrane as an early apoptosis marker could be detected in both radiolabeled [^{64}Cu]PMN-MDSCs (10.22 ± 0.20 %) and [^{64}Cu]M-MDSCs (0.81 ± 1.70 %) at 3 h post radiolabeling normalized to untreated controls by PE-Annexin V staining (Figure 47 B). At 48 h post radiolabeling, an increase in Annexin V-positive [^{64}Cu]M-MDSCs could be detected (2.47 ± 1.28 %) while no further increase was observed in [^{64}Cu]PMN-MDSCs (10.04 ± 0.47 %) (Figure 47 B).

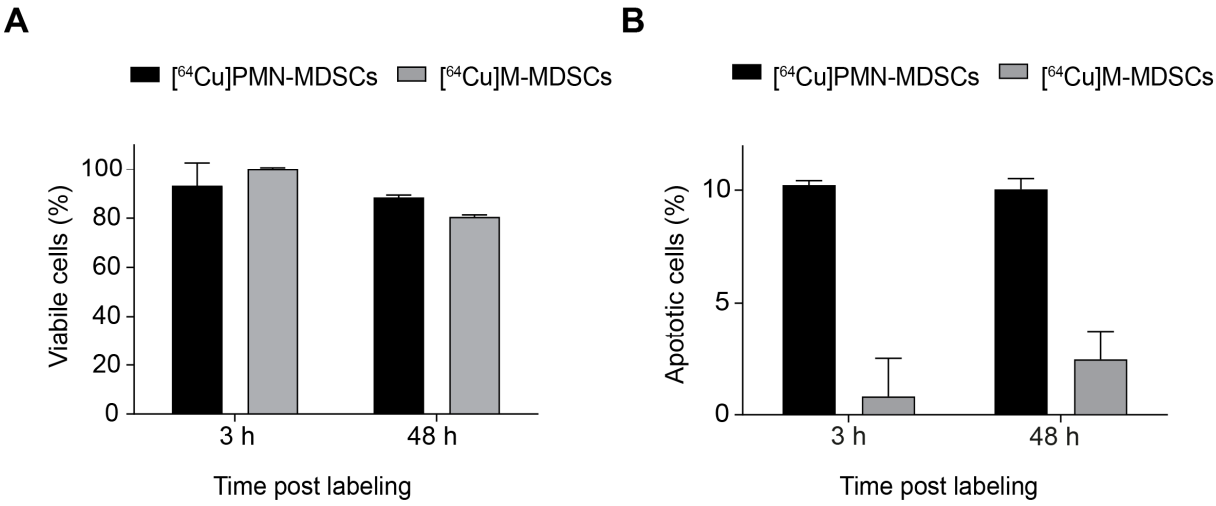

Figure 47: Evaluation of viability and induction of apoptosis in MDSCs after labeling with [^{64}Cu]NOTA-anti-CD11b mAb.

Flow cytometric analysis of viability (**A**) and apoptosis induction (**B**) of PMN- and M-MDSCs 3 and 48 h after labeling with the [^{64}Cu]NOTA-anti-CD11b mAb normalized to unlabeled controls revealed high viability of PMN- and M-MDSCs, and limited apoptosis induction after radiolabeling (mean ± SEM in percent, n=3).

The internalization of ^{64}Cu into the cells lead to radiation-induced DNA double strand breaks in both [^{64}Cu]PMN- and [^{64}Cu]M-MDSCs only at 48 h post radiolabeling, as detected by phosphorylation of the histone H2AX (Figure 48).

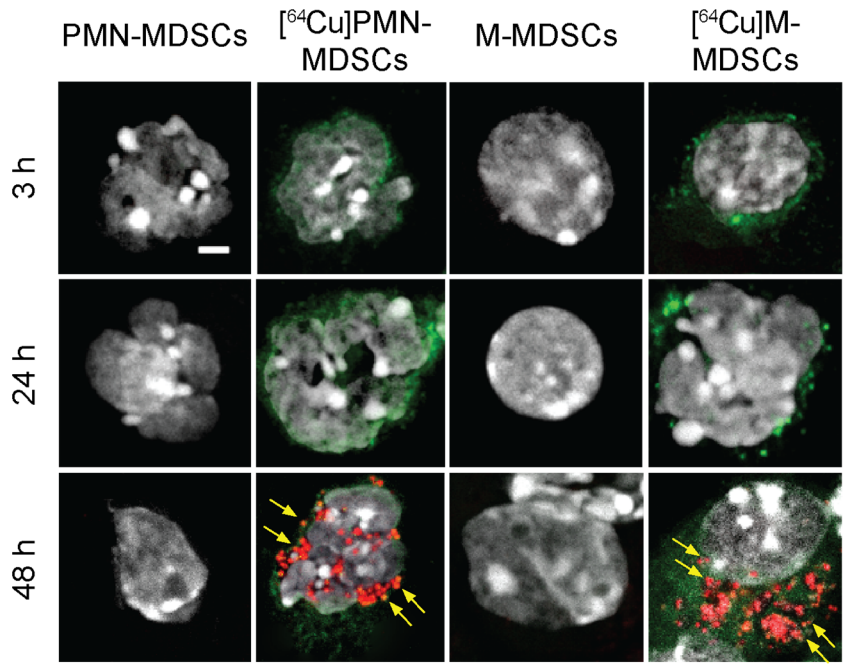

Figure 48: Immunofluorescence staining for DNA double strand breaks in MDSCs after labeling with [^{64}Cu]NOTA-anti-CD11b mAb.

Representative images of immunofluorescence staining for phosphorylated H2AX as early marker for DNA damage at 3, 24 and 48 h after radiolabeling with [^{64}Cu]NOTA-anti-CD11b mAb revealed DNA damage only at 48 h post radiolabeling in [^{64}Cu]PMN- and [^{64}Cu]M-MDSCs while no signs for DNA damage were be detected in unlabeled controls. Yellow arrows indicate phosphorylated H2AX (green – anti-rat mAb, white – DAPI, red - phosphorylated H2AX, scale bar 2 µm).

Suppression of antigen-independent or antigen-dependent T cell proliferation can serve as a measure of MDSC functionality after [^{64}Cu]NOTA-anti-CD11b mAb-labeling. Consequently, the capacity of PMN- and M-MDSCs to suppress antigen-induced T cell proliferation was assessed after labeling with the [^{64}Cu]NOTA-anti-CD11b mAb in comparison to anti-CD11b mAb-labeled and naïve PMN- and M-MDSCs, respectively, as controls.

Labeling with the non-radioactive anti-CD11b mAb did not significantly influence the immunosuppressive capacity of PMN-MDSCs (Figure 49 A) in MDSC:T cell ratios of 1:1 (22.20 ± 1.35 % vs. 25.43 ± 3.91 %), 0.5:1 (29.20 ± 0.24 % vs. 24.70 ± 1.22 %) and 0.25:1 (19.40 ± 3.40 % vs. 21.17 ± 1.52 %) in comparison to unlabeled control PMN-MDSCs. No significant effect on immunosuppressive activity was observed for M-MDSCs labeled with the non-radioactive anti-CD11b mAb in comparison to unlabeled M-MDSCs (Figure 49 B) in MDSC:T cell ratios of 1:1 (29.64 ± 1.52 % vs. 25.83 ± 2.10 %), 0.5:1 (25.56 ± 3.02 % vs. 20.97 ± 1.47 %) and 0.25:1 (21.82 ± 1.75 vs. 19.50 ± 1.34 %).

[^{64}Cu]NOTA-anti-CD11b mAb-labeling did not significantly impair the suppressive activity of PMN-MDSCs (Figure 49 A) in comparison to unlabeled control PMN-MDSCs in MDSC:T cell ratios of 1:1 (23.90 ± 1.50 % vs. 25.43 ± 3.91 %), 0.5:1 (24.25 ± 0.81 % vs. 24.70 ± 1.22 %) and 0.25:1 (18.63 ± 1.73 % vs. 21.17 ± 1.52 %). Likewise, no significant effect of [^{64}Cu]NOTA-anti-CD11b mAb-labeling on the suppressive activity of M-MDSCs (Figure 49 B) was observed in MDSC:T cell ratios of 1:1 (25.44 ± 2.37 % vs. 25.83 ± 2.10 %), 0.5:1 (24.08 ± 1.84 vs. 20.97 ± 1.47 %) and 0.25:1 (20.90 ± 3.01 % vs. 19.50 ± 1.34 %) in comparison to unlabeled control M-MDSCs.

Additionally, naïve PMN- and M-MDSCs, anti-CD11b mAb-labeled PMN- and M-MDSCs as well as [^{64}Cu]NOTA-anti-CD11b mAb-labeled PMN- and M-MDSCs suppressed antigen-induced T cell proliferation significantly in comparison to the T cell control without MDSCs (38.96 ± 1.12 %) ($p<0.001$ for all conditions in comparison to the control).

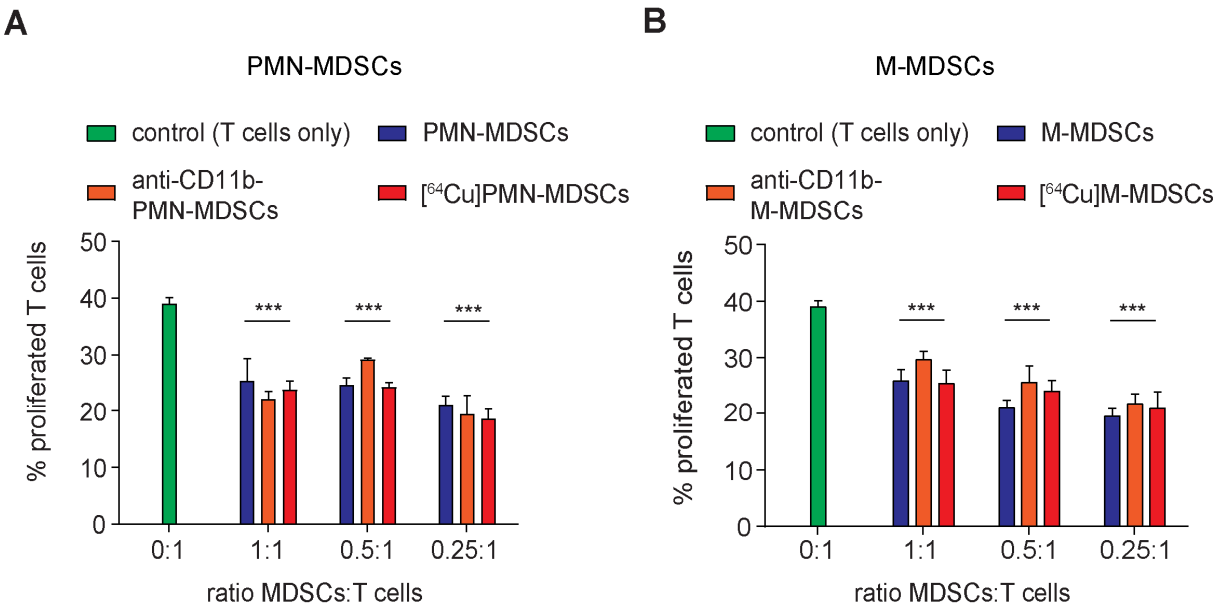

Figure 49: Evaluation of MDSC functionality after radiolabeling with [^{64}Cu]NOTA-anti-CD11b mAb.

Immunosuppression assay with *in vitro* expanded naïve PMN-MDSCs (**A**) and M-MDSCs (**B**), anti-CD11b mAb-labeled PMN-/M-MDSCs and [^{64}Cu]PMN- and [^{64}Cu]M-MDSCs demonstrated no significant loss in immunosuppressive functionality as measured by capacity to inhibit antigen-induced proliferation of CFSE-labeled OT-1 CD8^{+} T cells (mean ± SEM in percent of total T cells, n=4, statistics: Dunnett's Multiple Comparison Test, ***p<0.001).

In summary, radiolabeling of PMN- and M-MDSCs with [^{64}Cu]NOTA-anti-CD11b mAb proved feasible concerning cell viability and functionality, as well as labeling stability, enabling the utilization for *in vivo* cell tracking studies.

4.1.3.2 Tracking of MDSC migration to the primary TME

For the visualization of MDSC distribution and tumor homing *in vivo* with PET imaging, PMN- and M-MDSCs were labeled with 0.74 MBq corresponding to 1.6 µg [^{64}Cu]NOTA-anti-CD11b mAb. Either 2x10^6 [^{64}Cu]PMN- or [^{64}Cu]M-MDSCs were then *i.v.* injected into PyMT tumor- or B16-F10 melanoma-bearing mice. Static 20 min emission PET and T2-weighted anatomical MR scans were acquired 3, 24 and 48 h after adoptive MDSC transfer. In the following paragraphs, obtained results will first be presented for [^{64}Cu]PMN-MDSCs and second for [^{64}Cu]M-MDSCs in chronological order of the imaging time points (3, 24 and 48 h pt).

As control for cell migration experiments, control groups injected with [^{64}Cu]$CuCl_2$ were analyzed. Therefore, PyMT tumor- and B16-F10 melanoma-bearing animals were injected with approximately 0.37 MBq [^{64}Cu]$CuCl_2$ and static 20 min emission PET and T2-weighted anatomical MR scans were acquired 3, 24 and 48 h post injection. These controls will be presented after the results of the MDSC cell tracking experiments in chronological order of the imaging time points (3, 24 and 48 h post injection) and compared to the cell tracking data.

[^{64}Cu]PMN-MDSCs: 3 h post adoptive transfer

The lung, liver and spleen of PyMT tumor-, B16-F10 melanoma-bearing animals, and of naïve control littermates were the primary homing sites of [^{64}Cu]PMN-MDSCs (Figure 50). At this early time point, 3 h pt after [^{64}Cu]PMN-MDSCs injection, the distinctive pattern of uptake in the form of hot spot areas likely corresponding to cells could not be detected (in comparison to e.g. 24 h pt, Figure 51). Quantification of tumor homing was therefore performed by placing a ROI over the whole tumor tissue. The percentage of the adoptively transferred [^{64}Cu]PMN-MDSCs detected in both the primary PyMT breast cancer tumor (1.41 ± 0.11 %ID/cm³) and the B16-F10 melanoma (1.87 ± 0.23 %ID/cm³), however, was not significantly higher than in the calf muscle.

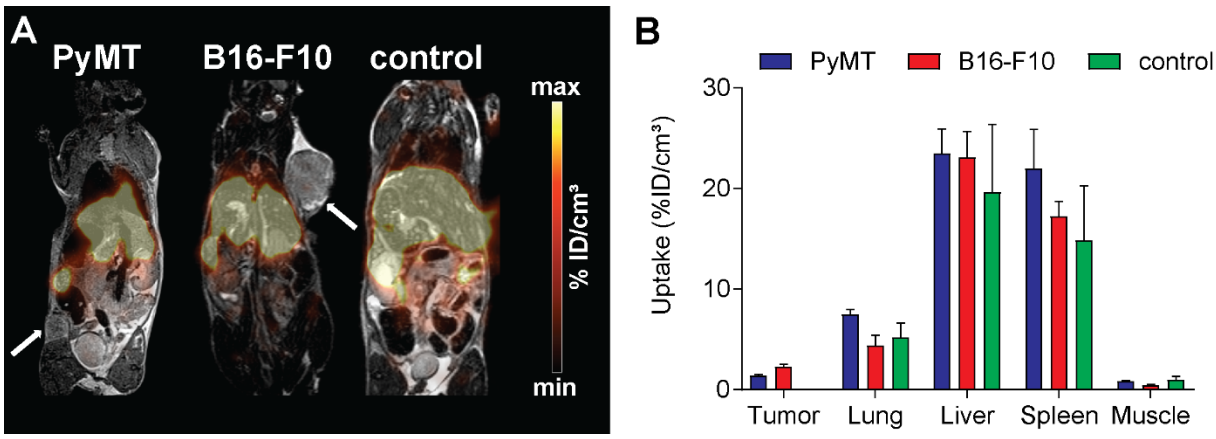

Figure 50: Visualization of the *in vivo* [^{64}Cu]PMN-MDSC distribution in primary tumor-bearing animals at 3 h pt.

Representative PET and MRI scans (**A**) of [^{64}Cu]PMN-MDSCs in primary PyMT breast tumor- (left panel), in primary B16-F10 melanoma-bearing animals (middle panel), and in untreated controls (right panel). Quantification (**B**) of cell distribution at 3 h pt revealed the liver, spleen and lung as early homing sites in all animals (mean ± SEM in %ID/cm³, n=5 for PyMT, n=6 for B16-F10 and n=5 for controls).

[^{64}Cu]PMN-MDSCs: 24 h post adoptive transfer

In comparison to the early imaging time point at 3 h pt, tumor homing of [^{64}Cu]PMN-MDSCs presented in hot spot areas representing the uptake of the cells (Figure 51, white arrows) and an overall increased homing at 24 h pt (Figure 51 B). Furthermore, a significantly higher fraction of [^{64}Cu]PMN-MDSCs could be located in B16-F10 melanomas in comparison to PyMT breast tumors (3.66 ± 0.34 %ID/cm³ vs. 1.67 ± 0.23 %ID/cm³, p<0.01).

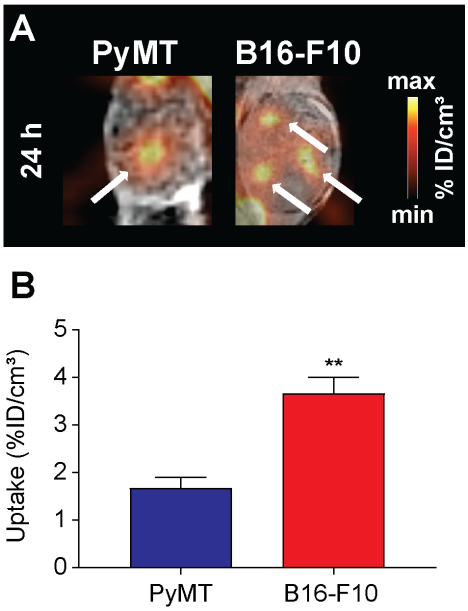

Figure 51: Homing of [^{64}Cu]PMN-MDSCs to the primary PyMT tumor and B16-F10 melanoma at 24 h pt.

Representative PET and MRI scans (**A**) of [^{64}Cu]PMN-MDSC uptake (white arrows) in primary PyMT breast tumors (left panel) and primary B16-F10 melanomas (right panel). Quantification (**B**) of [^{64}Cu]PMN-MDSC tumor homing at 24 h pt (mean ± SEM in %ID/cm³, n=5 for PyMT, n=6 for B16-F10, statistics: Student's t-test, **p<0.01).

The whole-body distribution of [^{64}Cu]PMN-MDSCs at 24 h pt (Figure 52) resembled the early whole-body distribution at 3 h pt: the primary sites of migration besides the primary tumor were still the liver and spleen, however, [^{64}Cu]PMN-MDSC uptake values decreased in all examined organs while tumor uptake was augmented. No significant differences in the whole-body distribution could be detected between the PyMT breast cancer-, the B16-F10 melanoma-bearing animals, and the naïve controls.

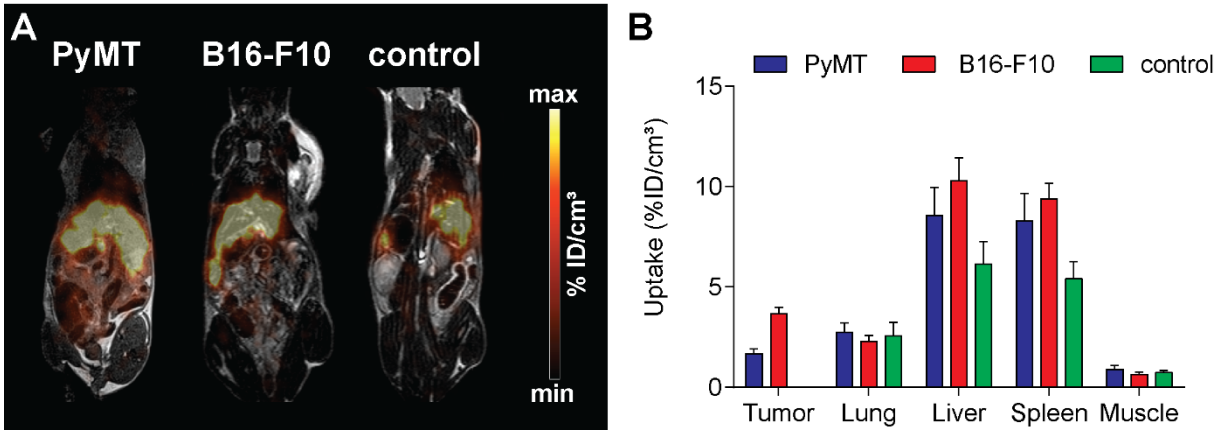

Figure 52: Whole-body distribution of [^{64}Cu]PMN-MDSCs in PyMT breast tumor-, B16-F10 melanoma-bearing mice and controls at 24 h pt.

Representative whole-body PET and MRI scans (**A**) of [^{64}Cu]PMN-MDSC uptake in primary PyMT breast tumor- (left panel), in primary B16-F10 melanoma-bearing (middle panel) animals, and in naïve littermate controls (right panel). Quantification (**B**) of [^{64}Cu]PMN-MDSC distribution at 24 h pt confirmed [^{64}Cu]PMN-MDSC migration to liver and spleen besides tumor homing and partial retention in the lung (mean ± SEM in %ID/cm³, n=5 for PyMT, n=6 for B16-F10 and n=5 for controls).

[^{64}Cu]PMN-MDSCs: 48 h post adoptive transfer

At 48 h pt, overall tumor uptake of [^{64}Cu]PMN-MDSCs was further increased (Figure 53), with significantly enhanced uptake values in the B16-F10 melanoma tumor compared to the PyMT breast tumor (5.66 ± 0.49 %ID/cm³ vs 2.21 ± 0.30 %ID/cm³, $p<0.01$).

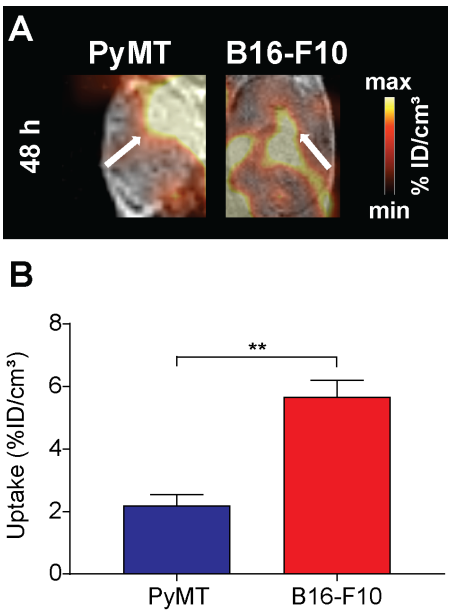

Figure 53: Tumor homing of [^{64}Cu]PMN-MDSCs to the primary PyMT breast tumor and primary B16-F10 melanoma tumor at 48 h pt.
Representative PET and MRI scans (**A**) of [^{64}Cu]PMN-MDSC uptake (white arrows) in primary PyMT breast tumors (left panel) and in primary B16-F10 melanomas (right panel). Quantification (**B**) at 48 h pt (mean ± SEM in %ID/cm³, n=5 for PyMT, n=6 for B16-F10, statistics: Student's t-test, **p<0.01).

Whole-body distribution of [^{64}Cu]PMN-MDSCs did neither change considerably from the 24 h pt imaging time point, nor show differences between PyMT breast tumor and the B16-F10 melanoma tumor in comparison to naïve controls (Figure 54 A). The injected [^{64}Cu]PMN-MDSCs were retained in liver, spleen and in the lungs, the uptake was further reduced in comparison to 24 h pt (Figure 54 B). The *ex vivo* biodistribution (Figure 54 C) confirmed tumor homing of [^{64}Cu]PMN-MDSCs to both the primary PyMT breast tumor and the B16-F10 melanoma. Differences in the image-derived uptake values and uptake values determined by γ-counting might be due to corrections in PET reconstruction, the partial volume effect and the different data evaluation methods with biodistribution analysis in %ID/g. In biodistribution analysis, [^{64}Cu]PMN-MDSC retention in the blood was higher in B16-F10 melanoma-bearing animals in comparison to naïve controls (1.85 ± 0.29 %ID/cm³ vs. 0.63 ± 0.13 %ID/cm³, p<0.05). Additionally, a significantly higher fraction of [^{64}Cu]PMN-MDSCs remained in the lungs of B16-F10 melanoma-bearing animals in comparison to naïve controls (6.78 ± 1.01 %ID/cm³ vs. 3.23 ± 0.92 %ID/cm³, p<0.05). [^{64}Cu]PMN-MDSCs could further be detected in the bone marrow in left tibia and the left femur. Uptake in the kidneys might point towards renal excretion of free copper.

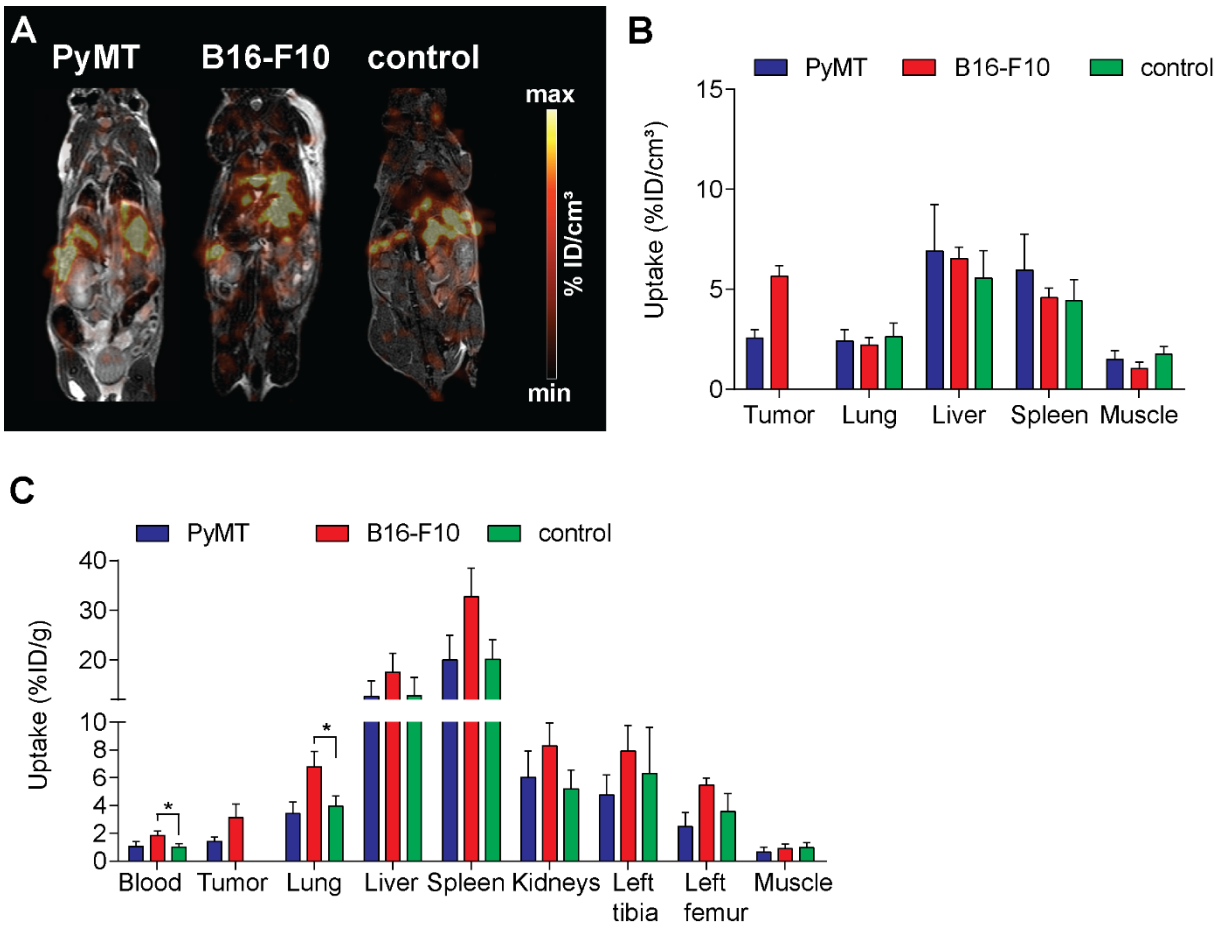

Figure 54: *In vivo* whole-body distribution and *ex vivo* biodistribution of [^{64}Cu]PMN-MDSCs in primary PyMT breast tumor- and primary B16-F10 melanoma-bearing mice at 48 h pt.
Representative whole-body PET and MRI scans (**A**) of [^{64}Cu]PMN-MDSCs in primary PyMT breast tumor- (left panel), in primary B16-F10 melanoma-bearing animals (middle panel), and in naïve controls (right panel). Quantification (**B**) of [^{64}Cu]PMN-MDSC distribution at 48 h pt presented retention of [^{64}Cu]PMN-MDSCs in the lungs, liver and spleen besides the examined tumors (mean ± SEM in %ID/cm³, n=5 for PyMT, n=6 for B16-F10 and n=5 for controls). (**C**) *Ex vivo* biodistribution analysis (γ-counting) confirmed [^{64}Cu]PMN-MDSC uptake in the primary PyMT breast tumor and the primary B16-F10 melanoma (mean ± SEM in %ID/g, n=5 for PyMT, n=6 for B16-F10 and n=5 for controls, statistics: Dunnett's Multiple Comparison Test; control mouse organs served as control for multiple comparisons).

[^{64}Cu]M-MDSCs: 3 h post adoptive transfer

Similar to [^{64}Cu]PMN-MDSCs, the early sites of [^{64}Cu]M-MDSC migration in primary PyMT tumor- and B16-F10 melanoma-bearing mice (Figure 55) were the lungs, liver and spleen. These organs were also the early sites of [^{64}Cu]M-MDSC migration in naïve control littermates (Figure 55). Comparable to [^{64}Cu]PMN-MDSCs, [^{64}Cu]M-MDSC were not strongly recruited to the PyMT primary tumor (1.30 ± 0.08 %ID/cm³) and the B16-F10 melanoma (1.30 ± 0.11 %ID/cm³) at 3 h pt. Additionally, characteristic hot spot areas of MDSC uptake could not yet be detected (in comparison to, e.g., 24 h pt, Figure 56).

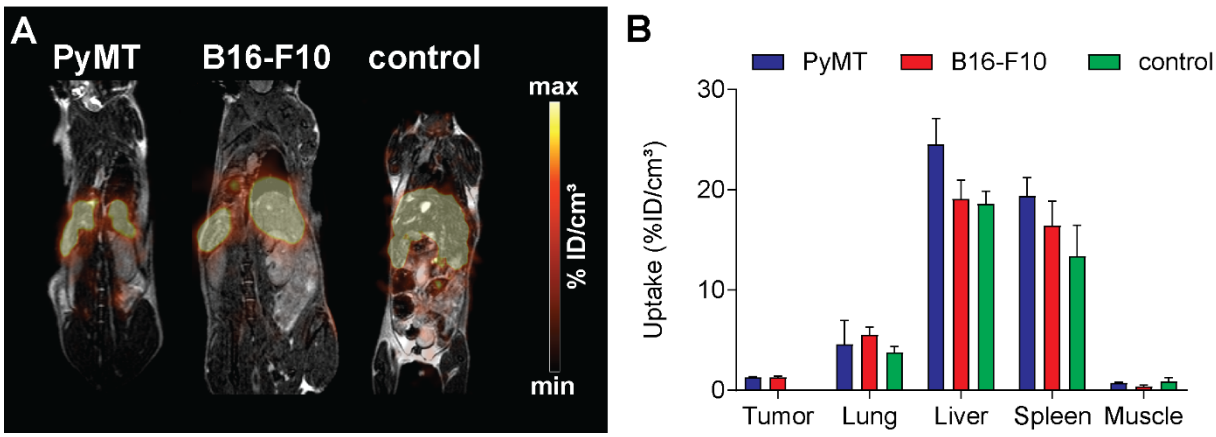

Figure 55: Visualization of the *in vivo* [^{64}Cu]M-MDSC distribution in primary tumor-bearing animals at 3 h pt.

Representative whole-body PET and MRI scans (**A**) of [^{64}Cu]M-MDSCs in primary PyMT breast tumor- (left panel), in primary B16-F10 melanoma-bearing animals (middle panel), and in naïve controls (right panel). Quantification (**B**) of cell distribution at 3 h pt revealed the lung, liver and spleen as early primary homing sites of [^{64}Cu]M-MDSCs in all groups (mean ± SEM in %ID/cm³, n=6 for PyMT, n=5 for B16-F10 and n=5 for controls).

[^{64}Cu]M-MDSCs: 24 h post adoptive transfer

Comparable to [^{64}Cu]PMN-MDSC migration, [^{64}Cu]M-MDSC migration to both primary tumors increased over time after adoptive cell transfer (Figure 56). At 24 h pt, [^{64}Cu]M-MDSC uptake in B16-F10 melanomas was significantly enhanced in comparison to PyMT breast tumors (3.14 ± 0.15 %ID/cm³ vs 1.74 ± 0.29 %ID/cm³, p<0.01, Figure 56 B).

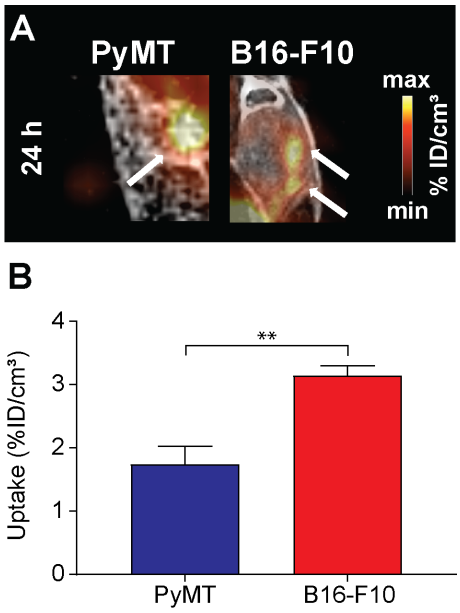

Figure 56: Homing of [^{64}Cu]M-MDSCs to the PyMT breast tumor and B16-F10 melanoma at 24 h pt.

Representative PET and MRI scans (**A**) of [^{64}Cu]M-MDSCs (white arrows) in primary PyMT breast tumor- (left panel) and in primary B16-F10 melanoma-bearing animals (right panel). Quantification (**B**) of [^{64}Cu]M-MDSC tumor homing at 24 h pt revealed increased [^{64}Cu]M-MDSC recruitment to the B16-F10 melanoma in comparison to the PyMT primary breast tumor (mean ± SEM in %ID/cm³, n=6 for PyMT, n=5 for B16-F10, statistics: Students' t-test, ** p<0.01).

Besides the primary tumors, the lungs, liver and spleen retained [^{64}Cu]M-MDSCs (Figure 57). As observed for [^{64}Cu]PMN-MDSCs (Figure 52), the fraction of adoptively transferred [^{64}Cu]M-MDSCs decreased in lungs, liver and spleen of tumor-bearing animals, while tumor homing was increased. No significant differences were observed between migration of [^{64}Cu]M-MDSCs in PyMT breast tumor-, B16-F10 melanoma-bearing animals and naïve controls. Surprisingly, an increase of [^{64}Cu]M-MDSC uptake was detected in the muscle of the control animals.

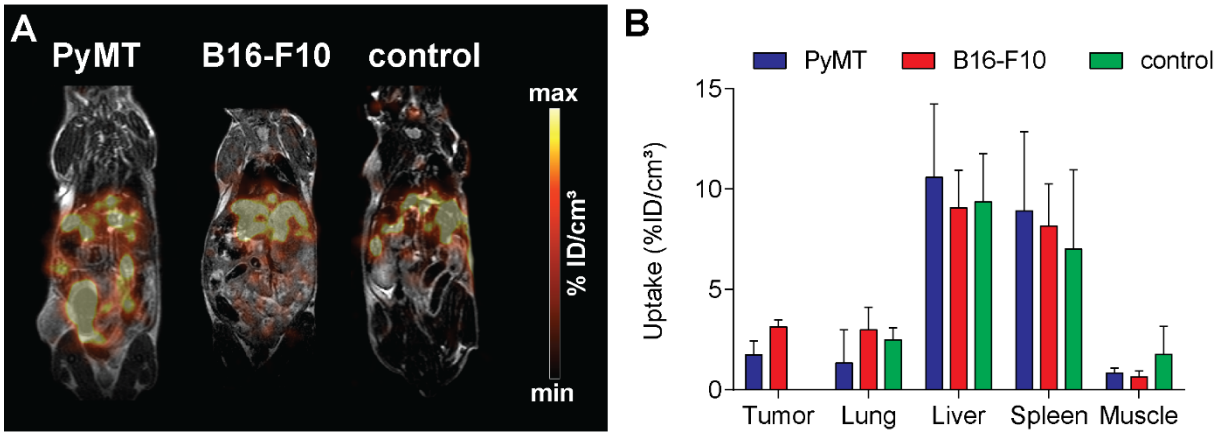

Figure 57: Whole-body distribution of [^{64}Cu]M-MDSCs in primary PyMT breast tumor- and primary B16-F10 melanoma-bearing mice at 24 h pt.
Representative whole-body PET and MRI scans (**A**) of [^{64}Cu]M-MDSCs in PyMT breast tumor- (left panel), in B16-F10 melanoma-bearing animals (middle panel), and in naïve controls (right panel). Quantification (**B**) of cell distribution at 24 h pt showed [^{64}Cu]M-MDSC uptake in the liver and spleen and retention in the lungs of animals of all groups (mean ± SEM in %ID/cm³, n=6 for PyMT, n=5 for B16-F10 and n=5 controls).

[^{64}Cu]M-MDSCs: 48 h post adoptive cell transfer

In vivo [^{64}Cu]M-MDSC tumor homing was further enhanced at 48 h pt in comparison to the earlier timepoints. Differences between the [^{64}Cu]M-MDSC cell uptake in the primary PyMT breast tumor and the primary B16-F10 melanoma tumor, however, did not show any significant differences (Figure 58).

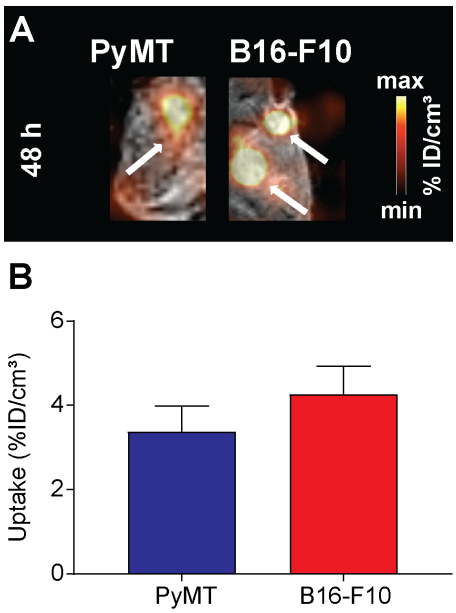

Figure 58: Tumor homing of [^{64}Cu]M-MDSCs to the primary PyMT tumor and B16-F10 melanoma at 48 h pt.

Representative PET and MRI scans (**A**) of [^{64}Cu]M-MDSCs (white arrows) in primary PyMT breast tumors (left panel) and in primary B16-F10 melanoma tumors (right panel). Quantification (**B**) of [^{64}Cu]M-MDSC tumor homing at 48 h pt revealed a tendency towards increased [^{64}Cu]M-MDSC recruitment to the primary B16-F10 melanoma in comparison to the primary PyMT breast tumor (mean ± SEM in %ID/cm³, n=6 for PyMT, n=5 for B16-F10).

Similar to [^{64}Cu]PMN-MDSCs, [^{64}Cu]M-MDSCs were retained in the lungs, liver and spleen at 48 h pt (Figure 59 B), and total cell uptake values declined in the individual organs compared to the 24 h time point. The *ex vivo* biodistribution analysis (γ-counting, Figure 59 C) confirmed [^{64}Cu]M-MDSC tumor uptake as well as cell uptake in the lungs, liver and spleen. Differences in the image-derived uptake values and uptake values determined by γ-counting might be due to corrections in PET reconstruction, partial volume effects and the different data evaluation methods with biodistribution analysis in %ID/g. A higher fraction of [^{64}Cu]M-MDSCs was retained in the blood of PyMT breast tumor-bearing animals in comparison to naïve controls (1.61 ± 0.12 %ID/cm³ vs. 0.79 ± 0.27 %ID/cm³, $p<0.05$). Additional sites of cell migration were the bone marrow in left tibia and left femur. Radioactivity detected in the kidneys of tumor-bearing animals and controls might point to renal excretion of free ^{64}Cu.

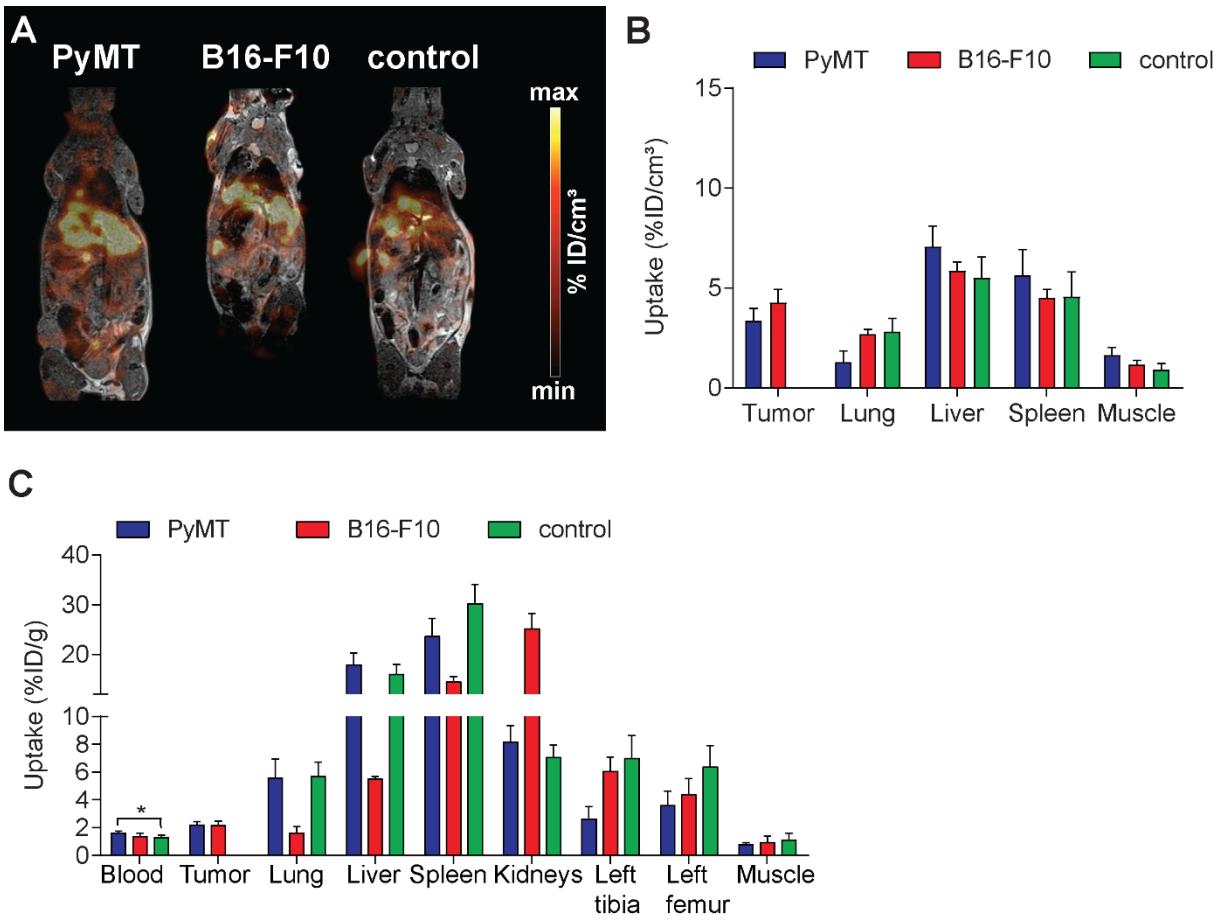

Figure 59: *In vivo* whole-body distribution and *ex vivo* biodistribution of [^{64}Cu]M-MDSCs in primary PyMT breast tumor- and in primary B16-F10 melanoma-bearing mice at 48 h pt.

Representative whole-body PET and MRI scans (**A**) of [^{64}Cu]M-MDSCs in primary PyMT breast tumor- (left panel), in primary B16-F10 melanoma-bearing animals (middle panel), and in naïve controls (right panel). Quantification (**B**) of cell distribution at 48 h pt showed [^{64}Cu]M-MDSC uptake in the lung, liver and spleen of animals of all groups (mean ± SEM in %ID/cm³, n=6 for PyMT, n=5 for B16-F10 and n=5 controls). *Ex vivo* biodistribution analysis (**C**) by γ-counting confirmed [^{64}Cu]M-MDSC tumor homing as well as cell uptake in the lungs, liver and spleen (mean ± SEM in %ID/g, n=6 for PyMT, n=5 for B16-F10 and n=5 controls, statistics: Dunnett's Multiple Comparison Test, *p<0.05).

[^{64}Cu]CuCu$_2$ controls

As control for *in vivo* imaging of [^{64}Cu]PMN- and [^{64}Cu]M-MDSC migration, primary PyMT tumor- or primary B16-F10 melanoma-bearing mice were injected with approximately 0.37 MBq [^{64}Cu]CuCl$_2$. Naïve littermates served as controls. Static 20 min emission PET and T2-weighted anatomical MR scans were acquired 3, 24 and 48 h post injection.

At 3 h post injection, the main organ of [^{64}Cu]CuCl$_2$ uptake was the liver of tumor-bearing animals and naïve controls (Figure 60). A weak PET-signal was detected in the primary PyMT breast tumor as well as the primary B16-F10 melanoma tumor. Further, an unspecific PET-signal could be located to the intestine of the experimental animals in all groups indicating hepatobiliary excretion of [^{64}Cu]CuCl$_2$ (Figure 60 A). Image-derived quantification at 3 h post injection confirmed [^{64}Cu]CuCl$_2$ uptake in the liver and primary tumors and revealed the lungs and spleen as sites of minor [^{64}Cu]CuCl$_2$ uptake (Figure 60 B).

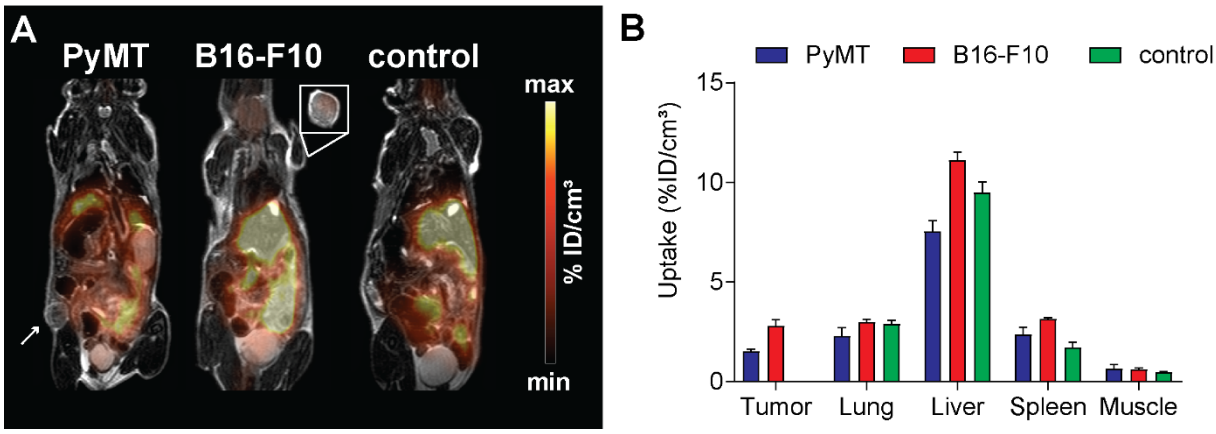

Figure 60: *In vivo* whole-body distribution of [^{64}Cu]CuCl$_2$ in PyMT breast tumor-, B16-F10 melanoma-bearing and naïve control mice at 3 h post injection.
Representative whole-body PET and MRI scans (**A**) of [^{64}Cu]CuCl$_2$ distribution in primary PyMT breast tumor- (left panel, white arrow), in primary B16-F10 melanoma-bearing animals (middle panel, white box with image section), and in naïve controls (right panel). Quantification (**B**) showed [^{64}Cu]CuCl$_2$ uptake mainly in the liver and spleen and in the lungs in all groups (mean ± SEM in %ID/cm³, n=3 for PyMT, n=3 for B16-F10 and n=3 for controls).

At 24 h post injection, tumor uptake of [^{64}Cu]CuCl$_2$ declined in both the PyMT primary breast tumor as well as the B16-F10 primary melanoma compared to the early time point at 3 h post injection (Figure 61 A). This decline of [^{64}Cu]CuCl$_2$ tumor uptake (Figure 61 B) was in direct contrast to the tumor homing of [^{64}Cu]PMN- and [^{64}Cu]M-MDSCs with increasing uptake values over the imaging time points indicating cell migration in the cell tracking experiments. [^{64}Cu]CuCl$_2$ was mainly retained in the liver of PyMT tumor-, B16-F10 melanoma-bearing and control animals at 24 h post injection. Further retention of [^{64}Cu]CuCl$_2$ was detected in the lungs and spleen as sites of minor uptake in the examined groups.

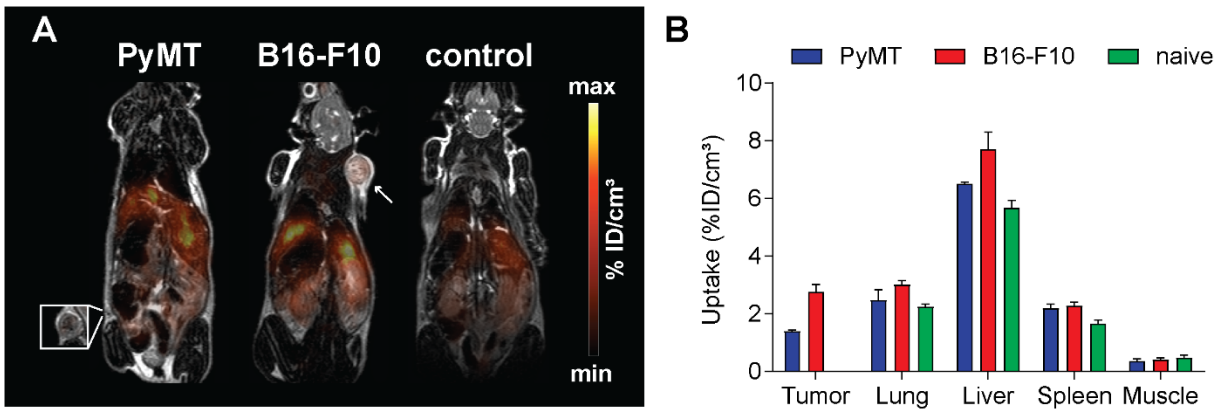

Figure 61: *In vivo* distribution of [^{64}Cu]$CuCl_2$ in primary PyMT breast tumor-, primary B16-F10 melanoma-bearing and naïve control mice at 24 h post injection.

Representative whole-body PET and MRI scans (**A**) of [^{64}Cu]$CuCl_2$ distribution in primary PyMT breast tumor- (left panel, white box with image section), primary B16-F10 melanoma-bearing animals (middle panel, white arrow) and naïve controls (right panel). Quantification (**B**) showed [^{64}Cu]$CuCl_2$ retention mainly in the liver but also in the lungs and the spleen in all groups while tumor uptake declined (mean ± SEM in %ID/cm³, n=3 for PyMT, n=3 for B16-F10 and n=3 controls).

In comparison to the earlier imaging time points at 3 and 24 h post injection, tumor uptake of [^{64}Cu]$CuCl_2$ declined further at 48 h post injection (Figure 62 A). The liver of tumor-bearing animals and naïve controls remained the organ with the highest uptake values of [^{64}Cu]$CuCl_2$ while the lungs and spleen as sites of minor uptake had retained [^{64}Cu]$CuCl_2$ in all examined groups comparably. In the image-derived quantification (Figure 62 B), muscle tissue is given as a reference. The *ex vivo* biodistribution analysis (γ-counting, Figure 62 C) confirmed the *in vivo* imaging data. In comparison to the image-derived quantification, blood, kidneys, left tibia and the femur were added to γ-counting analysis, as it was done for the cell tracking experiments and did show uptake of [^{64}Cu]$CuCl_2$. Interestingly, the kidneys showed high uptake values comparable to the liver in the biodistribution analysis. This indicated a partial renal elimination of [^{64}Cu]$CuCl_2$ - independent of the treatment group.

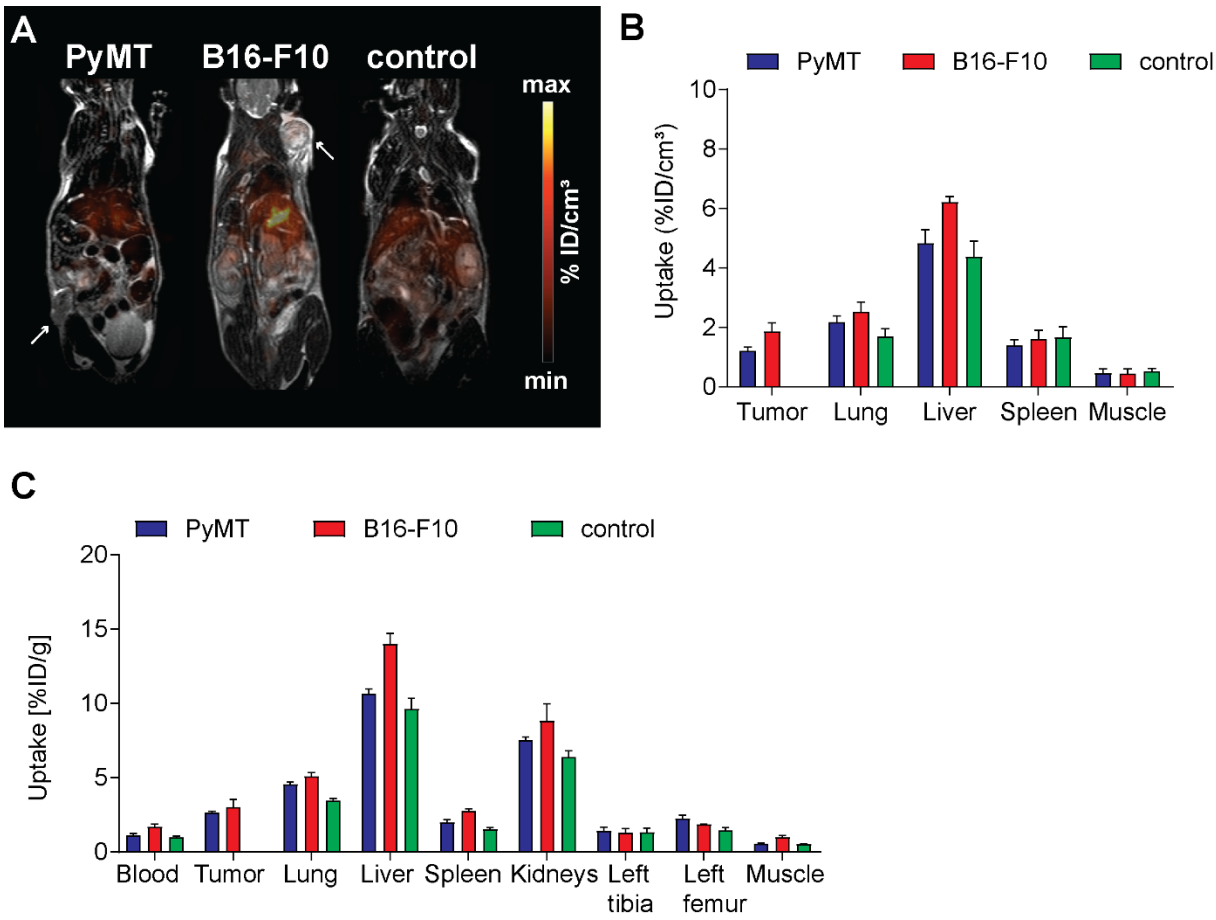

Figure 62: *In vivo* whole-body distribution and *ex vivo* biodistribution of [^{64}Cu]$CuCl_2$ in primary PyMT breast tumor-, primary B16-F10 melanoma-bearing and naïve control mice at 48 h post injection.

Representative whole-body PET and MRI scans (**A**) of [^{64}Cu]$CuCl_2$ distribution in primary PyMT breast tumor- (left panel, white arrow), in primary B16-F10 melanoma-bearing (middle panel, white arrow), and in naïve control animals (right panel). Quantification (**B**) showed [^{64}Cu]$CuCl_2$ retention mainly in the liver but also in lungs and spleen in all groups while tumor uptake declined further. *Ex vivo* biodistribution analysis (γ-counting, **C**) confirmed [^{64}Cu]$CuCl_2$ uptake in the primary tumors of tumor-bearing animals but mainly in the liver and kidney of tumor-bearing animals and naïve controls (mean ± SEM in %ID/cm³ and mean ± SEM in %ID/g, n=3 for PyMT, n=3 for B16-F10 and n=3 for controls).

A direct comparison between the *in vivo* [^{64}Cu]PMN- and [^{64}Cu]M-MDSC cell tracking data and [^{64}Cu]$CuCl_2$ uptake in the primary PyMT breast cancer tumor model (Figure 63, left panel) and the primary B16-F10 melanoma model (Figure 63, right panel) was drawn to compare the temporal dynamics of MDSC migration and [^{64}Cu]$CuCl_2$ uptake. This direct comparison of [^{64}Cu]PMN-MDSC tumor homing and [^{64}Cu]$CuCl_2$ tumor uptake revealed differences in the uptake kinetics: as expected, [^{64}Cu]PMN-MDSC tumor homing increased over the imaging time period of 48 h pt while tumor uptake of [^{64}Cu]$CuCl_2$ had reached the highest values at 3 h post injection and subsequently decreased over 48 h post injection (Figure 63).

At 3 h pt, [^{64}Cu]PMN-MDSC uptake was significantly higher in the liver (23.50 ± 1.98 %ID/cm³ vs. 7.53 ± 0.45 %ID/cm³, $p<0.01$) and spleen (22.01 ± 3.17 %ID/cm³ vs. 2.36 ± 0.29 %ID/cm³, $p<0.01$) of PyMT breast tumor-bearing animals (Figure 63 A, left panel) and in the liver (23.08

± 2.37 %ID/cm³ vs. 11.11 ± 0.33 %ID/cm³, p<0.05) and spleen (17.26 ± 1.32 %ID/cm³ vs. 3.14 ± 0.05 %ID/cm³, p<0.001) of B16-F10 melanoma-bearing animals (Figure 63 A, right panel) compared to the respective tumor-bearing control animals injected with [^{64}Cu]$CuCl_2$. Tumor uptake of [^{64}Cu]PMN-MDSCs, however, was significantly lower than uptake of [^{64}Cu]$CuCl_2$ in the B16-F10 melanoma model (1.87 ± 0.23 %ID/cm³ vs. 2.79 ± 0.24 %ID/cm³, p<0.05). At 24 h pt, [^{64}Cu]PMN-MDSC uptake in the spleen remained higher than [^{64}Cu]$CuCl_2$ uptake in both the PyMT breast tumor model (8.28 ± 1.24 %ID/cm³ vs. 2.18 ± 0.12 %ID/cm³, p<0.05, Figure 63 B, left panel) and the B16-F10 melanoma model (9.39 ± 0.70 %ID/cm³ vs. 2.28 ± 0.11 %ID/cm³, p<0.001, Figure 63 B, right panel). At the last imaging time point at 48 h pt (Figure 63 C, right panel), a significantly higher uptake of [^{64}Cu]PMN-MDSCs was detected in the primary B16-F10 melanoma tumor (5.66 ± 0.49 %ID/cm³ vs. 1.85 ± 0.25 %ID/cm³, p<0.01) and in the spleen (4.61 ± 0.44 %ID/cm³ vs. 1.61 ± 0.23 %ID/cm³, p<0.01) of B16-F10 melanoma-bearing mice in comparison to B16-F10 melanoma-bearing animals that were injected with [^{64}Cu]$CuCl_2$ as control.

The same was observed for [^{64}Cu]M-MDSCs: tumor homing of [^{64}Cu]M-MDSCs increased over 48 h pt while tumor uptake of [^{64}Cu]$CuCl_2$ had reached the peak values at 3 h post injection and subsequently decreased (Figure 63). At 3 h pt, [^{64}Cu]M-MDSC uptake in the liver (24.55 ± 2.35 %ID/cm³ vs. 7.53 ± 0.45 %ID/cm³, p<0.01) and spleen (19.42 ± 1.64 %ID/cm³ vs. 2.36 ± 0.29 %ID/cm³, p<0.001) were significantly higher in comparison to [^{64}Cu]$CuCl_2$ uptake in PyMT breast tumor-bearing mice (Figure 63 A, left panel). This was also the case for spleen uptake (16.47 ± 2.14 %ID/cm³ vs. 3.14 ± 0.06 %ID/cm³, p<0.01) in B16-F10 melanoma-bearing animals (Figure 63 A, right panel). Moreover, the uptake of [^{64}Cu]$CuCl_2$ was significantly higher in B16-F10 melanoma tumors compared to [^{64}Cu]M-MDSCs (2.79 ± 0.24 %ID/cm³ vs. 1.30 ± 0.11 %ID/cm³, p<0.01) at 3 h post injection. The previously observed higher uptake of [^{64}Cu]M-MDSCs than [^{64}Cu]$CuCl_2$ in the spleen of PyMT breast tumor-bearing animals (8.92 ± 3.64 %ID/cm³ vs. 2.19 ± 0.12 %ID/cm³, p<0.05, Figure 63 B, left panel) and B16-F10 melanoma-bearing animals (8.15 ± 0.85 %ID/cm³ vs. 2.28 ± 0.11 %ID/cm³, p<0.01, Figure 63 B, right panel) was further retained at 24 h pt. Interestingly, at 48 h pt, tumor uptake of [^{64}Cu]M-MDSCs was significantly higher in comparison to [^{64}Cu]$CuCl_2$ uptake in PyMT breast cancer tumors (3.38 ± 0.56 %ID/cm³ vs. 1.20 ± 0.11 %ID/cm³, p<0.05) and B16-F10 melanoma tumors (4.26 ± 0.61 %ID/cm³ vs. 1.85 ± 0.25 %ID/cm³, p<0.05, Figure 63 C, right panel). Retention of [^{64}Cu]M-MDSCs in the spleen of B16-F10 melanoma-bearing animals resulted in significantly higher uptake values at 48 h pt in comparison to [^{64}Cu]$CuCl_2$ uptake (4.52 ± 0.35 %ID/cm³ vs. 1.61 ± 0.23 %ID/cm³, p<0.01, Figure 63 C, right panel).

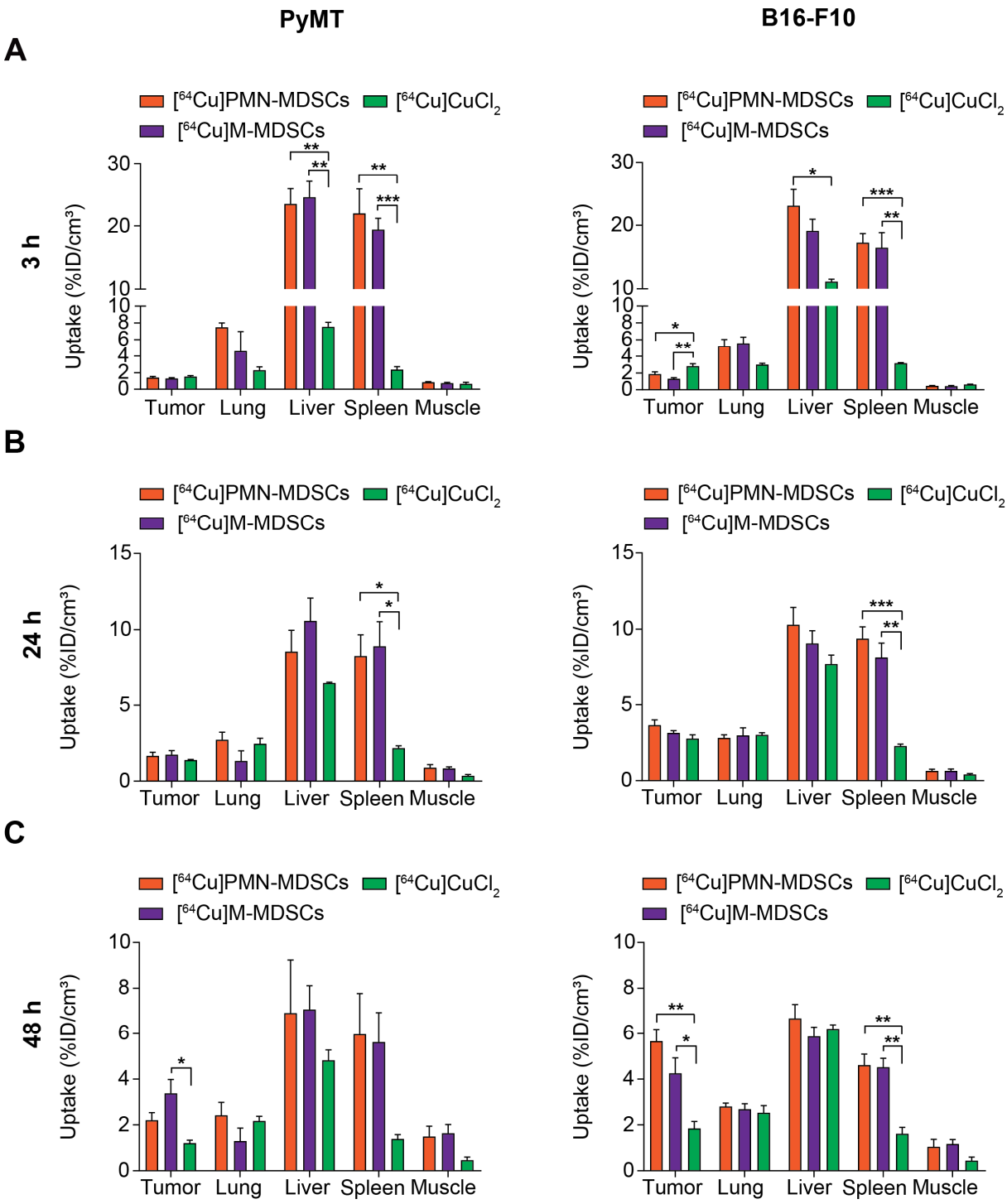

Figure 63: Comparison of the *in vivo* uptake of [^{64}Cu]PMN-MDSCs, [^{64}Cu]M-MDSCs and [^{64}Cu]$CuCl_2$ in the PyMT breast cancer and B16-F10 melanoma model.

Quantification of [^{64}Cu]PMN-MDSC migration, [^{64}Cu]M-MDSC migration and [^{64}Cu]$CuCl_2$ uptake in the primary PyMT breast tumor model (left panel) and the B16-F10 melanoma model (right panel) at 3 h (**A**), 24 h (**B**) and 48 h (**C**) post injection elucidated differential kinetics of [^{64}Cu]PMN-MDSC and [^{64}Cu]M-MDSC homing and [^{64}Cu]$CuCl_2$ uptake in the examined primary tumors (mean ± SEM in %ID/cm³, [^{64}Cu]PMN-MDSC: n=5 for PyMT and n=6 for B16-F10, n=3 for [^{64}Cu]$CuCl_2$, statistics: Dunnett's Multiple Comparison Test, *p<0.05, **p<0.01, ***p<0.001; organs of respective tumor-bearing animals injected with [^{64}Cu]$CuCl_2$ served as control for multiple comparisons).

Ex vivo histological validation of the MDSC tracking data

For the *ex vivo* validation of the *in vivo* MDSC cell tracking data acquired by PET imaging, formalin-fixed, paraffin-embedded primary PyMT breast cancer tumors and primary B16-F10 melanoma tumors were used for histological immunofluorescence stainings to confirm [^{64}Cu]PMN- or [^{64}Cu]M-MDSC infiltration in the tumor tissue (Figure 64). As immunohistochemical staining for MDSCs is not feasible due to the lack of a MDSC-specific cell surface marker or CD marker, adoptively transferred MDSCs were detected in the tumor tissues by means of the internalized rat anti-mouse anti-CD11b mAb.

Both adoptively transferred PMN- and M-MDSCs could be detected in PyMT breast cancer tumors (Figure 64, upper panel) while only adoptively transferred M-MDSCs were detected in B16-F10 melanoma tumors (Figure 64, lower panel) due to technical difficulties (discussed in detail in the discussion, section 5). Independent of the MDSC subpopulation and the tumor type, adoptively transferred MDSCs were detected in clusters. This clustering of cells was already seen in the *in vivo* PET data, where the cell clusters correspond to hot spots of radioactivity.

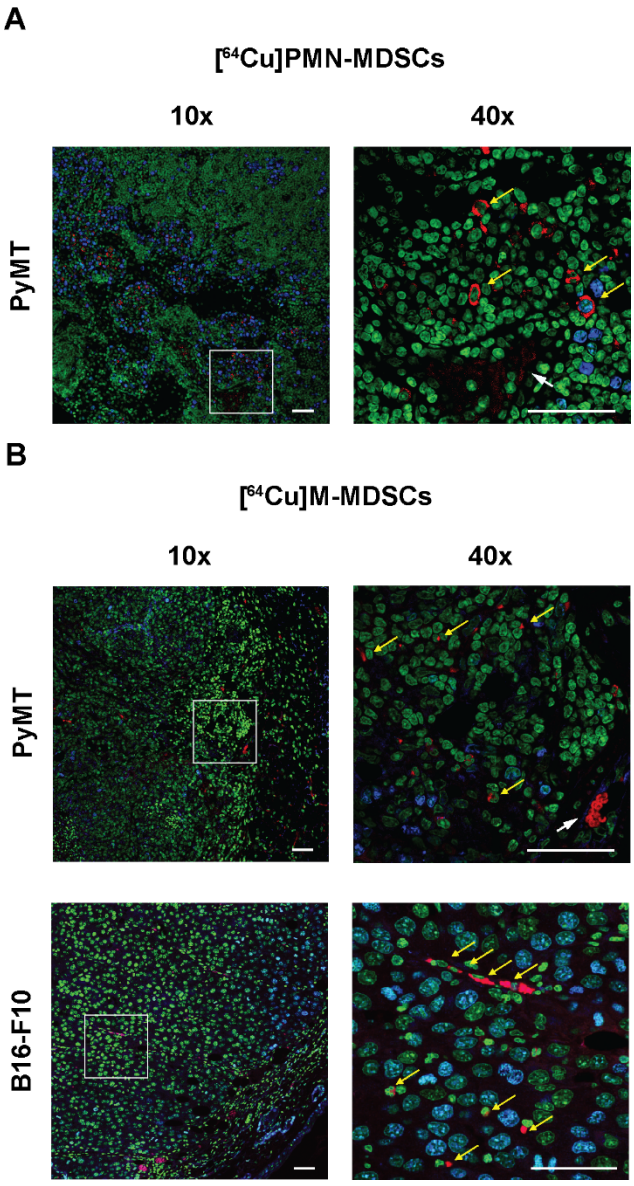

Figure 64: Immunofluorescence staining confirmed the *in vivo* cell tracking data and tumor homing of [^{64}Cu]PMN- and [^{64}Cu]M-MDSCs.

Representative immunofluorescence staining of PyMT breast tumors and B16-F10 melanoma tumors after adoptive transfer of [^{64}Cu]PMN-MDSCs (**A**) or [^{64}Cu]M-MDSCs (**B**), respectively, confirmed that the *in vivo* PET-signal in primary PyMT breast tumors and primary B16-F10 melanoma tumors was derived from adoptively transferred [^{64}Cu]PMN-MDSCs or [^{64}Cu]M-MDSCs (yellow arrows indicate MDSCs, blue - Ki-67, green – YO-PRO nuclear dye, red – anti-rat mAb, scale bars 50 µm).

The structure of the PyMT tumor depicted in Figure 64 A indicated the presence of high endothelial venules (HEVs) that are usually found in secondary lymphoid organs where they enable direct crossing of circulating lymphocytes into the lymph node. To further investigate the presence of HEVs in the PyMT breast cancer tumor, consecutive paraffin slices were stained with hematoxylin and eosin (H&E) for anatomical reference and with anti-peripheral node addressin (PNAd) (Figure 65).

Both, the anatomical structure (H&E staining, Figure 65 A), as well as the positive staining for PNAd in the tumor blood vessels indicated the presence of a lymphoid structure (Figure 65 B) that might have enabled MDSC migration into the primary PyMT breast cancer tumor.

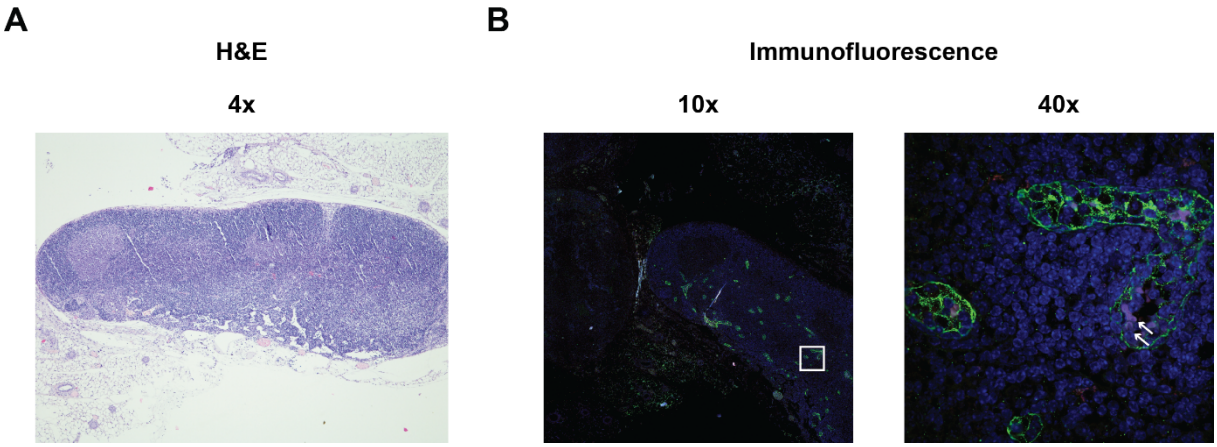

Figure 65: Immunofluorescence staining for the expression of PNAd in a PyMT tumor sample.
H&E staining (**A**) for anatomical and structural tissue reference and (**B**) staining for the expression of PNAd as marker for HEVs in the PyMT tumor (white arrows indicate erythrocytes, green – PNAd, blue - DAPI for DNA staining, red – anti-rat mAb).

4.1.3.3 Tracking of MDSC migration to the metastatic TME

In comparison to the distribution and primary tumor homing of MDSCs *in vivo*, MDSC migration and homing to established metastases was examined in a second step. Therefore, PMN- and M-MDSCs were labeled with 0.74 MBq corresponding to 1.6 µg [^{64}Cu]NOTA-anti-CD11b mAb. PyMT breast cancer metastases- or B16-F10 melanoma metastases-bearing mice identified by bioluminescence OI received an adoptive cell transfer of either 2x10^6 [^{64}Cu]PMN- or [^{64}Cu]M-MDSCs via *i.v.* injection. Static 20 min emission PET and T2-weighted anatomical MR scans were acquired 3, 24 and 48 h after MDSC injection. The results will be presented first for [^{64}Cu]PMN-MDSCs and second for [^{64}Cu]M-MDSCs in chronological order of the imaging time points.

[^{64}Cu]PMN-MDSC: 3 h post adoptive cell transfer

As early as 3 h pt (Figure 66), [^{64}Cu]PMN-MDSC migration to B16-F10 melanoma lung metastases was significantly enhanced compared to PyMT breast cancer lung metastases (8.29 ± 0.52 %ID/cm³ vs. 2.73 ± 0.79 %ID/cm³, p<0.01).

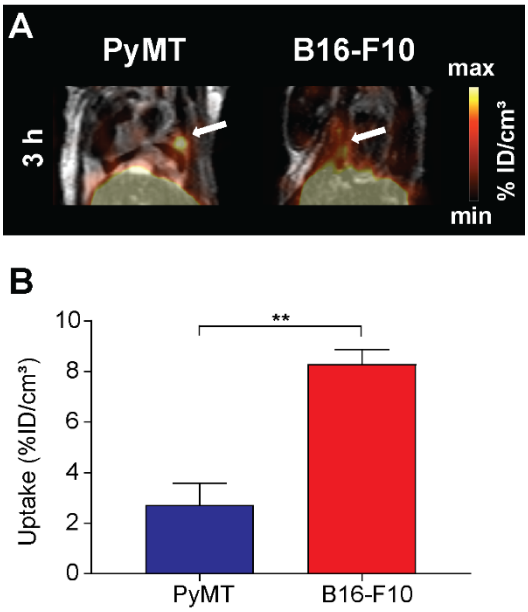

Figure 66: Early homing of [^{64}Cu]PMN-MDSCs to established PyMT breast cancer and B16-F10 melanoma lung metastatic lesions.
Representative PET and MRI scans (**A**) of the lungs of PyMT breast cancer metastases- (left panel) and B16-F10 melanoma metastases-bearing animals (right panel). Quantification (**B**) of [^{64}Cu]PMN-MDSC uptake in the metastatic lesions revealed enhanced [^{64}Cu]PMN-MDSC uptake (white arrows) in the B16-F10 melanoma metastases in comparison to PyMT breast cancer metastases as early as 3 h pt (mean ± SEM in %ID/cm³, n=7 for PyMT, n=6 for B16-F10, statistics: Student's t-test, **p<0.01).

Comparable to the respective primary tumor models (refer to section 4.1.3.2), early sites of [^{64}Cu]PMN-MDSC migration in the metastasis models were the liver and spleen (Figure 67). Lung metastatic lesions had higher uptake values for [^{64}Cu]PMN-MDSCs in the B16-F10

melanoma model when compared to healthy lung tissue. At this early imaging time point, the opposite was the case for the PyMT breast cancer metastasis model. In comparison to naïve controls, [^{64}Cu]PMN-MDSC uptake in the liver of B16-F10 melanoma metastases-bearing animals was significantly enhanced (38.35 ± 4.70 %ID/cm³ vs. 19.66 ± 6.02 %ID/cm³, p<0.05).

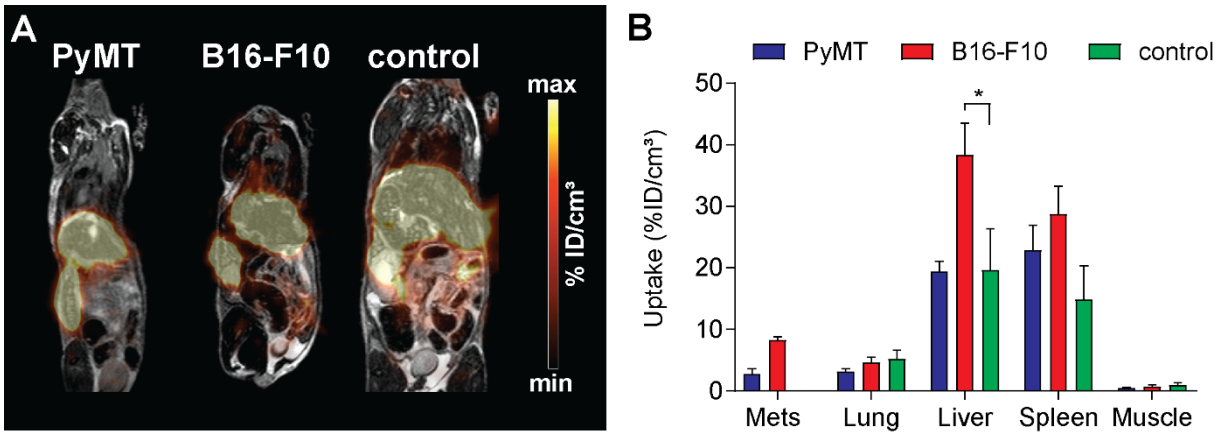

Figure 67: [^{64}Cu]PMN-MDSC whole-body distribution in PyMT breast cancer metastases-, B16-F10 melanoma metastases-bearing animals, and naïve controls at 3 h pt.
Representative whole-body PET and MRI scans (**A**) of PyMT breast cancer metastases- (left panel), B16-F10 melanoma metastases-bearing animals (middle panel) and naïve controls (right panel). Quantification (**B**) revealed lung metastases (denoted mets), healthy lung tissue (denoted lung), the liver and the spleen as early sites of [^{64}Cu]PMN-MDSC migration at 3 h pt (mean ± SEM in %ID/cm³, n=7 for PyMT, n=6 for B16-F10, n=5 for control, statistics: Dunnett's Multiple Comparison Test, *p<0.05; organs of control mice served as control for multiple comparison).

[^{64}Cu]PMN-MDSCs: 24 h post adoptive cell transfer

At 24 h pt (Figure 68), [^{64}Cu]PMN-MDSC uptake in PyMT breast cancer lung metastatic lesions was further enhanced while uptake in B16-F10 melanoma lung metastatic lesions did not change considerably in comparison to 3 h pt. Still, [^{64}Cu]PMN-MDSC uptake in B16-F10 melanoma metastases was significantly higher than to PyMT breast cancer metastases (8.22 ± 0.93 %ID/cm³ vs. 4.16 ± 0.73 %ID/cm³, p<0.05).

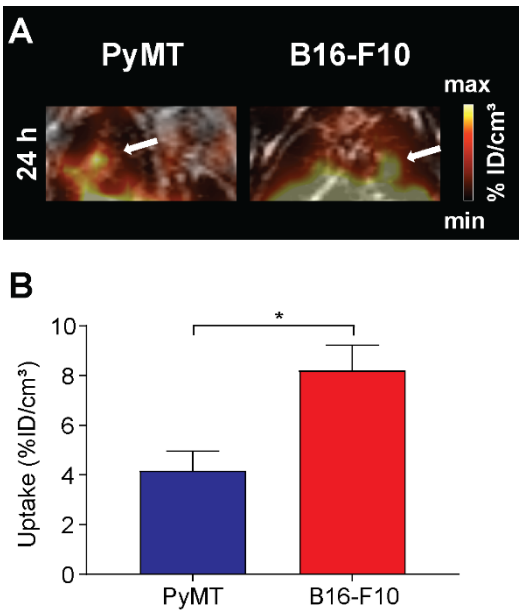

Figure 68: Homing of [^{64}Cu]PMN-MDSCs to established PyMT breast cancer and B16-F10 melanoma metastatic lesions in the lungs 24 h pt.
Representative PET and MRI scans (**A**) of the lungs of PyMT breast cancer metastases- (left panel) and B16-F10 melanoma metastases-bearing animals (right panel). Quantification (**B**) of [^{64}Cu]PMN-MDSC uptake in the metastatic lesions revealed higher [^{64}Cu]PMN-MDSC uptake (white arrows) in the B16-F10 melanoma metastases than in the PyMT breast cancer metastases at 24 h pt (mean ± SEM in %ID/cm³, n=7 for PyMT, n=6 for B16-F10, statistics: Student's t-test, *p<0.05).

Besides the lung metastases, the liver and spleen remained sites of [^{64}Cu]PMN-MDSC migration at 24 h pt (Figure 69), although with decreased values compared to 3 h pt. Further, the lungs retained [^{64}Cu]PMN-MDSCs. [^{64}Cu]PMN-MDSC uptake was higher in both PyMT breast cancer and B16-F10 lung metastatic lesions than in healthy lung tissue. Additionally, a significantly higher fraction of [^{64}Cu]PMN-MDSCs was found in the spleen of PyMT breast cancer metastases-bearing (14.72 ± 2.40 %ID/cm³ vs. 5.84 ± 1.16 %ID/cm³, p<0.05) and in the spleen of B16-F10 melanoma metastases-bearing animals (17.43 ± 2.61 %ID/cm³ vs. 5.84 ± 1.16 %ID/cm³, p<0.05) in comparison to naïve controls. Interestingly, the uptake of [^{64}Cu]PMN-MDSCs was significantly lower in the lungs of PyMT breast cancer metastases-bearing animals compared to naïve controls (1.24 ± 0.16 %ID/cm³ vs. 2.93 ± 0.62 %ID/cm³, p<0.05). In the B16-F10 melanoma metastasis model, [^{64}Cu]PMN-MDSC uptake in the liver (20.49 ± 2.29 %ID/cm³ vs. 6.88 ± 1.32 %ID/cm³, p<0.001) and the muscle (1.35 ± 0.23 %ID/cm³ vs. 0.91 ± 0.35 %ID/cm³, p<0.05) was significantly increased compared to naïve controls.

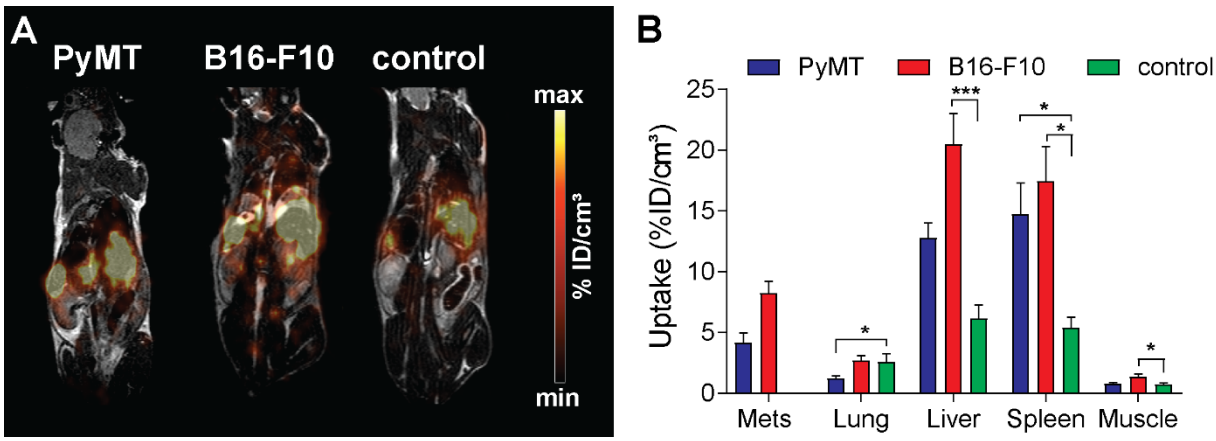

Figure 69: Whole-body distribution of [^{64}Cu]PMN-MDSCs in PyMT breast cancer and B16-F10 melanoma metastases-bearing animals and naïve controls at 24 h pt.

Representative whole-body PET and MRI scans (**A**) of PyMT breast cancer metastases- (left panel), B16-F10 melanoma metastases-bearing animals (middle panel) and naïve controls (right panel). Quantification (**B**) revealed lung metastases (denoted mets), healthy lung tissue (denoted lung), the liver and the spleen as sites of [^{64}Cu]PMN-MDSC uptake at 24 h pt (mean ± SEM in %ID/cm³, n=7 for PyMT, n=6 for B16-F10, n=5 for control, statistics: Dunnett's Multiple Comparison Test, *p<0.05, ***p<0.001; organs of control mice served as control for multiple comparison).

[^{64}Cu]PMN-MDSCs: 48 h post adoptive cell transfer

At 48 h pt (Figure 70), the elevated uptake of [^{64}Cu]PMN-MDSCs in both PyMT breast cancer and B16-F10 melanoma metastases in the lungs of the animals in comparison to 24 h pt suggested further recruitment. As already seen at both 3 h and 24 h pt, [^{64}Cu]PMN-MDSC uptake was significantly higher in B16-F10 melanoma lung metastatic lesions when compared to PyMT breast cancer metastatic lesions (10.11 ± 1.46 %ID/cm³ vs. 5.02 ± 0.77 %ID/cm³, p<0.05).

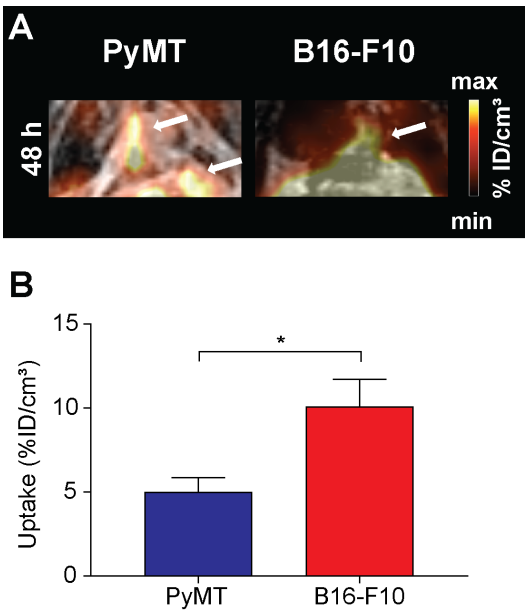

Figure 70: Homing of [^{64}Cu]PMN-MDSCs to established PyMT breast cancer and B16-F10 melanoma lung metastatic lesions 48 h pt.
Representative PET and MRI scans (**A**) of the lungs of PyMT breast cancer metastases- (left panel) and B16-F10 melanoma metastases-bearing animals (right panel). Quantification (**B**) of [^{64}Cu]PMN-MDSC homing to lung metastatic lesions showed [^{64}Cu]PMN-MDSC uptake (white arrows) at 48 h pt (mean ± SEM in %ID/cm³, n=7 for PyMT, n=6 for B16-F10, statistics: Student's t-test, *p<0.05).

The absolute uptake values of [^{64}Cu]PMN-MDSCs declined in the liver and spleen at 48 h pt (Figure 71) in comparison to the earlier imaging time points. However, [^{64}Cu]PMN-MDSC uptake in the liver (14.64 ± 1.87 %ID/cm³ vs. 5.57 ± 1.22 %ID/cm³, p<0.001) and spleen (9.35 ± 1.25 %ID/cm³ vs. 4.43 ± 0.94 %ID/cm³, p<0.01) in B16-F10 melanoma metastases-bearing mice was still significantly higher compared to naïve controls (Figure 71 B). As seen at 3 h and 24 h pt, [^{64}Cu]PMN-MDSC uptake was higher in metastatic lesions in the lungs than in healthy lung tissue.

For validation of the *in vivo* imaging data, *ex vivo* biodistribution analysis (γ-counting, Figure 71 D) was performed: metastases (Figure 71 C, dashed magenta circles, left panel: PyMT metastases, right panel: B16-F10 metastases) were identified by *ex vivo* bioluminescence OI, grossly separated from healthy tissue and denoted as 'origin tissue met', e.g. 'lung met' for metastases separated from the lungs. Here, all metastases detected by *ex vivo* OI were subjected to analysis by γ-counting even if identification *in vivo* was not possible. The *ex vivo* biodistribution analysis confirmed homing of [^{64}Cu]PMN-MDSCs to the PyMT breast cancer and B16-F10 melanoma lung metastases. Furthermore, in few PyMT breast cancer metastases- and B16-F10 melanoma metastases-bearing animals, further metastases were found in the heart, adrenal glands, ovaries, femurae and tibiae. These metastases did show [^{64}Cu]PMN-MDSC uptake as detected by γ-counting, however, due to the irregular, variable number of detected metastases and the absence of metastases in the healthy control animals, statistical analysis could not be performed on the *ex vivo* biodistribution analysis.

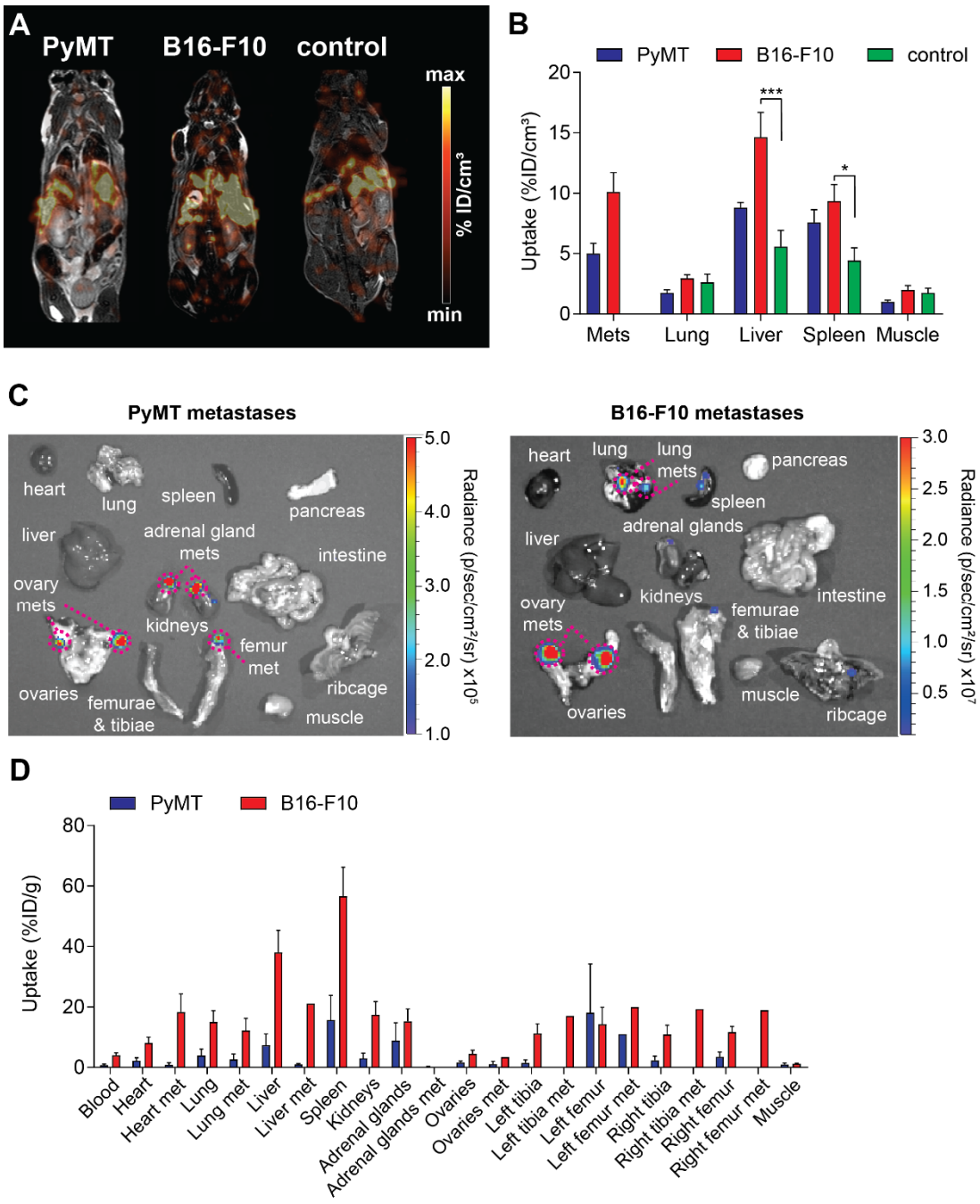

Figure 71: *In vivo* whole-body distribution and *ex vivo* biodistribution of [^{64}Cu]PMN-MDSCs in PyMT breast cancer metastases-, in B16-F10 melanoma metastases-bearing mice, and in naïve controls at 48 h pt.

Representative whole-body PET and MRI scans (**A**) of [^{64}Cu]PMN-MDSC distribution in PyMT breast cancer metastases- (left panel), B16-F10 melanoma metastases-bearing mice (middle panel) and naïve controls (right panel). Quantification (**B**) showed [^{64}Cu]PMN-MDSC retention mainly in the liver and spleen but also in the lung (mean ± SEM in %ID/cm³). *Ex vivo* bioluminescence OI images (**C**) were acquired to identify PyMT breast cancer metastases (dashed magenta circles, left panel) and B16-F10 melanoma metastases (dashed magenta circles, right panel). *Ex vivo* biodistribution analysis (**D**) by γ-counting of metastases-bearing animals confirmed [^{64}Cu]PMN-MDSC uptake mainly in the liver, and spleen, and in the lung and in the metastases of the heart, besides lung metastases and metastases in various other organs (mean ± SEM in %ID/g, n=7 for PyMT, n=6 for B16-F10, n=5 for control, statistics for B: Dunnett's Multiple Comparison Test, *p<0.05; organs of control mice served as control for multiple comparison).

[^{64}Cu]M-MDSC: 3 h post adoptive cell transfer

Beside [^{64}Cu]PMN-MDSCs, [^{64}Cu]M-MDSCs were also detected in both PyMT breast cancer and B16-F10 melanoma lung metastases as early as 3 h pt (Figure 72). In contrast to [^{64}Cu]PMN-MDSCs, no significant differences were observed for [^{64}Cu]M-MDSC homing to the lung metastases at this early time point after adoptive cell transfer.

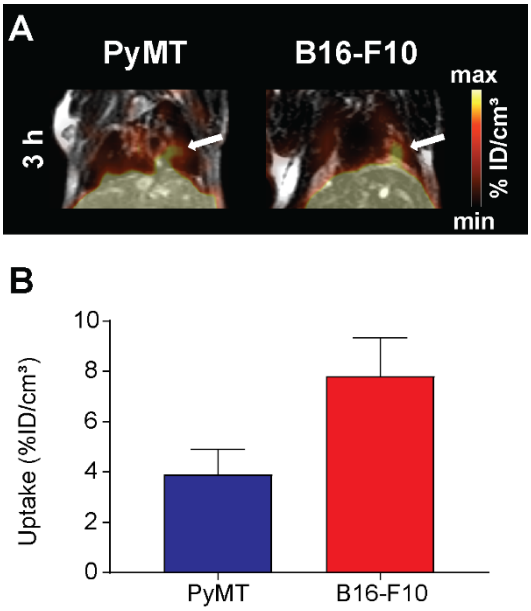

Figure 72: Homing of [^{64}Cu]M-MDSCs to established PyMT breast cancer and B16-F10 melanoma lung metastases at 3 h pt.
Representative PET and MRI scans (**A**) of the lungs of PyMT breast cancer metastases- (left panel) and B16-F10 melanoma metastases-bearing animals (right panel). Quantification of cell uptake (**B**) showed [^{64}Cu]M-MDSC homing to the lung metastases as early as 3 h pt (mean ± SEM in %ID/cm³, n=6 for PyMT, n=5 for B16).

The early migration sites of [^{64}Cu]M-MDSCs were, beside the lung metastases, mainly the liver and spleen but also the lungs in both examined metastasis models (Figure 73). Interestingly, in contrast to [^{64}Cu]PMN-MDSCs (Figure 67), both PyMT breast cancer and B16-F10 melanoma lung metastatic lesions had higher [^{64}Cu]M-MDSC uptake values than healthy lung tissue as early as 3 h pt (Figure 73). Furthermore, a significantly higher fraction of [^{64}Cu]M-MDSCs migrated to the liver of B16-F10 melanoma metastases-bearing animals compared to naïve littermate controls (33.40 ± 4.62 %ID/cm³ vs. 18.58 ± 1.17 %ID/cm³, $p<0.05$) at 3 h pt.

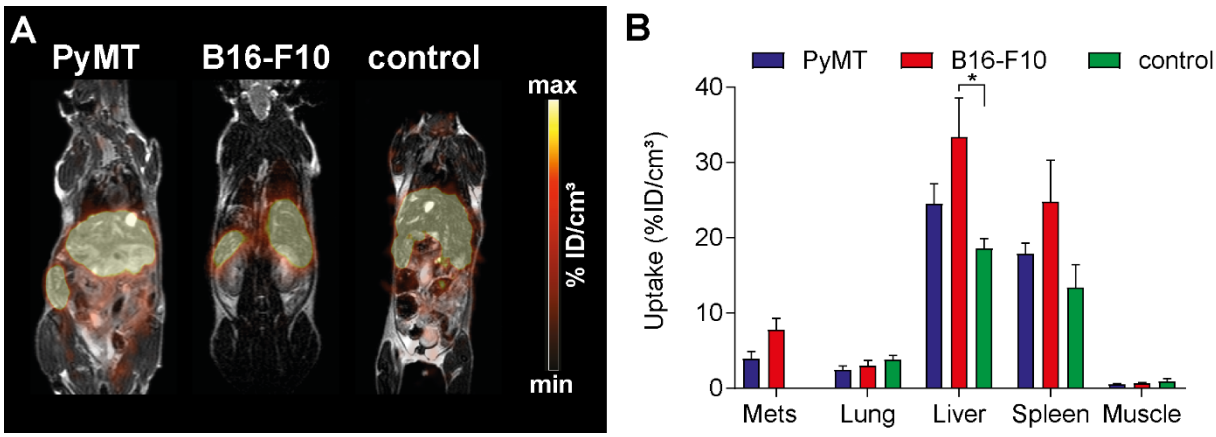

Figure 73: Whole-body distribution of [^{64}Cu]M-MDSCs in PyMT breast cancer metastases- and B16-F10 melanoma-bearing mice and naïve controls at 3 h pt.

Representative whole-body PET and MRI scans (**A**) of PyMT breast cancer metastases- (left panel), B16-F10 melanoma metastases-bearing animals (middle panel) and naïve controls (right panel) and quantification (**B**) revealed [^{64}Cu]M-MDSC migration to lung metastases (denoted mets), healthy lung tissue (denoted lung), the liver and the spleen at 3 h pt (mean ± SEM in %ID/cm³, n=6 for PyMT, n=5 for B16-F10, n=5 for control, statistics: Dunnett's Multiple Comparison Test, *p<0.05; organs of control mice served as control for multiple comparison).

[^{64}Cu]M-MDSCs: 24 h post adoptive cell transfer

At 24 h pt (Figure 74), the uptake of [^{64}Cu]M-MDSC was significantly higher in B16-F10 melanoma metastases in the lungs in comparison to PyMT breast cancer metastases in the lungs (8.28 ± 1.98 %ID/cm³ vs. 5.13 ± 0.70 %ID/cm³, p<0.05). Additionally, [^{64}Cu]M-MDSC homing to lung metastases was higher 24 h pt compared to 3 h pt.

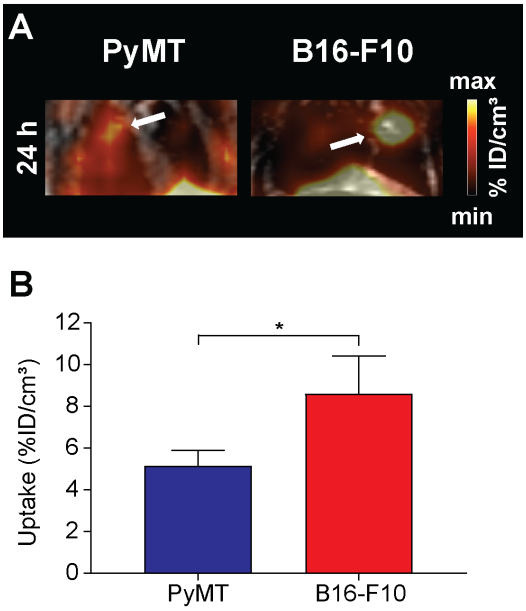

Figure 74: [^{64}Cu]M-MDSC homing to established PyMT breast cancer and B16-F10 melanoma lung metastases at 24 h pt.

Representative PET and MRI scans (**A**) of the lungs of PyMT breast cancer metastases- (left panel) and B16-F10 melanoma metastases-bearing animals (right panel). Quantification (**B**) of [^{64}Cu]M-MDSC homing to the lung metastases at 24 h pt (mean ± SEM in %ID/cm³, n=6 for PyMT, n=5 for B16, statistics: Student's t-test, *p<0.05).

At 24 h pt, the adoptively transferred [^{64}Cu]M-MDSCs were retained mainly in the liver and spleen of both PyMT breast cancer metastases- and B16-F10 metastases-bearing mice (Figure 75). At this time point, no significant differences were observed in the organ uptake compared to the naïve control animals, but a trend towards higher organ uptake was visible in the metastases-bearing animals. Additionally, lung metastatic lesions had higher [^{64}Cu]M-MDSC uptake than healthy lung tissue.

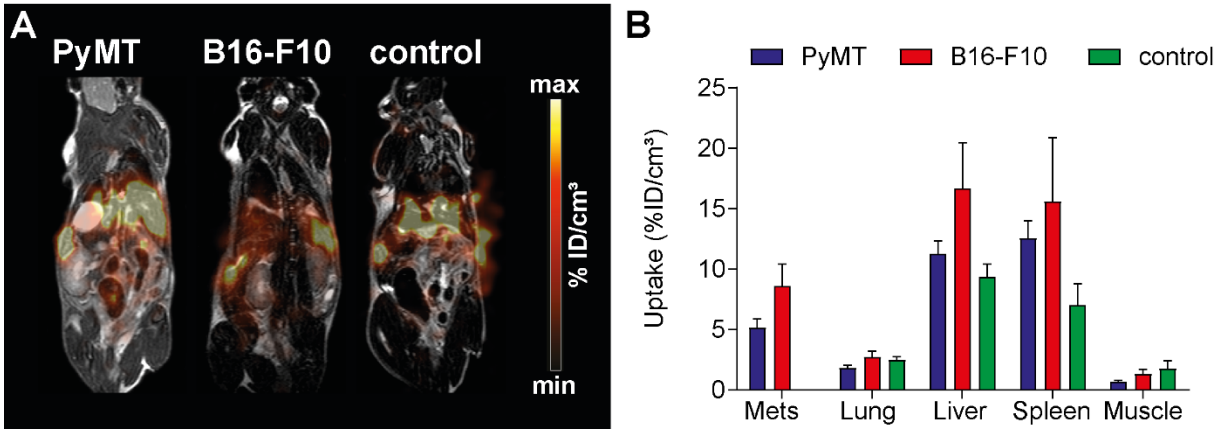

Figure 75: Whole-body distribution of [^{64}Cu]M-MDSCs in PyMT breast cancer metastases-, B16-F10 melanoma-bearing mice and naïve controls at 24 h pt.

Representative whole-body PET and MRI scans (**A**) of PyMT breast cancer metastases- (left panel), B16-F10 melanoma metastases-bearing animals (middle panel) and naïve controls (right panel). Quantification (**B**) revealed cell migration to lung metastases (denoted mets) and the retention of [^{64}Cu]M-MDSCs in healthy lung tissue (denoted lung), the liver and the spleen at 24 h pt (mean ± SEM in %ID/cm³, n=6 for PyMT, n=5 for B16-F10, n=5 for control)

[^{64}Cu]M-MDSCs: 48 h post adoptive cell transfer

At 48 h pt (Figure 76), [^{64}Cu]-M-MDSC homing to PyMT breast cancer lung metastatic lesions was enhanced in comparison to 24 h pt, while [^{64}Cu]-M-MDSC homing to B16-F10 melanoma metastatic lesions remained static and did not increase further in comparison to 24 h pt. In contrast to 24 h pt, the difference between [^{64}Cu]M-MDSC homing to PyMT breast cancer metastases and B16-F10 melanoma metastases in the lungs was not significant.

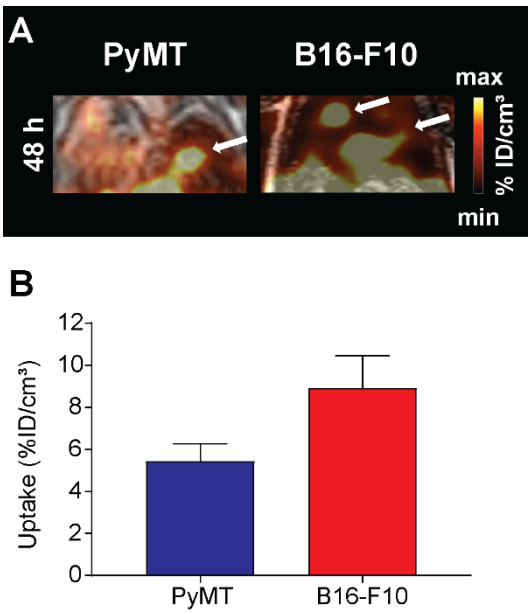

Figure 76: Homing of [^{64}Cu]M-MDSCs to established PyMT breast cancer and B16-F10 melanoma lung metastases at 48 h pt.
Representative PET and MRI scans (**A**) of the lungs of PyMT breast cancer metastases- (left panel) and B16-F10 melanoma metastases-bearing animals (right panel). Quantification (**B**) of [^{64}Cu]M-MDSC homing to the lung metastases at 48 h pt (mean ± SEM in %ID/cm³, n=6 for PyMT, n=5 for B16).

At 48 h pt (Figure 77), [^{64}Cu]M-MDSCs were retained mainly in liver and spleen of the metastases-bearing mice, although with reduced uptake in comparison to 24 h pt. [^{64}Cu]M-MDSC uptake in the liver of B16-F10 melanoma metastasis-bearing animals was significantly higher than in naïve controls (11.47 ± 2.15 %ID/cm³ vs. 5.52 ± 0.92 %ID/cm³, $p<0.05$). As described for [^{64}Cu]PMN-MDSCs (Figure 71), metastases were identified by *ex vivo* bioluminescence OI (Figure 77 C, dashed magenta circles, left panel: PyMT metastases, right panel: B16-F10 metastases), grossly separated from healthy tissue, subjected to *ex vivo* biodistribution analysis and denoted as 'origin tissue met' (Figure 77 D). The *ex vivo* biodistribution analysis confirmed homing of [^{64}Cu]M-MDSCs to lung metastatic lesions in PyMT breast cancer metastases- and B16-F10 melanoma-metastases bearing animals. Additionally to lung metastases, further metastases were found in the heart, adrenal glands, ovaries, femurae and tibiae. These tissues also constituted sites of [^{64}Cu]M-MDSC migration (Figure 77 D) as confirmed by γ-counting. However, due the irregular, variable number of detected metastases and the absence of metastases in the control animals, no statistical analysis was possible for the *ex vivo* biodistribution analysis.

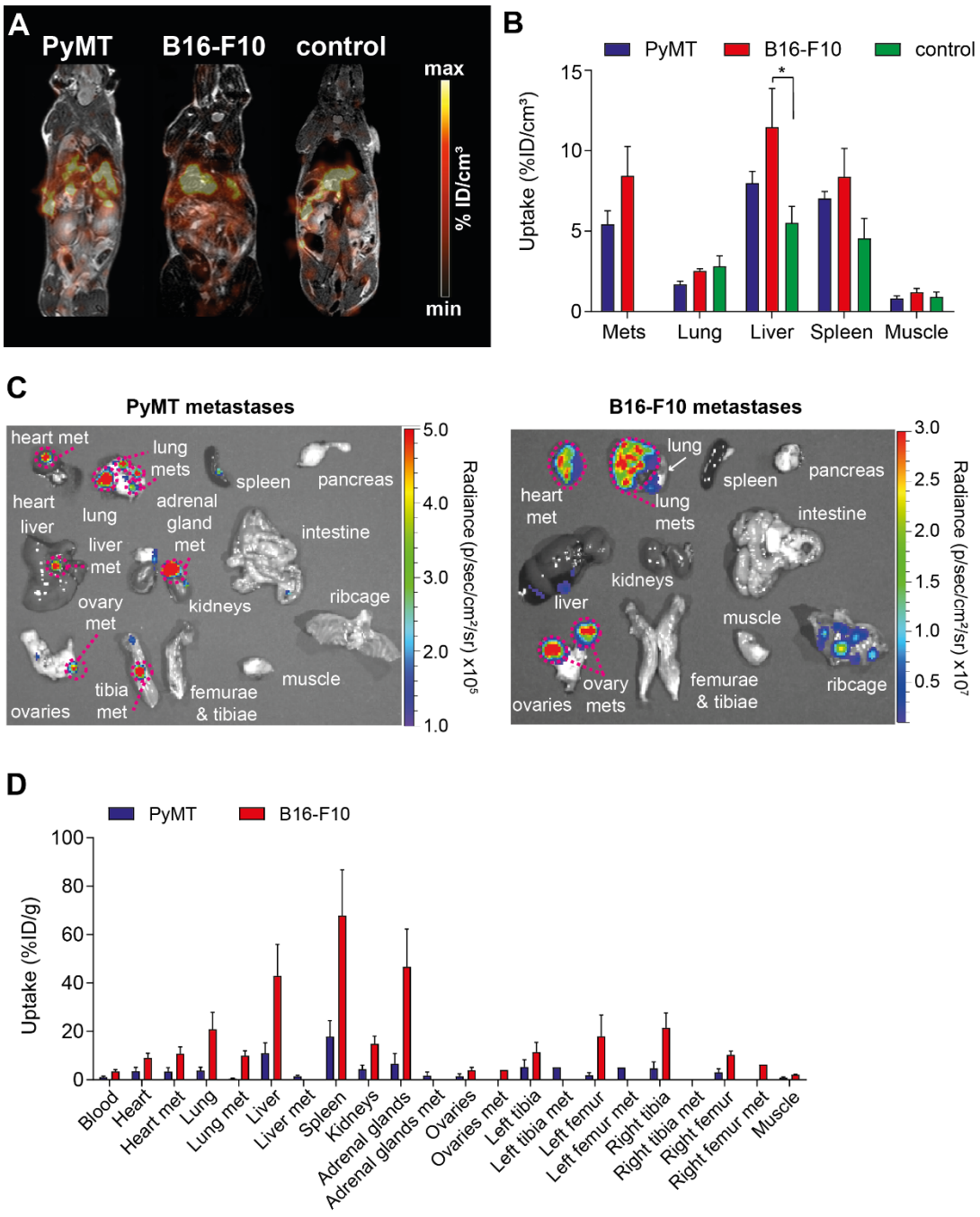

Figure 77: *In vivo* whole-body distribution and *ex vivo* biodistribution of [^{64}Cu]M-MDSCs in PyMT breast cancer metastases- and B16-F10 melanoma metastases-bearing mice, and naïve controls at 48 h pt.

Representative whole-body PET and MRI scans (**A**) of [^{64}Cu]M-MDSC distribution in PyMT breast cancer metastases- (left panel), in B16-F10 melanoma metastases-bearing mice (middle panel), and in naïve controls (right panel). Quantification (**B**) showed [^{64}Cu]M-MDSC retention mainly in the liver and spleen (mean ± SEM in %ID/cm³). *Ex vivo* bioluminescence OI images (**C**) were acquired to identify PyMT breast cancer metastases (dashed magenta circles, left panel) and B16-F10 melanoma metastases (dashed magenta circles, right panel). *Ex vivo* biodistribution analysis (**D**) by γ-counting confirmed [^{64}Cu]M-MDSC uptake mainly in the spleen, liver and the lungs, and in the metastases of the adrenal glands, besides lung metastases and metastases in various other organs (mean ± SEM in %ID/g, n=6 for PyMT, n=5 for B16-F10, n=5 for control, statistics for B: Dunnett's Multiple Comparison Test, *p<0.05; organs of control mice served as control for multiple comparison).

4.2 Pre-metastatic niche induction

Beside their immunosuppressive function facilitating tumor growth, MDSCs are important players in pre-metastatic niche formation. Pre-metastatic niche formation is thought to precede the arrival of the first metastatic tumor cells at the secondary organs.
In this part, two different mouse models for pre-metastatic niche formation were evaluated for MDSC cell tracking studies: pre-metastatic niche induction with tumor cell conditioned media (CM) as published by Kaplan *et al*. in their seminal study on the formation of the pre-metastatic niche (Kaplan *et al.*, 2005) and pre-metastatic niche induction with recombinant VEGF-C (Scherer and Sleeman, 2017).

4.2.1 Pre-metastatic niche induction with tumor cell conditioned media

For the induction of pre-metastatic niche formation in the lungs, experimental animals were *i.p.* injected with 300 µL of either S2WTP3 PyMT breast cancer cell CM or B16-F10 melanoma CM daily for 9 days. The animals were then sacrificed via CO_2 asphyxiation in deep anesthesia and the lungs and spleen were processed for immunoscoring by flow cytometry (Figure 78).

Although a higher abundance of both PMN-MDSCs and M-MDSCs was expected in the lungs of CM-treated animals, the fraction of PMN-MDSCs in the lungs of PyMT CM-treated and B16-F10 CM-treated mice did not increase (Figure 78 A). A marginal increase of M-MDSCs in the lungs of PyMT CM-treated animals could be detected, while, contrary to the expectations, the fraction of M-MDSCs in the lungs of B16-F10 CM-treated mice decreased slightly, but not significantly.
Immune cells of interest for PMN induction include, besides the MDSC subpopulations, T cells and NK cells. Controversially, in the lungs of B16-F10 CM-treated mice, the fraction of $CD4^+$ and $CD8^+$ T cells increased slightly, but no changes in the early activation status as monitored by CD69 expression were detected. NK cell abundance did not change significantly.
In the lungs of PyMT CM-treated mice, neither the abundance of $CD4^+$ or $CD8^+$ T cells, nor their activation status, nor the fraction of NK cells changed significantly.
The spleens of B16-F10 CM- and PyMT CM-treated animals (Figure 78 B) were processed as control and did not show significant differences between the CM-treated groups compared to the naïve control group. Nevertheless, M-MDSCs did show a tendency towards a decrease in abundance in both B16-F10 CM- and PyMT-CM-treated mice.
Overall, the expected increase of both PMN- and M-MDSCs in the lungs of CM-treated animals could not be detected indicating that the induction of PMN formation by daily *i.p.* injections of B16-F10 and PyMT CM was not successful.

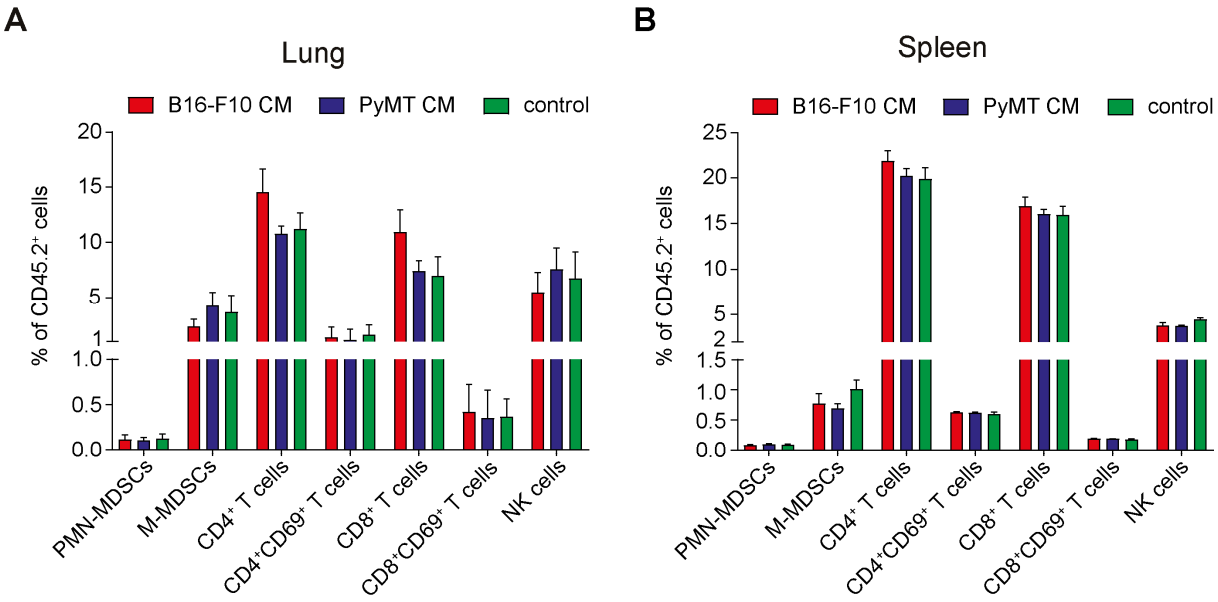

Figure 78: Immunoscoring of the lungs and spleen of CM-treated mice.
Immunoscoring of the immune cell populations in the lung (**A**) and spleen (**B**) of B16-F10 CM-treated mice and PyMT CM-treated mice did not reveal significant differences in any of the detected immune cell populations in comparison to naïve littermate controls (mean ± SEM in % of CD45.2$^+$ cells, n=3 for B16-F10 CM, n=3 for PyMT CM, n=3 for control).

4.2.2 Pre-metastatic niche induction with recombinant VEGF-C

In a second approach to induce a pre-metastatic niche in the lungs of mice, experimental animals were *i.v.* injected with 70 µg recombinant VEGF-C daily for 5 days. Murine serum albumin served as control. On day 4 of the VEGF-C or albumin treatment, mice received an adoptive transfer of 3x10^6 [^{64}Cu]PMN-MDSCs. Static 20 min emission PET scans and T2-weighted anatomical MRI scans were acquired at 3, 24 and 48 h pt. At 48 h pt, mice were sacrificed via CO_2 asphyxiation in deep anesthesia and *ex vivo* biodistribution analysis was performed by γ-counting of the isolated organs. The results of this study are presented in chronological order of data acquisition.

[^{64}Cu]PMN-MDSCs: 3 h post adoptive cell transfer

Early sites of [^{64}Cu]PMN-MDSC migration at 3 h pt were mainly the liver and spleen but also the lungs of both VEGF-C-treated mice and albumin-treated controls (Figure 79). Interestingly, there was no significant difference between the uptake values of [^{64}Cu]PMN-MDSCs in the lungs of VEGF-C-treated animals in comparison to the albumin-treated control group.

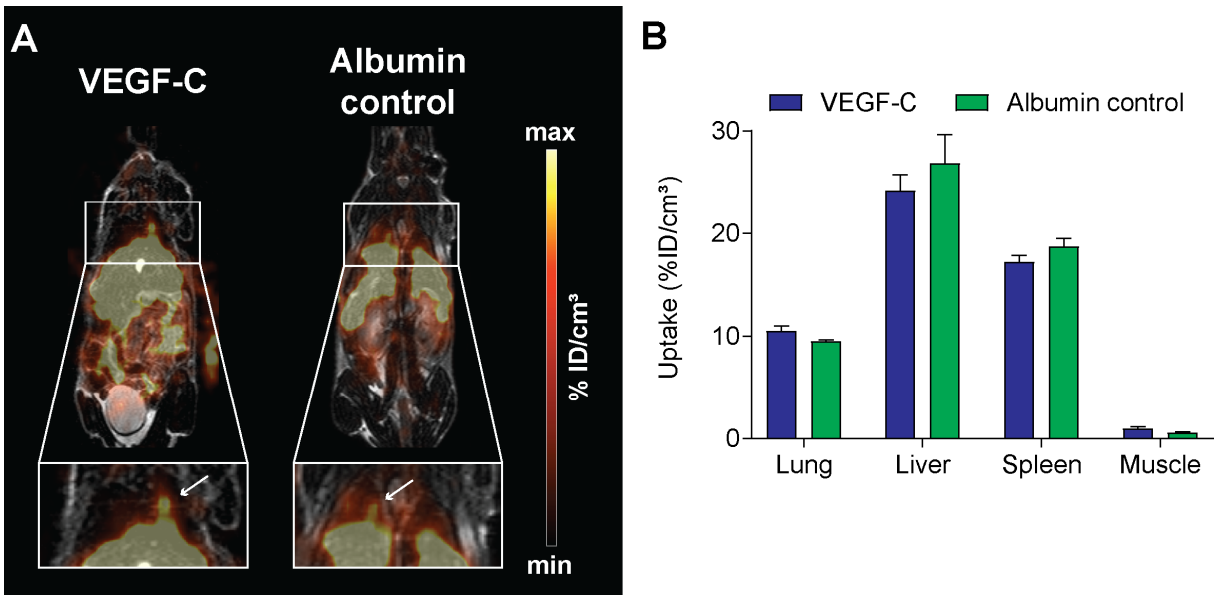

Figure 79: [^{64}Cu]PMN-MDSC distribution in VEGF-C- and albumin-treated mice at 3 h pt.
Representative whole-body PET and MRI scans (**A**) with zoom on the lungs (white boxes, white arrows indicating [^{64}Cu]PMN-MDSCs) of VEGF-C- and albumin-treated mice. Quantification (**B**) revealed [^{64}Cu]PMN-MDSC migration to the lungs, liver and spleen of the animals at 3 h pt (mean ± SEM in %ID/cm³, n=4 for VEGF-C, n=4 for albumin).

[^{64}Cu]PMN-MDSCs: 24 h post adoptive cell transfer

At 24 h pt, no differences between the uptake of [^{64}Cu]PMN-MDSCs in the lungs of VEGF-C-treated and albumin-treated mice was observed (Figure 80). Compared to the early time point at 3 h pt, [^{64}Cu]PMN-MDSC uptake values in the lungs of the VEGF-C- and albumin-treated mice were nearly unchanged. Overall, [^{64}Cu]PMN-MDSC uptake had decreased in the liver and spleen of both treatment groups in comparison to the early time point at 3 h pt.

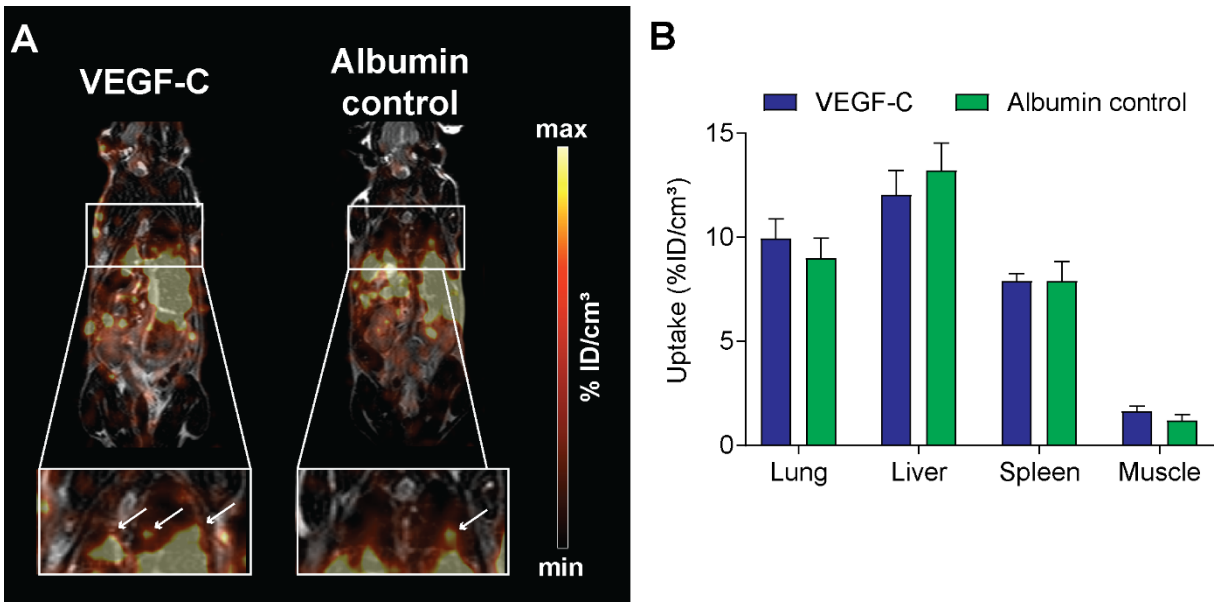

Figure 80: [^{64}Cu]PMN-MDSC distribution in VEGF-C- and albumin-treated mice at 24 h pt.
Representative whole-body PET and MRI scans (**A**) with zoom on the lungs (white boxes, white arrows indicating [^{64}Cu]PMN-MDSCs) of VEGF-C- and albumin-treated mice. Quantification (**B**) showed [^{64}Cu]PMN-MDSC retention in the the lungs, liver and spleen of the VEGF-C- and albumin-treated mice at 24 h pt (mean ± SEM in %ID/cm³, n=4 for VEGF-C, n=4 for albumin).

[^{64}Cu]PMN-MDSCs: 48 h post adoptive cell transfer

In concordance with the earlier imaging time points at 3 and 24 h post [^{64}Cu]PMN-MDSC transfer, no significant differences in the [^{64}Cu]PMN-MDSC uptake values were detected between the lungs of VEGF-C-treated mice and albumin-treated controls at 48 h pt (Figure 81). Further, the uptake values of [^{64}Cu]PMN-MDSCs in the liver and spleen of both VEGF-C-treated mice and albumin-treated littermate controls were decreased in comparison to the imaging time point at 24 h pt. The *ex vivo* biodistribution analysis (Figure 81 C) confirmed that there was no significant differences in the uptake of [^{64}Cu]PMN-MDSCs in the lungs, liver or spleen of VEGF-C-treated mice in comparison to albumin-treated controls. Interestingly, tibiae and femurae of VEGF-C-treated and albumin-treated mice showed uptake of [^{64}Cu]PMN-MDSCs in the *ex vivo* biodistribution study.

In summary, the expected significant increase of [^{64}Cu]PMN-MDSC uptake in the lungs of VEGF-C-treated mice was not detected.

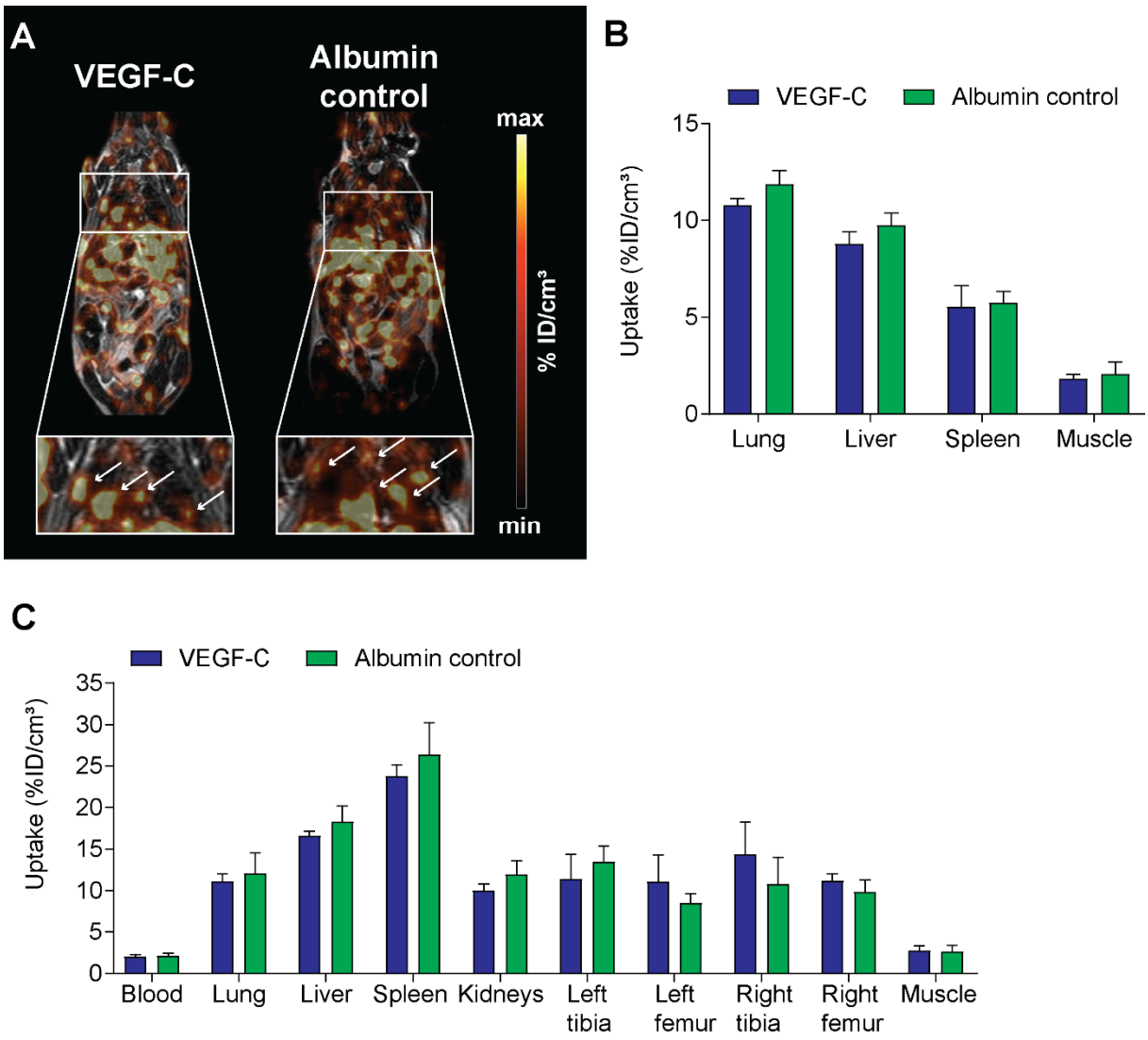

Figure 81: *In vivo* and *ex vivo* biodistribution of [^{64}Cu]PMN-MDSCs in VEGF-C-treated mice and albumin-treated controls at 48 h pt.

Representative whole-body PET and MRI scans (**A**) with zoom on the lungs (white boxes, white arrows indicating [^{64}Cu]PMN-MDSCs) of VEGF-C- and albumin-treated mice. Quantification (**B**, mean ± SEM in %ID/cm³) and *ex vivo* biodistribution analysis (**C**) showed no significant differences in [^{64}Cu]PMN-MDSC uptake in the lungs, liver and spleen of VEGF-C-treated mice compared to the albumin-treated control group at 48 h pt (mean ± SEM in %ID/g, n=4 for VEGF-C, n=4 for albumin).

4.3 Metabolic fingerprinting for markers for differential metastatic potency – Examination of the PyMT-derived cell lines S2WTP3 and ML1B1B1

As described in section 3.2.1, the cell line S2WTP3 was derived from the well-studied MMTV-PyMT mouse strain by Dr. Christina Wong (Wong *et al.*, 2012). The cell line ML1B1B1 was further derived from the established cell line S2WTP3 by repeated cycles of orthotopic and *intracardiac* injection and isolation of bone metastases. Therefore, the cell line ML1B1B1 was thought to be more aggressive and possess higher metastatic potency than its parental cell line S2WTP3 owing to this *in vivo* selection process. Due to the similarity in their generation procedure, the melanoma cell lines B16-F0 and B16-F10 were used as reference in the *in vitro* evaluations (Fidler, 1975).

4.3.1 Colony formation assay

As an *in vitro* survival assay, the colony formation assay examines the ability of cell-to-cell-contact independent growth and the ability to undergo unlimited division (Crowley *et al.*, 2016). Hence, an equal and low number of cells was seeded into culture dishes and left to grow colonies under regular cell culture conditions. To be able to distinguish cell colonies arising from individual cells, the assay was stopped before the respective faster growing cell line reached confluence. The resulting colonies were stained with crystal violet dye for visualization, counted and normalized to the respective parental cell line (Figure 82).

As expected for established tumor cell lines, all examined cell lines were able to grow colonies under the assay conditions (Figure 82 A, B). The absolute number of colonies was higher for both melanoma cell lines in comparison to the PyMT breast cancer cell lines. Interestingly, the relative difference to the respective parental cell line was higher for the PyMT breast cancer cell line S2WTP3 and ML1B1B1. This indicated a pronounced difference in the capability for cell-to-cell contact independent survival and growth in ML1B1B1 cells in comparison to S2WTP3 cells.

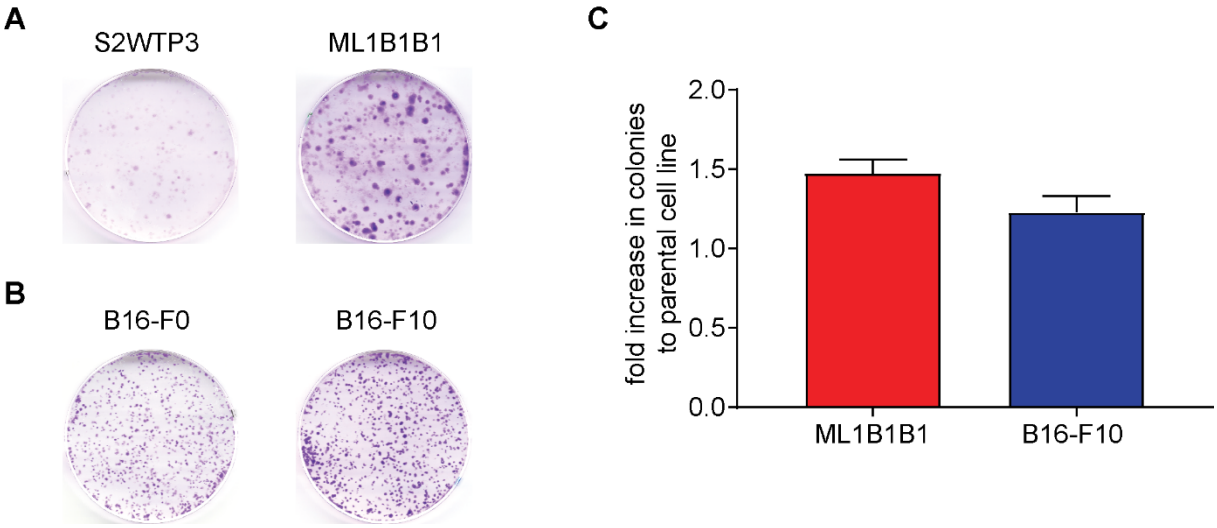

Figure 82: Colony formation assay of the PyMT cell lines S2WTP3 and ML1B1B1, and the melanoma cell lines B16-F0 and B16-F10.
Representative images of the cell culture dishes of the PyMT cell lines S2WTP3 and ML1B1B1 (**A**) and of the melanoma cell lines B16-F0 and B16-F10 (**B**). Quantification of the number of colonies (**C**) revealed that under similar survival and growth conditions, the melanoma cell lines grew more colonies in absolute numbers compared to the PyMT cell lines (not depicted), however, the relative difference between the PyMT cell lines was higher (n=5 for PyMT cell lines, n=5 for melanoma cell lines).

4.3.2 Glucose metabolism *in vitro* and *in vivo*

Cancer cells frequently rely on glycolysis to meet their high energy demand and to support proliferation. More aggressive cell populations often have a higher glucose consumption. Therefore, in a first step, the [^{18}F]FDG uptake of the cell lines S2WTP3 and ML1B1B1 was determined *in vitro* (Figure 83). *In vitro* uptake studies were performed under competitive conditions with 5 mM glucose in the medium. The melanoma cell lines B16-F0 and B16-F10 served as comparison.

The more aggressively growing PyMT cell line ML1B1B1 had a significantly 3.5-fold higher [^{18}F]FDG uptake *in vitro* compared to its parental cell line S2WTP3 (0.80 ± 0.03 % vs. 2.81 ± 0.05 %, $p<0.0001$). The melanoma cell lines B16-F0 and B16-F10 demonstrated similar results (2.49 ± 0.23 % vs. 4.09 ± 0.06 %, $p<0.01$), however, the [^{18}F]FDG uptake in B16-F10 cells was only 1.64-fold higher than in B16-F0 cells. This further reflects the relative difference in aggressive grow as detected in the colony formation assay (as described in section 4.3.1).

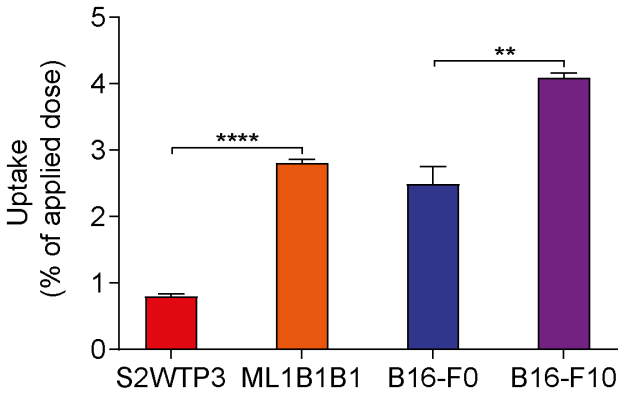

Figure 83: *In vitro* [^{18}F]FDG uptake study in the PyMT breast cancer and B16 melanoma cell lines. The *in vitro* [^{18}F]FDG uptake study by γ-counting as a surrogate for glucose consumption revealed a significantly higher [^{18}F]FDG uptake in ML1B1B1 cells compared to S2WTP3 cells. Likewise, B16-F10 cells had a significantly higher [^{18}F]FDG uptake compared to B16-F0 cells (values are normalized to the applied dose and given in percent, n=5 for all cell lines, statistics: Student's t-test,**p<0.01, ****p<0.0001).

To examine if the higher *in vitro* [^{18}F]FDG uptake in the more aggressive cell line ML1B1B1 would translate to a higher [^{18}F]FDG uptake under physiologic conditions *in vivo*, allografts of ML1B1B1 and S2WTP3 cells were induced in C57BL/6 mice (as described in section 3.1.3.1). Imaging time points for the ML1B1B1 and S2WTP3 allograft-bearing mice were adapted to the different growth kinetics of the ML1B1B1 and S2WTP3 allograft tumors: ML1B1B1 allograft-bearing mice were imaged 7 days post inoculation before reaching end stage while S2WTP3 allograft-bearing mice were imaged 14 post inoculation before reaching end stage. The experimental animals received a bolus injection of approximately 13 MBq [^{18}F]FDG. Subsequently, 70 min dynamic PET scans (Figure 84) were acquired simultaneously with T2-weighted anatomical MR images and ^{1}H *in vivo* MRS.

For statistical analysis, the [^{18}F]FDG uptake was determined for the last 10 min frame of the dynamic PET scans. Surprisingly, the ML1B1B1 allografts (Figure 84 B, lower panel) did not show a significantly higher [^{18}F]FDG uptake value in comparison to the S2WTP3 allografts (Figure 84 B, upper panel) (9.40 ± 0.54 %ID/cm³ in ML1B1B1 vs. 9.11 ± 0.83 %ID/cm³ in S2WTP3).

In conclusion, the *in vivo* [^{18}F]FDG uptake in S2WTP3 and ML1B1B1 allografts did not reflect the differences observed in the *in vitro* [^{18}F]FDG uptake of the cell lines S2WTP3 and ML1B1B1.

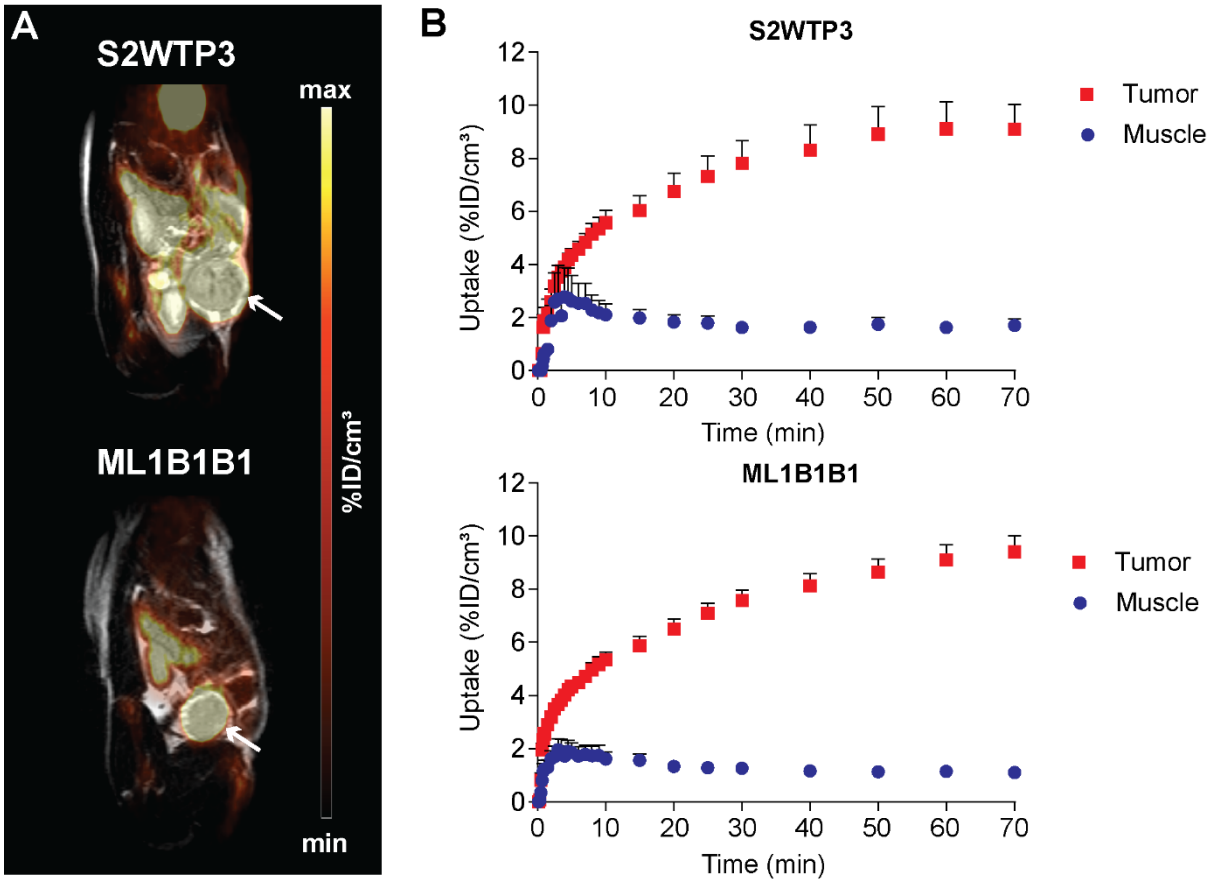

Figure 84: Simultaneous PET/MRI investigation of [^{18}F]FDG uptake in S2WTP3 and ML1B1B1 allograft-bearing mice.
Representative whole-body simultaneous PET/MR scans (**A**) of [^{18}F]FDG uptake in the S2WTP3 (upper panel) and ML1B1B1 (lower panel) allograft tumors (white arrows). Time activity curves (**B**) of the tumor and muscle as reference tissue revealed similar [^{18}F]FDG dynamics in S2WTP3 (**B**, upper panel) and ML1B1B1 (**B**, lower panel) allografts (mean ± SEM in %ID/cm³, n=5 for S2WTP3, n=5 for ML1B1B1).

4.3.3 *In vivo* ^{1}H spectroscopy and *ex vivo* ^{1}H HR-MAS NMR spectroscopy

The total choline content in tissue can indicate both malignant transformation and aggressive growth (Glunde *et al.*, 2011). In *in vivo* ^{1}H MRS, the total choline content is detected as a single peak at 3.2 ppm. Beside the choline peak at 3.2 ppm, fatty acid and lipid peaks are detected around 0.9 ppm, 1.3 ppm and 1.6 ppm. Further lipid peaks are detected at 2.1, 2.3 and 2.8 ppm. ^{1}H spectroscopic analysis was performed during the dynamic PET scans (section 4.3.2) to assess the total choline content in the S2WTP3 and ML1B1B1 allograft tumors with a standard water-suppressed STEAM protocol (TE 3 ms, TR 1800 ms, voxel size 3x3x3 mm³, 256 averages). Representative *in vivo* ^{1}H spectra of S2WTP3 and ML1B1B1 allograft tumors are given in Figure 102 provided in the appendix (section 10, page 253).

Quantification of the obtained *in vivo* ^{1}H spectra was performed with LCModel (Figure 85). The quantification of the lipids (Figure 85 A) in the tumor tissue revealed high variances between the individual tumors, rather reflecting the placement of the allograft in the fourth MFP than

differences in the lipid mass. A non-significant trend towards a higher total choline concentration (Figure 85 B) in the ML1B1B1 tumors compared to the S2WTP3 tumors was visible indicating a higher degree of aggressiveness. However, the variability of the choline concentration was relatively high in the ML1B1B1 allograft tumors (Figure 85 B).

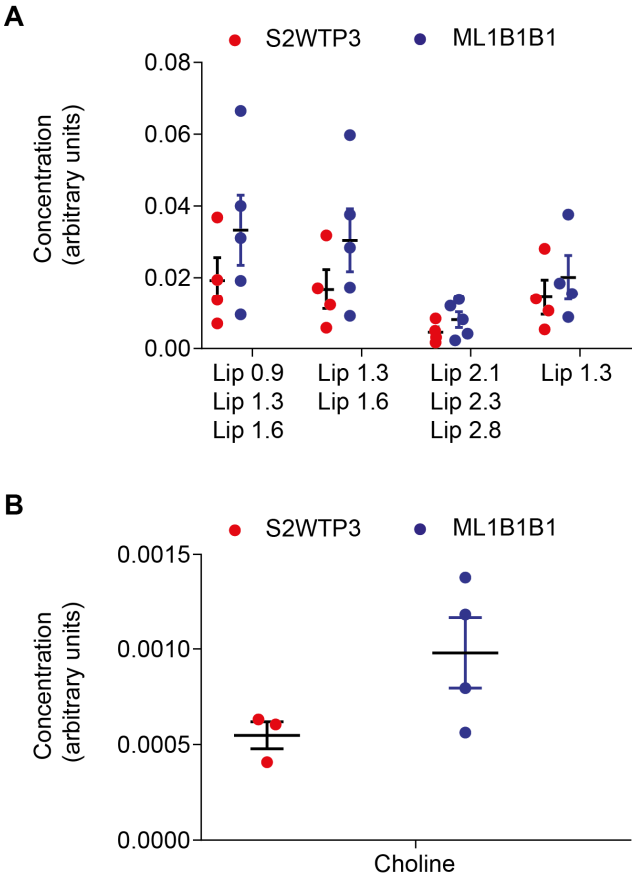

Figure 85: Quantification of the *in vivo* ^{1}H spectroscopic data of the S2WTP3 and ML1B1B1 allograft tumors.

Quantification of the *in vivo* ^{1}H MR spectra with LCModel revealed high variability in both the lipid (**A**) and the choline content (**B**) of the individual tumors and no significant differences between the groups (values are given as mean ± SEM in arbitrary units, Lip 0.9 – lipid resonance at 0.9 ppm, Lip 1.3 – lipid resonance at 1.3 ppm, Lip 1.6 – lipid resonance at 1.6 ppm, Lip 2.1 – lipid resonance at 2.1 ppm, Lip 2.3 – lipid resonance at 2.3 ppm, Lip 2.8 – lipid resonance at 2.8 ppm, n=5 for S2WTP3 and n=5 for ML1B1B1; scans with insufficient resolution were excluded from the analysis).

In comparison to *in vivo* ^{1}H MRS, ^{1}H HR-MAS NMR spectroscopy features a higher resolution and a lower metabolite detection limit (Glunde *et al.*, 2011). Therefore, the allograft tumors were excised at end stage and snap-frozen in liquid nitrogen for *ex vivo* analysis. Representative *ex vivo* HR-MAS ^{1}H NMR spectra of S2WTP3 and ML1B1B1 allografts are given in Figure 103 provided in the appendix (section 10, page 254).

Due to technical issues, only three out of five acquired spectra could be further processed for analysis. Furthermore, the spectra had to be corrected for shim and baseline before quantification (performed by Dr. Christoph Trautwein). Beside the choline species, 9 other metabolites were identified and quantified (Table 4).

Table 4: Metabolites detected in the ^{1}H HR-MAS NMR spectroscopic analysis of S2WTP3 and ML1B1B1 allograft tumor tissue.

Metabolite	δ (ppm)	S2WTP3 (AUC, mean ± SEM)	ML1B1B1 (AUC, mean ± SEM)
Alanine	1.47	2.49 ± 0.28	2.56 ± 0.80
Glutamate	2.07	3.83 ± 0.40	3.97± 1.08
Succinate	2.41	0.16 ± 0.05	0.17 ± 0.04
Creatine	3.03	2.96 ± 0.27	2.42 ± 0.36
Choline	3.19	2.73 ± 0.41	1.99 ± 0.48
Phophocholine	3.21	7.33 ± 0.72	6.52 ± 0.80
Glycerophophocholine	3.22	4.84 ± 0.44	8.16 ± 0.92
Taurine	3.25, 3.42	9.93 ± 1.07	9.06 ± 2.02
myo-inositol	3.27, 3.61	4.05 ± 0.37	2.55 ± 0.86
Glycine	3.55	1.49 ± 0.14	1.00 ± 0.21
Lactate	4.11	12.85 ± 0.34	14.34 ± 5.10
Ascorbate	4.49	1.95 ± 0.29	1.97 ± 0.42

The phosphocholine/choline (PCho/Cho) ratio indicates malignant transformation and aggressive growth in breast cancer lesions. Furthermore, remarkably high glycerophophocholine/phosphocholine (GCho/PCho) ratios and high GCho concentrations were found basal-like breast cancer, a particularly aggressive breast cancer. Concordantly, the ML1B1B1 allograft tumors had a significantly 1.9-fold higher GCho/PCho ratios (1.27 ± 0.11 vs. 0.66 ± 0.01, p<0.01) in comparison to S2WTP3 tumors (Figure 86).

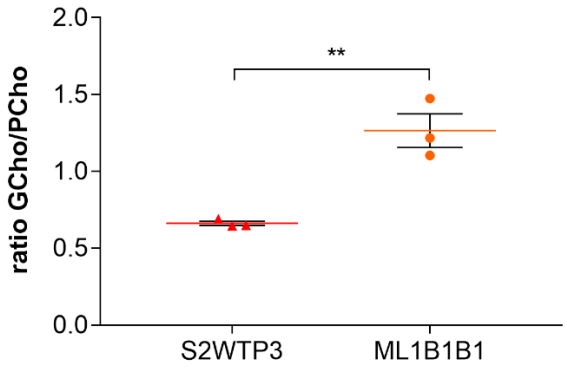

Figure 86: GCho/PCho ratio in S2WTP3 and ML1B1B1 allograft tumor tissue determined with ^{1}H HR-MAS NMR spectroscopy.
In *ex vivo* ^{1}H HR-MAS NMR spectroscopy, ML1B1B1 allografts had significantly higher GCho/PCho ratios than S2WTP3 tumors (mean ± SEM, n=3, statistics: Student's t-test, **p<0.01).

4.3.4 *In vitro* hyperpolarized [1-^{13}C]pyruate ^{13}C spectroscopy

In tumor cells, pyruvate, the end product of glycolysis, is frequently not further oxidized for energy generation but converted to lactate to replenish NAD^+ for glycolysis. To assess metabolism downstream of glycolysis, *in vitro* ^{13}C-MRS was performed with hyperpolarized [1-^{13}C]pyruate on cell suspensions of the PyMT cell lines S2WTP3 and ML1B1B1, and the melanoma cell lines B16-F0 and B16-F10 for comparison. *In vitro* ^{13}C-MRS was executed in collaboration with Dr. Marie-Aline Neveu.

In both S2WTP3 and ML1B1B1 cells, [1-^{13}C]alanine and [1-^{13}C]lactate were produced directly after injection of [1-^{13}C]pyruvate. The parental cell line S2WTP3 showed a non-significant trend towards higher overall [1-^{13}C]alanine (Figure 87 A) and [1-^{13}C]lactate production (Figure 87 B) *in vitro*.

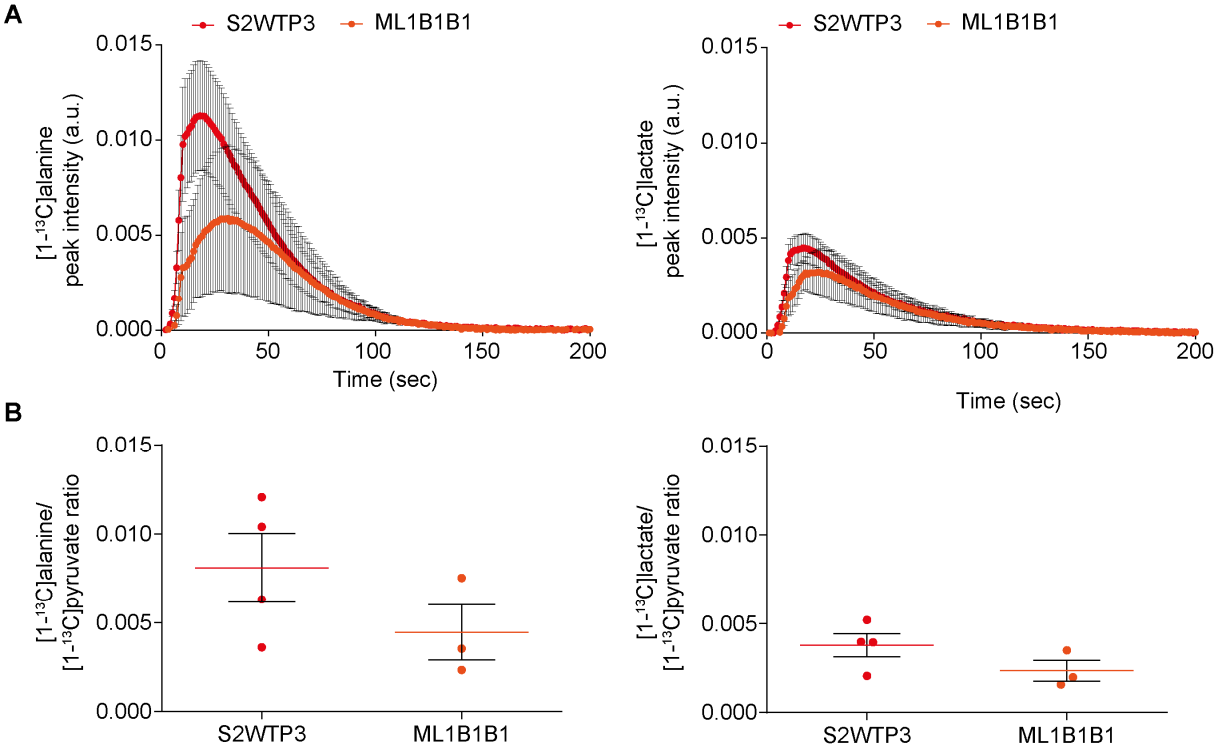

Figure 87: ^{13}C spectroscopic analysis of [1-^{13}C]pyruvate metabolism in S2WTP3 and ML1B1B1 cells.

Dynamic conversion of [1-^{13}C]pyruvate to [1-^{13}C]alanine (**A**, left panel) and [1-^{13}C]lactate (**A**, right panel) was detected in both PyMT cell lines S2WTP3 and ML1B1B1 (peak intensity in arbitrary units, a. u.) with the trend towards an overall higher [1-^{13}C]alanine (**B**, left panel) and [1-^{13}C]lactate (**B**, right panel) production in the parental cell line S2WTP3 (values are given as mean ± SEM, n=4 for S2WTP3, n=3 for ML1B1B1).

As seen in the PyMT breast cancer cell lines S2WTP3 and ML1B1B1, the dynamics of [1-^{13}C]alanine and [1-^{13}C]lactate production did not differ significantly between B16-F0 and B16-F10 cells (Figure 88 A). In comparison, a trend towards higher [1-^{13}C]alanine and [1-^{13}C]lactate

production was detected in the more aggressive cell line B16-F10 when compared to its parental cell line B16-F0 (Figure 88 B).

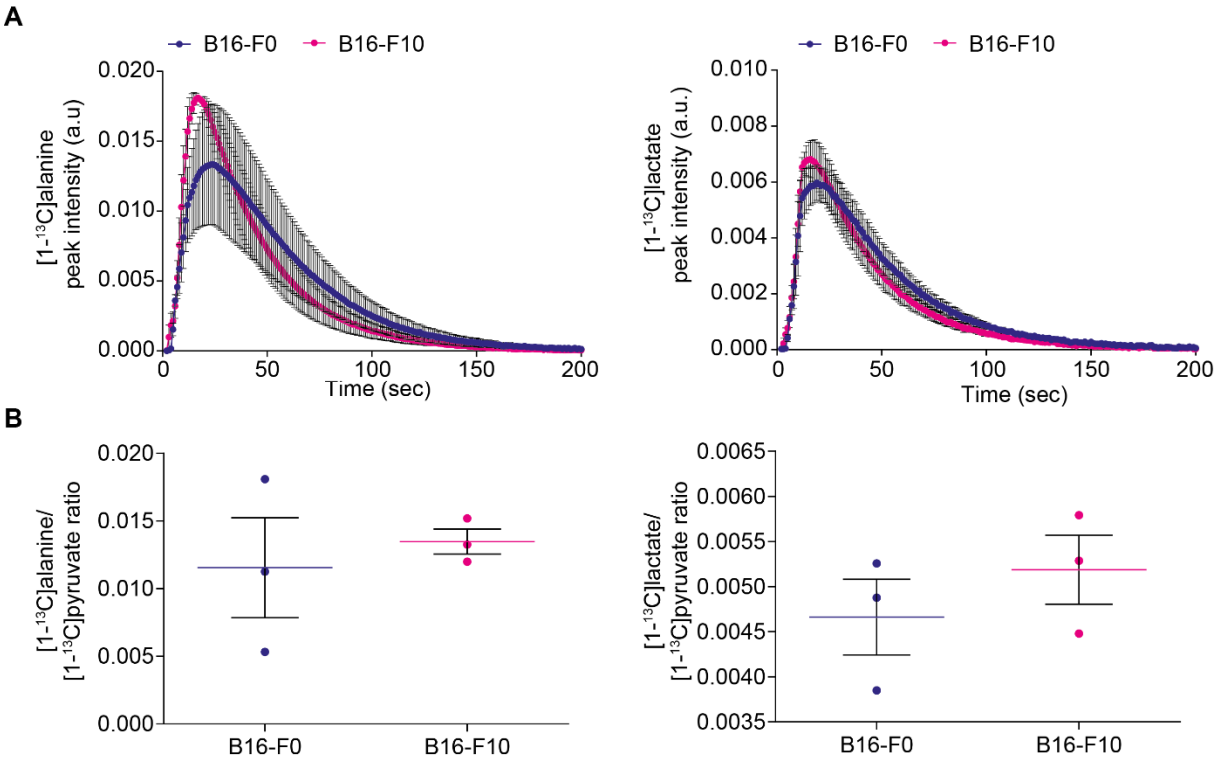

Figure 88: ^{13}C spectroscopic analysis of [1-^{13}C]pyruvate metabolism in B16-F0 and B16-F10 melanoma cells.

Dynamic conversion of [1-^{13}C]pyruvate to [1-^{13}C]alanine (**A**, left panel) and [1-^{13}C]lactate (**A**, right panel) in the melanoma cell lines B16-F0 and B16-F10 (peak intensity in arbitrary units, a. u.) resulted in a trend towards an overall higher [1-^{13}C]alanine (**B**, left panel) and [1-^{13}C]lactate (**B**, right panel) production in the more aggressive B16-F10 cell line compared to the parental cell line B16-F0 (values are given as mean ± SEM, n=3 for B16-F0, n=3 for B16-F10).

In direct comparison (Figure 89), the melanoma cell lines B16-F0 and B16-F10 metabolized more of the applied [1-^{13}C]pyruvate resulting in both higher concentrations of [1-^{13}C]alanine (Figure 89 A) and [1-^{13}C]lactate (Figure 89 B) in the B16-F0 and B16-F10 melanoma cells in comparison to the PyMT breast cancer cell lines S2WTP3 and ML1B1B1.

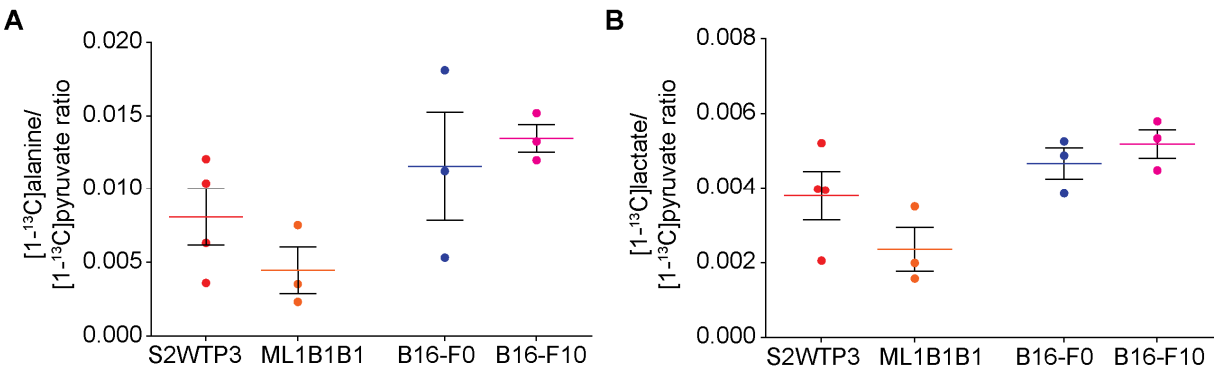

Figure 89: Summary of the ^{13}C spectroscopic analysis of [1-^{13}C]pyruvate metabolism in PyMT and melanoma cell lines.

[1-^{13}C]alanine/[1-^{13}C]pyruvate ratios (**A**) and [1-^{13}C]lactate/[1-^{13}C]pyruvate ratios (**B**) resulting from the dynamic conversion of applied hyperpolarized [1-^{13}C]pyruvate in the PyMT cell lines S2WTP3 and ML1B1B1 and the melanoma cell lines B16-F0 and B16-F10 (mean ± SEM, n=4 for S2WTP3, n=3 for ML1B1B1, B16-F0 and B16-F10).

4.3.5 Proteomic, transcriptomic and metabolomic analysis of cell extracts

The differential degree of aggressiveness seen in the PyMT cell lines S2WTP3 and ML1B1B1 was further investigated by untargeted analysis of the total protein content of the cells and metabolomic analysis of polar, soluble metabolites. Transcriptomic profiling was performed by qRT-PCR to confirm proteomic analysis. The analysis of the proteomics data was performed by Dr. Mohamed Ali Jarboui, metabolomic data was analyzed by Dr. Christoph Trautwein.

Proteomics

A total of 4351 proteins were confidentially detected with a false discovery rate of 0.01 at peptide and protein level. The detected proteins were analyzed against the Uniprot mouse database (Uniprot Consortium, 2017) to identify differentially expressed proteins. For the comparative analysis of the proteome of the two PyMT cell lines, the relative protein abundance was calculated as a ratio of ML1B1B1 to S2WTP3 (ML1B1B1/S2WTP3).

First, PCA analysis confirmed that the biological replicates did not show a high degree of intragroup heterogeneity (Figure 90) but protein intensities were largely homogenous throughout the replicates.

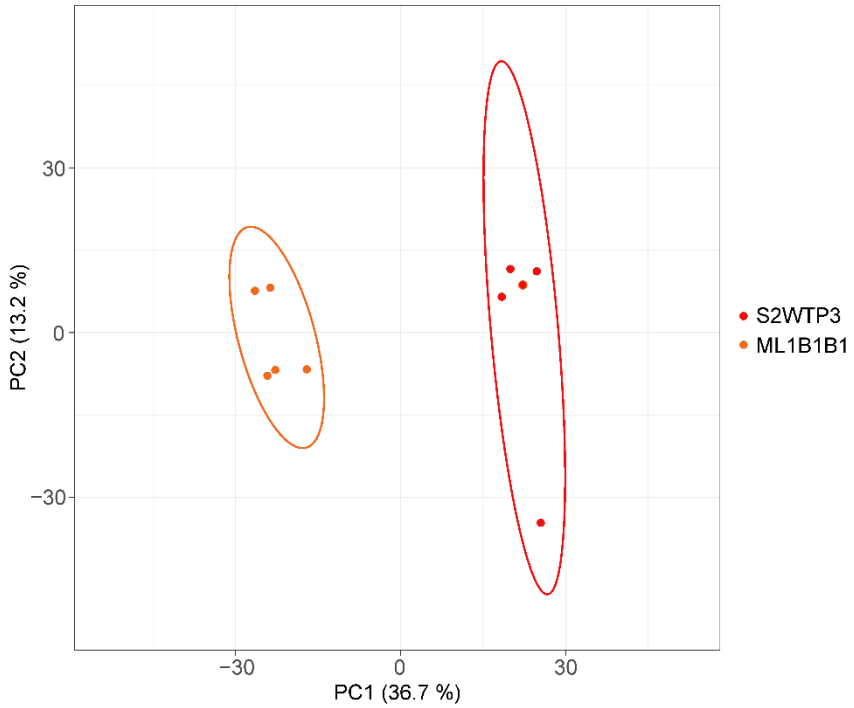

Figure 90: PCA analysis of protein abundance in the biological replicates.
PCA analysis performed on Log2 transformed label free quantification intensities from all biological replicates revealed homogeneity in protein expression and a clear segregation of the S2WTP3 and ML1B1B1 cell extract samples.

The mean ratio ML1B1B1/S2WTP3 for all biological replicates was calculated, subjected to statistical analysis (as described in section 3.9.1) and displayed as volcano plot on a logarithmic scale for visualization (Figure 91).

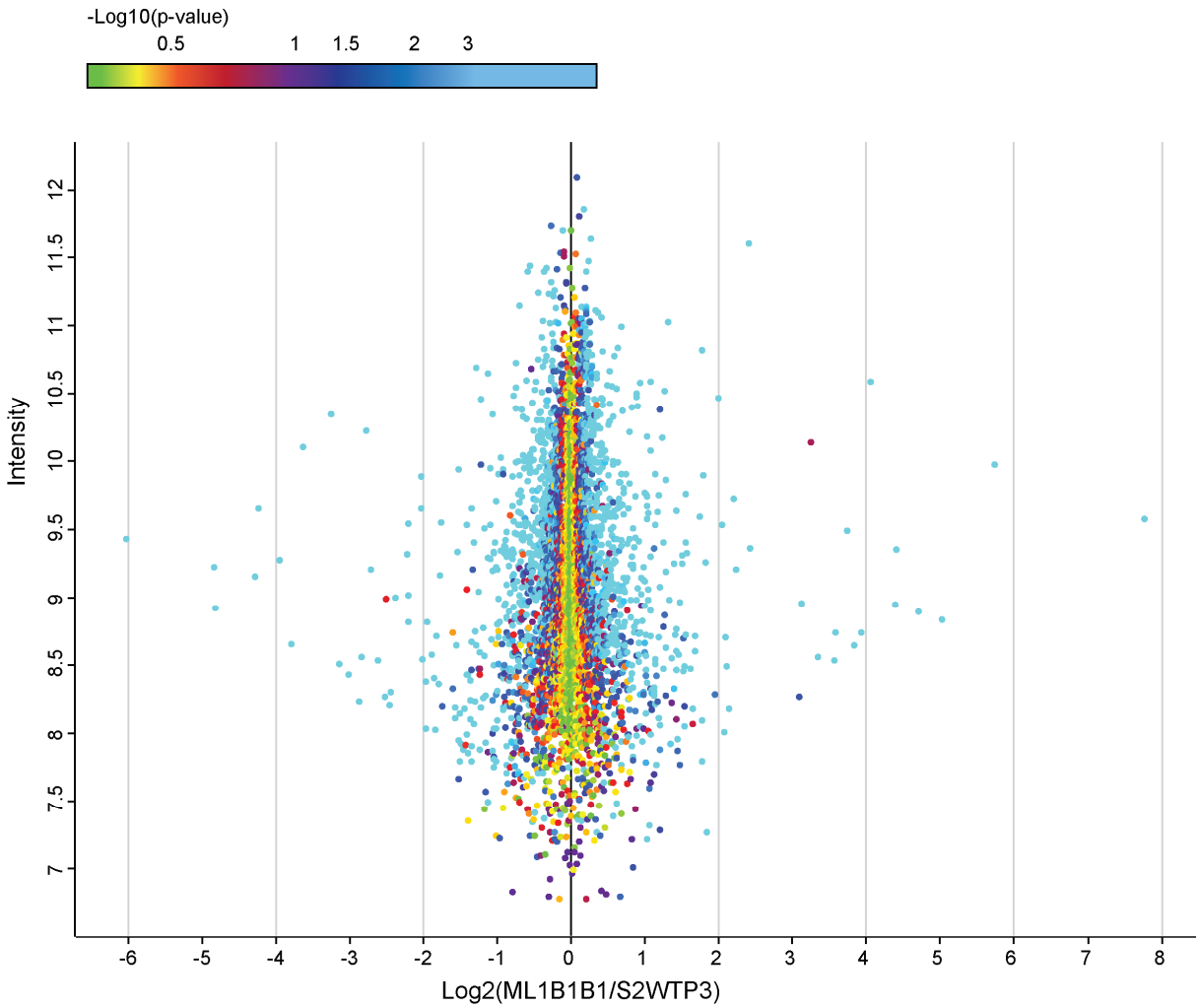

Figure 91: Scatter plot of the most significant changes in protein abundance.
The log2(ML1B1B1/S2WTP3) of protein abundance revealed differences in the proteome of the PyMT cell lines S2WTP3 and ML1B1B1: Proteins higher in abundance in ML1B1B1 are represented on the right side and proteins higher in abundance in S2WTP3 on the left side of the zero baseline in the central scatter plot. Proteins on the zero baseline did not significantly change in abundance when comparing the two cell lines.

Although PCA segregated the two examined groups clearly, tissue signature ontology analysis revealed several similarities in protein expression in S2WTP3 and ML1B1B1 cells (Figure 92). As the S2WTP3 cell line originates from the PyMT breast cancer mouse model, a high similarity in the expressed proteins to breast tissue (54.17 %, $p<0.001$) and breast cancer (62.60 %, $p<0.001$) was detected. Further, similarity to lung tissue (54.74 %, $p<0.01$) and lung cancer (69.47 %, $p<0.01$) was detected. Additionally, the S2WTP3 proteome exhibited low degrees of similarities to mesenchymal stromal cells (5.21 %, $p<0.01$), embryonal carcinoma cells (16.67 %, $p<0.001$) and embryonic stem cells (34.38 %, $p<0.001$).

The ML1B1B1 proteome exhibited higher similarities to mesenchymal stromal cells (8.42 %, $p<0.001$), embryonal carcinoma cells (20.00%, $p<0.001$) and embryonic stem cells (41.05 %) than the S2WTP3 proteome. Interestingly, the percentage of similarity in protein expression compared to breast tissue (47.43 %, $p<0.001$), breast cancer (55.79 %, $p<0.01$), lung tissue

(54.74 %, p<0.01) and lung cancer (69.47 %, p<0.01) was lower than in the S2WTP3 proteome.

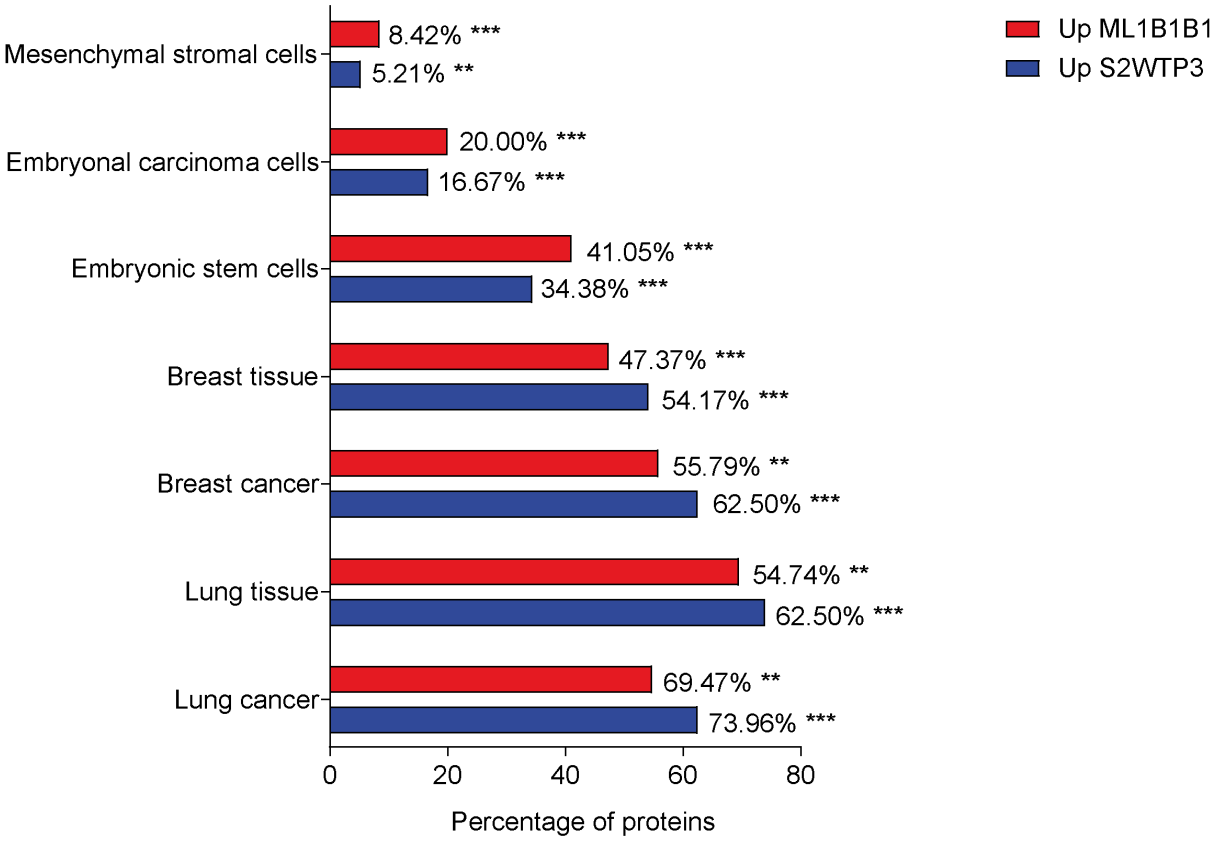

Figure 92: Tissue signature ontology analysis of the proteomes of S2WTP3 and ML1B1B1 cells. The proteome of both S2WTP3 and ML1B1B1 showed similarity to the proteome signature of mesenchymal stromal cells, embryonal carcinoma cells and embryonic stem cells. Further, a high degree of similarity in the expressed proteins in breast tissue, breast cancer, lung tissue and lung cancer was found (statistics: Students' t-test with **p<0.01 and ***p<0.001).

Biological pathway analysis (Figure 93) revealed a high likelihood of proteins specifically enriched in the salvage pathways of pyrimidine ribonucleotides in ML1B1B1 (3.85 %, p<0.01) in comparison to S2WTP3. Importantly, proteins specifically involved in EMT were more abundant in ML1B1B1 (5.77 %) than in S2WTP3 (1.96 %). Additionally, proteins in the SLC-mediated transmembrane transport (17.31 %, p<0.001 vs. 9.80 %, p<0.05), the S1P1 pathway (42.31 %, p<0.001 vs. 25.49 %), EGFR-dependent endothelin signaling events (42.31 %, p<0.001 vs. 25.49 %), integrin family cell surface interactions (42.15 %, p<0.001 vs. 25.49 %), proteoglycan syndecan-mediated signaling events (48.08 %, p<0.001 vs. 25.49 %), β1 integrin cell surface interactions (44.23 %, p<0.001 vs. 25.49 %) and nectin adhesion pathways (42.31 %, p<0.001 vs. 27.45 %) were more abundant in ML1B1B1 compared to S2WTP3, respectively. In contrast, proteins specifically involved in MET were more abundant in S2WTP3 than in ML1B1B1 (13.73 %, p<0.01 vs. 7.89 %).

Interestingly, besides the salvage pathway of pyrimidine ribonucleotides, no differences in abundance were confidentially detected for proteins involved in metabolic pathways.

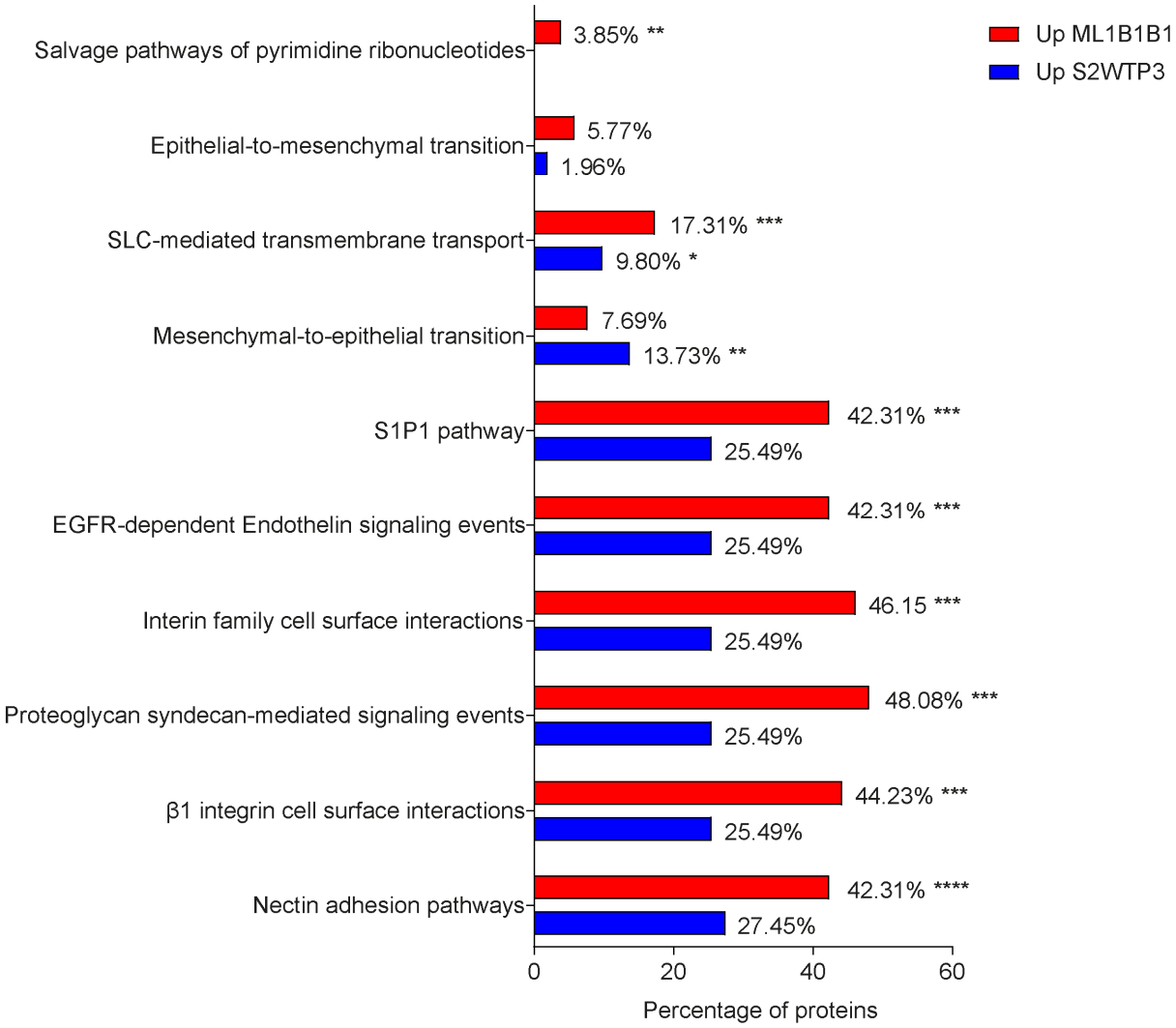

Figure 93: Biological pathway analysis of the S2WTP3 and ML1B1B1 proteomes.
The comparison of the S2WTP3 proteome and the ML1B1B1 proteome revealed striking differences in the percentages of the proteins involved in the respective biological pathway (mean in percent, statistics: Student's t-test, *p<0.05, **p<0.01, ***p<0.001).

The determining proteins for the ontology analysis include vimentin, plectin, nestin, galectin-1, galectin-3, CD44, CD63, CD109, notch1, R-ras, sphingosine kinase 1, embryonic stem cell-specific 5-hydroxymethylcytosine-binding protein (HMCES), cell division cycle-associated protein 3 (CDCA3). These proteins were enriched in ML1B1B1 compared to S2WTP3 (Figure 94).

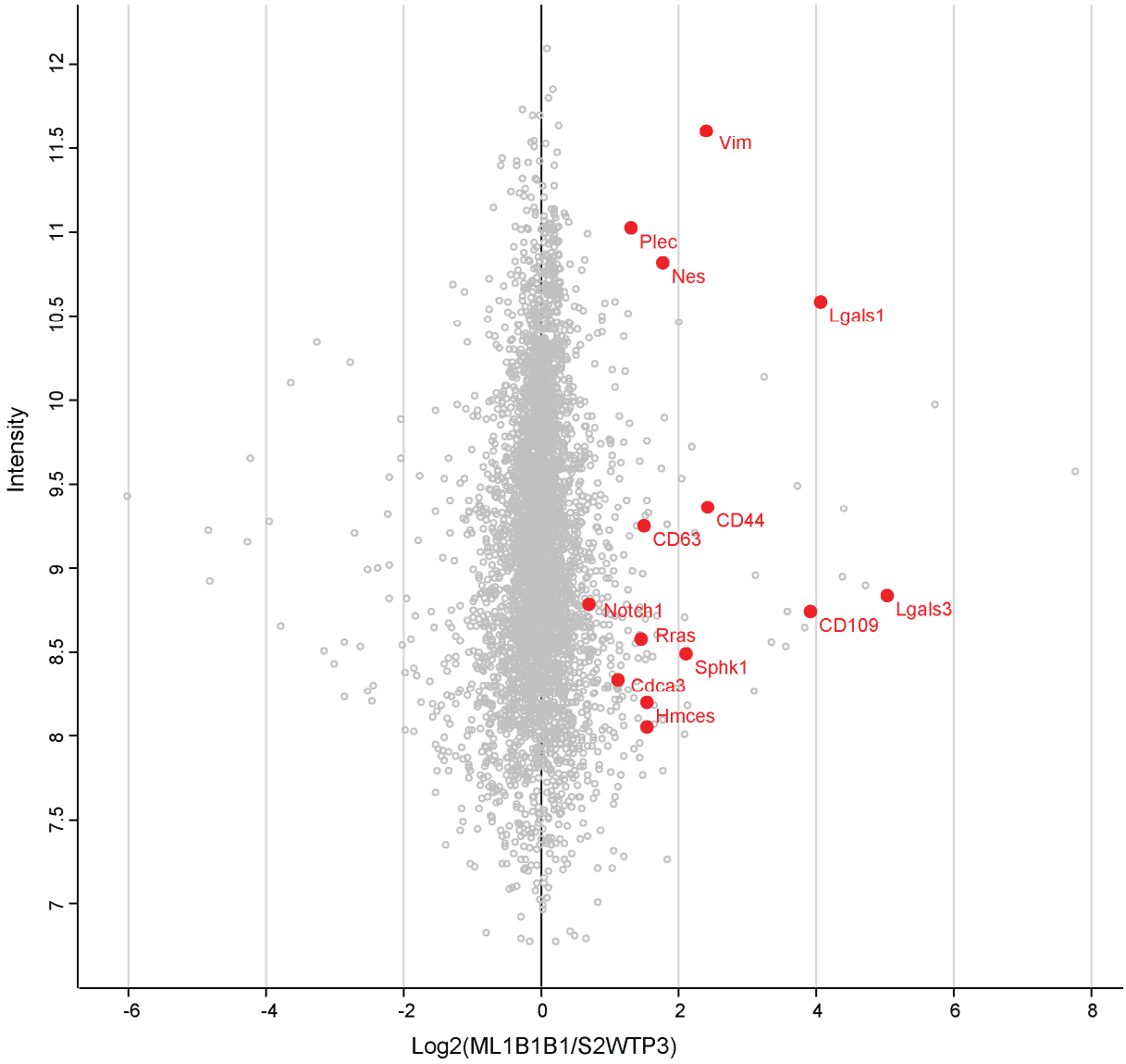

Figure 94: Scatter plot illustrating the log2(ML1B1B1/S2WTP3) of proteins involved in EMT and markers for cancer stemness.

The log2(ML1B1B1/S2WTP3) of the proteins vimentin, plectin, nestin, galectin-1, galectin-3, CD44, CD63, CD109, notch1, R-ras, sphingosine kinase 1, HMCES and CDCA3 were highlighted in red (for visualization, proteins are referred to by the name of their encoding gene: Vimentin-Vim, Plectin-Plec, Nestin-Nes, Galectin-1-Lgals1, Galectin-3-Lgals3, CD44, CD63, CD109, Notch1, R-Ras-Rras, Sphingosine Kinase 1-Sphk1, Embryonic stem cell-specific 5-hydroxymethylcytosine-binding protein - Hmces, Cell division cycle-associated protein 3-Cdca3).

Transcriptomic analysis

For gene expression analysis of S2WTP3 and ML1B1B1 cells, and of B16-F0 and B16-F10 melanoma cells, RT-PCR was performed. The genes of interest were chosen due to their involvement in EMT, invasion and metastasis such as *Mmp9*, *Vim*, *Fak*, *Cdh1* and *Cdh2* or metabolism encoding key enzymes such as *Fasn*, *Pdha1*, *Acaca*, *Gapdh* and *Aldoa*. Further, expression of the glucose transporter GLUT1 (*Slc2a1*) was examined as differences in the [^{18}F]FDG uptake were detected between the cell lines *in vitro* (refer to section 4.3.2). Changes

in gene expression were calculated with the standard $\Delta\Delta C_t$ method resulting in a fold change normalized to the respective parental cell line.

Expression of *Mmp9* and *Fak* did not increase in ML1B1B1 cells, while - in concordance to proteomics - *Vim* and *Cdh1* expression did increase. Interestingly, no expression of *Cdh2* could be found in ML1B1B1 cells (Figure 95 A). The genes *Acaca* and *Gapdh* (Figure 95 B) were expressed to a higher degree in ML1B1B1 while S2WTP3 cells expressed higher levels of *Fasn*, *Pdha1*, *Slc2a1* and *Aldoa*. Interestingly, the reduced expression of *Slc2a1* is in contrast to the increased [^{18}F]FDG uptake in the more aggressive cell line ML1B1B1 (refer to section 4.3.2).

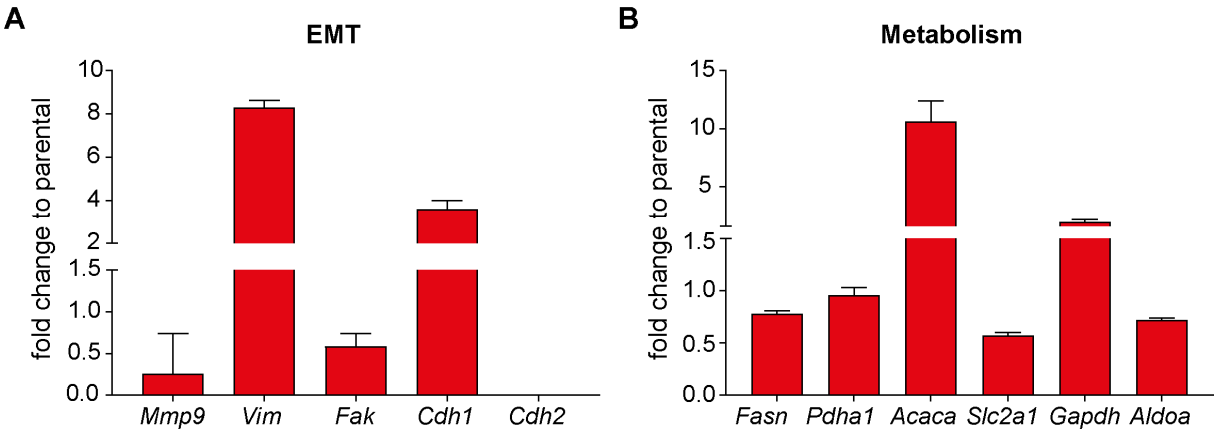

Figure 95: Gene expression analysis of the PyMT cell lines S2WTP3 and ML1B1B1.
Expression profiling of certain genes involved in EMT (**A**) and key metabolic pathways (**B**) by qRT-PCR revealed striking differences in ML1B1B1 cells compared to S2WTP3 cells (fold change + error in ML1B1B1 normalized to S2WTP3 calculated according to the $\Delta\Delta C_t$ method, β-actin served as reference gene, n=3 for all conditions).

The correlation of the gene expression profiling analysis with the proteomics data for S2WTP3 and ML1B1B1 cells confirmed proteomics data revealing a higher abundance of the corresponding protein for the genes *Vim*, *Acaca*, *Cdh1*, and a lower abundance of the corresponding protein for the genes *Aldoa*, *Aldoc*, *Pdha1* and *Cdh2* (Figure 96).

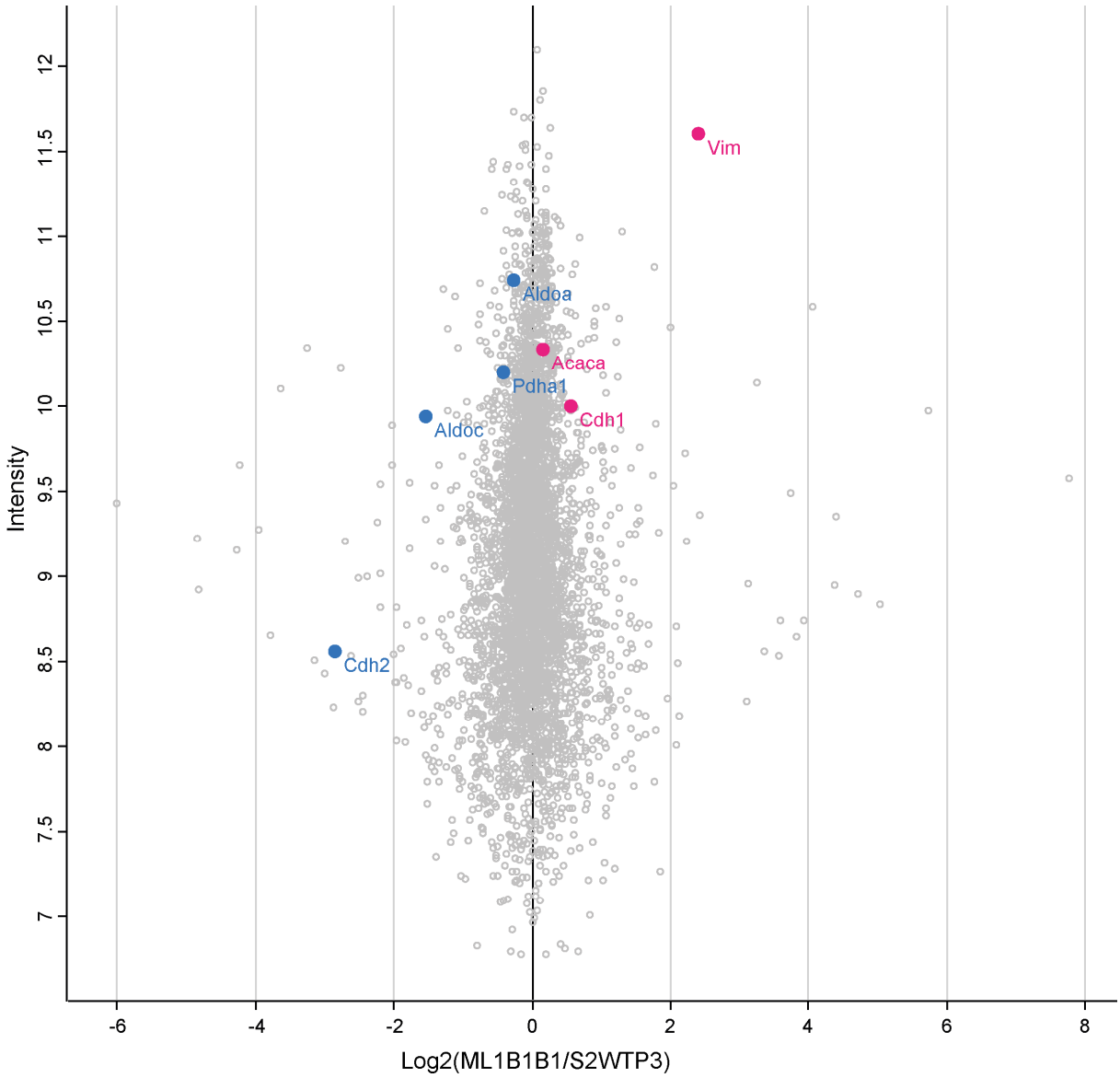

Figure 96: Volcano plot correlating transcriptomic profiling by RT-PCR and proteomic analysis. By transcriptomic profiling with RT-PCR, the mRNA levels of gene expression and protein abundance were successfully correlated in the scatter plot visualization of the Log2(ML1B1B1/S2WTP3) (downregulated proteins in ML1B1B1 are highlighted in blue, upregulated proteins in ML1B1B1 in magenta).

Additionally, gene expression analysis by RT-PCR was performed for the melanoma cell lines B16-F0 and B16-F10 (Figure 97). Interestingly, in contrast to the PyMT cell lines, the more aggressive B16-F10 cells had upregulated both *Mmp9* and *Cdh2* while no upregulation of *Vim* and *Cdh1* was observed (Figure 97 A). Additionally, gene expression of *Aldoa* encoding the glycolysis rate-determining enzyme aldolase was upregulated in B16-F10 cells as compared to B16-F0 while *Pdha1* was downregulated B16-F10 cells as compared to B16-F0 (Figure 97 B). Further, gene expression of *Fasn*, *Acaca*, *Slc2a1* and *Gapdh* was downregulated in B16-F10 cells compared to B16-F0 cells. As already mentioned before, the reduced expression of *Slc1a1* is in contrast to the increased [^{18}F]FDG uptake in the more aggressive B16-F10 cell line (refer to section 4.3.2).

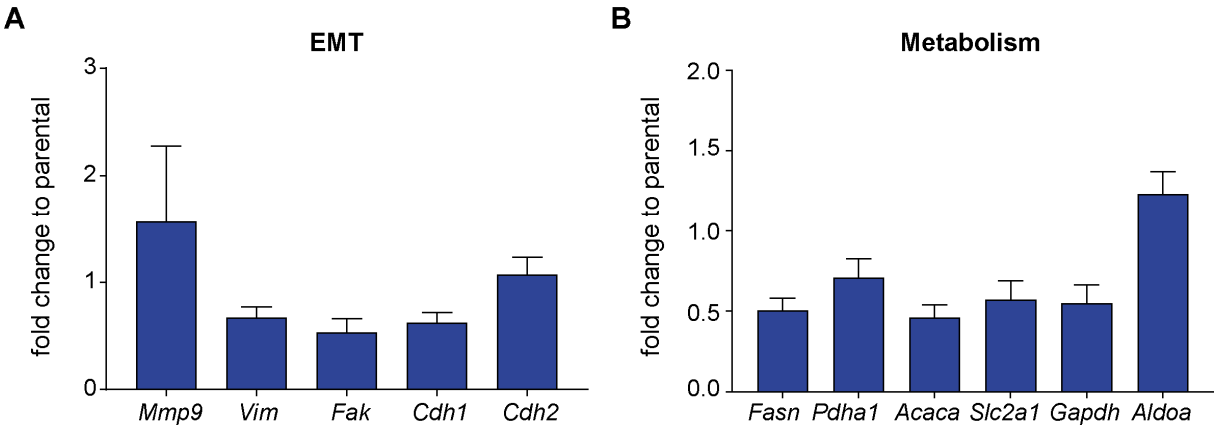

Figure 97: Gene expression analysis of the melanoma cell lines B16-F0 and B16-F10.
Expression profiling of genes involved in EMT (**A**) and key metabolic pathways (**B**) by RT-PCR revealed differences in B16-F10 cells compared to B16-F0 cells (fold change + error in B16-F10 normalized to B16-F0 according to the $\Delta\Delta C_t$ method, β-actin served as reference gene, n=3 for all conditions).

Metabolomics

For metabolomic analysis, 5 replicates each of $3x10^7$ S2WTP3 cells and $3x10^7$ ML1B1B1 cells were prepared. Cellular metabolism was stopped by addition of methanol and, subsequently, a 2-phase cell extraction was performed with methyl tert-butyl ether. The polar fraction of S2WTP3 and ML1B1B1 cell extracts was used for metabolomic fingerprinting by ^{1}H NMR spectroscopy. The obtained ^{1}H spectra of S2WTP3 and ML1B1B1 cell extracts are given Figure 104 and Figure 105, respectively, which are provided in the appendix (section 10, page 255 and 256). Metabolomics data was analyzed by Dr. Christoph Trautwein and Dr. Mohamed Ali Jarboui.

In chemometric analysis, 73 metabolite resonances were detected and assigned to 35 different metabolites in both groups. PCA analysis of the metabolomic fingerprinting demonstrated a clear segregation of S2WTP3 and ML1B1B1 polar cell extracts (Figure 98).

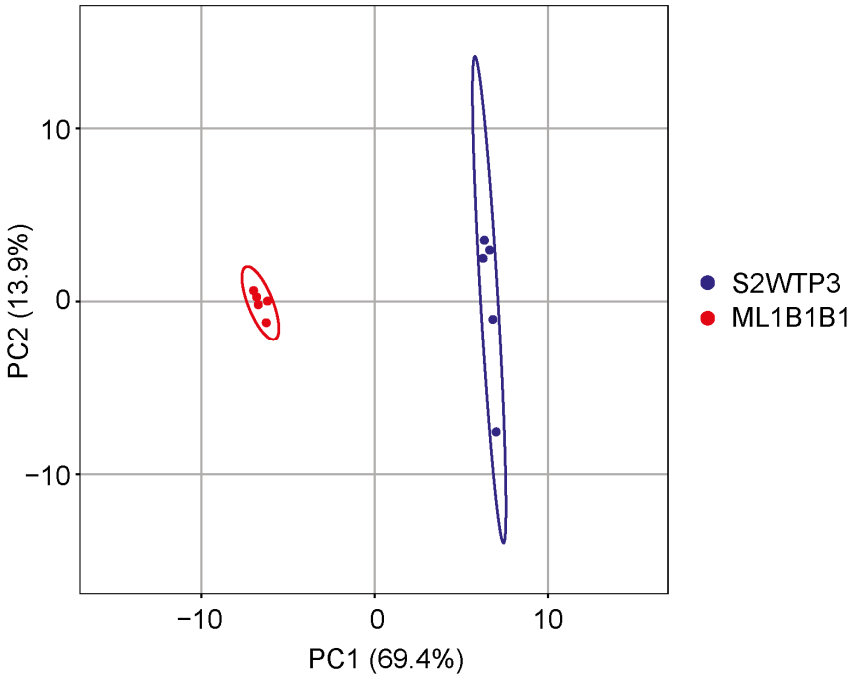

Figure 98: PCA of the metabolome of S2WTP3 and ML1B1B1 cells.
PCA analysis revealed an accurate discrimination of metabolites for the two groups S2WTP3 and ML1B1B1.

Hierarchical clustering analysis (Figure 99) resulted in the separation of the metabolite intensities in 5 clusters. Cluster 1 and 2 covered metabolite resonances increased in ML1B1B1 in comparison to S2WTP3. Cluster 1 was composed of the essential amino acids leucine and valine and the non-essential amino acids proline. Cluster 2 encompassed uridine diphosphate (UDP)-activated glucose, -N-acetylglucosamine (GlcNAc) and –N-acetylgalactoseamine (GalNAc) as well as the adenosine nucleotides AMP, ADP, ATP. Further small metabolites included hypoxanthine, lactate, succinate, glutamate, phosphocholine and the amino acids isoleucine and β-alanine. Cluster 3 and 4 encompassed metabolite resonances with pronounced changes, however, there was a higher variability between the replicates and intensities of the amino acids threonine, phenylalanine and tyrosine and the small metabolites uracil, inosine, taurine and acetate. Cluster 5 contained metabolite resonances that had decreased in ML1B1B1 in comparison S2WTP3. Detected resonances in cluster 5 included amino acids aspartate, methionine, glycine and threonine, the antioxidant glutathione, pantothenate, myo-inositol, uridine and the nucleosides adenosine and guanosine.

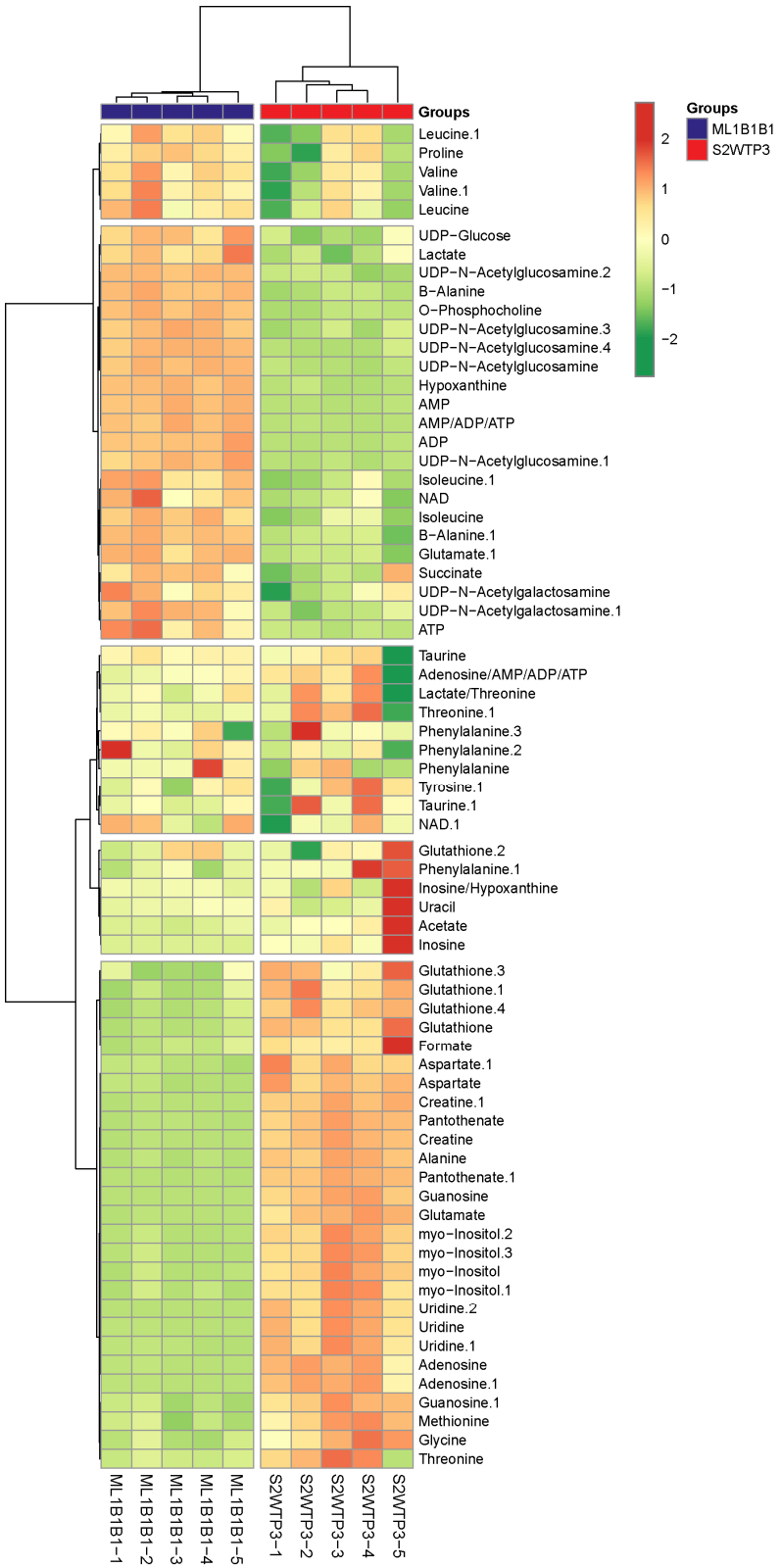

Figure 99: Hierarchical clustering of the detected metabolite resonances of the ^{1}H NMR metabolomic fingerprinting of S2WTP3 and ML1B1B1 cell extracts.

Euclidean distance measure and Ward clustering were used for hierarchical clustering heat map. The determined intensity is plotted in red-green color scale: red indicates significantly higher intensity, green low intensity metabolomic data were normalized and autoscaled to minimum and maximum of each feature. The top features were selected based on Student's t-test p-value threshold <0.05.

A focus on the top 20 most significantly changed resonances of metabolites is given in Figure 100. Significant increases in the metabolite intensities were observed for hypoxanthine and the adenosine nucleotide species AMP, ADP and ATP in ML1B1B1 cell extracts (Figure 100, upper panel). Furthermore, higher intensities of UDP-GlcNAc and β-alanine were detected in ML1B1B1 cell extracts. Interestingly, higher intensities of phosphocholine were detected in ML1B1B1 cell extracts.

In S2WTP3 cell extracts, pantothenate intensities increased significantly (Figure 100, lower panel). Besides, the intensities of the amino acids aspartate, glutamate, alanine and the amino acid derivate creatine were higher in S2WTP3 cell extracts in comparison to ML1B1B1 cell extracts. Further, the nucleosides uridine and guanosine as well as *myo*-inositol had higher intensities in S2WTP3 cell extracts compared to ML1B1B1 cell extracts. Interestingly, higher alanine intensity were detected in the S2WTP3 cell extracts in comparison to ML1B1B1 cell extracts.

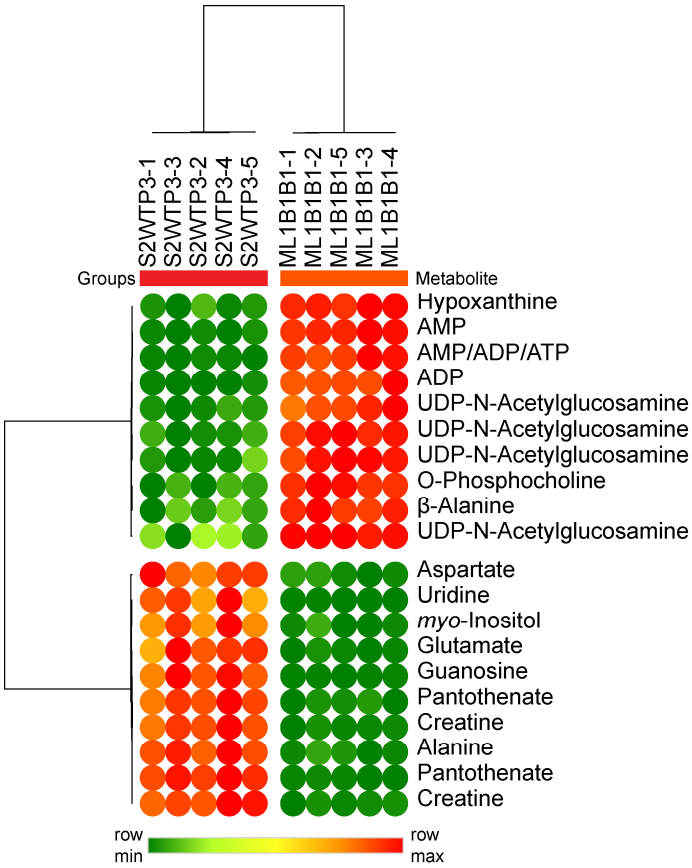

Figure 100: Heat map representation of the top 20 changes of ^{1}H resonances in the metabolomic analysis of S2WTP3 and ML1B1B1 cell extracts.

Heat map analysis of the metabolite resonances in the S2WTP3 and ML1B1B1 cell extracts revealed significantly higher intensities for the top panel of metabolites and significantly lower intensities for the lower panel of metabolites in ML1B1B1 cell extracts compared to S2WTP3 cell extracts (data was processed as follows: quantile normalization, pareto scaling, fold change threshold >2.0, false discovery rate adjusted p-value threshold <0.05).

A summary of the results of the multiparametric comparative analyses of the metabolic behavior of the more aggressive cell line ML1B1B1 in comparison to S2WTP3 is given in Table 5. The summarized results elucidate a mismatch between the metabolism of the cell line *in vitro* and the cell line-derived allograft tumors *in vivo*/*ex vivo*.

Table 5: Summary of the metabolomic analyses of the PyMT-derived cell line ML1B1B1 in comparison to S2WTP3.

***In vitro* experiments**	***In vivo* and *ex vivo* experiments**
• [^{18}F]FDG uptake increased in ML1B1B1 (refer to section 4.3.2)	• no significant differences in [^{18}F]FDG uptake between ML1B1B1 allografts and S2WTP3 allografts (refer to section 4.3.2)
• [1-^{13}C]alanine and [1-^{13}C]lactate production decreased (refer to section 4.3.4) in ML1B1B1 cells in comparison to S2WTP3 cells • decreased alanine concentration in ^{1}H metabolomics in ML1B1B1 cells in comparison to S2WTP3 cells (see above)	• no significant differences in alanine and lactate intensity between ML1B1B1 allografts and S2WTP3 allografts in *ex vivo* ^{1}H HR-MAS NMR (refer to section 4.3.3)
• *In vitro* PCho/Cho ratio higher in ^{1}H metabolomic fingerprinting in ML1B1B1 cells in comparison to S2WTP3 cells (see above)	• *In vivo* and *ex vivo* PCho/Cho ratio higher in ML1B1B1 allografts than in S2WTP3 allografts in ^{1}H spectroscopy (refer to section 4.3.3)

5 DISCUSSION

5.1 MDSC cell tracking with non-invasive imaging modalities

5.1.1 Characterization of bone marrow-derived, *in vitro* differentiated MDSCs

MDSCs, considered incompletely differentiated, aberrantly activated myeloid cells, are characterized by the expression of $CD11b^{+}/Ly6C^{int}/Ly6G^{+}$ in PMN- and $CD11b^{+}/Ly6C^{high}/Ly6G^{-}$ in M-MDSCs and suppressive activity against immune cell function (Bronte *et al.*, 2016). PMN- and M-MDSCs with the capacity to suppress both antigen-induced and unspecifically provoked proliferation of $CD8^{+}$ T cells were differentiated from BMDCs of wild type C57BL/6 mice according to a previously published protocol (Sceneay *et al.*, 2018). This protocol represents an adaptation of the frequently cited culture protocol for the expansion of bone marrow-derived MDSCs by Marigo *et al.* (Marigo *et al.*, 2010).

Current literature reports differences in the immunosuppressive capacity of PMN- and M-MDSCs on a cell basis with M-MDSCs exhibiting a more potent immunosuppressive activity (Kumar *et al.*, 2016). Divergent from these findings, *in vitro* expanded MDSC subpopulations did not exhibit differences in their immunosuppressive capacity. GM-CSF, however, was reported to determine the immunosuppressive strength of MDSC subsets (Dolcetti *et al.*, 2010). The PMN- and M-MDSCs used for cell tracking experiments were isolated from the same *in vitro* culture system and therefore experienced the same concentration of GM-CSF during their expansion. It is therefore possible that the *in vitro* culture system used in this work abrogated the hierarchy in the immunosuppressive strength of PMN- and M-MDSCs. Although the expansion of PMN- and M-MDSCs *in vivo* in tumor-bearing animals would have produced the exact phenotype of biologically relevant MDSCs, this approach was not feasible in C57BL/6 mice. Indeed, even as tumor growth in PyMT-bearing mice was accompanied by expansion of both MDSC subpopulations *in vivo*, the cell numbers for PMN- and M-MDSCs needed for cell tracking studies could not be obtained from tumor-bearing mice.

The use of tumor cell CM supplemented with GM-CSF represents another method to expand and differentiate myeloid BMDCs to MDSCs *in vitro* (Liechtenstein *et al.*, 2014). The content of cytokines, growth factors and CSFs in tumor cell CM, however, might change between lots, especially in self-made CM. As the comparison of the migration dynamics and tumor homing of PMN- and M-MDSCs in different mouse models for primary and metastatic cancer was one aim of this work, the culture conditions for MDSCs had to be kept constant and possible biological variances between tumor cell CM aliquots were avoided by using clean, efficiency-tested recombinant cytokines.

Although the CD marker-defined phenotype and immunosuppressive function of both MDSC subpopulations conformed to the recently published recommendations for the identification of

PMN- and M-MDSCs (Bronte *et al.*, 2016), gene expression profiling of both MDSC populations from the *in vitro* culture system revealed significant differences in the mRNA expression levels of proteins relevant for MDSC function. Interestingly, the expression of *S100A8*- and *S100A9*- as well as *Arg1*- and *Arg2*-mRNA varied considerably between MDSCs isolated from different tissues of PyMT tumor-bearing mice. This is, however, consistent with the view of MDSCs as a continuum of myeloid cells with immunosuppressive function (Kumar *et al.*, 2016). Tumor-resident MDSCs did show the highest expression of *Arg1*-mRNA pointing towards high expression and activity of ARG1 and, consequently, high suppressive activity as seen in tumor-infiltrating MDSCs (Maenhout *et al.*, 2014).

5.1.2 MDSC tracking with optical imaging

Although tumor-, PMN- and metastasis-promoting functions of MDSCs were recognized a few decades ago leading to a spike in preclinical and clinical studies on MDSC functional characterization and biology, scarcely any studies aimed to characterize MDSC migration behavior *in vivo*.

Non-invasive imaging of the migration of adoptively transferred MDSCs *in vivo* by fluorescence OI requires labeling of the cells, either indirectly or directly, with a fluorescent reporter such as a fluorescent dye before adoptive cell transfer (Kircher *et al.*, 2011; Ottobrini *et al.*, 2011). Direct cell labeling with fluorescent compounds that insert into the cell membrane, as performed in this work, represents a straightforward, feasible method for cell migration studies (Sutton *et al.*, 2008). Labeling of PMN-MDSCs with the dye DiD for *in vivo* fluorescence OI was performed previously in an international research collaboration project with the QIMR Berghofer Medical Research Institute in Brisbane, Australia (Sceneay *et al.*, 2018). In the consecutive study presented in section 4.1.2, the same labeling approach was used for of M-MDSCs to assess if DiD-M-MDSCs home to the primary breast cancer TME and compare tumor homing dynamics of DiD-M-MDSCs and DiD-PMN-MDSCs. Consequently, this imaging approach represented a preliminary study to assess if M-MDSCs were eligible for PET imaging studies as previously shown for PMN-MDSCs. Hence, in this preliminary proof-of-concept study for M-MDSC migration, the effects of the dye DiD on viability and functionality of PMN- and M-MDSCs were not further evaluated.

Indeed, both DiD-PMN- and DiD-M-MDSCs could be detected in the primary PyMT breast cancer tumor at 48 h pt *in vivo* by fluorescence OI. The fluorescence signal of both DiD-PMN- and DiD-M-MDSCs seemed to decrease over the experimental time of 96 h, however, quantification of the *in vivo* fluorescence signal was not performed due to the methodological and physical restrictions of planar fluorescence OI (Ntziachristos, 2006). Quantification of

isolated organs was performed on *ex vivo* fluorescence OI images to reduce absorption of photons and eliminate photon scattering in the tissue and at the skin. The semi-quantitative analysis of the isolated organs clearly substantiated the accumulation of both DiD-PMN- and DiD-M-MDSCs in the primary PyMT breast tumor. Interestingly, the fluorescence signal from DiD-M-MDSCs in the breast cancer allograft was higher than the DiD-PMN-MDSCs signal indicating the recruitment of a greater fraction of the adoptively transferred DiD-M-MDSCs. Significant differences between the two MDSC subpopulations, however, could only be detected in the heart and lungs but not in the tumor. Additionally to the signal derived from DiD-PMN- and DiD-M-MDSCs in the liver of the tumor-bearing animals, the signal in the liver might partially constitute artifacts form the labeling procedure with the fluorescent dye formulation DiD. DiD and dye formulations with the same mode of action integrate into the cell membrane after a short incubation time. Cell labeling with these formulations does not result in a covalent chemical bond but is mediated via non-covalent interactions. Consequently, the labeling is not stabile and the dye can be transferred to other cell types, e.g. macrophages, after close cell-to-cell interactions and via exchange of membrane microdomains (Boomsma and Geenen, 2014; Lassailly *et al.*, 2010). In one of the very few MDSC tracking studies published to date, Combes *et al*. further demonstrated a high liver accumulation of dead cells and cellular debris labeled with the dye 1,1′-dioctadecyl-3,3,3′,3′-tetramethylindotricarbocyanine iodide (DiR), a dye closely related to DiD (Combes *et al.*, 2018). Cellular debris might result from physical sheering stress during *i.v.* injection into the lateral tail vein. In this study, the authors did not separate MDSC subpopulations before *i.v.* injection into syngeneic 4T1 breast tumor-bearing BALB/c mice but only identified PMN-MDSCs as predominant MDSC subpopulation. Additionally, PMN-MDSCs are rather short-lived cells in comparison to M-MDSCs (Kumar *et al.*, 2016). DiD released from DiD-PMN-MDSCs could have been taken up by Kupffer cells in the liver resulting in a pronounced liver signal in the DiD-PMN-MDSC group. Hepatobiliary and renal elimination were observed for fluorescent dyes in mice (Press *et al.*, 2017) further suggesting that elimination of the fluorescent dye DiD released from DiD-PMN- or DiD-M-MDSCs resulted in liver signal in both adoptive cell transfer groups.

The *in vivo* OI data was further confirmed *ex vivo* by flow cytometric analysis of the tumor tissue, the lungs and spleen. In concordance with previous work (Sceneay *et al.*, 2018), DiD-PMN-MDSC accumulation was detected in the primary tumor. DiD-positive subpopulations were further found in tumor-resident $CD11b^+/F4/80^+$ macrophages and $CD11b^+/CD11c^+$ DCs. In the lungs and spleen of tumor-bearing animals, a small fraction of DiD-PMN-MDSCs and DiD-positive populations of macrophages and DCs could be detected.

In concordance with the *ex vivo* OI images, the percentage of DiD-M-MDSCs detected in the primary PyMT tumor by flow cytometry was higher than the fraction of DiD-PMN-MDSCs. The

same was the case in both the lung and the spleen. Interestingly, M-MDSCs were also the predominant MDSC subpopulation in the tumor-bearing control animals. This is in concordance to current literature and first studies distinguishing between MDSC subpopulations and reporting $CD14^{+}$/HLA-$DR^{low/-}$ MDSCs in breast cancer patients (Bergenfelz *et al.*, 2015; Diaz-Montero *et al.*, 2009; Speigl *et al.*, 2018). Comparable to the DiD-PMN-MDSC treatment group, DiD-positive macrophage subpopulations were found in the tumor, lung and spleen of mice in the DiD-M-MDSC group. The fraction of DiD-positive DCs, however, was strikingly lower than in the DiD-PMN-MDSC group. M-MDSCs originate from the common precursor of DCs and macrophages and, according to current literature, represent a continuum of cells of incomplete differentiation and alternative activation. Differentiation of M-MDSCs to macrophages or DCs in response to a stimulus encountered in the TME was shown in different tumor models (Franklin *et al.*, 2014; Movahedi *et al.*, 2008) including the transgenic MMTV-PyMT model (Qian *et al.*, 2011) that served as basis for the experiment breast cancer model used in this work.

Additionally to OI, confocal laser endomicroscopy was performed in a preliminary effort to confirm the *in vivo* OI imaging data. For *ex vivo* image acquisition, isolated organs of one mouse that had received an adoptive transfer of DiD-PMN- or DiD-M-MDSCs, respectively, was examined with the confocal probe. *Ex vivo* confocal laser endomicroscopy resulted in the detection and acquisition of DiD-PMN-MDSCs in the tumor, lungs, liver, spleen and bone marrow. Due to the extreme motion sensitivity of the endomicroscopy system, images of DiD-M-MDSCs were only recorded in the tumor, liver and spleen although DiD-M-MDSCs could be observed in the lungs and bone marrow as well. Confocal laser microscopy was therefore able to confirm *in vivo* and *ex vivo* OI imaging data and represented an *ex vivo* validation for the homing of DiD-PMN- and DiD-M-MDSCs to the primary breast cancer TME.

Possible causes and mechanisms of this difference in recruitment between PMN- and M-MDSCs to the PyMT breast tumor will be discussed in section 5.1.4.

5.1.3 Labeling of PMN- and M-MDSCs for non-invasive cell tracking by PET

Although OI exemplifies a fast and relatively inexpensive imaging modality for cell tracking studies with straightforward approaches for direct *ex vivo* cell labeling, photon absorbance and scattering preventing absolute quantification, restriction to 2-dimensional imaging as well as the restricted tissue penetration - in the wavelength spectrum of DiD - constitute major drawbacks of planar fluorescence OI (Ntziachristos, 2006). The central aim of the first part of this work was therefore the establishment and evaluation of an *ex vivo* labeling method for cell tracking of murine MDSCs after adoptive transfer by PET (section 4.1.3.1). In comparison to

OI, PET surpasses OI with picomolar sensitivity for the detection of PET-tracers (Cherry, 2001) and enables 3-dimensional imaging, however, radiation might impact the labeled cells more profoundly.

In previous work at the Werner Siemens Imaging Center, an antibody-based labeling approach was developed to image the temporal and spatial distribution of murine $CD4^+$ T cells in an airway hypersensitivity mouse model *in vivo* by PET. Herein, a mAb was functionalized for PET imaging by covalent modification with 1,4,7,10-tetraazacyclododecane-1,4,7,10-tetraacetic acid (DOTA) to chelate the radioisotope ^{64}Cu. The use of this [^{64}Cu]DOTA-conjugated mAb targeting the TCR and subsequent internalization of the mAb-receptor complex resulted in enhanced retention of radioactivity in the T cells in comparison to [^{64}Cu]PTSM (Griessinger *et al.*, 2015; Hoffmann *et al.*, 2017).

The use of a mAb to specifically target and radiolabel the cell population of interest for PET imaging represents an elegant way for *ex vivo* cell labeling. Murine MDSCs, however, do not express an unambiguous cell surface marker allowing for clear identification of the cells. Consequently, the integrin CD11b (ITGAM, integrin α_M) was chosen as antigen for radiolabeling as it is expressed on murine PMN- and M-MDSCs. CD11b forms a heterodimeric complex with the common integrin β_2 and is, as integrin $\alpha_M\beta_2$ or macrophage antigen 1 (Mac-1), involved in the adhesion of neutrophils and monocytes to activated endothelial cells (Solovjov *et al.*, 2005; Zhang, 1999). As blockade of CD11b with the [^{64}Cu]NOTA-anti-CD11b mAb used for radiolabeling of PMN- and M-MDSCs might perturb cellular migration and cell trafficking *in vivo*, PMN- and M-MDSCs were pre-labeled with a naïve anti-CD11b mAb and stained with a fluorescent Cy5-conjugated anti-CD11b mAb to assess blockade of CD11b at different time points after pre-labeling. In flow cytometric analysis, CD11b cell surface expression was reduced at 3 h post labeling. Confocal microscopy, however, indicated complete internalization of the CD11b-antibody complex (section 4.1.3.1). Membrane trafficking of integrin receptors is involved, amongst other processes, in the regulation of cell-cell- and cell-ECM contacts. These highly dynamic interactions require fast trafficking. Integrin receptors at the plasma membrane are endocytosed in a Rab5- or Rab21-dependent way to early endosomes where further processing depends on the activation status. Inactive integrin heterodimers are directly recycled from early endosomes while activated integrins are trafficked to the late endosome and lysosome compartment (De Franceschi *et al.*, 2015). The reduction of cell surface-expressed CD11b molecules at 3 h post labeling indicated the trafficking of the internalized CD11b-antibody complex through the lysosomal compartment and, consequently, a temporal delay in re-expression. As CD11b expression at the cell membrane of both PMN- and M-MDSCs was reduced only at 3 h post pre-labeling, impairments in cellular trafficking of the MDSCs were not expected in the subsequent cell

tracking experiments. Furthermore, CD11b expression was enhanced in both MDSC subpopulations at 24 and 48 h post pre-labeling possibly indicating activation.

For radioactive cell tracking experiments, in comparison to earlier work, the anti-CD11b mAb was conjugated with NOTA instead of DOTA. Dependent on the chemical activation for conjugation, NOTA forms a 5-coordinate complex or 6-coordinate distorted prismatic complex with Cu^{2+}. This complex has proven to be more stable than the [^{64}Cu]DOTA complex both *in vitro* and *in vivo* (Cooper *et al.*, 2012; De Silva *et al.*, 2012). For all *in vitro* and *in vivo* experiments, the [^{64}Cu]NOTA-anti-CD11b mAb was utilized directly after radiolabeling to avoid radiolysis of the mAb (Kishore *et al.*, 1986). 10^6 PMN-MDSCs and M-MDSCs were labeled with 0.74 MBq corresponding to 1.6 µg [^{64}Cu]NOTA-anti-CD11b mAb. Indeed, the main fraction of PMN- and M-MDSCs were viable after radiolabeling as assessed by trypan blue staining. Cell loss during labeling resulted from [^{64}Cu]PMN- and [^{64}Cu]M-MDSCs adhering to the low-adherence well plate.

The stability of the [^{64}Cu]NOTA-anti-CD11b mAb in PMN-MDSCs, [^{64}Cu]PMN-MDSCs, and M-MDSCs, [^{64}Cu]M-MDSCs, was determined by γ-counting at 5, 24, and 48 h post radiolabeling (section 4.1.3.1). The efflux of radioactivity from [^{64}Cu]PMN-MDSCs and [^{64}Cu]M-MDSCs was higher than expected from a previous study on murine $CD4^+$ T cells (Griessinger *et al.*, 2015) but expected to be lower than efflux of, for example, [^{64}Cu]PTSM. In this previous study, below 10 % of the initially applied dose of [^{64}Cu]PTSM was retained in the T cells. The retention of the [^{64}Cu]NOTA-anti-CD11b mAb in [^{64}Cu]PMN-MDSCs and [^{64}Cu]M-MDSCs, with approximately 38 % and 35 % of applied radioactivity respectively, was therefore still considered superior to [^{64}Cu]PTSM.

Internalization of [^{64}Cu]NOTA-anti-CD11b mAb brings the radioisotope ^{64}Cu in closer proximity to the nucleus where highly energetic Auger electrons, for example, can cause DNA double strand breaks. In normal cells that have not been subject to malignant transformation, apoptosis is considered the main cell death mechanism following exposure to ionizing radiation (Eriksson and Stigbrand, 2010). The exposition of the glycerophospholipid phosphatidylserine that is located only in the inner lipid bilayer leaflet in intact cells on the cell surface is an early marker for apoptosis. To distinguish apoptosis from other forms of programmed cell death such as necroptosis, the cell membrane, however, has to be intact and impenetrable to DNA-intercalating dyes such as 7-AAD (Chaabane *et al.*, 2013). Consequently, apoptotic PMN- and M-MDSCs were identified as Annexin V^+/7-AAD^-. Fractions of up to 10 % of [^{64}Cu]PMN- and [^{64}Cu]M-MDSCs, normalized to naïve PMN- and M-MDSCs, were identified as Annexin V^+/7-AAD^- and referred to as apoptotic cells at both 3 and 48 h post radiolabeling with [^{64}Cu]NOTA-anti-CD11b mAb (section 4.1.3.1). The assessment of the apoptotic cell fraction was performed on cells that were kept *in vitro* in cell culture. Although the medium was supplemented with both FCS and the combination of GM-CSF and IL-6 used for expansion of

the MDSC subpopulations, *in vitro* culture is not able to mimic the environment [^{64}Cu]PMN- and [^{64}Cu]M-MDSCs experience after adoptive transfer *in vivo*. It can be cautiously assumed that the cytokines and growth factors secreted by tumors have a sustaining effect on the adoptively transferred MDSCs and further reduce the induction of apoptosis *in vivo*.

In a cross-examination approach, [^{64}Cu]PMN- and [^{64}Cu]M-MDSCs were stained for phosphorylated H2AX as early sign for DNA double strand breaks (Lobrich *et al.*, 2010) at 3, 24 and 48 h post initial radiolabeling with [^{64}Cu]NOTA-anti-CD11b mAb (section 4.1.3.1). At both 3 and 24 h post radiolabeling, no sign of DNA damage in the form of phosphorylated H2AX was detected. At 48 h post radiolabeling, phosphorylated H2AX was detected in both [^{64}Cu]PMN- and [^{64}Cu]M-MDSCs. Considering that the examination time window for *in vivo* imaging of MDSC migration was set to 48 h post adoptive cell transfer and no DNA double strand breaks were detected before, induction of DNA double strand at this late time point post radiolabeling was not suspected to impact neither cell migration nor the results of imaging studies. In the case of a prolonged imaging time window, however, careful evaluation of the effects of DNA double strand breaks on MDSC migration and function would be compulsory.

Furthermore, PMN- and M-MDSC functional activity was measured as potency to suppress antigen-induced T cell proliferation after labeling with either naïve anti-CD11b mAb or [^{64}Cu]NOTA-anti-CD11b mAb (section 4.1.3.1). Here, either 1.6 µg of the naïve anti-CD11b mAb or 0.74 MBq of [^{64}Cu]NOTA-anti-CD11b mAb on average corresponding to 1.6 µg was used for radiolabeling to estimate the additional effect of the radioisotope ^{64}Cu on MDSC function in comparison of mAb labeling only. Freshly isolated naïve PMN- and M-MDSCs suppressed OT-1 T cells proliferation significantly in comparison to the untreated OT-1 T cell control. Likewise, neither anti-CD11b mAb-labeling nor [^{64}Cu]NOTA-anti-CD11b mAb-labeling did reduce or impair the suppressive potency of PMN- and M-MDSCs. There was no significant difference in the measured OT-1 T cell proliferation, however, when comparing the different MDSC:OT-1 T cell ratios examined in these experiments. Contrary to the expectations, the use of higher MDSCs numbers did not further reduce OT-1 T cell proliferation. The immunosuppressive function of bone marrow-derived MDSCs *in vitro* is the result of bidirectional interactions with activated T lymphocytes (Solito *et al.*, 2011). In all *in vitro* co-culture experiments, however, T cell activation proved difficult. Neither unspecific nor specific activation and stimulation of $CD8^+$ T cells with their cognate antigen in experiments with mAb and radiolabeled MDSCs did result in the expected high degree of $CD8^+$ T cell proliferation (Lewis *et al.*, 2015b) but resulted in only approximately 37 % of all cells undergoing at least one cell division cycle. Moreover, in *in vitro* co-culture assays with human bone marrow-derived MDSCs, suppressed T cells secrete IL-10 that, in turn, activates the transcription factor STAT3 in MDSCs. STAT3 leads to the upregulation of the immune checkpoint molecule programmed cell death 1 ligand 1 (PD-L1) that negatively regulates the activity of lymphocytes when

engaging its receptor programmed cell death protein 1 (PD-1) (Pinton *et al.*, 2016). Besides ARG1 activity and L-cysteine sequestration, the PD-1-PD-L1 receptor-ligand interactions might therefore be pivotal for the immunosuppression of T cell activity proliferation mediated by bone marrow-derived MDSCs *in vitro*.

5.1.4 MDSC recruitment to the primary and metastatic TME

Current literature reports both an increased abundance of MDSCs in the peripheral blood of patients with prostate cancer (Idorn *et al.*, 2014; Vuk-Pavlovic *et al.*, 2010), hepatocellular carcinoma (Arihara *et al.*, 2013; Hoechst *et al.*, 2008), non-small cell lung cancer (Huang *et al.*, 2013; Vetsika *et al.*, 2014), chronic lymphocytic leukemia (Liu *et al.*, 2015), melanoma (Jordan *et al.*, 2013; Rudolph *et al.*, 2014) and breast cancer (Bergenfelz *et al.*, 2015; Yu *et al.*, 2013) and a correlation to disease stage, progression and overall survival. Due to the phenotypical heterogeneity of human MDSCs with up to 14 subsets found in cancer patients (Gros *et al.*, 2012), clear differentiation between the subtypes when comparing different clinical studies might pose difficulties. In tumor-bearing mice, however, so far only the two MDSCs subpopulations PMN- and M-MDSCs have been described in the literature facilitating comparative analysis. The frequency of PMN-MDSCs was found to be consistently increased and static independent of mouse strains and tumor types while M-MDSCs were increased dynamically and only in few models (Movahedi *et al.*, 2008; Youn *et al.*, 2008). While recent and current literature predominantly described functional mechanisms involved in MDSC-mediated immunosuppression (Pinton *et al.*, 2016) and targeting of MDSCs to improve chemo- and immunotherapy outcomes (Iclozan *et al.*, 2013; Le *et al.*, 2009; Mirza *et al.*, 2006; Tobin *et al.*, 2018; Vincent *et al.*, 2010), only few studies examined the migration of adoptively transferred MDSCs *in vivo* with non-invasive imaging techniques. To date, aside from the collaboration project with the Tumor Microenvironment Laboratory in Brisbane, Australia, (Sceneay *et al.*, 2018) only two MDSC tracking studies have been published. As mentioned above, Combes *et al*. labeled *in vitro* generated MDSCs and MDSCs isolated from bone marrow of tumor-bearing mice with the fluorescent dye DiR for cell tracking by OI in the syngeneic 4T1 breast cancer model. The authors, however, did not separate MDSC subpopulations before adoptive transfer into 4T1 breast tumor-bearing BALB/c mice. Nevertheless, PMN-MDSCs were identified as predominant MDSC subpopulation (Combes *et al.*, 2018). As discussed above, this planar OI study was further restricted to 2-dimensional imaging possibly affected by artefacts due to photon absorption and scattering. In the second study, Gr-1$^+$ MDSCs, likely corresponding to PMN-MDSCs, were isolated from the spleen of murine cervical cancer-bearing mice treated either with a vaccine or a control vehicle formulation. The Gr-1$^+$ MDSCs were incubated with SPIOs overnight and *i.v.* injected into subcutaneous cervical cancer-bearing mice for MR imaging. Adoptively transferred MDSCs

were then detected as locally constricted hypointensities in the tumors (Tremblay *et al.*, 2018). The detection of a negative signal in the form of hypointense regions, however, represents one major drawback of cell tracking with SPIOs: both necrotic and cystic areas in tumors might appear hypointense and lead to artifacts in the quantification of the cell-derived signal. Moreover, loss of the SPIOs from the cells, for example mediated by exocytosis or as a consequence of cell death, can lead to the extracellular deposition of SPIOs in tissues resulting in background in the MR images and possibly signal misidentification (Cianciaruso *et al.*, 2014; Danhier *et al.*, 2017). Additionally, MRI as a molecular imaging modality is inherently less sensitive than PET (Ahrens and Bulte, 2013).

To current knowledge, the first PET-based MDSC tracking study examining tumor tropism of experimentally separated murine MDSC subpopulations, namely PMN- and M-MDSCs, was presented in this work (section 4.1.3.2). By experimental separation and isolated examination of tumor homing of PMN- and M-MDSCs, respectively, differences in overall MDSC recruitment to primary breast cancer tumors and primary melanomas as well as tumor tropism of the examined MDSC subpopulations could be visualized. The breast cancer and melanoma mouse models, respectively, were chosen for cell tracking studies as breast cancer and melanoma represent global health issues with different mutational burden and aggressiveness (Alexandrov *et al.*, 2013). Primary B16-F10 melanomas showed overall enhanced recruitment of both [^{64}Cu]PMN- and [^{64}Cu]M-MDSCs *in vivo* in comparison to primary PyMT breast cancer tumors. Moreover, primary B16-F10 melanomas recruited higher fractions of [^{64}Cu]PMN-MDSCs than primary PyMT breast tumors. In contrast, primary PyMT breast cancer tumors showed higher uptake values for [^{64}Cu]M-MDSCs than [^{64}Cu]PMN-MDSCs. When interpreting the results of the cell tracking data, it has to be considered that proportions of the adoptively transferred M-MDSCs might have acquired the ability to transdifferentiate into PMN-MDSCs *in vivo* (Youn *et al.*, 2013). The likelihood of this transdifferentiation step, however, has not yet been closely examined and effects on cellular migration were not yet described and would need further investigation. In all examined tumors, uptake of [^{64}Cu]PMN- and [^{64}Cu]M-MDSCs was not homogeneously distributed throughout the tumor but presented in hot spot areas possibly reflecting cellular migration. *In vivo* uptake of [^{64}Cu]PMN- and [^{64}Cu]M-MDSCs could be confirmed by *ex vivo* biodistribution analysis by γ-counting. Tumor uptake of [^{64}Cu]PMN- and [^{64}Cu]M-MDSCs, however, was reduced by approximately factor 2 in the *ex vivo* biodistribution analysis probably reflecting differences in tumor tissue density (image-derived %ID/cm³ compared to %ID/g in biodistribution analysis), corrections of the PET data during reconstruction and partial volume effects (Mannheim *et al.*, 2012). Additionally, the kidneys showed uptake in the *ex vivo* biodistribution analysis. As examined in section 4.1.3.1, the [^{64}Cu]NOTA-anti-CD11b mAb was not completely retained in neither [^{64}Cu]PMN-MDSCs nor [^{64}Cu]M-MDSCs. The portion of the radioactive [^{64}Cu]NOTA-anti-CD11b mAb that leaked from

the radiolabeled MDSCs circulates in the blood pool, explaining the *ex vivo* detected uptake in the blood, and is subject to hepatobiliary excretion. Free ^{64}Cu dissociated from the chelator NOTA, however, might be eliminated via the kidneys (Peng *et al.*, 2006).

As discussed above, MDSCs are involved in pre-metastatic niche formation and suppress immune responses in the metastatic TME. It was therefore suspected that B16-F10 melanoma and PyMT breast cancer metastases recruit a higher proportion of [^{64}Cu]PMN- and [^{64}Cu]M-MDSCs. Indeed, in comparison to the examined primary tumor models, recruitment of [^{64}Cu]PMN- and [^{64}Cu]M-MDSCs was more pronounced in the corresponding metastasis models. Interestingly, the same trends that were observed in the primary tumor models were reflected in the metastatic cancer models. First, B16-F10 melanoma lung metastatic lesions recruited overall higher fractions of [^{64}Cu]PMN- and [^{64}Cu]M-MDSCs than PyMT breast cancer lung metastatic lesions. Second, PyMT-derived breast cancer lung metastatic lesions showed higher uptake of [^{64}Cu]M-MDSCs. And third, B16-F10 melanoma lung metastatic lesions had higher uptake values of [^{64}Cu]PMN-MDSCs than [^{64}Cu]M-MDSCs although the differences were not as pronounced as in the primary tumor models. As immunosuppressive cells are thought to arrive early at the pre-metastatic site, during pre-metastatic niche formation, to support metastatic outgrowth, the homing of [^{64}Cu]PMN- and [^{64}Cu]M-MDSCs to the metastatic TME indicated further recruitment, possibly even turnover, of immunosuppressive cells even at this late stage of metastatic growth. As for the primary tumor models, PyMT breast cancer and B16-F10 melanoma metastases were subjected to biodistribution analysis by γ-counting for *ex vivo* validation of the *in vivo* imaging data. The *ex vivo* analysis confirmed [^{64}Cu]PMN-MDSC and [^{64}Cu]M-MDSC uptake in the lung metastatic lesions of both PyMT breast cancer and B16-F10 melanoma. Significant differences between healthy lung tissue and lung metastatic lesions, however, could not be detected. As isolation of the small-sized metastatic lesion was not feasible, only major lesions were subjected to γ-counting as metastatic tissue while the remaining lung tissue was analyzed as remaining healthy lung tissue. Consequently, the experimental dissection and preparation of the lung metastatic lesions needs to be improved. Additionally, as discussed above, differences in obtained image-derived %ID/cm³ values compared to %ID/g in biodistribution analysis might be caused by the different analysis methods, corrections of the PET data during reconstruction and partial volume effects (Mannheim *et al.*, 2012).

Mechanistically, the tumor tropism observed for PMN- and M-MDSCs might reflect differences in cell recruitment: the migration of distinct MDSC subsets into the TME is mediated by different chemokines (Sawanobori *et al.*, 2008; Umansky and Sevko, 2013). Cell recruitment and retention can be controlled by different but largely redundant mechanisms that vary within

certain limits between tumor types and stages of tumor development. Gaining increasing recognition in tumor biology in last years, the inflammatory proteins S100A8 and S100A9 mediate recruitment of both MDSC subpopulations via the RAGE receptor. The secretion of S100A8 and S100A9 proteins by recruited MDSCs can then result in a positive feedback loop (Kowanetz *et al.*, 2010). Moreover, cyclooxygenase 2-produced prostaglandin E2 was shown to induce MDSCs and promote MDSC accumulation, however, without further specification of the subpopulation referred to (Eruslanov *et al.*, 2010; Sinha *et al.*, 2007).

Concerning the MDSC subsets, PMN-MDSC migration is mediated primarily via CXC chemokines including CXCL1, CXCL5, CXCL6, CXCL8 and CXCL12 and to a lesser extent via CCL2 and CCL3. The chemokines CXCL1, CXCL2 and CXCL5 bind to the same receptor, namely CXCR2. Disruption of CXCR2-mediated MDSC tumor trafficking was reported to enhance the efficacy of immunotherapy in the form of immune checkpoint blockade with an anti-PD-1 antibody (Highfill *et al.*, 2014). M-MDSC migration is mediated primarily via the CCL2-CCR2 axis and, to a lesser extent, via CCL5, CCL7, CXCL8 and CXCL12 (Huang *et al.*, 2007; Lesokhin *et al.*, 2012; Obermajer *et al.*, 2011). The CCL2-CCR2-axis is further implicated in recruitment and retention of metastasis-associated macrophages in breast cancer (Kitamura *et al.*, 2015). Additionally, macrophage migration inhibitory factor was shown to recruit M-MDSCs specifically to tumors (Simpson *et al.*, 2012). The higher recruitment of [^{64}Cu]PMN- and [^{64}Cu]M-MDSCs to primary B16-F10 melanomas and melanoma metastases might be caused by a more pronounced overall chemoattractant secretion in comparison to the PyMT breast cancer models. The chemokines CCL2, also referred to as MCP-1, and CCL5 (also referred to as regulated on activation, normal T cell expressed and secreted; RANTES) have a special rank amongst the chemokines involved in breast cancer by promoting TAM recruitment, angiogenesis and metastasis (Soria and Ben-Baruch, 2008). While CCL2 and CCL5 seem to represent central chemokines in breast cancer, chemokine expression seems to be more divers in melanomas including CXCL1, CXCL2, CXCL3, CXCL8, CCL2 and CCL5 (Payne and Cornelius, 2002). It seems therefore conclusive that an overall more pronounced MDSC recruitment to melanoma tumors than to breast cancer tumors was observed. Likewise, PyMT breast cancer tumors and metastases recruited a higher proportion of [^{64}Cu]M-MDSCs than [^{64}Cu]PMN-MDSCs presumably via the CCL2-CCR2-axis. This assumption, however, would need further confirmation by, for example, experimental determination of cytokine and chemokine levels in B16-F10 melanoma- and PyMT breast cancer-bearing mice. In a second step, MDSC cell tracking studies could be performed after the depletion of chemokines suspected to mediate cell recruitment to further validate the significance of the chemokines in MDSC recruitment.

[^{64}Cu]$CuCl_2$ controls for MDSC cell tracking experiments

As the signal detected by PET imaging is attributed to the radioisotope ^{64}Cu, one might critically argue that, in the above described and discussed MDSC cell tracking experiments, [^{64}Cu]Cu^{2+} released from the chelator NOTA and effused from the cells was detected but not migration of [^{64}Cu]PMN- and [^{64}Cu]M-MDSCs. Therefore, as a control for cell migration of [^{64}Cu]PMN- and [^{64}Cu]M-MDSCs, PyMT tumor-bearing mice and B16-F10 melanoma-bearing mice were injected with 0.37 MBq [^{64}Cu]$CuCl_2$ to visualize the spatial and temporal distribution of free [^{64}Cu]Cu^{2+} in these tumor models. Indeed, [^{64}Cu]Cu^{2+} was taken up into both the PyMT breast cancer tumor and the B16-F10 melanoma. The distribution pattern of [^{64}Cu]Cu^{2+} resembled the distribution of radioactive MDSC subset with the lungs, liver and spleen exhibiting the highest uptake values of [^{64}Cu]Cu^{2+} beside the primary tumors. The uptake of [^{64}Cu]Cu^{2+} in the lungs, liver and spleen was probably unspecific and caused by perfusion of these organs. Tumor uptake of [^{64}Cu]Cu^{2+} was most likely mediated by enhanced permeability of the tumor vasculature and enhanced retention due to the lack of effective lymphatic drainage (Matsumura and Maeda, 1986). Furthermore, a variety of human and murine cancers including the B16-F10 melanoma overexpress copper transporters leading to an enhanced uptake of [^{64}Cu]Cu^{2+} (Avila-Rodriguez *et al.*, 2017; Cai *et al.*, 2014; Qin *et al.*, 2014). The dynamic of [^{64}Cu]Cu^{2+} distribution in both B16-F10 melanoma and PyMT breast cancer primary tumors, however, was strikingly different in comparison to the dynamics of [^{64}Cu]PMN- and [^{64}Cu]M-MDSCs uptake: [^{64}Cu]Cu^{2+} uptake in both the primary PyMT breast cancer tumor and the B16-F10 melanoma had reached peak values already at 3 h post injection with decreasing uptake values during the examination period until 48 h post injection. Hence, the differences detected between the *in vivo* biodistribution of [^{64}Cu]$CuCl_2$ and [^{64}Cu]PMN- and [^{64}Cu]M-MDSCs respectively suggested the visualization of cell migration in the MDSC cell tracking experiments.

Histological validation of *in vivo* cell tracking experiments in the primary PyMT breast cancer and B16-F10 melanoma model

The *in vivo* infiltration of [^{64}Cu]PMN- and [^{64}Cu]M-MDSCs in the primary PyMT breast tumors and B16-F10 melanoma tumors was further confirmed by immunohistochemical stainings. Neither PMN- nor M-MDSCs express unique cell surface markers for their identification in histological stainings. As the adoptively transferred murine MDSCs were radiolabeled with the rat anti-mouse [^{64}Cu]NOTA-anti-CD11b mAb prior to injection, adoptively transferred PMN- and M-MDSCs were identified according to the internalized rat anti-mouse mAb by staining with a secondary anti-rat antibody. Adoptively transferred M-MDSCs were successfully detected in both primary PyMT breast cancer tumors and primary B16-F10 melanoma tumors while adoptively transferred PMN-MDSC detection was only feasible in PyMT breast cancer

tumors. The tissue structure of the B16-F10 melanoma tumors from tumor-bearing mice that had received an adoptive transfer of adoptively transferred PMN-MDSCs did, unfortunately, not permit the preparation of paraffin slices.

Interestingly, both adoptively transferred PMN- and M-MDSCs were found near blood vessels. Although specific staining for a vascular marker was not performed to identify blood vessels, the vessels were clearly identified according to the contained erythrocytes' shape and unspecific fluorescence signal in all recorded fluorescence channels (Whittington and Wray, 2017).

The shape of the examined PyMT breast tumor further prompted the question about the presence of tertiary lymphoid structures (TLS) in the tumor. Tumor-associated TLS organization resembles the structure of classical LNs closely: a T cell zone composed of T cells and mature DCs is close to a follicular zone with active B cell proliferation. Moreover, TLS are characterized by the presence of HEVs that enable lymphocyte trafficking and infiltration into the TLS (Dieu-Nosjean *et al.*, 2014; Goc *et al.*, 2013). HEV presence as indicator for the manifestation of TLS was verified by positive staining for PNAd. It was consequently suspected that adoptively transferred PMN-MDSCs emigrated the vasculature via HEVs. However, this assumption needs further confirmation as the presence of HEV was only illustrated in one tumor sample.

5.1.4.1 Outlook: MDSC tracking

In accordance with current literature, diverging migration of [^{64}Cu]PMN- and [^{64}Cu]M-MDSCs to different cancer types could be visualized with the employed radiolabeling approach for adoptive cell transfer in the MDSC tracking experiments presented in this work. In this work, the common myeloid marker CD11b was targeted with a mAb for radiolabeling of *in vitro* generated MDSCs prior to adoptive transfer into tumor-bearing mice. The anti-CD11b mAb was modified with the chelator NOTA for radiolabeling with ^{64}Cu. The use of the chelator 1,4,7-triazacyclononane,1-glutaric acid-4,7-acetic acid (NODAGA), however, might further enhance the stability of the ^{64}Cu-chelator-complex and consequently reduce background. Furthermore, the functionalization of the anti-CD11b mAb with a fluorescent dye for a combined multimodal imaging approach would further open the possibility for *ex vivo* validation of MDSC migration by flow cytometry. But more interestingly, in the respective transgenic mouse model, intravital imaging of cell-cell-interactions of adoptively transferred, dually labeled MDSCs with specific, transgenically labeled immune cell populations could be achieved.

The selected cancer types, namely the syngeneic PyMT-derived breast cancer and the syngeneic B16-F10 melanoma model both originate from the C57BL/6 mouse strain. Therefore, the transferal of the experimental setup to a syngeneic murine cancer model of

another mouse strain would further affirm the presented findings. The transplantable syngeneic 4T1 murine breast cancer model on BALB/c background would represent a suitable candidate for MDSC cell tracking experiments. First, myeloid cells represent the major fraction of immune cell infiltrates in 4T1 tumors indicating the relevance of this model for myeloid cell tracking studies (Combes *et al.*, 2018). Expansion of MDSCs from bone marrow progenitor cells isolated from BALB/c mice in the *in vitro* culture system discussed above was an efficient process resulting in high yields of MDSCs (own observations). Furthermore, mice bearing 4T1 mammary tumors have been reported to possess a remarkable high number of MDSCs in their bone marrow compared to naive mice (Danilin *et al.*, 2012; Donkor *et al.*, 2009; Youn *et al.*, 2008). It would further be interesting to use *in vivo*, in tumor-bearing mice, expanded MDSCs for cell tracking studies. Then, cell trafficking studies with *in vivo* expanded MDSCs might further visualize if the primary tumor-derived factors prime MDSC tumor homing already in the bone marrow.

Additionally, 4T1 tumors and especially the more aggressive and more metastatic subtype tumors 4T1.2 spontaneously metastasize to the lungs. In the experimental metastasis model used in this work, tumor cells were directly introduced in the circulation via *intracardiac* injection to induce metastatic growth in secondary organs thereby mimicking the late steps of the metastatic cascade. The depiction of MDSC migration in the early stages of the metastatic cascade was therefore not in the scope of this model. Indeed, the involvement of MDSCs in pre-metastatic niche formation and the metastatic cascade is well described in literature. However, visualization of MDSC involvement in the early steps of the metastatic cascade *in vivo* in a spontaneously metastasizing tumor model might further confirm current views or even elucidate spatial and temporal details in MDSC migration not yet described in the literature.

Recent literature further described a negative involvement of MDSCs in cancer therapy, specifically in rising immunotherapeutic approaches, and consequently targeting of MDSCs to abrogate their negative effects on cancer therapeutics (Draghiciu *et al.*, 2015; Highfill *et al.*, 2014; Kumar *et al.*, 2017; Shou *et al.*, 2016; Ugel *et al.*, 2009). Translation of the MDSC imaging approach combined with *ex vivo* examinations such as flow cytometry to humanized mouse models with patient-derived xenograft tumors might reveal efficacy and pharmacodynamic effects on circulating MDSCs and the mode of action of each therapeutic compound considered to target MDSCs and MDSC-mediated immunosuppression during cancer therapy.

5.1.5 MDSC tracking in pre-metastatic niche models

Following the seminal study of Kaplan *et al.* first published in 2005 (Kaplan *et al.*, 2005), scientific interest in first the concept and then the formation of the pre-metastatic niche has spiked tremendously (Kaplan *et al.*, 2006; Peinado *et al.*, 2017; Psaila and Lyden, 2009; Sceneay *et al.*, 2013). As MDSCs are recruited in early stages of pre-metastatic niche formation and act as key regulators, visualization of an established pre-metastatic niche in the lungs was attempted by tracking of adoptively transferred [^{64}Cu]PMN- and [^{64}Cu]M-MDSCs. In an attempt to induce a lung pre-metastatic niche in wild type C57BL/6 mice, the animals were treated with tumor cell CM on 9 consecutive days according to the experimental protocol published by Kaplan *et al.* (Kaplan *et al.*, 2005). Unfortunately, no enhanced [^{64}Cu]PMN- and [^{64}Cu]M-MDSCs migration to the lungs could be detected *in vivo* in a preliminary imaging study (data not presented). It was therefore hypothesized that either treatment with tumor cell CM was ineffective and did not result in pre-metastatic niche induction or [^{64}Cu]PMN- and [^{64}Cu]M-MDSCs did not migrate to the induced pre-metastatic niche *in vivo*. To assess if pre-metastatic niche formation was achieved *in vivo* after treatment with B16-F10 melanoma CM or PyMT breast cancer CM, flow cytometric analysis of the immune cell composition of the lungs and spleen of CM-treated mice was performed. As pre-metastatic niche formation is characterized by the recruitment of bone marrow cells, it was hypothesized that an increase in BMDCs such as PMN- and M-MDSCs or NK cells in the lungs of CM-treated mice might be detected by flow cytometric analysis (Sceneay *et al.*, 2012). This was, however, not the case (section 4.2.1) indicating that tumor cell CM-treatment did not result in pre-metastatic niche induction in the lungs of the treated mice. Sceneay *et al.* reported the successful induction of a lung pre-metastatic niche with CM conditioned in a hypoxic environment (Sceneay *et al.*, 2012). The effect of hypoxic conditioning on B16-F10 melanoma CM and PyMT breast cancer CM and consequently on lung pre-metastatic niche induction was further evaluated in a separated master's thesis at the Werner Siemens Imaging Center but found to be neglectable in this experimental setup (Reck, 2017).

Kaplan *et al.* described the recruitment of VEGF receptor 1-positive hematopoietic bone marrow progenitors in their seminal work on pre-metastatic niche induction (Kaplan *et al.*, 2005). VEGF-C was further found to enhance the adherence of breast cancer cells in the lungs via prostaglandin E2 production in mouse pulmonary microvascular endothelial cells (Liu *et al.*, 2014). It was therefore hypothesized that *i.v.* injection of pure recombinant VEGF-C might be sufficient to induce a lung pre-metastatic niche *in vivo*. Pre-metastatic niche formation was detected by *ex vivo* immunohistochemical staining of the lungs of BALB/c mice after treatment with recombinant VEGF-C on 5 consecutive days (Scherer and Sleeman, 2017). Consecutive injections of VEGF-C following the experimental protocol obtained from Prof. Sleeman's group in a scientific collaboration, however, did not lead to pre-metastatic niche formation detectable

by enhanced migration of [^{64}Cu]PMN-MDSCs to the lungs (section 4.2.2). Either *in vitro* expanded [^{64}Cu]PMN-MDSCs were not recruited to the lung pre-metastatic niche or, more likely, the induction of a lung pre-metastatic niche was not successful in C57BL/6 mice with the described experimental protocol. Nevertheless, it was assumed that pre-metastatic niche induction in the C57BL/6 mouse strain was more complex and co-dependent on other pre-metastatic niche-inducing cytokines or growth factors than in the BALB/c mouse strain employed by Scherer *et al*. (Scherer and Sleeman, 2017).

In the literature, only two experimental approaches for imaging the pre-metastatic niche have been described so far. The first study focused on the recruitment of BMDCs to visualize the pre-metastatic niche: by targeting very late antigen-4 on BMDCs with a ^{64}Cu-labeled PET probe, very late antigen-4-positive BMDC clusters corresponding to the sites of metastasis could be detected in mice bearing human MDA-MB-231 xenograft breast cancer tumors (Shokeen *et al.*, 2012). The second approach for molecular imaging of the pre-metastatic niche has only recently been described. Eisenblätter *et al.* detected the inflammatory proteins S100A8/A9 as marker for pre-metastatic lung priming with an antibody-based SPECT tracer in the syngeneic, invasive and *in vivo* metastatic 4T1.2 breast cancer mouse model. The authors claimed that S100A8/A9 imaging reflected MDSC abundance in the lungs and therefore corresponded to the establishment of an immunosuppressive microenvironment, a pre-metastatic niche (Eisenblaetter *et al.*, 2017). In this study, the authors elegantly made use of the positive autocrine feedback loop between stromal cell-derived S100A8/A9 recruiting MDSCs and S100A8/A9 secreted by recruited MDSCs.

5.1.5.1 Outlook: MDSC tracking in pre-metastatic niche models

As discussed above, pre-metastatic niche induction in the lungs of BALB/c mice can be provoked by consecutive *i.v.* of recombinant VEGF-C. Concordantly, the translation of the experimental setup for MDSC cell tracking to the BALB/c mouse strain might represent a straightforward approach for the visualization of pre-metastatic niche formation *in vivo* by recruitment of radiolabeled [^{64}Cu]PMN- or [^{64}Cu]M-MDSCs. Additionally, other experimental approaches to induce secondary organ pre-metastatic niches have recently been described. Application of tumor-derived exosomes would represent another applicable way to induce secondary organ pre-metastatic niches for molecular PET imaging of MDSC trafficking to the pre-metastatic niche (Wen *et al.*, 2016). Niche-mimicking engineered biomaterials are under discussion for their use in *in vivo* preclinical and clinical studies with a focus on factors mediating tumor cell recruitment to the niches and the immune cells infiltrates in the engineered niches before and after arrival of metastatic cancer cells (Aguado *et al.*, 2017; Aguado *et al.*, 2015; Azarin *et al.*, 2015). If these emerging niche-mimicking engineered biomaterials present

sophisticated scaffolds to further investigate contribution of individual chemokines or growth factors of MDSC trafficking to the pre-metastatic niche, however, remains to be established. According to current knowledge and as shown by Eisenblätter *et al.* (Eisenblaetter *et al.*, 2017), metastasis was preceded by pre-metastatic niche formation *in vivo* in 4T1.2 breast cancer bearing mice. Consequently, the use of a spontaneously metastasizing murine cancer model such as the 4T1.2 breast cancer model would be the option of choice for MDSC tracking to the pre-metastatic niche (Eckhardt *et al.*, 2005; Lelekakis *et al.*, 1999).

5.2 Metabolic fingerprinting for metabolic markers for differential metastatic potency

5.2.1 Metabolic examination of the PyMT-derived cell lines S2WTP3 and ML1B1B1

5.2.1.1 Cell line description and evaluation of aggressiveness

In this part, the metabolism, predominantly glucose metabolism, of the two MMTV-PyMT-derived murine breast cancer cell lines S2WTP3 and ML1B1B1 was examined and compared. The PyMT-derived cell lines S2WTP3 and ML1B1B1 were obtained from Dr. Christina Wong of the group of Prof. Andreas Möller at the QIMR Berghofer Medical Research Institute, Brisbane, Australia. Briefly, epithelial carcinoma cells from tumor-bearing MMTV-PyMT mice were isolated and established for *in vitro* cultivation as the cell line S2WTP3 (Wong *et al.*, 2012). The cell line ML1B1B1 was generated from spontaneous bone metastases of orthotopic tumors of the parental cell line S2WTP3 and further selected for by *intracardiac* injection into wild type C57BL/6 mice and isolation of bone metastases (refer to section 3.2.1). Therefore, the ML1B1B1 cells were considered the more aggressive, metastatic counterpart of the S2WTP3 cells. Owing to the similarity in their generation (Fidler, 1973), the murine melanoma cell lines B16-F0 and B16-F10 were used for comparison in *in vitro* assays whenever feasible. The higher aggressiveness of ML1B1B1 tumors was confirmed by enhanced cell-cell-contact independent growth and colony formation under experimental conditions *in vitro* in a colony formation assay (section 4.3.1) and represented by enhanced growth kinetics *in vivo* in syngeneic wild type C57BL/6 mice. Interestingly, the relative difference in the number of colonies was higher in the PyMT-derived cell lines S2WTP3 and ML1B1B1 than in the control melanoma cell lines B16-F0 and B16-F10 indicating a relative higher difference in the degree of aggressiveness. Although a straightforward way to assess the more aggressive growth kinetics of ML1B1B1 compared to S2WTP3 cells *in vitro*, the colony formation assay describes invasiveness only to a limited extend. Therefore, to measure invasive growth *in vitro*, a transwell-migration and transwell-invasion assay should be performed to further substantiate an increased metastatic potential of ML1B1B1 compared to S2WTP3 cells.

5.2.1.2 Glucose and pyruvate metabolism

The connection between malignant transformation and cellular metabolism has first been described by Otto Warburg in the early 1920s; metabolic changes have since been recognized as common feature of cancerous cells and tissue (Hanahan and Weinberg, 2011). In recent years, it has become evident that numerous signaling pathways affected by oncogenic mutations and implicated in tumorigenesis profoundly affect cellular metabolism. The

adaptation of cellular metabolism may give rise to metabolic phenotypes supporting cancer cell survival and primary tumor growth. Furthermore, emerging evidence suggests metabolic reprogramming as one driver in invasion and metastasis (Obre and Rossignol, 2015).

The glycolytic phenotype as described by Otto Warburg is frequently found in cancer cells, primary tumors and, particularly, in tumor metastases. The enhanced uptake of glucose under normoxic conditions and, therefore, the Warburg effect is the molecular basis for the identification and demarcation of cancerous lesion by [^{18}F]FDG-PET (Gambhir, 2002). While up to 30 % of all primary tumors are considered [^{18}F]FDG-PET negative and do not exhibit an enhanced [^{18}F]FDG uptake (Gambhir *et al.*, 2001), [^{18}F]FDG-PET sensitivity and specificity for the identification of distant metastases were historically considered higher than 90 % (Gillies *et al.*, 2008). Consequently, the uptake of [^{18}F]FDG was determined first *in vitro* in competition with glucose and then *in vivo* in S2WTP3 and ML1B1B1 breast cancer allografts (section 4.3.2). Indeed, ML1B1B1 cells exhibited a significantly higher [^{18}F]FDG uptake than S2WTP3 cells *in vitro*. Likewise, the aggressive B16-F10 melanoma cells had a significantly higher [^{18}F]FDG uptake *in vitro* than their less aggressive B16-F0 counterparts. Hence, *in vitro*, ML1B1B1 cells and B16-F10 cells, considered the more aggressive counterpart to S2WTP3 and B16-F0 cells, respectively, exhibited an higher [^{18}F]FDG uptake pointing at a higher glycolytic activity under normoxic conditions. Interestingly, the [^{18}F]FDG uptake *in vivo* in ML1B1B1 allograft tumors was not higher than the [^{18}F]FDG uptake *in vivo* in S2WTP3 allograft tumors. One possible cause for this discrepancy between the *in vitro* and *in vivo* data on [^{18}F]FDG uptake might be tumor hypoxia. Hypoxia is known to cause elevated glycolytic activity in primary tumors and represents, to a certain degree, the physiological cellular response to reduced oxygen availability. Non-transformed normal tissue cells enhance their chances of survival in temporary oxygen-deprived adverse conditions by upregulating anaerobic glycolysis. Normal tissue cells, however, switch their metabolism back to OxPhos when oxygen becomes available, a phenomenon known as the Pasteur effect (Berg *et al.*, 2007). Under hypoxic conditions, cancer cells might reduce the cellular respiration rate and adapt their metabolism so that a metabolic phenotype such as an oxidative phenotype might be masked *in vivo* as glycolytic. Although the tumor-bearing mice were anesthetized with 1.5 % isoflurane in pure oxygen, tumor allografts might still have been hypoxic. Depending on the distance to the nearest blood vessel, tumor cells experience considerable differences in the surrounding oxygen levels ranging between normoxia (2-4 % oxygen tension), hypoxia (<2 % oxygen tension) or anoxia (<0.1 % oxygen tension): 200 µm mean distance to the next vessel results in hypoxia (Solaini *et al.*, 2011). Consequently, it should further be examined if S2WTP3 and ML1B1B1 allograft tumors were hypoxic *in vivo* by either *ex vivo* pimonidazol staining for HIF-1α stabilization or *in vivo* with the hypoxia PET tracers [^{18}F]FMISO or [^{18}F]-fluoroazomycin arabinoside ([^{18}F]FAZA), respectively (Peeters *et al.*, 2015; Piert *et al.*, 2005). Additionally, a

longitudinal imaging study with [^{18}F]FDG and either [^{18}F]FMISO or [^{18}F]FAZA during the tumor growth period with repeated measurements could further expose differences in glucose metabolism while concurrently elucidating the oxygenation status of the S2WTP3 and ML1B1B1 tumor allografts.

The metabolic mismatch between cancer cell glucose metabolism *in vitro* and tumor glucose metabolism *in vivo* has been described for different human cancer cell lines. Neveu *et al.*, for example, recently described the same *in vivo* metabolic behavior of the human breast cancer cell line MDA-MB-231, subject to the Warburg effect and known to be metastatic, and the human cervical cancer cell line SiHa, subject to the Pasteur effect, stressing the limitations of *in vitro* studies to characterize *in vivo* tumor metabolic behavior (Neveu *et al.*, 2016). The observed mismatch between the metabolic behavior of cancer cells *in vitro* and tumors, microenvironment-embedded tumor cells, *in vivo* might also point towards underlying conditions different from tumor hypoxia. Davidson *et al*. established the microenvironment as determinant of the metabolic phenotype *in vivo*: while lung cancer cells oxidized only the minor part of glucose taken up into the cells *in vitro*, glucose oxidation was necessary for tumor formation *in vivo* (Davidson *et al.*, 2016). Additionally to the demonstration of a mismatch between metabolism *in vitro* and *in vivo*, Hensley *et al.* could reveal metabolic heterogeneity of human lung cancer tumors *in vivo*. According to the authors, poorly perfused tumor areas relied on glycolysis while oxidation of non-glucose metabolites was found in well-perfused areas (Hensley *et al.*, 2016).

Moreover, emerging experimental evidence points towards an oxidative phenotype in some cancer types including melanoma, pancreatic cancer, leukemia and breast cancer, for example (Obre and Rossignol, 2015). The importance of cellular respiration was recently demonstrated in the murine B16 melanoma model as well as the 4T1 breast cancer model (Tan *et al.*, 2015). Deletion of mitochondrial DNA abolishing mitochondrial respiration resulted in considerably delayed primary tumor growth. Strikingly, mitochondrial respiration increased in CTCs and was completely restored in metastatic cells (Tan *et al.*, 2015). The need of a functional OxPhos in metastatic cancer cells for metastatic dissemination was further demonstrated in human breast cancer cells lines (LeBleu *et al.*, 2014) and oxidative cancer cells could be identified in metastatic lymph nodes of human breast cancer patients (Sotgia *et al.*, 2012). Additionally, lactate and ketone bodies were found to fuel metastatic behavior of breast cancer cells (Bonuccelli *et al.*, 2010). Besides, mitochondrial respiration is one of the main sources of ROS. High levels of oxidative stress were found to be essential to sustain a metastatic phenotype in several melanomas (Piskounova *et al.*, 2015). In summary, these experimental findings point towards a significant metabolic plasticity of cancer cells and tumors and the possibility of a rapid metabolic regulation.

Glycolytic tumor cells do not completely oxidize pyruvate, the end product of glycolysis, in the TCA and subsequent OxPhos. Consequently, glycolytic tumor cells subject to the Warburg effect would, classically, convert pyruvate to lactate via LDH activity to regenerate NAD^+ and maintain glycolytic flux. Additionally, pyruvate can be converted to alanine in a transamination reaction catalyzed by ALAT. Thus, the fate of [1-^{13}C]pyruvate was evaluated in the PyMT-derived cell lines S2WTP3 and ML1B1B1 *in vitro* (section 4.3.4). Interestingly, S2WTP3 cells converted a higher proportion of the injected [1-^{13}C]pyruvate to [1-^{13}C]alanine and [1-^{13}C]lactate than the more aggressively growing ML1B1B1 cells indicating a more classical glycolytic phenotype characterized by lactate and alanine production in the S2WTP3 cells. The B16 melanoma cell lines had an overall increased transformation of [1-^{13}C]pyruvate to [1-^{13}C]alanine and [1-^{13}C]lactate in comparison to the PyMT-derived breast cancer cell lines. In contrast to the PyMT-derived cell lines, a non-significant trend towards higher [1-^{13}C]lactate production was observed in B16-F10 cells in comparison to B16-F0 cells. This is in concordance to the central dogma of the last decades of higher lactate production in more aggressive cancer cells (Schwickert *et al.*, 1995; Yokota *et al.*, 2007). The trend towards a reduced [1-^{13}C]alanine and [1-^{13}C]lactate production in ML1B1B1 cells should further be validated in ML1B1B1 allograft tumors as a mismatch between the *in vitro* and *in vivo* glucose metabolism has been detected in ML1B1B1 cancer cells and allograft tumors (as discussed above).

Since mitochondrial defects, suggested by Warburg, were eliminated as cause of the glycolytic phenotype, advantages of aerobic glycolysis were further investigated in the recent years. The three major drivers of aerobic glycolysis in tumor cells are currently thought to be the following: first, a faster ATP production by decoupling glycolysis from the TCA and OxPhos meeting the high energetic demand of proliferating cells. Second, the reduction of ROS stress produced by the complexes of the respiratory chain and third, the only recently recognized provision of biosynthetic and therefore proliferative advantages due to the high flux of glucose. Glucose-derived carbon building blocks can be diverted towards the PPP fueling ribonucleotide synthesis and towards the hexosamine biosynthetic pathway for the synthesis of glucosamine (Lunt and Vander Heiden, 2011). Hence, metabolomic analysis of cell extracts was performed to further investigate diversion of glucose-derived carbon building blocks in ML1B1B1 in comparison to S2WTP3 cells (discussed below in section 5.2.1.3).

5.2.1.2.1 Technical considerations

In vivo [^{18}F]FDG-PET measurements were performed on tumor allografts of S2WTP3 and ML1B1B1 cells at one time point only. Therefore, as discussed above, a longitudinal imaging study during the tumor growth period might uncover early differences in glucose metabolism.

Quantification of the *in vivo* dynamic [^{18}F]FDG-PET measurements was performed on the whole tumor allografts of S2WTP3 and ML1B1B1 cells. Both tumor types did, however, show signs of beginning necrosis as indicated in the anatomical MR scans. As necrotic areas do not take up [^{18}F]FDG, the presence of necrotic areas in the tumor allografts certainly affected the quantification of whole tumor [^{18}F]FDG uptake. Consequently, voxel-wise analysis of the imaging data might uncover differences in the [^{18}F]FDG uptake that could not be detected with the analytic method used in this work. Moreover, as the S2WTP3 and ML1B1B1 allografts might have had hypoxic areas next to necrotic areas, [^{18}F]FDG uptake might not be suitable as marker of aggressiveness in this model.

5.2.1.3 Metabolomic analysis – Diversion of glucose

The decrease in the observed [1-^{13}C]pyruvate transformation to [1-^{13}C]alanine and [1-^{13}C]lactate in ML1B1B1 might point towards lactate catabolism in the breast cancer cells (Kennedy *et al.*, 2013) or rather towards the divergence of glycolytic intermediates to other biosynthetic metabolic pathways. Adaptations in the metabolism of cancer cells and tumors, respectively, include all four major classes of macromolecules: carbohydrates, proteins, lipids and nucleic acids. The PPP, for example, uses the glycolytic intermediate glucose-6-phosphate for biosynthesis of ribose-5-phosphate and, finally, nucleotides and generation of NADPH for the detoxification of ROS and reductive biosynthesis. Dysregulation or inhibition of the PPP therefore impacts cancer growth and survival (De Preter *et al.*, 2016; Jiang *et al.*, 2011). Metabolomic analysis of polar, water-soluble metabolites from ML1B1B1 cell extracts in comparison to S2WTP3 cell extracts revealed higher concentrations of hypoxanthine, a metabolite involved in the salvage pathway of purine and pyrimidine nucleotides and the adenosine nucleotides AMP/ADP/ATP.

Furthermore, the detected nucleotide sugars UDP-GlcNAc and UDP-GalNAc indicated a diversion of the glycolytic intermediate fructose-6-phosphate into the hexosamine biosynthesic pathway. The hexosamine pathway contributes to syntheses of glycolipids, proteoglycans and glycosaminoglycans and provides the substrate for O- and N-glycosylation, post-translational modifications mediated by *O*-GlcNAc transferases, of proteins (Chiaradonna *et al.*, 2018). Aberrant protein glycosylation has been associated, amongst other cancer types, with breast cancer and breast cancer metastasis (Gu *et al.*, 2010; Krzeslak *et al.*, 2012). In summary, metabolomics analysis of the polar phase of S2WTP3 and ML1B1B1 cell extracts points towards the diversion of glucose-derived carbons towards biosynthesis pathways sustaining cell proliferation in the ML1B1B1 cells.

Interestingly, a comparable metabolic shift towards enhanced glucose utilization and production of biomass building blocks via the PPP was detected in brain metastatic human

breast cancer cells generated via repeated selection in immunocompromised mice. The brain metastatic cells relied on enhanced mitochondrial respiration in their energy metabolism and maintenance of cellular redox systems (Chen *et al.*, 2007). The generation of this brain metastatic cell line was comparable to the generation of ML1B1B1 cells and had overall comparable effects on the human cells: both murine and human metastatic breast cancer cells had enhanced glucose utilization. Proteomic analysis of the human cell line revealed higher abundances of enzymes involved in glycolysis, the TCA and OxPhos and enhanced activation of the PPP. Proteomic analysis of the murine breast cancer cell lines S2WTP3 and ML1B1B1 is discussed in section 5.2.2.

5.2.1.4 Choline metabolism

In addition to the AMP/ADP/ATP species, UDP-GlcNAc and UDP-GalNAc, and hypoxanthine, ML1B1B1 cell extracts presented higher concentrations of PCho than S2WTP3 cell extracts (section 4.3.5). The higher concentrations of PCho in the ML1B1B1 cell extracts were reflected in higher tCho concentrations detected in *in vivo* ^{1}H spectroscopy of ML1B1B1 allograft tumors. Additionally, a significantly higher GCho/PCho ratio was detected in *ex vivo* ^{1}H HR-MAS NMR spectroscopy of the resected ML1B1B1 tumor allografts (refer to section 4.3.3).

PCho is an intermediate metabolite in the synthesis and degradation of phosphatidylcholine, one of the most abundant phospholipid components in the cell membrane. An overview of the cellular Cho metabolism is given in Figure 101. Deregulated Cho metabolism has been observed in different types of cancers, including brain (Horská and Barker, 2010), prostate (Kobus *et al.*, 2012) and breast cancer (Jagannathan *et al.*, 2001; Kvistad *et al.*, 1999). Overexpression of choline kinase, the enzyme catalyzing the phosphorylation of Cho to PCho in the biosynthetic pathway of phosphatidylcholine, was observed in these types of cancers. The PCho/Cho ratio indicated malignant transformation of normal cells to cancer cells and increased tCho levels were associated with aggressiveness in breast cancer (Chen *et al.*, 2011). Choline kinase overexpression was experimentally shown to increase invasiveness and drug resistance in human breast cancer cells confirming the value of PCho as biomarker for aggressive breast cancer (Shah *et al.*, 2010). MRI and *in vivo* ^{1}H MRS have also been used to assess therapeutic response in breast cancer patients (Sharma *et al.*, 2011). ML1B1B1 allografts showed nearly 2-fold increased levels of GCho in comparison to S2WTP3 allografts in ^{1}H HR-MAS NMR spectroscopy resulting in a higher GCho/PCho ratio. Evidence from breast cancer patient biopsies and patient-derived xenografts points towards higher GCho concentrations in the most aggressive breast cancer subtypes (Giskeodegard *et al.*, 2010; Moestue *et al.*, 2010) and reduced concentrations of GCho in response to therapy (Cao *et al.*, 2012).

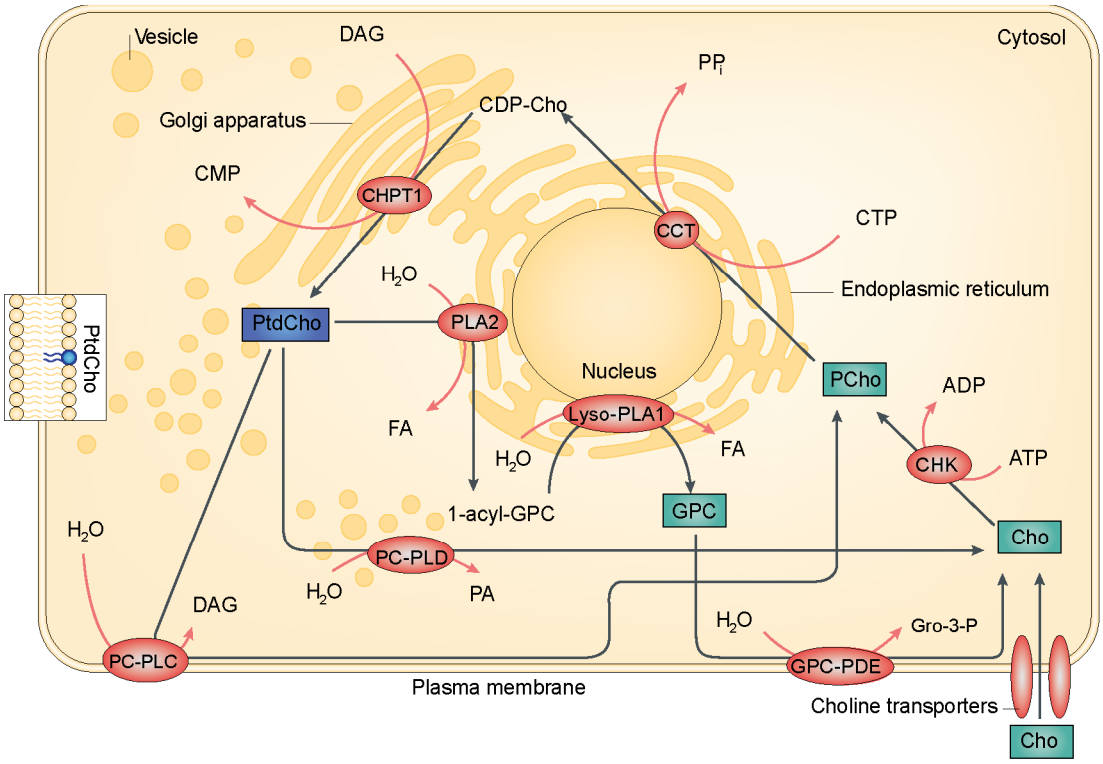

Figure 101: Cellular choline metabolism.
Cellular Cho metabolism includes the biosynthesis and cleavage of phosphatidlycholine (PtdCho, highlighted in blue). Enzymes involved in Cho metabolism are highlighed in red (catalyzed enzymatic reaction given with black arrows, reaction products with red arrows). Metabolites detected in this work are highlighted in green. CCT-CTP: phosphocholine cytidylyltransferase, CDP-Cho-cytidine diphosphate-choline, CHKα-choline kinase-α, CHPT1-diacylglycerol cholinephosphotransferase 1, CMP-cytidine monophosphate, CTP-cytidine triphosphate, FA-fatty acid, GPC-glycerophosphocholine, GPC-PDE-glycerophosphocholine phosphodiesterase, Gro-3-P-glycerol-3-phosphate, Lyso-PLA1-lyso-phospholipase A1, PCho-phosphocholine, PC-PLC-phosphatidylcholine-specific phospholipase C, PC-PLD-phosphatidylcholine-specific phospholipase D, PLA2-cytoplasmic phosphatidylcholine-specific phospholipase A2, PPi-diphosphate. Figure adapted from Glunde *et al.* 2011.

5.2.1.4.1 Technical considerations

Due to the limitation of the *in vivo* ^{1}H spectroscopic resolution, *ex vivo* ^{1}H HR-MAS NMR spectroscopy was performed to receive ^{1}H spectra of the S2WTP3 and ML1B1B1 allograft tumor sample with higher resolution permitting the disintegration of the tCho peak detected at 3.2 ppm in ^{1}H *in vivo* spectroscopy into its components Cho, PCho and GCho. ^{1}H HR-MAS NMR spectroscopy was performed on snap-frozen allograft tumor punch-biopsies that were submerged in D_2O for the measurement. As punch-biopsies were performed on frozen tumor samples, it was not possible to distinguish between viable and necrotic tissue possibly affecting the analysis. Additionally, during the measurement, the D_2O solvent leaked into the rotor cup leading to the formation of two different spin systems during acquisition. Correction of the

spectra (performed by Dr. Christoph Trautwein) by removal of double peaks or double peak multiplets allowed for the interpretation of the data, however, for further *ex vivo* investigations of metabolites from tumor samples, a different approach will be considered. Tumor samples measured with ^{1}H HR-MAS NMR spectroscopy were subjected to high centrifugal forces and measured at 4 °C possibly provoking decomposition of susceptible metabolites. Metabolite extraction should therefore be useful to confirm the obtained data and furthermore improve the resolution of the spectra. However, the metabolite extraction protocol needs careful evaluation to avoid reduction of accuracy caused by differences in solubility and volatility of different metabolites. Additionally, lipophilic metabolites and lipids such as phosphatidylcholine could be analyzed using a compatible extraction method. Addition of a defined concentration of a reference standard would further allow for absolute quantification of the detected metabolites (Moestue *et al.*, 2011).

5.2.2 Proteomics of the PyMT-derived cell lines S2WTP3 and ML1B1B1

In an experimental approach to elucidate possible causes for the observed changes in metabolism and aggressiveness, S2WTP3 and ML1B1B1 cell extracts were subjected to untargeted proteomic analysis. When interpreting the results of the proteomic analysis, it has to be considered that comparisons were drawn between two cancer cell lines and differences in the proteomes might not be as pronounced as when comparing the proteome of a cancer cell line to the proteome of its tissue of origin.

4351 proteins were confidentially detected by identification of unique peptides in the tryptic digests of the isolated proteins from S2WTP3 and ML1B1B1 cells (section 4.3.5). Comparative analysis of S2WTP3 and ML1B1B1 cells revealed largely homogenous abundances in the detected proteins. Additionally, intragroup homogeneity was substantiated by statistical analysis performed by Dr. Mohamed A. Jarboui before analysis of the intergroup differences between the S2WTP3 and ML1B1B1 proteomes. Consequently, mean values from the biological replicates were utilized for the following comparisons. Additionally, the transcriptomic screening performed on selected genes as further validation confirmed with proteomic analysis.

Comparative analysis of the S2WTP3 proteome and the ML1B1B1 proteome reflected the evolution of the two cell lines by a similar tissue signature in ontology analysis. Both cell lines shared overall common features with slight differences revealed in this analysis. The S2WTP3 proteome showed a closer relation to breast tissue and breast cancer than the ML1B1B1 proteome. As breast cancer frequently metastasizes to the lung (Yousefi *et al.*, 2018), the proteomic signatures of S2WTP3 and ML1B1B1 cells were also compared to lung tissue and lung cancer. The proteomic signature of S2WTP3 cells was closer to both lung tissue and lung cancer than the signature of ML1B1B1 cells. Interestingly, the *in vivo* evolution or *in vivo*

selection, which was unfortunately not further defined during cell line generation, resulted in a closer relation of the ML1B1B1 proteome to embryonal carcinoma cells, mesenchymal stromal cells and embryonic stem cells. This change in the signature of the proteome of ML1B1B1 cells towards embryonal cells and more specifically mesenchymal stromal cells prompted the question if ML1B1B1 cells might undergone EMT.

Pathway analysis assigned the detected protein abundances to the corresponding biological pathways and further affirmed the hypothesis that ML1B1B1 cell have initiated the EMT transdifferentiation program. In contrast, the reverse differentiation program, MET, was associated more closely with S2WTP3 cells. In comparison to the S2WTP3 proteome, proteins of ML1B1B1 cells were associated more closely with the solute carrier (SLC)-mediated transmembrane transport, the S1P1 pathway, epidermal growth factor receptor (EGFR)-dependent endothelin signaling events, integrin family cell surface interactions, proteoglycan syndecan-mediated signaling, β1 integrin cell surface interactions and nectin adhesion pathways. Interestingly, the only metabolic pathway identified in this analysis was the salvage pathway of pyrimidine ribonucleotides. ML1B1B1 cells presented higher abundance of proteins involved in the salvage pathway of pyrimidine ribonucleotides. In concordance, the metabolomic analysis of ML1B1B1 cell extractes revealed higher concentrations of hypoxanthin. The possibility that other metabolic pathways might be affected by changes in the proteome, however, was not excluded as only confidentially detected proteins were included in the analysis.

SLC-mediated transmembrane transport

Proteins involved in SLC-mediated transmembrane transport were identified as more abundant in ML1B1B1 compared to S2WTP3. The SLC superfamily of transmembrane transporters comprises 55 gene families with more than 200 putatively functional transporter-coding genes and controls uptake and efflux of different types of metabolites including carbohydrates, carboxylates and other organic anions, amino acids and oligopeptides, fatty acids and lipids as well as inorganic cations and anions (He *et al.*, 2009). Interestingly, the expression of membrane solute carrier SLC3A2 was correlated to higher tumor grade and poor patient outcome in a large breast cancer patient cohort (El Ansari *et al.*, 2018). Furthermore, the subfamily SLC2 comprises the 14 members of the facilitative GLUT family of glucose transmembrane transporters. Enhanced abundance of proteins of the SLC superfamily therefore substantiated the significantly higher [^{18}F]FDG uptake in the ML1B1B1 cells compared to S2WTP3 cells and pointed towards an overall elevated nutrient uptake to sustain proliferation.

S1P1 pathway

The S1P1 pathway refers to sphingosine-1-phosphate signaling as bioactive lipid mediator. Sphingosine kinase 1, a central enzyme in sphingolipid metabolism, was found in relative higher abundance in ML1B1B1 compared to S2WTP3 substantiating ontology analysis. Sphingosine-1-phoshate is synthetized from sphingosine derived from ceramide catabolism by either sphingosine kinase 1 or sphingosine kinase 2. The intracellularly produced sphingosine-1-phoshate can then be exported via specific transporters for inside-out signaling via a family of five G-protein coupled receptors. Generally, sphingosine-1-phoshate signaling is involved in the regulation of several hallmarks of cancer promoting neoangiogenesis, tumor cell proliferation and growth, resistance to apoptosis, as well as invasion and metastasis. The S1P1 receptor, or $S1PR_1$, is the most abundant of the five receptors and ubiquitously expressed. The S1P1 receptor is coupled to a G_i G-protein signaling predominantly via a RAC-CDC42 pathway and further correlating with ERK activation. Activation of this pathway leads to enhanced cell migration with further downstream targets depending on the cell type (Pyne and Pyne, 2010; Pyne *et al.*, 2012; Shida *et al.*, 2008). In a 4T1 murine breast cancer mouse model, elevated levels of sphingosine-1-phosphate were found to promote tumor progression (Nagahashi *et al.*, 2012) and altered gene expression of enzymes in the sphingolipid metabolism were found to correlate with poor prognosis in human breast cancer patients (Ruckhaberle *et al.*, 2008).

EGFR-dependent endothelin signaling events

Beside the emerging role of sphingolipid mediators in cancer, endothelin is gaining recognition in breast cancer. Endothelin expression in breast cancer correlates with higher vascularity and angiogenesis and has further been associated with an invasive phenotype. The underlying molecular mechanisms for endothelin induced invasiveness are not fully understood to date, however, might comprise the activation of downstream signaling cascades involved in cell survival and proliferation such as EGFR signaling, as detected in the ontology pathway analysis, and PKC, modulation of MMP activity, induction of pro-invasive cytokines and modulation of the tumor stroma. In turn, the tumor stroma might secrete EMT-inducing factor promoting invasion and stemness in the tumor cells (Nelson *et al.*, 2003).

Integrin family cell surface interactions and nectin adhesion pathways

The β-galactoside-binding proteins galectin-1 and galectin-3 are associated with malignant transformation: their expression is frequently altered in human cancer (Thijssen *et al.*, 2015). Integrins and nectin are involved in cell migration and invasion. Integrins mediate adhesion to the ECM and, in their function as inside-out and outside-in signaling molecules, regulate intracellular pathways controlling cytoskeletal organization (Hood and Cheresh, 2002). Nectin

can, either cooperatively with or independent of, cadherin organize intercellular junctions, for example E cadherin-based adherens junctions and claudin-based tight junctions in epithelial cells (Takai *et al.*, 2003; Takai and Nakanishi, 2003). The detected relative higher abundance of vimentin, plectin, nestin and galectin-1 and galectin-3 and the cell surface glycoprotein CD44 in ML1B1B1 in comparison to S2WTP3 cells further substantiated the hypothesis that ML1B1B1 cells have further progressed in the EMT program in comparison to S2WTP3 cells.

R-RAS protein abundance

Within the proteomic analysis, the oncoprotein RAS-related R-RAS was of special interest. The Ras genes *NRAS*, *HRAS* and *KRAS* are the most common oncogenes in human cancer (Hobbs *et al.*, 2016). The RAS downstream signaling pathways control, for example, cell survival, tumor growth, invasiveness and angiogenesis. R-RAS was shown to engage the same downstream targets Ras (Liu *et al.*, 2017). Mitogenic activity of RAS is mediated, for example, via the RAS-adaptor serine/threonine kinase RAF activating a kinase cascade of mitogen-activated protein kinase kinases (MEK), extracellular signal-regulated kinases (ERK) and MAPK, the MEK/ERK/MAPK pathway. Beside MAPK, ERK phosphorylates and activates transcription factors such as c-JUN leading to the expression of cell cycle regulatory proteins, such as CDCA3 that was identified in proteomic analysis and is associated with the cell division cycle. ERK-mediated upregulation of angiogenic factors and MMPs promote angiogenesis and invasion (Downward, 2003). R-RAS was found to promote migration and invasion of breast epithelial cells through interactions with integrins, predominantly with the integrin α_2 (Keely *et al.*, 1999). This was further in concordance with the integrin cell surface interactions elucidated in ontology analysis. Furthermore, R-RAS can directly interact with PI3K and stimulate AKT activity. Activated AKT has anti-apoptotic effects by negatively regulating pro-apoptotic proteins such as the Bcl-2-associated death promoter and inhibiting caspase-9 activation by direct phosphorylation and further by positively regulating transcription factors responsible for expression of pro-survival genes. By activation of AKT, RAS also affects cellular metabolism: AKT activity stimulates the expression of glycolytic enzymes through HIF which might be one major factor contributing to enhanced glucose uptake in tumor cells (Manning and Cantley, 2007). Interestingly, in human epithelial cells, mutated H-RAS has been shown to enhance glucose uptake without enhanced lactate production but conversion into anabolic substrates in the TCA (Telang *et al.*, 2007). Likewise, oncogenic K-RAS signaling diverted high amounts of glucose towards the PPP while glutamine fueled mitochondrial metabolism for ATP and NADPH generation and biosynthesis of amino acids and lipids (Weinberg *et al.*, 2010). Both the PI3K/AKT pathway and the RAF/MEK/ERK pathway additionally inhibit negative regulators of the mechanistic target of rapamycin (mTOR) complex 1 (mTORC1), a master regulator of cell growth. Activation of mTORC1 drives cell growth by enhancing biomass-synthesizing

anabolic processes such as synthesis of proteins and nucleotide precursors (Guertin and Sabatini, 2007; Tee, 2018). Moreover, experimental evidence from mouse fibroblast cells pointed towards increased nucleotide triphosphate concentrations and higher levels of PCho after transfection with *H-Ras* (Ronen *et al.*, 2001). Higher concentrations of PCho were also detected in human breast cancer cell lines in MRS and linked to higher expression levels of phospholipase C (Glunde *et al.*, 2004), however, if activation of phospholipase C was mediated by RAS was not assessed in this study.

In summary, the higher abundance of R-RAS in ML1B1B1 cells compared to S2WTP3 cells, under the assumption that the higher abundance of R-RAS resulted in a higher protein activity, might explain some distinctive features observed in ML1B1B1 cells: the more aggressive growth and stronger invasive phenotype, the higher [^{18}F]FDG uptake *in vitro* and the elevated synthesis of biomass precursors detected in the form of nucleotides and nucleotide sugars UDP-GlcNAc and UDP-GalNAc.

EMT and MET

The possibly most important pathways detected in ontology analysis elucidating the phenotypic differences in aggressiveness between ML1B1B1 and S2WTP3 cells might be EMT and MET with EMT-related proteins higher in abundance in ML1B1B1 and MET-related proteins higher in abundance in S2WTP3. The transdifferentiation of epithelial to mesenchymal phenotypes in cancer cells entails loss of epithelial characteristics and acquisition of a migratory and mesenchymal phenotype: A hallmark characteristic of EMT is the accompanying loss of E-cadherin expression or function and reduced abundance of proteins forming tight junctions on the one hand and, on the other hand, heightened expression of mesenchymal markers such as vimentin, N-cadherin or fibronectin (Bruner and Derksen, 2018; Leduc and Etienne-Manneville, 2015; Thiery *et al.*, 2009; Tiwari *et al.*, 2012). The switch in the transcriptional program towards EMT is induced, for example, by TGF-β and bone morphogenetic protein, signaling via the Wnt/β-catenin pathway, Notch and Hedgehog (Gonzalez and Medici, 2014). Additionally, EMT in cancer cells leads to the generation of cancer-initiating cells or CSCs with increased self-renewal capacities, resistance to apoptosis and chemotherapy (Mani *et al.*, 2008; Morel *et al.*, 2008). EMT and MET in tumor cells are thought to be transient processes: once a circulating or metastatic tumor cell has invaded a secondary tissue, the EMT-provoked mesenchymal phenotype is suppressed along with mesenchymal markers while the MET program upregulates epithelial markers (Polyak and Weinberg, 2009; Thiery *et al.*, 2009). During both EMT and the reverse MET process, distinct EMT transition states occur that can be characterized according to the parental cell type (Pastushenko *et al.*, 2018). It has further become evident that EMT and MET are associated with reversible epigenetic modifications

including histone modifications. The modifying enzymes, on the one hand, rely on substrate availability for reversible modifications while, on the other hand, increased metabolite availability can inhibit certain enzymes. One prominent example are dioxygenases, especially of the α-ketoglutarate-dependent dioxygenase family. Dioxygenases can regulate gene transcription on an epigenetic level. High levels of the oncometabolites succinate, as found in ML1B1B1, and fumarate, for example, are thought to inhibit α-ketoglutarate-dependent dioxygenases affecting genes involved in differentiation and EMT. High levels of 2-hydroxyglutarate were shown to induce an EMT-like phenotype by upregulation of one key EMT transcription factor, ZEB1, in HCT116 colorectal cancer cells and MCF-10A mammary epithelial cells (Grassian *et al.*, 2012).

The higher expression of both CD44 and nestin in ML1B1B1 cells pointed towards a more progressed EMT stage in ML1B1B1 cells: both CD44 and nestin have been identified as markers for cancer initiating cells or CSCs. CD44 is a cell surface glycoprotein involved in adhesion, enhanced cell proliferation and angiogenesis and was found to modulate invasion in breast cancer (Louderbough and Schroeder, 2011). Increased nestin expression was shown to correlate with grade and prognosis of breast carcinomas (Neradil and Veselska, 2015). In triple negative breast cancer samples, immunohistochemical staining correlated nestin expression with invasiveness and disease outcome. Furthermore, nestin expression was correlated with EMT by activation of the Wnt/β-catenin signaling pathway (Shan *et al.*, 2015; Zhao *et al.*, 2014). Both ML1B1B1 and S2WTP3 cells were derived from the transgenic MMTV-PyMT mouse model of breast cancer metastasizing to the lungs. Breast cancers cells in this model were shown to undergo EMT resulting in a state of epithelial-mesenchymal plasticity. The epithelial phenotype could be detected by the expression of E-cadherin (Beerling *et al.*, 2016). In another study in this mouse model, cancer cells in the primary tumor and in established lung metastases showed an epithelial phenotype as detected by higher expression of E-cadherin than vimentin while single disseminated tumor cells presented a more mesenchymal phenotype with higher expression levels of vimentin. Interestingly, in this experimental setting, bone marrow-derived $CD11b^{+}/Ly6C^{high}$ myeloid cells were found to express high levels of the ECM chondroitin sulfate proteoglycan protein versican (Gao *et al.*, 2012b). Versican expressed by myeloid progenitor cells enhanced cell proliferation and promoted metastatic outgrowth in the MMTV-PyMT mouse model *in vivo* and enhanced cell proliferation in the human breast cancer cell line MDA-MB-231 *in vitro* (Gao *et al.*, 2012a). Comparable to the data gathered on murine breast cancer cells, the metastatic human breast cancer cell line MDA-MB-231 was characterized as an $E\text{-cadherin}^{-}/\text{vimentin}^{+}$ mesenchymal post-EMT phenotype. In severely immunocompromised mice, the MDA-MB-231 cells gave rise to $E\text{-cadherin}^{+}$ metastases. Metastatic outgrowth, however, was dependent on versican-expressing bone marrow-derived progenitor cells stimulating MET (Chao *et al.*, 2010). This

experimental data indicated a contribution of environmental factors in the regulation of EMT and MET in tumor cells.

Additionally, the proteomic analysis showed a dependency on TGF-β in ML1B1B1 cells also indicating EMT progression in the ML1B1B1 cells. A recently published report further highlighted the importance of TGF-β for EMT in the MMTV-PyMT model. Although studied in a cell line derived from female MMTV-PyMT mice on FVB/N background, the authors could show that TGF-β alone was sufficient to induce functional EMT in this cell line while removal of TGF-β resulted in MET (Saxena *et al.*, 2018). The RAS signaling pathway already discussed above for its role in the regulation of cancer metabolism also takes a special place in EMT: RAS is the central downstream effector of growth factors inducing EMT including TGF-β. *In vitro*, aberrant activation of the RAS-MAPK pathway in cooperation with TGF-β lead to EMT in human mammary epithelial cells accompanied by an $CD44^{+}/CD24^{-/low}$ breast CSC phenotype (Morel *et al.*, 2008). The role of TGF-β in promotion or sustainance of cancer initiating cells or CSCs was further demonstrated in breast cancer (Bruna *et al.*, 2012) and breast cancer invasion (Drabsch and ten Dijke, 2011) with TGF-β being considered a major regulator of cancer stemness and metastasis. Furthermore, a connection between RAS signaling and EMT-mediating transcription factors was established: RAS-mediated activation of AKT inhibits glycogen synthase kinase 3β that directly negatively regulates the EMT-promoting transcription factors SNAIL1/2 and lymphoid enhancer-binding factor 1 under the control of β-catenin (Gonzalez and Medici, 2014). UDP-GlcNAc modifications also affect protein stability of SNAIL1. SNAIL1, the transcriptional repressor of E-cadherin, for example, is stabilized by UDP-GlcNAc modification opposite to O-phophorylation-mediated proteasomal degradation (Park *et al.*, 2010). Enhanced levels of UDP-GlcNAc, as observed in the metabolomic analysis of polar ML1B1B1 cell extracts, might therefore directly influence SNAIL1 protein stability and lead to SNAIL1-mediated EMT. Aberrant glycosylation was found in different types of cancers and was further associated with increased malignancy. Activation of the hexosamine biosynthetic pathway, increase of cellular UDP-GlcNAc levels and consequently increasing levels of cell surface glycoconjugates was further demonstrated in human lung adenocarcinoma cells upon stimulation with TGF-β (Lucena *et al.*, 2016).

As already briefly mentioned in section 5.2.1.3, brain metastatic human breast cancer cells exhibited a similar phenotype as ML1B1B1 cells. These cells exhibited higher abundances of enzymes involved in glycolysis, the TCA and OxPhos and the PPP in proteomic analysis (Chen *et al.*, 2007). Although the human metastatic breast cancer cells exhibited a similar metabolic phenotype, on the contrary, higher abundances of metabolic enzymes involved in these pathways could not be confidently detected in the murine breast cancer cell line ML1B1B1.

5.2.2.1.1 Technical considerations

While proteomic analysis elucidated differences in protein abundance between the cell lines S2WTP3 and ML1B1B1 and further associated these proteins with different pathways in ontology analysis, proteomic analysis was performed neglecting the activation status of the proteome. The relevance of cellular signaling pathways was discussed under the assumption that the detected higher abundances of cellular signaling proteins correlated with higher protein activities. This assumption, however, should further be verified by either phosphoproteomics or phospho-western blotting analysis to assess the phosphorylation status and therefore activation status for proteins regulated by phosphorylation such as R-RAS.

5.2.3 Outlook

The metabolic examinations of the S2WTP3 and ML1B1B1 cells and tumor allografts were focused on primarily glucose and secondarily pyruvate metabolism. Although experiments on glucose and pyruvate metabolism did provide insights into the metabolic phenotype of S2WTP3 and ML1B1B1 allografts *in vitro* and *in vivo* and elucidate a certain mismatch between the metabolic behavior *in vitro* and *in vivo*, further characterization of the cell lines and -derived allografts should include additional metabolic profiling.

Additionally to glucose and pyruvate metabolism, lipid metabolism should be examined. Differences in the choline metabolism as detected by the differences in GCho/PCho ratios between S2WTP3 and ML1B1B1 allografts further prompts the *in vivo* investigation of choline metabolism, for example, with radiolabeled choline, [^{11}C]choline, or the radiolabeled choline derivative [^{18}F]fluoromethylcholine targeting choline kinases in the choline metabolic pathway. As differences in fatty acid and lipid content of the allograft tumors could not confidently be assessed *in vivo* due to the placement of the allograft tumors in the 4th MFP and metabolomic analysis of cell extract focused on polar extracts, the impact of fatty acid metabolism in this model system should further be elucidated as a role for fatty acid metabolism in EMT, cancer stemness and metastasis was described in the literature for some cancer types undermining the need for further investigations (Kuo and Ann, 2018; Luo *et al.*, 2017). The fatty acid analogue PET tracer 14(*R,S*)-[^{18}F]fluoro-6-thia-heptadecanoic acid is metabolically trapped in the cells and subsequently should be committed to the fatty acid catabolic pathway β-oxidation (DeGrado *et al.*, 1991) which should allow the estimation of fatty acid catabolism in S2WTP3 and ML1B1B1 tumors. Fatty acid synthesis might be probed with the radiolabeled [^{11}C]acetate: in lipogenic tumors, [^{11}C]acetate is converted into [1-^{11}C]acetyl-CoA that can enter the fatty acid synthesis pathway (DeFord-Watts *et al.*, 2013).

Then, the oxygenation of the tumor allografts or rather tumor hypoxia should be assessed with, for example, [^{18}F]FAZA- or [^{18}F]FMISO-PET imaging *in vivo* as [^{18}F]FDG uptake might have

been influenced by tumor hypoxia. Beside the assessment of tumor hypoxia *in vivo*, oxygen consumption could be determined by [^{15}O]O_2-PET imaging, ^{17}O-MRS (Neveu *et al.*, 2017), electron paramagnetic resonance oximetry (Danhier *et al.*, 2012), blood or tissue oxygenation level dependent contrast MRI (Hallac *et al.*, 2014; Li *et al.*, 2015) or ^{19}F-MRI with perfluorocarbons (Shi *et al.*, 2013).

Additionally to glucose, cancer cells frequently rely on glutamine catabolism for sustenance, a phenomenon termed glutamine addiction. Glutaminolysis is not only used for ATP production but also to replenish the TCA with anaplerotic intermediates. The oncogenes *MYC* and *RAS* are major regulators in cancer metabolism with RAS regulating both glycolysis and glutaminolysis (Kim and Kim, 2013; Perera and Bardeesy, 2015). The emergence of the essential role of glutaminolysis in cancer metabolism led to the development of novel glutamine-based PET radiotracers. 4-[^{18}F]-fluoroglutamine, for example, showed high uptake in murine mammary gland tumors and imaging of human glioma patients revealed promising first results (Venneti *et al.*, 2015). *In vivo* examinations of glutamine metabolism of S2WTP3 and ML1B1B1 tumor allografts would therefore be beneficial for the characterization of the metabolic phenotype of these allograft tumors. As indicated by metabolomics, alterations in the activity of the PPP and hexosamine biosynthesis pathways are suspected in the more aggressive ML1B1B1 cells. To date, however, no radiotracers are available to assess or image the activity of these two pathways.

Besides PET imaging, *in vivo* ^{13}C-MRS enables real-time detection of the metabolic flux of hyperpolarized ^{13}C-labeled small molecule metabolites. Hyperpolarized [1-^{13}C]acetate next to the radioactive [^{11}C]acetate, for example, allows an estimation of fatty acid metabolism: [1-^{13}C]acetate is activated to [1-^{13}C]acetyl-CoA and used for fatty acid synthesis or transported into mitochondria for catabolism in the TCA (Flori *et al.*, 2015). Next, application of [5-^{13}C]glutamine enables probing of the first step of glutaminolysis and downstream metabolism, respectively (Gallagher *et al.*, 2008). The activity of the TCA cycle can be assessed with [2-^{13}C]pyruvate: ^{13}C-labeling of pyruvate at the second carbon position leads to the incorporation of the ^{13}C-label into citrate in the first step of the TCA and further metabolic conversion into [5-^{13}C]α-ketoglutarate and [5-^{13}C]glutamate (Josan *et al.*, 2014; Park *et al.*, 2016a; Schroeder *et al.*, 2009). ^{13}C-MRS can further be employed to assess the redox status of cancer cells: an increase in the reduction of hyperpolarized [1-^{13}C]dehydroascorbate to [1-^{13}C]ascorbate indicates high concentrations of glutathione (Keshari *et al.*, 2011).

Furthermore, cancer cells are thought to utilize aerobic glycolysis to minimize oxidative stress that in part arises from ROS production in the respiratory chain (Cairns *et al.*, 2011). An increase in ROS is frequently observed in cancer cells as ROS in concentrations below a critical threshold increase cell proliferation and survival (Havens *et al.*, 2006; Liou and Storz, 2010). ROS generation was also found to be essential for K-RAS mediated tumorigenicity

(Weinberg *et al.*, 2010). Furthermore, a mitochondrial switch was shown to promote tumor metastasis in the B16 melanoma model. The authors found, in their self-generated "superinvasive" B16 tumor cells, that an increased mitochondrial activity and ROS production led to the activation of SRC and the downstream FAK family member PYK2 and, consequently, the promotion of invasion (Porporato *et al.*, 2014). Therefore, ROS measurements in the cell lines S2WTP3 and ML1B1B1 and phospho-western blotting analysis of possibly involved kinases of the FAK family could further contribute to the understanding of the underlying mechanisms causing the more aggressive phenotype of ML1B1B1 cells.

Additionally to the factors and pathways involved in EMT discussed above, the microRNA family miR-200 seems to play an important role in EMT (Humphries and Yang, 2015). Assessment of the expression levels of miRNA200 should therefore further affirm or contradict the hypothesis of progressed EMT in ML1B1B1 cells. Additionally, as ML1B1B1 cells have been associated with embryonic stem cells in ontology analysis, CSC-like traits were assumed. As CSCs and CSC-like cancer cells are considered resistant to chemotherapy, it would further be interesting to test the resistance of S2WTP3 and ML1B1B1 cells to chemotherapeutics. Furthermore, as ML1B1B1 cells were isolated from metastases following several rounds of *in vivo* selection, the ML1B1B1 cells should further be profiled for the acquisition of oncogenic driver mutations.

As discussed above, phenotypic plasticity between EMT and MET can result in transitional hybrid states that are characterized by an overlap of both epithelial and mesenchymal markers. ML1B1B1 cells could therefore just have entered the EMT transdifferentiation program or just initiated the reverse MET transdifferentiation program. As ML1B1B1 cells represent the third generation of *in vivo* metastatic progeny of S2WTP3, further profiling of either the first generation of the metastatic progeny, ML1, or the fifth generation, ML1B5, should provide further inside into the evolution of ML1B1B1 cells during this selection process and should allow closer placement of ML1B1B1 cells on the continuum of EMT-MET plasticity.

6 SUMMARY

6.1 Summary

The clinical relevance of MDSCs, immature myeloid cells that are pathologically activated and immunosuppressive in cancer patients, in primary tumor growth, pre-metastatic niche formation and metastasis has led to an increased scientific interest in these cells in the last decades. Homing of PMN-MDSCs to the primary breast TME was been previously demonstrated *in vivo* by OI. In a preliminary study, murine PMN- and M-MDSC migration could be tracked to the primary breast cancer TME after labeling with the fluorescent dye DiD for *in vivo* imaging by OI. The *in vivo* imaging data could further be validated by *ex vivo* OI, confocal laser endomicroscopy and flow cytometry. Interestingly, a higher fraction of M-MDSCs seemed to have been recruited to the primary breast cancer. Absolute quantification of *in vivo* tumor homing of the fluorescently labeled MDSC subpopulations, however, was not possible due to the physical restriction of planar OI.

The primary aim of this work therefore was the establishment, evaluation and application of an antibody-based radiolabeling approach for murine MDSCs enabling non-invasive cell tracking *in vivo* by PET. Labeling of *in vitro* expanded MDSC subpopulations with the [^{64}Cu]NOTA-anti-CD11b mAb was feasible and resulted in the internalization of the [^{64}Cu]NOTA-anti-CD11b mAb-CD11b complex. Incorporation of the radioisotope ^{64}Cu had no significant effect on MDSC viability or immunosuppressive function in comparison to unlabeled controls; DNA double strand breaks were detected only at 48 h post radiolabeling. The established radiolabeling method enabled *in vivo* MDSC tracking in a PyMT-derived primary breast cancer and breast cancer metastasis models as well as in a primary B16-F10 melanoma and melanoma metastasis model. In concordance to current literature, the examined different tumor types exhibited different degrees in MDSC recruitment. Primary B16-F10 melanomas showed an overall enhanced recruitment of [^{64}Cu]PMN- and [^{64}Cu]M-MDSCs in comparison to primary PyMT-derived breast tumors. Additionally, primary melanomas recruited higher fractions of [^{64}Cu]PMN-MDSCs while PyMT-derived breast tumors recruited higher fractions of [^{64}Cu]M-MDSCs. In comparison to the primary tumor models, recruitment of [^{64}Cu]PMN- and [^{64}Cu]M-MDSCs was more pronounced in the corresponding metastasis models but reflecting the observed trends in primary tumor tropism: B16-F10 melanoma lung metastatic lesions recruited overall higher fractions of [^{64}Cu]PMN- and [^{64}Cu]M-MDSCs compared to breast cancer lung metastatic lesion and [^{64}Cu]PMN-MDSC uptake was higher than [^{64}Cu]M-MDSC uptake. Moreover, PyMT breast cancer metastases exhibited higher uptake of [^{64}Cu]M-MDSCs.

Detection of secondary organ pre-metastatic niche formation *in vivo* by visualization of enhanced MDSC migration to the affected organ, however, could not be realized due to the

lack of adequate mouse models. Different experimental approaches for the induction of the pre-metastatic niche *in vivo* should therefore by employed for further imaging studies.

The metabolic switch towards aerobic glycolysis in cancer cells was already observed in the early 20th century. Consequently, the deregulation of the energy metabolism in tumors was recognized as a hallmark of cancer. Current research focuses on metabolic flexibility and metabolic drivers of cancer metastasis. Therefore, the second aim of this work was the metabolic examination of two PyMT-derived breast cancer cell lines, the parental cell line S2WTP3 and it's more aggressive, metastatic progeny ML1B1B1 with focus on glucose metabolism. Wherever feasible, a comparison was drawn to the well-known, established B16 melanoma model with the B16-F0 parental cells and the metastatic B16-F10 progeny which *in vivo* generation resembled the ML1B1B1 cell line.

In concordance to literature reports suggesting a high [^{18}F]FDG uptake in metastatic tumors, *in vitro* [^{18}F]FDG uptake was higher in B16-F10 cells in comparison to B16-F0 cells. While ML1B1B1 cells were characterized by an elevated [^{18}F]FDG uptake *in vitro* in comparison to S2WTP3 cells, *in vivo* [^{18}F]FDG uptake in the ML1B1B1 tumors was not higher in comparison to S2WTP3 tumors. This discrepancy between the *in vitro* and *in vivo* [^{18}F]FDG uptake might be explained by tumor hypoxia and further tumor characterization will include *in vivo* measurements assessing tumor hypoxia. Beside high glucose uptake, the glycolytic metabolic phenotype is further characterized by excretion of lactate and alanine. Therefore, real-time metabolic conversion of pyruvate, the end product of glycolysis, was determined in S2WTP3 and ML1B1B1 cell suspensions by hyperpolarized [1-^{13}C]pyruvate MRS. Conversion of [1-^{13}C]pyruvate into [1-^{13}C]lactate and [1-^{13}C]alanine was higher in the parental S2WTP3 cells than in ML1B1B1 cells resulting in higher [1-^{13}C]lactate/[1-^{13}C]pyruvate and [1-^{13}C]alanine/[1-^{13}C]pyruvate ratios in the parental cell line. In contrast, the [1-^{13}C]lactate/[1-^{13}C]pyruvate and [1-^{13}C]alanine/[1-^{13}C]pyruvate ratios were higher in the metastatic B16-F10 melanomas cells in comparison to the parental B16-F0 generation indicating that the metastatic B16-F10 melanomas cells exhibit the classical glycolytic phenotype characterized by high glucose uptake and high lactate production. As metabolic intermediates of glycolysis can be diverted to biosynthetic metabolic pathways such as the PPP and hexosamine biosynthetic pathway, metabolomic analysis was performed on polar cell extracts of S2WTP3 and ML1B1B1 cells. The detected metabolites substantiated the diversion of glycolytic intermediates to the PPP and hexosamine biosynthetic pathway. Interestingly, deregulation of choline metabolism resulted in higher concentrations of GCho and PCho in the metastatic ML1B1B1 cells *in vitro* and tCho *in vivo*. Untargeted proteomic analysis of S2WTP3 and ML1B1B1 cell extracts further linked the metabolic phenotype of ML1B1B1 cells to the more aggressive behavior. Although higher abundances of metabolically active enzymes could not be detected in ML1B1B1 cells

in comparison to S2WTP3 cells, a relative higher abundance of oncogenic protein R-RAS was detected in ML1B1B1 cells. Under the assumption that R-RAS protein abundance correlated with R-RAS activity in the ML1B1B1 cells, R-RAS signaling likely contributed to the observed enhanced glycolysis and flux of glycolytic intermediated to the PPP. Moreover, proteomic analysis pointed towards EMT progression in the ML1B1B1 cells in comparison to S2WTP3 cells contributing to the aggressive, metastatic phenotype of ML1B1B1 cells. Transcriptomic profiling conformed with proteomic analysis, however, further steps to validate the proteomic analysis should include western blotting of phosphoproteins to assess the activation status of key signaling proteins in EMT and R-RAS. Further studies characterizing the EMT state and metabolic phenotype of ML1B1B1 cells would provide additional insight into the correlation between EMT, metabolism and metastasis in this model.

6.2 Zusammenfassung

Die Entdeckung von myeloiden Suppressorzellen (MDSCs), unvollständig differenzierten, immunsupprimierende myeloiden Vorläuferzellen, im peripheren Blut von Krebspatienten und die negative Korrelation zwischen der Anzahl von MDSCs im peripheren Blut und dem Wachstum eines malignen Tumors, der Bildung von Metastasen sowie des Patientenüberlebens haben zu einem gesteigerten wissenschaftlichen Interesse an diesen Zellen geführt.

In einer früheren Bildgebungsstudie konnte bereits mittels optischer Bildgebung gezeigt werden, dass polymorphonukleäre (PMN-)MDSCs in die Tumormikroumgebung (TME, von engl. tumor microenvironment) eines murinen Brustkrebstumors rekrutiert werden. In einer Vorstudie konnte zunächst erfolgreich mittels optischer Bildgebung *in vivo* gezeigt werden, dass auch die zweite murine MDSC-Population, monozytäre (M-)MDSCs, zum primären Brusttumor rekrutiert wird. Die *in vivo* Bildgebungsdaten konnten zusätzlich *ex vivo* mittels einer speziellen konfokalen *in vivo* Mikroskopiertechnik und Durchflusszytometrie validiert werden.

Das Ziel des ersten Experimentalteils war die Etablierung und Evaluierung einer Markierungsmethode für murine MDSCs für die nicht-invasive Bildgebung mit Positronenemissionstomographie (PET) sowie die Anwendung dieser Markierungsmethode zur Darstellung der Migration von MDSCs in murinen Tumor- und Metastasierungsmodellen.

Die Radiomarkierung von *in vitro* expandierten PMN- und M-MDSCs für die PET-Bildgebung konnte erfolgreich mit dem radioaktiv-markierten, CD11b-spezifschen monoklonalen Antikörper [^{64}Cu]NOTA-anti-CD11b durchgeführt werden. Die Markierung von PMN- und M-MDSCs mit diesem Antikörper resultierte in der Internalisierung des Antikörper-CD11b-

Komplexes innerhalb von 3 Stunden nach der Radiomarkierung. Die Radiomarkierung hatte keinen signifikanten Effekt auf die Zellviabilität und die Induktion von Apoptose im Vergleich zu nicht-markierten Zellen. Die Bildung von Doppelstrangbrüchen in der DNA wurde erstmals nach 48 Stunden nach der Radiomarkierung mit diesem radioaktiven Antikörper festgestellt. Die Funktionalität von PMN- und M-MDSCs wurde durch die Markierung mit dem [^{64}Cu]NOTA-anti-CD11b Antikörper nicht beeinträchtigt.

Mittels der beschriebenen Radiomarkierungsmethode konnte die Migration von MDSCs in einem Brustkrebs-, einem Melanom-, sowie den zugehörigen Brustkrebsmetastasierungs- und Melanommetastasierungsmodellen verfolgt werden. In Übereinstimmung mit gegenwärtiger Literatur, die das Vorkommen der PMN- und M-MDSC-Populationen in Krebspatienten beschreibt, konnten Unterschiede in der Rekrutierungsdynamik der radiomarkierten PMN- und M-MDSCs festgestellt werden. Während sich im Melanom-Modell mehr radiomarkierte PMN-MDSCs als M-MDSCs im Primärtumor anreicherten, konnten mehr radiomarkierte M-MDSCs als PMN-MDSCs im Brustkrebs-Modell gefunden werden. Dieser Trend zeigte sich so auch in den zugehörigen Modellen der Tumormetastasierung: Lungenmetastasen des Melanoms zeigten eine erhöhte Anreicherung von radiomarkierten PMN-MDSCs im Vergleich zu radiomarkierten M-MDSCs während Lungenmetastasen des Brustkrebses mehr radiomarkierte M-MDSCs als radiomarkierten PMN-MDSCs anreicherten. Sowohl primäre Melanome als auch Melanom-Metastasen reicherten mehr PMN-MDSCs und M-MDSCs an als primäre Brustkrebstumore und Brustkrebs-Metastasen.

MDSCs spielen neben der Beeinflussung des Tumorwachstums auch eine entscheidende Rolle in der Bildung einer Nische in prämetastatischen Geweben. Die *in vivo* Darstellung der prämetastatischen Nische in der Lunge mittels der Bildung der MDSC Migration gelang jedoch nicht in den dafür herangezogenen Tiermodellen. Um die Bildung einer prämetastatischen Nische durch die Anreichung von radiomarkierten MDSCs in zukünftigen Bildgebungsstudien darzustellen, werden folglich andere experimentelle Vorgehen und Modelle evaluiert werden.

Der zweite Experimentalteil dieser Arbeit beschäftigte sich näher mit dem Tumormetabolismus. Die als Warburg-Effekt bezeichnete Änderung des Glukosestoffwechsels zur unvollständigen Verstoffwechselung von Glukose in der Glykolyse und die darauffolgende Ausscheidung von Laktat bei ausreichender Sauerstoffversorgung in Tumorzellen wurde bereits Anfang des zwanzigsten Jahrhunderts beobachtet und galt lange als zentrales Dogma des Tumormetabolismus. Weitere Adaptionen des Energiestoffwechsels wurden jedoch erst in den letzten Jahren als besonderes Merkmal von Tumorerkrankungen weitestgehend anerkannt. Die metabolische Flexibilität von Tumoren und einzelnen zirkulierenden Tumorzellen sowie metabolische Modulatoren der Tumormetastasierung sind zentrale Gegenstand aktueller Forschungsarbeiten zum Tumormetabolismus. Das Ziel des

zweiten Teils dieser Arbeit war die metabolische Untersuchung von zwei Brustkrebstumorzelllinien, die von dem endogenen MMTV-PyMT-Brustkrebsmausmodell abstammen: die parentale Zelllinie S2WTP3 sowie die aggressivere, metastatische Zelllinie ML1B1B1, die durch wiederholte Metastasierung der Zelllinie S2WTP3 in der Maus und Selektion dieser Metastasen generiert wurde. Der zentrale Fokus der metabolischen Untersuchungen in diesem Versuchsteil war der Glukosemetabolismus. Sofern technisch und wirtschaftlich sinnvoll wurden die Melanom-Zelllinien B16-F0 und B16-F10 zum Vergleich herangezogen, da die Generierung der Tochterzelllinie B16-F10 aus der parentalen B16-F0 Zelllinie experimentell sehr ähnlich durchgeführt wurde.

Stellvertretend für den Glukoseverbrauch wurde die Aufnahme des radioaktiven Glukoseanalogs [^{18}F]FDG *in vitro* in einer Zellsuspension und *in vivo* in Brustkrebstumoren bestimmt. Die aggressiven Zelllinien, die Melanom-Zelllinie B16-F10 sowie die Brustkrebs-Zelllinie ML1B1B1, zeigten eine höhere Aufnahme von [^{18}F]FDG *in vitro* im Vergleich zur jeweiligen parentalen Zelllinie. Die erhöhte Aufnahme von [^{18}F]FDG *in vitro* konnte *in vivo* in ML1B1B1-Brustkrebstumoren im Vergleich zu S2WTP3-Brustkrebstumoren nicht bestätigt werden. Diese Diskrepanz könnte die Folge von Hypoxie sein, die in weiteren Studien untersucht werden sollte. Da der Warburg-Effekt weiterhin durch eine erhöhte Ausscheidung von Laktat aus Tumorzellen und Tumoren gekennzeichnet ist, wurde die Verwertung von Pyruvat, dem Endprodukt der Glykolyse, in Zellsuspensionen von S2WTP3 und ML1B1B1 Zellen mittels ^{13}C-Magnetresonanzspektroskopie nach Applikation von hyperpolarisiertem [1-^{13}C]Pyruvat charakterisiert. Das Verhältnis von [1-^{13}C]Laktat zu [1-^{13}C]Pyruvat sowie [1-^{13}C]Alanin zu [1-^{13}C]Pyruvat war in der parentalen Zelllinie S2WTP3 leicht erhöht im Vergleich zur metastatischen Zelllinie ML1B1B1. Im Gegensatz hierzu war das Verhältnis von [1-^{13}C]Laktat zu [1-^{13}C]Pyruvat sowie [1-^{13}C]Alanin zu [1-^{13}C]Pyruvat in der metastatischen Zelllinie B16-F10 erhöht im Vergleich zur parentalen Zelllinie B16-F0. Dies deutete auf den glykolytischen Phänotypen in B16-F10 Zellen hin, während die metastatischen ML1B1B1-Zellen die intermediären Metabolite der Glykolyse wahrscheinlich in Biosynthesewege wie den Pentosephosphatweg und den Hexosamin-Biosyntheseweg umleiteten. Neben der Glykolyse konnten Veränderungen im Metabolismus von Cholin in den ML1B1B1-Zellextrakten und in ML1B1B1-Tumoren im Vergleich zu S2WTP3-Zellextrakten und S2WTP3-Tumoren festgestellt werden.

Die Analyse des Proteoms nach Proteinextraktion aus ML1B1B1-Zellen und S2WTP3-Zellen führte zur zentralen Hypothese einer fortgeschrittenen epithelialen-mesenchymalen Transition in ML1B1B1-Zellen im Vergleich zu den parentalen S2WTP3-Zellen und konnte den metabolischen Phänotypen mit dem aggressiven Wachstum in Verbindung bringen. Das aggressivere Wachstum und die erhöhte Metastasierungspotenz im Vergleich zur parentalen Zelllinie könnte durch diese Transition erklärt werden. Obwohl keine erhöhten Mengen an

metabolischen Schrittmacherenzymen in ML1B1B1-Proteom im Vergleich zum S2WTP3-Proteom gefunden wurden, konnten erhöhte Mengen des Onkoproteins R-RAS im ML1B1B1-Proteom relativ zum S2WTP3-Proteom detektiert werden. Das Onkoprotein R-RAS beeinflusst nicht nur das Überleben und die Proliferation von Tumorzellen, sondern hat weiterreichende Effekte auf den Glukosemetabolismus. Diese Effekte konnten zuvor schon in mittels [^{18}F]FDG und [1-^{13}C]Pyruvat in den ML1B1B1-Zellen detektiert wurden. Eine Transkriptomanalyse wurde herangezogen, um die Expressionslevel einzelner Proteine der Proteomanalyse zu bestätigen, jedoch sollten weitere Analysen durchgeführt werden, um die funktionale Aktivität der Schlüsselproteine nachzuweisen.

Zukünftige Studien auf diesem Gebiet werden sich näher mit Adaptionen des Metabolismus der Brustkrebszellen ML1B1B1 während der epithelial-mesenchymalen Transition beschäftigen. Hierzu sollen sowohl die erste Muttergeneration, ML1, sowie die fünfte Tochtergeneration, ML1B5, der metastatischen Brustkrebszellen untersucht werden, um geeignete metabolische Marker für den Prozess der epithelial-mesenchymalen Transition zu finden, die die nicht-invasive Bildgebung der Zelltransition zu einem metastatischen Phänotypen ermöglichen.

7 STATEMENT

Ich erkläre hiermit, dass ich die zur Promotion eingereichte Arbeit mit dem Titel „Cellular and Metabolic Processes in Tumor Growth and Metastasis - Recruitment of Myeloid-Derived Suppressor Cells to the Primary and Metastatic Tumor Microenvironment and Multiparametric Metabolic Fingerprinting of Murine Breast Cancer Cells“ selbständig verfasst, nur die angegebenen Quellen und Hilfsmittel benutzt und wörtlich oder inhaltlich übernommene Stellen als solche gekennzeichnet habe. Ich erkläre, dass die Richtlinien zur Sicherung guter wissenschaftlicher Praxis der Universität Tübingen (Beschluss des Senats vom 25.5.2000) beachtet wurden. Ich versichere an Eides statt, dass diese Angaben wahr sind und dass ich nichts verschwiegen habe. Mir ist bekannt, dass die falsche Abgabe einer Versicherung an Eides statt mit Freiheitsstrafe bis zu drei Jahren oder mit Geldstrafe bestraft wird.

Tübingen, 2019

7.1 Declaration of contributions

Tracer synthesis was performed by the staff of the Radiopharmacy, Department of Preclinical Imaging and Radiopharmacy, University of Tübingen. Dr. Andreas Maurer and Natalie Mucha performed antibody-chelator-conjugations and antibody radiolabeling.
Murine cell culture procedures (tumor cell culture, MDSC expansion, isolation and radiolabeling, immunosuppression assays) were performed by me, as was induction of tumors and tumor metastases in the experimental animal models.
All PET and MRI measurements were performed by me, partially supported by Dr. Christoph M. Grießinger, Dr. Andreas Schmid and Dorothea I. Reck, and evaluated by me. Support for PET and MRI measurements was provided by technical personnel.
Histological stainings were performed by Birgit Fehrenbacher and Renate Nordin, Department of Dermatology, University of Tübingen.
Dr. Marie-Aline Neveu supported the acquisition of ^{13}C spectroscopic data and analyzed raw data. Dr. Mohamed Jarboui analyzed raw proteomic data and prepared respective figures for Part 3 in the results section. Dr. Christoph Trautwein performed parts of ^{1}H metabolomic analysis including cell extraction, acquisition of the spectra and raw data analysis. I interpreted the results in the context of this work.
All contributions to this work are further stressed in the Material and Methods section.

8 LIST OF PUBLICATIONS

8.1 Publications in scientific journals

Hoffmann, S.H.L., Reck, D.I., Maurer, A., Fehrenbacher, B., Sceneay, J.E., Poxleitner, M., Öz, H.H., Ehrlichmann, W., Reischl, G., Fuchs, K., Schaller, M., Hartl, D., Kneilling, M., Möller, A., Pichler, B.J., Griessinger, C.M. (2019). Visualization and quantification of *in vivo* homing kinetics of myeloid-derived suppressor cells in primary and metastatic cancer. Theranostics 9(20):5869-5885.

Hoffmann, S.H.L., Maurer, A., Reck, D.I., Reischl, G., Pichler, B.J., Kneilling, M., Griessinger, C.M. (2017). Labeling of murine lymphocytes by ^{64}Cu-antibody receptor targeting for *in vivo* cell trafficking by PET/CT. Journal of Visualized Experiments. 122.

Sceneay, J., Griessinger, C.M., **Hoffmann, S.H.L**, Wen, S.W., Wong, C.S.F., Krumeich, S., Kneilling, M., Pichler, B.J., Möller, A. (2018). Tracking the fate of adoptively transferred myeloid-derived suppressor cells in the primary breast tumor microenvironment. PLoS One. 13(4):e0196040.

Hage, C., Gremse, F., Griessinger, C.M., Maurer, A., **Hoffmann, S.H.L.**, Osl, F., Pichler, B.J., Kiessling, F., Scheuer, W., Pöschinger, T. (2018). Comparison of the Accuracy of FMT/CT and PET/MRI for the Assessment of Antibody Biodistribution in Squamous Cell Carcinoma Xenografts. The Journal of Nuclear Medicine, *59*(1), 44-50.

Schwenck, J., Fuchs, K., **Eilenberger, S.H.**, Rolle, A.M., Castaneda Vega, S., Thaiss, W.M., Maier, F.C. (2016). Fluorescence and Cerenkov luminescence imaging. Applications in small animal research. Nuklearmedizin. *55*(2), 63-70.

8.2 Contributions to scientific conferences

8.2.1 Oral presentations at scientific conferences

Eilenberger, S.H.L., Sceneay, J.E., Wong, C.S.F., Ehrlichmann, W., Reischl, G., Kneilling, M., Möller, A., Pichler, B.J., Griessinger, C.M.: *In vivo* imaging of ^{64}Cu-NOTA-CD11b-radiolabeled granulocytic myeloid-derived suppressor cells in a murine PyMT breast cancer model by

PET/MRI. Annual Meeting of the German Society for Nuclear Medicine (Deutsche Gesellschaft für Nuklearmedizin), 2016, April 20–23, Dresden, Germany.

Eilenberger, S.H.L., Sceneay, J.E., Wong, C.S.F., Ehrlichmann, W., Reischl, G., Kneilling, M., Möller, A., Pichler, B.J., Griessinger, C.M.: *In vivo* imaging of ^{64}Cu-NOTA-CD11b-radiolabeled granulocytic myeloid-derived suppressor cells in a murine PyMT breast cancer model by PET/MRI. Novel concepts in Innate Immunity, 2015, September 23-25, Tuebingen, Germany.

Eilenberger, S.H.L., Sceneay, J.E., Wong, C.S.F., Ehrlichmann, W., Reischl, G., Kneilling, M., Möller, A., Pichler, B.J., Griessinger, C.M.: *In vivo* tracking of ^{64}Cu-NOTA-CD11b-labeled granulocytic myeloid-derived suppressor cells in PyMT breast cancer by PET/MRI. World Molecular Imaging Congress, 2015, September 2-5, Honolulu, HI, USA.

8.2.2 Poster presentations at scientific conferences

Hoffmann, S.H.L., Neveu, M.A., Jarboui, M.A., Trautwein, C., Wong, C.S.F, Sceneay, J.E., Möller, A., Pichler, B.J., Griessinger, C.M.: A multiparametric approach towards metabo-proteomic fingerprinting of murine breast cancer cells. European Molecular Imaging Meeting, 2019, March 19-22, Glasgow, United Kingdom.

Hoffmann, S.H.L., Reck, D.I., Maurer, A., Sceneay, J.E., Wong, C.S.F., Ehrlichmann, W., Reischl, G., Kneilling, M., Möller, A., Pichler, B.J., Griessinger, C.M.: Non-invasive *in vivo* imaging of ^{64}Cu-NOTA-αCD11b-labeled myeloid-derived suppressor cell homing to the primary and metastatic tumor microenvironment. International Cancer Immunotherapy Conference, 2017, September 6-9, Mainz/Frankfurt, Germany.

Hoffmann, S.H.L., Reck, D.I., Maurer, A., Sceneay, J.E., Wong, C.S.F., Ehrlichmann, W., Reischl, G., Kneilling, M., Möller, A., Pichler, B.J., Griessinger, C.M.: Visualization of the recruitment of ^{64}Cu-NOTA-CD11b-labeled myeloid-derived suppressor cells to the primary and metastatic tumor microenvironment by PET/MRI. European Molecular Imaging Meeting, 2017, April 5-7, Cologne, Germany.

Eilenberger, S.H.L., Reck, D.I., Sceneay, J.E., Wong, C.S.F., Ehrlichmann, W., Reischl, G., Kneilling, M., Möller, A., Pichler, B.J., Griessinger, C.M.: Comparison of the migration patterns of granulocytic and monocytic myeloid-derived suppressor cells to primary and metastatic breast cancer by PET/MRI. World Molecular Imaging Congress, 2016, September 7-10, New York, NY, USA.

9 BIBLIOGRAPHY

Adonai, N., Nguyen, K.N., Walsh, J., Iyer, M., Toyokuni, T., Phelps, M.E., McCarthy, T., McCarthy, D.W., and Gambhir, S.S. (2002). *Ex vivo* cell labeling with ^{64}Cu-pyruvaldehyde-bis(N4-methylthiosemicarbazone) for imaging cell trafficking in mice with positron-emission tomography. Proceedings of the National Academy of Sciences of the United States of America *99*, 3030-3035.

Aguado, B.A., Bushnell, G.G., Rao, S.S., Jeruss, J.S., and Shea, L.D. (2017). Engineering the pre-metastatic niche. Nature Biomedical Engineering *1*, 0077.

Aguado, B.A., Wu, J.J., Azarin, S.M., Nanavati, D., Rao, S.S., Bushnell, G.G., Medicherla, C.B., and Shea, L.D. (2015). Secretome identification of immune cell factors mediating metastatic cell homing. Scientific Reports *5*, 17566.

Ahrens, E.T., and Bulte, J.W. (2013). Tracking immune cells *in vivo* using magnetic resonance imaging. Nature Reviews Immunology *13*, 755-763.

Ai, T., Morelli, J.N., Hu, X., Hao, D., Goerner, F.L., Ager, B., and Runge, V.M. (2012). A historical overview of magnetic resonance imaging, focusing on technological innovations. Investigative Radiology *47*, 725-741.

Akins, E.J., and Dubey, P. (2008). Noninvasive imaging of cell-mediated therapy for treatment of cancer. Journal of Nuclear Medicine *49*, 180s-195s.

Alexandrov, L.B., Nik-Zainal, S., Wedge, D.C., Aparicio, S.A.J.R., Behjati, S., Biankin, A.V., Bignell, G.R., Bolli, N., Borg, A., Børresen-Dale, A.-L.*, et al.* (2013). Signatures of mutational processes in human cancer. Nature *500*, 415.

Ardenkjaer-Larsen, J.H. (2016). On the present and future of dissolution-DNP. Journal of Magnetic Resonance *264*, 3-12.

Ardenkjaer-Larsen, J.H., Fridlund, B., Gram, A., Hansson, G., Hansson, L., Lerche, M.H., Servin, R., Thaning, M., and Golman, K. (2003). Increase in signal-to-noise ratio of > 10,000 times in liquid-state NMR. Proceedings of the National Academy of Sciences of the United States of America *100*, 10158-10163.

Ardenkjaer-Larsen, J.H., Leach, A.M., Clarke, N., Urbahn, J., Anderson, D., and Skloss, T.W. (2011). Dynamic nuclear polarization polarizer for sterile use intent. NMR in Biomedicine *24*, 927-932.

Arihara, F., Mizukoshi, E., Kitahara, M., Takata, Y., Arai, K., Yamashita, T., Nakamoto, Y., and Kaneko, S. (2013). Increase in $CD14^{+}HLA\text{-}DR^{-/low}$ myeloid-derived suppressor cells in hepatocellular carcinoma patients and its impact on prognosis. Cancer Immunology, Immunotherapy *62*, 1421-1430.

Atkins, P.W., de Paula, J. (2008). Kurzlehrbuch Physikalische Chemie (Wiley-VCH Verlag GmbH & Co. KGaA).

Avila-Rodriguez, M.A., Rios, C., Carrasco-Hernandez, J., Manrique-Arias, J.C., Martinez-Hernandez, R., García-Pérez, F.O., Jalilian, A.R., Martinez-Rodriguez, E., Romero-Piña, M.E., and Diaz-Ruiz, A. (2017). Biodistribution and radiation dosimetry of [^{64}Cu]copper dichloride: first-in-human study in healthy volunteers. EJNMMI Research *7*, 98.

Azarin, S.M., Yi, J., Gower, R.M., Aguado, B.A., Sullivan, M.E., Goodman, A.G., Jiang, E.J., Rao, S.S., Ren, Y., Tucker, S.L.*, et al.* (2015). *In vivo* capture and label-free detection of early metastatic cells. Nature Communications *6*, 8094.

Baley, D.L. (2005). Positron Emission Tomograpy Basic Sciences (Singapore: Springer Science+Business Media).

Becker, A., Thakur, B.K., Weiss, J.M., Kim, H.S., Peinado, H., and Lyden, D. (2016). Extracellular vesicles in cancer: cell-to-cell mediators of metastasis. Cancer Cell *30*, 836-848.

Beckford Vera, D.R., Smith, C.C., Bixby, L.M., Glatt, D.M., Dunn, S.S., Saito, R., Kim, W.Y., Serody, J.S., Vincent, B.G., and Parrott, M.C. (2018). Immuno-PET imaging of tumor-infiltrating lymphocytes using zirconium-89 radiolabeled anti-CD3 antibody in immune-competent mice bearing syngeneic tumors. PloS One *13*, e0193832.

Beerling, E., Seinstra, D., de Wit, E., Kester, L., van der Velden, D., Maynard, C., Schäfer, R., van Diest, P., Voest, E., van Oudenaarden, A.*, et al.* (2016). Plasticity between Epithelial and Mesenchymal States Unlinks EMT from Metastasis-Enhancing Stem Cell Capacity. Cell Reports *14*, 2281-2288.

Berg, J., Tymoczko, J., and Stryer, L. (2007). Glycolysis and Gluconeogenesis. In Biochemistry, Sixth edition (New York, New York, United States of America: W. H. Freeman and Company), pp. 485-512.

Bergenfelz, C., Larsson, A.M., von Stedingk, K., Gruvberger-Saal, S., Aaltonen, K., Jansson, S., Jernstrom, H., Janols, H., Wullt, M., Bredberg, A.*, et al.* (2015). Systemic Monocytic-MDSCs Are Generated from Monocytes and Correlate with Disease Progression in Breast Cancer Patients. PloS One *10*, e0127028.

Bhaumik, S., and Gambhir, S.S. (2002). Optical imaging of *Renilla* luciferase reporter gene expression in living mice. Proceedings of the National Academy of Sciences *99*, 377-382.

Bingol, K., and Bruschweiler, R. (2014). Multidimensional approaches to NMR-based metabolomics. Analytical chemistry *86*, 47-57.

Bonuccelli, G., Tsirigos, A., Whitaker-Menezes, D., Pavlides, S., Pestell, R.G., Chiavarina, B., Frank, P.G., Flomenberg, N., Howell, A., Martinez-Outschoorn, U.E.*, et al.* (2010). Ketones and lactate "fuel" tumor growth and metastasis: Evidence that epithelial cancer cells use oxidative mitochondrial metabolism. Cell Cycle *9*, 3506-3514.

Boomsma, R.A., and Geenen, D.L. (2014). Evidence for Transfer of Membranes from Mesenchymal Stem Cells to HL-1 Cardiac Cells. Stem Cells International *2014*, 653734.

Brindle, K.M. (2015). Imaging Metabolism with Hyperpolarized ^{13}C-Labeled Cell Substrates. Journal of the American Chemical Society *137*, 6418-6427.

Brindle, K.M., Bohndiek, S.E., Gallagher, F.A., and Kettunen, M.I. (2011). Tumor imaging using hyperpolarized 13C magnetic resonance spectroscopy. Magnetic Resonance in Medicine *66*, 505-519.

Bronte, V., Brandau, S., Chen, S.H., Colombo, M.P., Frey, A.B., Greten, T.F., Mandruzzato, S., Murray, P.J., Ochoa, A., Ostrand-Rosenberg, S.*, et al.* (2016). Recommendations for myeloid-derived suppressor cell nomenclature and characterization standards. Nature Communications *7*, 12150.

Bruna, A., Greenwood, W., Le Quesne, J., Teschendorff, A., Miranda-Saavedra, D., Rueda, O.M., Sandoval, J.L., Vidakovic, A.T., Saadi, A., Pharoah, P.*, et al.* (2012). TGF-β induces the formation of tumour-initiating cells in claudin^{low} breast cancer. Nature Communications *3*, 1055.

Bruner, H.C., and Derksen, P.W.B. (2018). Loss of E-Cadherin-Dependent Cell-Cell Adhesion and the Development and Progression of Cancer. Cold Spring Harbor Perspectives in Biology *10*, a029330.

Bulte, J.W., and Kraitchman, D.L. (2004). Iron oxide MR contrast agents for molecular and cellular imaging. NMR in Biomedicine *17*, 484-499.

Cai, H., Wu, J.S., Muzik, O., Hsieh, J.T., Lee, R.J., and Peng, F. (2014). Reduced ^{64}Cu uptake and tumor growth inhibition by knockdown of human copper transporter 1 in xenograft mouse model of prostate cancer. Journal of Nuclear Medicine *55*, 622-628.

Cairns, R.A., Harris, I.S., and Mak, T.W. (2011). Regulation of cancer cell metabolism. Nature Reviews Cancer *11*, 85.

Cao, M.D., Sitter, B., Bathen, T.F., Bofin, A., Lonning, P.E., Lundgren, S., and Gribbestad, I.S. (2012). Predicting long-term survival and treatment response in breast cancer patients receiving neoadjuvant chemotherapy by MR metabolic profiling. NMR in Biomedicine *25*, 369-378.

Carlsen, H., Moskaug, J.Ø., Fromm, S.H., and Blomhoff, R. (2002). *In Vivo* Imaging of NF-κB Activity. The Journal of Immunology *168*, 1441-1446.

Chaabane, W., User, S.D., El-Gazzah, M., Jaksik, R., Sajjadi, E., Rzeszowska-Wolny, J., and Los, M.J. (2013). Autophagy, apoptosis, mitoptosis and necrosis: interdependence between those pathways and effects on cancer. Archivum Immunologiae et Therapiae Experimentalis *61*, 43-58.

Chao, Y.L., Shepard, C.R., and Wells, A. (2010). Breast carcinoma cells re-express E-cadherin during mesenchymal to epithelial reverting transition. Molecular Cancer *9*, 179.

Chen, E.I., Hewel, J., Krueger, J.S., Tiraby, C., Weber, M.R., Kralli, A., Becker, K., Yates, J.R., and Felding-Habermann, B. (2007). Adaptation of Energy Metabolism in Breast Cancer Brain Metastases. Cancer Research *67*, 1472-1486.

Chen, J.H., Mehta, R.S., Baek, H.M., Nie, K., Liu, H., Lin, M.Q., Yu, H.J., Nalcioglu, O., and Su, M.Y. (2011). Clinical Characteristics and Biomarkers of Breast Cancer Associated with Choline Concentration Measured by ^{1}H MR Spectroscopy. NMR in Biomedicine *24*, 316-324.

Cherry, S.R. (2001). Fundamentals of positron emission tomography and applications in preclinical drug development. Journal of Clinical Pharmacology *41*, 482-491.

Cherry, S.R., and Dahlbom, M. (2006). PET Physics, Instrumentation, and Scanners (New York, New York, United States of America: Springer Science+Business Media).

Chiaradonna, F., Ricciardiello, F., and Palorini, R. (2018). The Nutrient-Sensing Hexosamine Biosynthetic Pathway as the Hub of Cancer Metabolic Rewiring. Cells *7*.

Cianciaruso, C., Pagani, A., Martelli, C., Bacigaluppi, M., Squadrito, M.L., Lo Dico, A., De Palma, M., Furlan, R., Lucignani, G., Falini, A.*, et al.* (2014). Cellular magnetic resonance with iron oxide nanoparticles: long-term persistence of SPIO signal in the CNS after transplanted cell death. Nanomedicine *9*, 1457-1474.

Combes, F., Mc Cafferty, S., Meyer, E., and Sanders, N.N. (2018). Off-Target and Tumor-Specific Accumulation of Monocytes, Macrophages and Myeloid-Derived Suppressor Cells after Systemic Injection. Neoplasia *20*, 848-856.

Comment, A., and Merritt, M.E. (2014). Hyperpolarized Magnetic Resonance as a Sensitive Detector of Metabolic Function. Biochemistry *53*, 7333-7357.

Condamine, T., Ramachandran, I., Youn, J.-I., and Gabrilovich, D.I. (2015). Regulation of Tumor Metastasis by Myeloid-Derived Suppressor Cells. Annual Review of Medicine *66*, 97-110.

Cooper, M.S., Ma, M.T., Sunassee, K., Shaw, K.P., Williams, J.D., Paul, R.L., Donnelly, P.S., and Blower, P.J. (2012). Comparison of ^{64}Cu-complexing bifunctional chelators for radioimmunoconjugation: labeling efficiency, specific activity, and *in vitro*/*in vivo* stability. Bioconjugate Chemistry *23*, 1029-1039.

Corrie, P., Hategan, M., Fife, K., and Parkinson, C. (2014). Management of melanoma. British Medical Bulletin *111*, 149-162.

Crowley, L.C., Christensen, M.E., and Waterhouse, N.J. (2016). Measuring Survival of Adherent Cells with the Colony-Forming Assay. Cold Spring Harbor Protocols *2016*, pdb.prot087171.

Danhier, F., Danhier, P., Magotteaux, N., De Preter, G., Ucakar, B., Karroum, O., Jordan, B., Gallez, B., and Préat, V. (2012). Electron Paramagnetic Resonance Highlights That the Oxygen Effect Contributes to the Radiosensitizing Effect of Paclitaxel. PloS One *7*, e40772.

Danhier, P., Deumer, G., Joudiou, N., Bouzin, C., Leveque, P., Haufroid, V., Jordan, B.F., Feron, O., Sonveaux, P., and Gallez, B. (2017). Contribution of macrophages in the contrast loss in iron oxide-based MRI cancer cell tracking studies. Oncotarget *8*, 38876-38885.

Danhier, P., Magat, J., Leveque, P., De Preter, G., Porporato, P.E., Bouzin, C., Jordan, B.F., Demeur, G., Haufroid, V., Feron, O*., et al.* (2015). *In vivo* visualization and *ex vivo* quantification of murine breast cancer cells in the mouse brain using MRI cell tracking and electron paramagnetic resonance. NMR in Biomedicine *28*, 367-375.

Danilin, S., Merkel, A.R., Johnson, J.R., Johnson, R.W., Edwards, J.R., and Sterling, J.A. (2012). Myeloid-derived suppressor cells expand during breast cancer progression and promote tumor-induced bone destruction. OncoImmunology *1*, 1484-1494.

Davidson, S.M., Papagiannakopoulos, T., Olenchock, B.A., Heyman, J.E., Keibler, M.A., Luengo, A., Bauer, M.R., Jha, A.K., O'Brien, J.P., Pierce, K.A*., et al.* (2016). Environment impacts the metabolic dependencies of Ras-driven non-small cell lung cancer. Cell Metabolism *23*, 517-528.

Day, S.E., Kettunen, M.I., Gallagher, F.A., Hu, D.-E., Lerche, M., Wolber, J., Golman, K., Ardenkjaer-Larsen, J.H., and Brindle, K.M. (2007). Detecting tumor response to treatment using hyperpolarized ^{13}C magnetic resonance imaging and spectroscopy. Nature Medicine *13*, 1382.

De Franceschi, N., Hamidi, H., Alanko, J., Sahgal, P., and Ivaska, J. (2015). Integrin traffic – the update. Journal of Cell Science *128*, 839-852.

de la Fuente, A., Alonso-Alconada, L., Costa, C., Cueva, J., Garcia-Caballero, T., Lopez-Lopez, R., and Abal, M. (2015). M-Trap: Exosome-Based Capture of Tumor Cells as a New Technology in Peritoneal Metastasis. Journal of the National Cancer Institute *107*.

De Preter, G., Neveu, M.A., Danhier, P., Brisson, L., Payen, V.L., Porporato, P.E., Jordan, B.F., Sonveaux, P., and Gallez, B. (2016). Inhibition of the pentose phosphate pathway by dichloroacetate unravels a missing link between aerobic glycolysis and cancer cell proliferation. Oncotarget *7*, 2910-2920.

De Silva, R.A., Jain, S., Lears, K.A., Chong, H.S., Kang, C.S., Sun, X., and Rogers, B.E. (2012). ^{64}Cu radiolabeling and biological evaluation of bifunctional chelators for radiopharmaceutical development. Nuclear Medicine and Biology *39*, 1099-1104.

DeBerardinis, R.J., and Cheng, T. (2010). Q's next: the diverse functions of glutamine in metabolism, cell biology and cancer. Oncogene *29*, 313-324.

DeFord-Watts, L.M., Mintz, A., and Kridel, S.J. (2013). The Potential of ^{11}C-acetate PET for Monitoring the Fatty Acid Synthesis Pathway in Tumors. Current Pharmaceutical Biotechnology *14*, 300-312.

DeGrado, T.R., Coenen, H.H., and Stocklin, G. (1991). 14(*R,S*)-[^{18}F]fluoro-6-thia-heptadecanoic acid (FTHA): evaluation in mouse of a new probe of myocardial utilization of long chain fatty acids. Journal of Nuclear Medicine *32*, 1888-1896.

Diaz-Montero, C.M., Salem, M.L., Nishimura, M.I., Garrett-Mayer, E., Cole, D.J., and Montero, A.J. (2009). Increased circulating myeloid-derived suppressor cells correlate with clinical cancer stage, metastatic tumor burden, and doxorubicin-cyclophosphamide chemotherapy. Cancer Immunology, Immunotherapy *58*, 49-59.

Diepenbruck, M., and Christofori, G. (2016). Epithelial–mesenchymal transition (EMT) and metastasis: yes, no, maybe? Current Opinion in Cell Biology *43*, 7-13.

Dieu-Nosjean, M.-C., Goc, J., Giraldo, N.A., Sautès-Fridman, C., and Fridman, W.H. (2014). Tertiary lymphoid structures in cancer and beyond. Trends in Immunology *35*, 571-580.

Dolcetti, L., Peranzoni, E., Ugel, S., Marigo, I., Fernandez Gomez, A., Mesa, C., Geilich, M., Winkels, G., Traggiai, E., Casati, A.*, et al.* (2010). Hierarchy of immunosuppressive strength among myeloid-derived suppressor cell subsets is determined by GM-CSF. European Journal of Immunology *40*, 22-35.

Donkor, M.K., Lahue, E., Hoke, T.A., Shafer, L.R., Coskun, U., Solheim, J.C., Gulen, D., Bishay, J., and Talmadge, J.E. (2009). Mammary tumor heterogeneity in the expansion of myeloid-derived suppressor cells. International Immunopharmacology *9*, 937-948.

Downward, J. (2003). Targeting RAS signalling pathways in cancer therapy. Nature Reviews Cancer *3*, 11.

Drabsch, Y., and ten Dijke, P. (2011). TGF-β Signaling in Breast Cancer Cell Invasion and Bone Metastasis. Journal of Mammary Gland Biology and Neoplasia *16*, 97-108.

Draghiciu, O., Lubbers, J., Nijman, H.W., and Daemen, T. (2015). Myeloid derived suppressor cells—An overview of combat strategies to increase immunotherapy efficacy. OncoImmunology *4*, e954829.

Eckhardt, B.L., Parker, B.S., van Laar, R.K., Restall, C.M., Natoli, A.L., Tavaria, M.D., Stanley, K.L., Sloan, E.K., Moseley, J.M., and Anderson, R.L. (2005). Genomic analysis of a spontaneous model of breast cancer metastasis to bone reveals a role for the extracellular matrix. Molecular Cancer Research *3*, 1-13.

Eisenblaetter, M., Flores-Borja, F., Lee, J.J., Wefers, C., Smith, H., Hueting, R., Cooper, M.S., Blower, P.J., Patel, D., Rodriguez-Justo, M.*, et al.* (2017). Visualization of Tumor-Immune Interaction - Target-Specific Imaging of S100A8/A9 Reveals Pre-Metastatic Niche Establishment. Theranostics *7*, 2392-2401.

El Ansari, R., Craze, M.L., Diez-Rodriguez, M., Nolan, C.C., Ellis, I.O., Rakha, E.A., and Green, A.R. (2018). The multifunctional solute carrier 3A2 (SLC3A2) confers a poor prognosis in the highly proliferative breast cancer subtypes. British Journal of Cancer *118*, 1115-1122.

Eriksson, D., and Stigbrand, T. (2010). Radiation-induced cell death mechanisms. Tumour Biology *31*, 363-372.

Eruslanov, E., Daurkin, I., Ortiz, J., Vieweg, J., and Kusmartsev, S. (2010). Pivotal Advance: Tumor-mediated induction of myeloid-derived suppressor cells and M2-polarized macrophages by altering intracellular PGE2 catabolism in myeloid cells. Journal of Leukocyte Biology *88*, 839-848.

Ewing, J. (1928). Neoplastic Diseases: A Treatise on Tumours (W. B. Saunders Company).

Ferlay, J., Colombet, M., Soerjomataram, I., Dyba, T., Randi, G., Bettio, M., Gavin, A., Visser, O., and Bray, F. (2018). Cancer incidence and mortality patterns in Europe: Estimates for 40 countries and 25 major cancers in 2018. European Journal of Cancer *103*, 356-387.

Fidler, I.J. (1973). Selection of successive tumour lines for metastasis. Nature: New biology *242*, 148-149.

Fidler, I.J. (1975). Biological Behavior of Malignant Melanoma Cells Correlated to Their Survival *in Vivo*. Cancer Research *35*, 218-224.

Fidler, I.J., and Nicolson, G.L. (1976). Organ selectivity for implantation survival and growth of B16 melanoma variant tumor lines. Journal of the National Cancer Institute *57*, 1199-1202.

Flori, A., Liserani, M., Frijia, F., Giovannetti, G., Lionetti, V., Casieri, V., Positano, V., Aquaro, G.D., Recchia, F.A., Santarelli, M.F.*, et al.* (2015). Real-time cardiac metabolism assessed with hyperpolarized [1-^{13}C]acetate in a large-animal model. Contrast Media & Molecular Imaging *10*, 194-202.

Franken, N.A.P., Rodermond, H.M., Stap, J., Haveman, J., and van Bree, C. (2006). Clonogenic assay of cells *in vitro*. Nature Protocols *1*, 2315.

Franklin, R.A., Liao, W., Sarkar, A., Kim, M.V., Bivona, M.R., Liu, K., Pamer, E.G., and Li, M.O. (2014). The cellular and molecular origin of tumor-associated macrophages. Science *344*, 921-925.

Freise, A.C., and Wu, A.M. (2015). *In vivo* imaging with antibodies and engineered fragments. Molecular Immunology *67*, 142-152.

Freise, A.C., Zettlitz, K.A., Salazar, F.B., Lu, X., Tavare, R., and Wu, A.M. (2017). ImmunoPET Imaging of Murine CD4$^+$ T Cells Using Anti-CD4 Cys-Diabody: Effects of Protein Dose on T Cell Function and Imaging. Molecular Imaging and Biology *19*, 599-609.

Fridman, W.H., Galon, J., Pages, F., Tartour, E., Sautes-Fridman, C., and Kroemer, G. (2011). Prognostic and predictive impact of intra- and peritumoral immune infiltrates. Cancer Research *71*, 5601-5605.

Fridman, W.H., Zitvogel, L., Sautes-Fridman, C., and Kroemer, G. (2017). The immune contexture in cancer prognosis and treatment. Nature Reviews Clinical Oncology *14*, 717-734.

Fujii, W., Ashihara, E., Hirai, H., Nagahara, H., Kajitani, N., Fujioka, K., Murakami, K., Seno, T., Yamamoto, A., Ishino, H.*, et al.* (2013). Myeloid-derived suppressor cells play crucial roles in the regulation of mouse collagen-induced arthritis. Journal of Immunology *191*, 1073-1081.

Furuya, H., Shimizu, Y., and Kawamori, T. (2011). Sphingolipids in cancer. Cancer and Metastasis Reviews *30*, 567-576.

Fuxa, M., and Busslinger, M. (2007). Reporter gene insertions reveal a strictly B lymphoid-specific expression pattern of Pax5 in support of its B cell identity function. The Journal of Immunology *178*, 8222-8228.

Gabrilovich, D.I. (2017). Myeloid-Derived Suppressor Cells. Cancer Immunology Research *5*, 3-8.

Gabrilovich, D.I., Bronte, V., Chen, S.-H., Colombo, M.P., Ochoa, A., Ostrand-Rosenberg, S., and Schreiber, H. (2007). The terminology issue for myeloid-derived suppressor cells. Cancer Research *67*, 425-426.

Gabrilovich, D.I., Ostrand-Rosenberg, S., and Bronte, V. (2012). Coordinated regulation of myeloid cells by tumours. Nature Reviews Immunology *12*, 253-268.

Gallagher, F.A., Kettunen, M.I., Day, S.E., Lerche, M., and Brindle, K.M. (2008). ^{13}C MR spectroscopy measurements of glutaminase activity in human hepatocellular carcinoma cells using hyperpolarized ^{13}C-labeled glutamine. Magnetic Resonance in Medicine *60*, 253-257.

Gambhir, S.S. (2002). Molecular imaging of cancer with positron emission tomography. Nature Reviews Cancer *2*, 683-693.

Gambhir, S.S., Czernin, J., Schwimmer, J., Silverman, D.H., Coleman, R.E., and Phelps, M.E. (2001). A tabulated summary of the FDG PET literature. Journal of Nuclear Medicine *42*, 1s-93s.

Gao, D., Joshi, N., Choi, H., Ryu, S., Hahn, M., Catena, R., Sadik, H., Argani, P., Wagner, P., Vahdat, L.T.*, et al.* (2012a). Myeloid progenitor cells in the premetastatic lung promote metastases by inducing mesenchymal to epithelial transition. Cancer Research *72*, 1384-1394.

Gao, D., Vahdat, L.T., Wong, S., Chang, J.C., and Mittal, V. (2012b). Microenvironmental regulation of epithelial-mesenchymal transitions in cancer. Cancer Research *72*, 4883-4889.

Gatenby, R.A., and Gillies, R.J. (2004). Why do cancers have high aerobic glycolysis? Nature Reviews Cancer *4*, 891-899.

Gaykema, S.B., Brouwers, A.H., Lub-de Hooge, M.N., Pleijhuis, R.G., Timmer-Bosscha, H., Pot, L., van Dam, G.M., van der Meulen, S.B., de Jong, J.R., Bart, J.*, et al.* (2013). ^{89}Zr-bevacizumab PET imaging in primary breast cancer. Journal of Nuclear Medicine *54*, 1014-1018.

Gillies, R.J., Robey, I., and Gatenby, R.A. (2008). Causes and consequences of increased glucose metabolism of cancers. Journal of Nuclear Medicine *49 Suppl 2*, 24s-42s.

Giraldo, N.A., Becht, E., Remark, R., Damotte, D., Sautès-Fridman, C., and Fridman, W.H. (2014). The immune contexture of primary and metastatic human tumours. Current Opinion in Immunology *27*, 8-15.

Giskeodegard, G.F., Grinde, M.T., Sitter, B., Axelson, D.E., Lundgren, S., Fjosne, H.E., Dahl, S., Gribbestad, I.S., and Bathen, T.F. (2010). Multivariate modeling and prediction of breast cancer prognostic factors using MR metabolomics. Journal of Proteome Research *9*, 972-979.

Glunde, K., Bhujwalla, Z.M., and Ronen, S.M. (2011). Choline metabolism in malignant transformation. Nature Reviews Cancer *11*, 835-848.

Glunde, K., Jie, C., and Bhujwalla, Z.M. (2004). Molecular causes of the aberrant choline phospholipid metabolism in breast cancer. Cancer Research *64*, 4270-4276.

Goc, J., Fridman, W.-H., Sautès-Fridman, C., and Dieu-Nosjean, M.-C. (2013). Characteristics of tertiary lymphoid structures in primary cancers. OncoImmunology *2*, e26836.

Gómez-Cuadrado, L., Tracey, N., Ma, R., Qian, B., and Brunton, V.G. (2017). Mouse models of metastasis: progress and prospects. Disease Models & Mechanisms *10*, 1061-1074.

Gonzalez, D.M., and Medici, D. (2014). Signaling mechanisms of the epithelial-mesenchymal transition. Science Signaling *7*, re8.

Grassian, A.R., Lin, F., Barrett, R., Liu, Y., Jiang, W., Korpal, M., Astley, H., Gitterman, D., Henley, T., Howes, R.*, et al.* (2012). Isocitrate dehydrogenase (IDH) mutations promote a reversible ZEB1/microRNA (miR)-200-dependent epithelial-mesenchymal transition (EMT). The Journal of Biological Chemistry *287*, 42180-42194.

Griessinger, C.M., Kehlbach, R., Bukala, D., Wiehr, S., Bantleon, R., Cay, F., Schmid, A., Braumuller, H., Fehrenbacher, B., Schaller, M.*, et al.* (2014). *In vivo* tracking of Th1 cells by PET reveals quantitative and temporal distribution and specific homing in lymphatic tissue. Journal of Nuclear Medicine *55*, 301-307.

Griessinger, C.M., Maurer, A., Kesenheimer, C., Kehlbach, R., Reischl, G., Ehrlichmann, W., Bukala, D., Harant, M., Cay, F., Brück, J.*, et al.* (2015). ^{64}Cu antibody-targeting of the T-cell receptor and subsequent internalization enables *in vivo* tracking of lymphocytes by PET. Proceedings of the National Academy of Sciences *112*, 1161-1166.

Gros, A., Turcotte, S., Wunderlich, J.R., Ahmadzadeh, M., Dudley, M.E., and Rosenberg, S.A. (2012). Myeloid cells obtained from the blood but not from the tumor can suppress T-cell proliferation in patients with melanoma. Clinical Cancer Research *18*, 5212-5223.

Gu, Y., Mi, W., Ge, Y., Liu, H., Fan, Q., Han, C., Yang, J., Han, F., Lu, X., and Yu, W. (2010). GlcNAcylation plays an essential role in breast cancer metastasis. Cancer Research *70*, 6344-6351.

Guertin, D.A., and Sabatini, D.M. (2007). Defining the Role of mTOR in Cancer. Cancer Cell *12*, 9-22.

Gupta, G.P., and Massagué, J. (2006). Cancer Metastasis: Building a Framework. Cell *127*, 679-695.

Guy, C.T., Cardiff, R.D., and Muller, W.J. (1992). Induction of mammary tumors by expression of polyomavirus middle T oncogene: a transgenic mouse model for metastatic disease. Molecular and Cellular Biology *12*, 954-961.

Hajek, M., and Dezortova, M. (2008). Introduction to clinical *in vivo* MR spectroscopy. European Journal of Radiology *67*, 185-193.

Hallac, R.R., Zhou, H., Pidikiti, R., Song, K., Stojadinovic, S., Zhao, D., Solberg, T., Peschke, P., and Mason, R.P. (2014). Correlations of noninvasive BOLD and TOLD MRI with pO2 and relevance to tumor radiation response. Magnetic Resonance in Medicine *71*, 1863-1873.

Hanahan, D., and Coussens, L.M. (2012). Accessories to the crime: functions of cells recruited to the tumor microenvironment. Cancer Cell *21*, 309-322.

Hanahan, D., and Weinberg, R.A. (2000). The Hallmarks of Cancer. Cell *100*, 57-70.

Hanahan, D., and Weinberg, Robert A. (2011). Hallmarks of Cancer: The Next Generation. Cell *144*, 646-674.

Hasenberg, A., Hasenberg, M., Mann, L., Neumann, F., Borkenstein, L., Stecher, M., Kraus, A., Engel, D.R., Klingberg, A., Seddigh, P.*, et al.* (2015). Catchup: a mouse model for imaging-based tracking and modulation of neutrophil granulocytes. Nature Methods *12*, 445-452.

Havens, C.G., Ho, A., Yoshioka, N., and Dowdy, S.F. (2006). Regulation of Late G_1/S Phase Transition and APC^{Cdh1} by Reactive Oxygen Species. Molecular and Cellular Biology *26*, 4701-4711.

He, L., Vasiliou, K., and Nebert, D.W. (2009). Analysis and update of the human solute carrier (SLC) gene superfamily. Human Genomics *3*, 195-205.

Hennig, J., Nauerth, A., and Friedburg, H. (1986). RARE imaging: a fast imaging method for clinical MR. Magnetic Resonance in Medicine *3*, 823-833.

Hensley, C.T., Faubert, B., Yuan, Q., Lev-Cohain, N., Jin, E., Kim, J., Jiang, L., Ko, B., Skelton, R., Loudat, L.*, et al.* (2016). Metabolic Heterogeneity in Human Lung Tumors. Cell *164*, 681-694.

Highfill, S.L., Cui, Y., Giles, A.J., Smith, J.P., Zhang, H., Morse, E., Kaplan, R.N., and Mackall, C.L. (2014). Disruption of CXCR2-Mediated MDSC Tumor Trafficking Enhances Anti-PD1 Efficacy. Science Translational Medicine *6*, 237-267.

Hirakawa, S., Brown, L.F., Kodama, S., Paavonen, K., Alitalo, K., and Detmar, M. (2007). VEGF-C-induced lymphangiogenesis in sentinel lymph nodes promotes tumor metastasis to distant sites. Blood *109*, 1010-1017.

Hobbs, G.A., Der, C.J., and Rossman, K.L. (2016). RAS isoforms and mutations in cancer at a glance. Journal of Cell Science *129*, 1287-1292.

Hoechst, B., Ormandy, L.A., Ballmaier, M., Lehner, F., Kruger, C., Manns, M.P., Greten, T.F., and Korangy, F. (2008). A new population of myeloid-derived suppressor cells in hepatocellular carcinoma patients induces $CD4^+CD25^+Foxp3^+$ T cells. Gastroenterology *135*, 234-243.

Hoffmann, S.H.L., Maurer, A., Reck, D.I., Reischl, G., Pichler, B.J., Kneilling, M., and Griessinger, C.M. (2017). Murine Lymphocyte Labeling by ^{64}Cu-Antibody Receptor Targeting for *In Vivo* Cell Trafficking by PET/CT. Journal of Visualized Experiments.

Holland, J.P., Ferdani, R., Anderson, C.J., and Lewis, J.S. (2009). Copper-64 Radiopharmaceuticals for Oncologic Imaging. PET Clinics *4*, 49-67.

Hood, J.D., and Cheresh, D.A. (2002). Role of integrins in cell invasion and migration. Nature Reviews Cancer *2*, 91.

Hood, J.L., San, R.S., and Wickline, S.A. (2011). Exosomes released by melanoma cells prepare sentinel lymph nodes for tumor metastasis. Cancer Research *71*, 3792-3801.

Horská, A., and Barker, P.B. (2010). Imaging of Brain Tumors: MR Spectroscopy and Metabolic Imaging. Neuroimaging Clinics of North America *20*, 293-310.

Hoshino, A., Costa-Silva, B., Shen, T.L., Rodrigues, G., Hashimoto, A., Tesic Mark, M., Molina, H., Kohsaka, S., Di Giannatale, A., Ceder, S*., et al.* (2015). Tumour exosome integrins determine organotropic metastasis. Nature *527*, 329-335.

Huang, A., Zhang, B., Wang, B., Zhang, F., Fan, K.X., and Guo, Y.J. (2013). Increased $CD14^{+}HLA\text{-}DR^{-/low}$ myeloid-derived suppressor cells correlate with extrathoracic metastasis and poor response to chemotherapy in non-small cell lung cancer patients. Cancer Immunology, Immunotherapy *62*, 1439-1451.

Huang, B., Lei, Z., Zhao, J., Gong, W., Liu, J., Chen, Z., Liu, Y., Li, D., Yuan, Y., Zhang, G.M*., et al.* (2007). CCL2/CCR2 pathway mediates recruitment of myeloid suppressor cells to cancers. Cancer Letters *252*, 86-92.

Huang, J., Lee, C.C., Sutcliffe, J.L., Cherry, S.R., and Tarantal, A.F. (2008). Radiolabeling rhesus monkey $CD34^{+}$ hematopoietic and mesenchymal stem cells with ^{64}Cu-pyruvaldehyde-bis(N4-methylthiosemicarbazone) for microPET imaging. Molecular Imaging *7*, 1-11.

Humphries, B., and Yang, C. (2015). The microRNA-200 family: small molecules with novel roles in cancer development, progression and therapy. Oncotarget *6*, 6472-6498.

Iclozan, C., Antonia, S., Chiappori, A., Chen, D.T., and Gabrilovich, D. (2013). Therapeutic regulation of myeloid-derived suppressor cells and immune response to cancer vaccine in patients with extensive stage small cell lung cancer. Cancer Immunology, Immunotherapy *62*, 909-918.

Idorn, M., Kollgaard, T., Kongsted, P., Sengelov, L., and Thor Straten, P. (2014). Correlation between frequencies of blood monocytic myeloid-derived suppressor cells, regulatory T cells and negative prognostic markers in patients with castration-resistant metastatic prostate cancer. Cancer Immunology, Immunotherapy *63*, 1177-1187.

Jablonski, A. (1933). Efficiency of Anti-Stokes Fluorescence in Dyes. Nature *131*, 839.

Jagannathan, N.R., Kumar, M., Seenu, V., Coshic, O., Dwivedi, S.N., Julka, P.K., Srivastava, A., and Rath, G.K. (2001). Evaluation of total choline from *in vivo* volume localized proton MR spectroscopy and its response to neoadjuvant chemotherapy in locally advanced breast cancer. British Journal of Cancer *84*, 1016-1022.

Jiang, P., Du, W., Wang, X., Mancuso, A., Gao, X., Wu, M., and Yang, X. (2011). p53 regulates biosynthesis through direct inactivation of glucose-6-phosphate dehydrogenase. Nature Cell Biology *13*, 310-316.

Jordan, K.R., Amaria, R.N., Ramirez, O., Callihan, E.B., Gao, D., Borakove, M., Manthey, E., Borges, V.F., and McCarter, M.D. (2013). Myeloid-derived suppressor cells are associated with disease progression and decreased overall survival in advanced-stage melanoma patients. Cancer Immunology, Immunotherapy *62*, 1711-1722.

Josan, S., Hurd, R., Park, J.M., Yen, Y.-F., Watkins, R., Pfefferbaum, A., Spielman, D., and Mayer, D. (2014). Dynamic metabolic imaging of hyperpolarized [2-^{13}C]pyruvate using spiral chemical shift imaging with alternating spectral band excitation. Magnetic Resonance in Medicine *71*, 2051-2058.

Joyce, J.A., and Pollard, J.W. (2009). Microenvironmental regulation of metastasis. Nature Reviews Cancer *9*, 239-252.

Kaplan, R.N., Rafii, S., and Lyden, D. (2006). Preparing the “Soil”: The Premetastatic Niche. Cancer Research *66*, 11089-11093.

Kaplan, R.N., Riba, R.D., Zacharoulis, S., Bramley, A.H., Vincent, L., Costa, C., MacDonald, D.D., Jin, D.K., Shido, K., Kerns, S.A.*, et al.* (2005). VEGFR1-positive haematopoietic bone marrow progenitors initiate the pre-metastatic niche. Nature *438*, 820-827.

Keely, P.J., Rusyn, E.V., Cox, A.D., and Parise, L.V. (1999). R-Ras Signals through Specific Integrin α Cytoplasmic Domains to Promote Migration and Invasion of Breast Epithelial Cells. The Journal of Cell Biology *145*, 1077-1088.

Keshari, K.R., Kurhanewicz, J., Bok, R., Larson, P.E., Vigneron, D.B., and Wilson, D.M. (2011). Hyperpolarized ^{13}C dehydroascorbate as an endogenous redox sensor for *in vivo* metabolic imaging. Proceedings of the National Academy of Sciences *108*, 18606-18611.

Keu, K.V., Witney, T.H., Yaghoubi, S., Rosenberg, J., Kurien, A., Magnusson, R., Williams, J., Habte, F., Wagner, J.R., Forman, S.*, et al.* (2017). Reporter gene imaging of targeted T cell immunotherapy in recurrent glioma. Science Translational Medicine *9*.

Khanna, C., and Hunter, K. (2005). Modeling metastasis *in vivo*. Carcinogenesis *26*, 513-523.

Kim, M.H., and Kim, H. (2013). Oncogenes and Tumor Suppressors Regulate Glutamine Metabolism in Cancer Cells. Journal of Cancer Prevention *18*, 221-226.

Kircher, M.F., Gambhir, S.S., and Grimm, J. (2011). Noninvasive cell-tracking methods. Nature Reviews Clinical Oncology *8*, 677-688.

Kircher, M.F., and Willmann, J.K. (2012). Molecular body imaging: MR imaging, CT, and US. part I. principles. Radiology *263*, 633-643.

Kishore, R., Eary, J.F., Krohn, K.A., Nelp, W.B., Menard, T.W., Beaumier, P.L., Hellstrom, K.E., and Hellstrom, I. (1986). Autoradiolysis of iodinated monoclonal antibody preparations. International Journal of Radiation Applications and Instrumentation *13*, 457-459.

Kitamura, T., Qian, B.Z., Soong, D., Cassetta, L., Noy, R., Sugano, G., Kato, Y., Li, J., and Pollard, J.W. (2015). CCL2-induced chemokine cascade promotes breast cancer metastasis by enhancing retention of metastasis-associated macrophages. The Journal of Experimental Medicine *212*, 1043-1059.

Klose, U. (2008). Measurement sequences for single voxel proton MR spectroscopy. European Journal of Radiology *67*, 194-201.

Knowles, S.M., and Wu, A.M. (2012). Advances in immuno-positron emission tomography: antibodies for molecular imaging in oncology. Journal of Clinical Oncology *30*, 3884-3892.

Kobayashi, H., Ogawa, M., Alford, R., Choyke, P.L., and Urano, Y. (2010). New strategies for fluorescent probe design in medical diagnostic imaging. Chemical Reviews *110*, 2620-2640.

Kobus, T., Vos, P.C., Hambrock, T., De Rooij, M., Hulsbergen-Van de Kaa, C.A., Barentsz, J.O., Heerschap, A., and Scheenen, T.W. (2012). Prostate cancer aggressiveness: *in vivo* assessment of MR spectroscopy and diffusion-weighted imaging at 3 T. Radiology *265*, 457-467.

Kowanetz, M., Wu, X., Lee, J., Tan, M., Hagenbeek, T., Qu, X., Yu, L., Ross, J., Korsisaari, N., Cao, T.*, et al.* (2010). Granulocyte-colony stimulating factor promotes lung metastasis through mobilization of $Ly6G^+Ly6C^+$ granulocytes. Proceedings of the National Academy of Sciences *107*, 21248-21255.

Krzeslak, A., Forma, E., Bernaciak, M., Romanowicz, H., and Brys, M. (2012). Gene expression of O-GlcNAc cycling enzymes in human breast cancers. Clinical and Experimental Medicine *12*, 61-65.

Kumar, V., Donthireddy, L., Marvel, D., Condamine, T., Wang, F., Lavilla-Alonso, S., Hashimoto, A., Vonteddu, P., Behera, R., Goins, M.A.*, et al.* (2017). Cancer-Associated Fibroblasts Neutralize the Anti-tumor Effect of CSF1 Receptor Blockade by Inducing PMN-MDSC Infiltration of Tumors. Cancer Cell *32*, 654-668.e655.

Kumar, V., Patel, S., Tcyganov, E., and Gabrilovich, D.I. (2016). The Nature of Myeloid-Derived Suppressor Cells in the Tumor Microenvironment. Trends in Immunology *37*, 208-220.

Kuo, C.-Y., and Ann, D.K. (2018). When fats commit crimes: fatty acid metabolism, cancer stemness and therapeutic resistance. Cancer Communications *38*, 47.

Kvistad, K.A., Bakken, I.J., Gribbestad, I.S., Ehrnholm, B., Lundgren, S., Fjosne, H.E., and Haraldseth, O. (1999). Characterization of neoplastic and normal human breast tissues with *in vivo* ^{1}H MR spectroscopy. Journal of Magnetic Resonance Imaging *10*, 159-164.

Lambert, A.W., Pattabiraman, D.R., and Weinberg, R.A. (2017). Emerging Biological Principles of Metastasis. Cell *168*, 670-691.

Lassailly, F., Griessinger, E., and Bonnet, D. (2010). “Microenvironmental contaminations” induced by fluorescent lipophilic dyes used for non-invasive *in vitro* and *in vivo* cell tracking. Blood *115*, 5347-5354.

Le, H.K., Graham, L., Cha, E., Morales, J.K., Manjili, M.H., and Bear, H.D. (2009). Gemcitabine directly inhibits myeloid derived suppressor cells in BALB/c mice bearing 4T1 mammary carcinoma and augments expansion of T cells from tumor-bearing mice. International Immunopharmacology *9*, 900-909.

LeBleu, V.S., O'Connell, J.T., Gonzalez Herrera, K.N., Wikman, H., Pantel, K., Haigis, M.C., de Carvalho, F.M., Damascena, A., Domingos Chinen, L.T., Rocha, R.M.*, et al.* (2014). PGC-1α mediates mitochondrial biogenesis and oxidative phosphorylation in cancer cells to promote metastasis. Nature Cell Biology *16*, 992-1003, 1001-1015.

Lechner, M.G., Karimi, S.S., Barry-Holson, K., Angell, T.E., Murphy, K.A., Church, C.H., Ohlfest, J.R., Hu, P., and Epstein, A.L. (2013). Immunogenicity of murine solid tumor models as a defining feature of *in vivo* behavior and response to immunotherapy. Journal of Immunotherapy *36*, 477-489.

Leduc, C., and Etienne-Manneville, S. (2015). Intermediate filaments in cell migration and invasion: the unusual suspects. Current Opinion in Cell Biology *32*, 102-112.

Lelekakis, M., Moseley, J.M., Martin, T.J., Hards, D., Williams, E., Ho, P., Lowen, D., Javni, J., Miller, F.R., Slavin, J.*, et al.* (1999). A novel orthotopic model of breast cancer metastasis to bone. Clinical & Experimental Metastasis *17*, 163-170.

Lesokhin, A.M., Hohl, T.M., Kitano, S., Cortez, C., Hirschhorn-Cymerman, D., Avogadri, F., Rizzuto, G.A., Lazarus, J.J., Pamer, E.G., Houghton, A.N.*, et al.* (2012). Monocytic $CCR2^+$

myeloid-derived suppressor cells promote immune escape by limiting activated CD8 T-cell infiltration into the tumor microenvironment. Cancer Research *72*, 876-886.

Lewis, D.Y., Soloviev, D., and Brindle, K.M. (2015a). Imaging tumor metabolism using positron emission tomography. The Cancer Journal *21*, 129-136.

Lewis, M.D., de Leenheer, E., Fishman, S., Siew, L.K., Gross, G., and Wong, F.S. (2015b). A reproducible method for the expansion of mouse $CD8^+$ T lymphocytes. Journal of Immunological Methods *417*, 134-138.

Li, D., Wang, X., Wang, S., and Cheng, J. (2015). Correlation between BOLD-MRI and HIF expression level in renal carcinoma. International Journal of Clinical and Experimental Pathology *8*, 13759-13763.

Li, J., and Zhu, J.J. (2013). Quantum dots for fluorescent biosensing and bio-imaging applications. The Analyst *138*, 2506-2515.

Liechtenstein, T., Perez-Janices, N., Gato, M., Caliendo, F., Kochan, G., Blanco-Luquin, I., Van der Jeught, K., Arce, F., Guerrero-Setas, D., Fernandez-Irigoyen, J.*, et al.* (2014). A highly efficient tumor-infiltrating MDSC differentiation system for discovery of anti-neoplastic targets, which circumvents the need for tumor establishment in mice. Oncotarget *5*, 7843-7857.

Lin, E.Y., Jones, J.G., Li, P., Zhu, L., Whitney, K.D., Muller, W.J., and Pollard, J.W. (2003). Progression to malignancy in the polyoma middle T oncoprotein mouse breast cancer model provides a reliable model for human diseases. The American Journal of Pathology *163*, 2113-2126.

Liou, G.-Y., and Storz, P. (2010). Reactive oxygen species in cancer. Free Radical Research *44*, 10.3109/10715761003667554.

Liu, J., Zhou, Y., Huang, Q., and Qiu, L. (2015). $CD14^+HLA\text{-}DR^{low/-}$ expression: A novel prognostic factor in chronic lymphocytic leukemia. Oncology Letters *9*, 1167-1172.

Liu, S., Jiang, M., Zhao, Q., Li, S., Peng, Y., Zhang, P., and Han, M. (2014). Vascular endothelial growth factor plays a critical role in the formation of the pre-metastatic niche via prostaglandin E2. Oncology Reports *32*, 2477-2484.

Liu, W.N., Yan, M., and Chan, A.M. (2017). A thirty-year quest for a role of R-Ras in cancer: from an oncogene to a multitasking GTPase. Cancer Letters *403*, 59-65.

Livak, K.J., and Schmittgen, T.D. (2001). Analysis of relative gene expression data using real-time quantitative PCR and the 2(-Delta Delta C(T)) Method. Methods *25*, 402-408.

Lobrich, M., Shibata, A., Beucher, A., Fisher, A., Ensminger, M., Goodarzi, A.A., Barton, O., and Jeggo, P.A. (2010). γH2AX foci analysis for monitoring DNA double-strand break repair: strengths, limitations and optimization. Cell Cycle *9*, 662-669.

Louderbough, J.M.V., and Schroeder, J.A. (2011). Understanding the Dual Nature of CD44 in Breast Cancer Progression. Molecular Cancer Research *9*, 1573-1586.

Lucena, M.C., Carvalho-Cruz, P., Donadio, J.L., Oliveira, I.A., de Queiroz, R.M., Marinho-Carvalho, M.M., Sola-Penna, M., de Paula, I.F., Gondim, K.C., McComb, M.E.*, et al.* (2016). Epithelial Mesenchymal Transition Induces Aberrant Glycosylation through Hexosamine Biosynthetic Pathway Activation. The Journal of Biological Chemistry *291*, 12917-12929.

Lunt, S.Y., and Vander Heiden, M.G. (2011). Aerobic glycolysis: meeting the metabolic requirements of cell proliferation. Annual Review of Cell and Developmental Biology *27*, 441-464.

Luo, X., Cheng, C., Tan, Z., Li, N., Tang, M., Yang, L., and Cao, Y. (2017). Emerging roles of lipid metabolism in cancer metastasis. Molecular Cancer *16*, 76.

Maenhout, S.K., Van Lint, S., Emeagi, P.U., Thielemans, K., and Aerts, J.L. (2014). Enhanced suppressive capacity of tumor-infiltrating myeloid-derived suppressor cells compared with their peripheral counterparts. International Journal of Cancer *134*, 1077-1090.

Maglione, J.E., Moghanaki, D., Young, L.J., Manner, C.K., Ellies, L.G., Joseph, S.O., Nicholson, B., Cardiff, R.D., and MacLeod, C.L. (2001). Transgenic Polyoma middle-T mice model premalignant mammary disease. Cancer Research *61*, 8298-8305.

Makela, A.V., and Foster, P.J. (2018). Imaging macrophage distribution and density in mammary tumors and lung metastases using fluorine-19 MRI cell tracking. Magnetic Resonance in Medicine *80*, 1138-1147.

Makela, A.V., Gaudet, J.M., and Foster, P.J. (2017). Quantifying tumor associated macrophages in breast cancer: a comparison of iron and fluorine-based MRI cell tracking. Scientific Reports *7*, 42109.

Malinowski, R.M., Lipsø, K.W., Lerche, M.H., and Ardenkjær-Larsen, J.H. (2016). Dissolution Dynamic Nuclear Polarization capability study with fluid path. Journal of Magnetic Resonance *272*, 141-146.

Malviya, G., Galli, F., Sonni, I., and Signore, A. (2014). Imaging T-lymphocytes in inflammatory diseases: a nuclear medicine approach. The Quarterly Journal of Nuclear Medicine and Molecular Imaging *58*, 237-257.

Mani, S.A., Guo, W., Liao, M.-J., Eaton, E.N., Ayyanan, A., Zhou, A.Y., Brooks, M., Reinhard, F., Zhang, C.C., Shipitsin, M.*, et al.* (2008). The Epithelial-Mesenchymal Transition Generates Cells with Properties of Stem Cells. Cell *133*, 704-715.

Mannheim, J.G., Judenhofer, M.S., Schmid, A., Tillmanns, J., Stiller, D., Sossi, V., and Pichler, B.J. (2012). Quantification accuracy and partial volume effect in dependence of the attenuation correction of a state-of-the-art small animal PET scanner. Physics in Medicine and Biology *57*, 3981-3993.

Mannheim, J.G., Schmid, A.M., and Pichler, B.J. (2017). Influence of Co-57 and CT Transmission Measurements on the Quantification Accuracy and Partial Volume Effect of a Small Animal PET Scanner. Molecular Imaging and Biology *19*, 825-836.

Manning, B.D., and Cantley, L.C. (2007). AKT/PKB signaling: navigating downstream. Cell *129*, 1261-1274.

Marchand, J., Martineau, E., Guitton, Y., Dervilly-Pinel, G., and Giraudeau, P. (2017). Multidimensional NMR approaches towards highly resolved, sensitive and high-throughput quantitative metabolomics. Current Opinion in Biotechnology *43*, 49-55.

Marcotte, R., and Muller, W.J. (2008). Signal transduction in transgenic mouse models of human breast cancer--implications for human breast cancer. Journal of Mammary Gland Biology and Neoplasia *13*, 323-335.

Marigo, I., Bosio, E., Solito, S., Mesa, C., Fernandez, A., Dolcetti, L., Ugel, S., Sonda, N., Bicciato, S., Falisi, E*., et al.* (2010). Tumor-induced tolerance and immune suppression depend on the C/EBPβ transcription factor. Immunity *32*, 790-802.

Marvel, D., and Gabrilovich, D.I. (2015). Myeloid-derived suppressor cells in the tumor microenvironment: expect the unexpected. Journal of Clinical Investigation *125*, 3356-3364.

Matsumura, Y., and Maeda, H. (1986). A new concept for macromolecular therapeutics in cancer chemotherapy: mechanism of tumoritropic accumulation of proteins and the antitumor agent smancs. Cancer Research *46*, 6387-6392.

McDonald, E.S., Clark, A.S., Tchou, J., Zhang, P., and Freedman, G.M. (2016). Clinical Diagnosis and Management of Breast Cancer. Journal of Nuclear Medicine *57 Suppl 1*, 9s-16s.

Mirza, N., Fishman, M., Fricke, I., Dunn, M., Neuger, A.M., Frost, T.J., Lush, R.M., Antonia, S., and Gabrilovich, D.I. (2006). All-trans-retinoic acid improves differentiation of myeloid cells and immune response in cancer patients. Cancer Research *66*, 9299-9307.

Mlynárik, V. (2017). Introduction to nuclear magnetic resonance. Analytical Biochemistry *529*, 4-9.

Moestue, S., Sitter, B., Bathen, T.F., Tessem, M.B., and Gribbestad, I.S. (2011). HR-MAS MR spectroscopy in metabolic characterization of cancer. Current Topics in Medicinal Chemistry *11*, 2-26.

Moestue, S.A., Borgan, E., Huuse, E.M., Lindholm, E.M., Sitter, B., Borresen-Dale, A.L., Engebraaten, O., Maelandsmo, G.M., and Gribbestad, I.S. (2010). Distinct choline metabolic profiles are associated with differences in gene expression for basal-like and luminal-like breast cancer xenograft models. BMC Cancer *10*, 433.

Moonen, C.T., von Kienlin, M., van Zijl, P.C., Cohen, J., Gillen, J., Daly, P., and Wolf, G. (1989). Comparison of single-shot localization methods (STEAM and PRESS) for *in vivo* proton NMR spectroscopy. NMR in Biomedicine *2*, 201-208.

Morel, A.-P., Lièvre, M., Thomas, C., Hinkal, G., Ansieau, S., and Puisieux, A. (2008). Generation of Breast Cancer Stem Cells through Epithelial-Mesenchymal Transition. PloS One *3*, e2888.

Moses, W.W. (2011). Fundamental limits of spatial resolution in PET. In Nuclear Instruments and Methods in Physics Research Section A: Accelerators, Spectrometers, Detectors and Associated Equipment, pp. S236-S240.

Movahedi, K., Guilliams, M., Van den Bossche, J., Van den Bergh, R., Gysemans, C., Beschin, A., De Baetselier, P., and Van Ginderachter, J.A. (2008). Identification of discrete tumor-induced myeloid-derived suppressor cell subpopulations with distinct T cell-suppressive activity. Blood *111*, 4233-4244.

Muylle, K., Flamen, P., Vugts, D.J., Guiot, T., Ghanem, G., Meuleman, N., Bourgeois, P., Vanderlinden, B., van Dongen, G.A., Everaert, H*., et al.* (2015). Tumour targeting and radiation dose of radioimmunotherapy with ^{90}Y-rituximab in CD20^{+} B-cell lymphoma as predicted by ^{89}Zr-rituximab immuno-PET: impact of preloading with unlabelled rituximab. European Journal of Nuclear Medicine and Molecular Imaging *42*, 1304-1314.

Nagahashi, M., Ramachandran, S., Kim, E.Y., Allegood, J.C., Rashid, O.M., Yamada, A., Zhao, R., Milstien, S., Zhou, H., Spiegel, S*., et al.* (2012). Sphingosine-1-phosphate produced

by sphingosine kinase 1 promotes breast cancer progression by stimulating angiogenesis and lymphangiogenesis. Cancer Research *72*, 726-735.

Najjar, A.M., Nishii, R., Maxwell, D.S., Volgin, A., Mukhopadhyay, U., Bornmann, W.G., Tong, W., Alauddin, M., and Gelovani, J.G. (2009). Molecular–Genetic PET Imaging Using an HSV1-tk Mutant Reporter Gene with Enhanced Specificity to Acycloguanosine Nucleoside Analogs. Journal of Nuclear Medicine *50*, 409-416.

Nelson, J., Bagnato, A., Battistini, B., and Nisen, P. (2003). The endothelin axis: emerging role in cancer. Nature Reviews Cancer *3*, 110.

Neveu, M.A., De Preter, G., Marchand, V., Bol, A., Brender, J.R., Saito, K., Kishimoto, S., Porporato, P.E., Sonveaux, P., Gregoire, V.*, et al.* (2016). Multimodality Imaging Identifies Distinct Metabolic Profiles In Vitro and In Vivo. Neoplasia *18*, 742-752.

Neveu, M.A., Joudiou, N., De Preter, G., Dehoux, J.P., Jordan, B.F., and Gallez, B. (2017). ^{17}O MRS assesses the effect of mild hypothermia on oxygen consumption rate in tumors. NMR in Biomedicine *30*.

Nolting, D.D., Gore, J.C., and Pham, W. (2011). NEAR-INFRARED DYES: Probe Development and Applications in Optical Molecular Imaging. Current Organic Synthesis *8*, 521-534.

Noy, R., and Pollard, J.W. (2014). Tumor-associated macrophages: from mechanisms to therapy. Immunity *41*, 49-61.

Ntziachristos, V. (2006). Fluorescence molecular imaging. Annual Review of Biomedical Engineering *8*, 1-33.

Ntziachristos, V., Ripoll, J., Wang, L.V., and Weissleder, R. (2005). Looking and listening to light: the evolution of whole-body photonic imaging. Nature Biotechnology *23*, 313-320.

Obermajer, N., Muthuswamy, R., Odunsi, K., Edwards, R.P., and Kalinski, P. (2011). PGE2-Induced CXCL12 Production and CXCR4 Expression Controls the Accumulation of Human MDSCs in Ovarian Cancer Environment. Cancer Research *71*, 7463-7470.

Obre, E., and Rossignol, R. (2015). Emerging concepts in bioenergetics and cancer research: metabolic flexibility, coupling, symbiosis, switch, oxidative tumors, metabolic remodeling, signaling and bioenergetic therapy. The International Journal of Biochemistry & Cell Biology *59*, 167-181.

Ottobrini, L., Martelli, C., Trabattoni, D.L., Clerici, M., and Lucignani, G. (2011). *In vivo* imaging of immune cell trafficking in cancer. European Journal of Nuclear Medicine and Molecular Imaging *38*, 949-968.

Overwijk, W.W., and Restifo, N.P. (2001). B16 as a Mouse Model for Human Melanoma. Current Protocols in Immunology *Chapter 20:Unit 20.1.*

Paget, G. (1889). Remarks on a Case of Alternate Partial Anaesthesia. British Medical Journal *1*, 1-3.

Park, J.M., Josan, S., Jang, T., Merchant, M., Watkins, R., Hurd, R.E., Recht, L.D., Mayer, D., and Spielman, D.M. (2016a). Volumetric Spiral Chemical Shift Imaging of Hyperpolarized [2-^{13}C]Pyruvate in a Rat C6 Glioma Model. Magnetic Resonance in Medicine *75*, 973-984.

Park, J.W., Jung, K.H., Lee, J.H., Moon, S.H., Cho, Y.S., Choe, Y.S., and Lee, K.H. (2016b). Imaging Early Fate of Cancer Stem Cells in Mouse Hindlimbs with Sodium Iodide Symporter Gene and I-124 PET. Molecular Imaging and Biology *18*, 748-757.

Park, S.Y., Kim, H.S., Kim, N.H., Ji, S., Cha, S.Y., Kang, J.G., Ota, I., Shimada, K., Konishi, N., Nam, H.W.*, et al.* (2010). Snail1 is stabilized by *O*-GlcNAc modification in hyperglycaemic condition. The EMBO Journal *29*, 3787-3796.

Pascual, G., Domínguez, D., and Benitah, S.A. (2018). The contributions of cancer cell metabolism to metastasis. Disease Models and Mechanisms *11*.

Pastushenko, I., Brisebarre, A., Sifrim, A., Fioramonti, M., Revenco, T., Boumahdi, S., Van Keymeulen, A., Brown, D., Moers, V., Lemaire, S.*, et al.* (2018). Identification of the tumour transition states occurring during EMT. Nature *556*, 463-468.

Payne, A.S., and Cornelius, L.A. (2002). The role of chemokines in melanoma tumor growth and metastasis. The Journal of Investigative Dermatology *118*, 915-922.

Peeters, S.G., Zegers, C.M., Lieuwes, N.G., van Elmpt, W., Eriksson, J., van Dongen, G.A., Dubois, L., and Lambin, P. (2015). A comparative study of the hypoxia PET tracers [^{18}F]HX4, [^{18}F]FAZA, and [^{18}F]FMISO in a preclinical tumor model. International Journal of Radiation Oncology, Biology, Physics *91*, 351-359.

Peinado, H., Zhang, H., Matei, I.R., Costa-Silva, B., Hoshino, A., Rodrigues, G., Psaila, B., Kaplan, R.N., Bromberg, J.F., Kang, Y.*, et al.* (2017). Pre-metastatic niches: organ-specific homes for metastases. Nature Reviews Cancer *17*, 302.

Peng, F., Lu, X., Janisse, J., Muzik, O., and Shields, A.F. (2006). PET of human prostate cancer xenografts in mice with increased uptake of $^{64}CuCl_2$. Journal of Nuclear Medicine *47*, 1649-1652.

Penheiter, A.R., Russell, S.J., and Carlson, S.K. (2012). The sodium iodide symporter (NIS) as an imaging reporter for gene, viral, and cell-based therapies. Current Gene Therapy *12*, 33-47.

Perera, R.M., and Bardeesy, N. (2015). Pancreatic Cancer Metabolism: Breaking It Down to Build It Back Up. Cancer Discovery *5*, 1247-1261.

Piert, M., Machulla, H.J., Picchio, M., Reischl, G., Ziegler, S., Kumar, P., Wester, H.J., Beck, R., McEwan, A.J., Wiebe, L.I.*, et al.* (2005). Hypoxia-specific tumor imaging with ^{18}F-fluoroazomycin arabinoside. Journal of Nuclear Medicine *46*, 106-113.

Pinton, L., Solito, S., Damuzzo, V., Francescato, S., Pozzuoli, A., Berizzi, A., Mocellin, S., Rossi, C.R., Bronte, V., and Mandruzzato, S. (2016). Activated T cells sustain myeloid-derived suppressor cell-mediated immune suppression. Oncotarget *7*, 1168-1184.

Piskounova, E., Agathocleous, M., Murphy, M.M., Hu, Z., Huddlestun, S.E., Zhao, Z., Leitch, A.M., Johnson, T.M., DeBerardinis, R.J., and Morrison, S.J. (2015). Oxidative stress inhibits distant metastasis by human melanoma cells. Nature *527*, 186.

Polyak, K., and Weinberg, R.A. (2009). Transitions between epithelial and mesenchymal states: acquisition of malignant and stem cell traits. Nature Reviews Cancer *9*, 265.

Ponomarev, V., Doubrovin, M., Lyddane, C., Beresten, T., Balatoni, J., Bornman, W., Finn, R., Akhurst, T., Larson, S., Blasberg, R.*, et al.* (2001). Imaging TCR-dependent NFAT-mediated T-cell activation with positron emission tomography *in vivo*. Neoplasia *3*, 480-488.

Porporato, Paolo E., Payen, Valéry L., Pérez-Escuredo, J., De Saedeleer, Christophe J., Danhier, P., Copetti, T., Dhup, S., Tardy, M., Vazeille, T., Bouzin, C.*, et al.* (2014). A Mitochondrial Switch Promotes Tumor Metastasis. Cell Reports *8*, 754-766.

Press, A.T., Butans, M.J., Haider, T.P., Weber, C., Neugebauer, S., Kiehntopf, M., Schubert, U.S., Clemens, M.G., Bauer, M., and Kortgen, A. (2017). Fast simultaneous assessment of renal and liver function using polymethine dyes in animal models of chronic and acute organ injury. Scientific Reports *7*, 15397.

Prince, H.M., Wall, D.M., Ritchie, D., Honemann, D., Harrrison, S., Quach, H., Thompson, M., Hicks, R., Lau, E., Davison, J.*, et al.* (2008). *In vivo* tracking of dendritic cells in patients with multiple myeloma. Journal of Immunotherapy *31*, 166-179.

Provencher, S.W. (1993). Estimation of metabolite concentrations from localized *in vivo* proton NMR spectra. Magnetic Resonance in Medicine *30*, 672-679.

Psaila, B., and Lyden, D. (2009). The metastatic niche: adapting the foreign soil. Nature Reviews Cancer *9*, 285-293.

Pyne, N.J., and Pyne, S. (2010). Sphingosine 1-phosphate and cancer. Nature Reviews Cancer *10*, 489-503.

Pyne, N.J., Tonelli, F., Lim, K.G., Long, J.S., Edwards, J., and Pyne, S. (2012). Sphingosine 1-phosphate signalling in cancer. Biochemical Society Transactions *40*, 94-100.

Qian, B.-Z., Li, J., Zhang, H., Kitamura, T., Zhang, J., Campion, L.R., Kaiser, E.A., Snyder, L.A., and Pollard, J.W. (2011). CCL2 recruits inflammatory monocytes to facilitate breast-tumour metastasis. Nature *475*, 222.

Qin, C., Liu, H., Chen, K., Hu, X., Ma, X., Lan, X., Zhang, Y., and Cheng, Z. (2014). Theranostics of Malignant Melanoma with $^{64}CuCl_2$. Journal of Nuclear Medicine *55*, 812-817.

Qu, P., Wang, L.-z., and Lin, P.C. (2016). Expansion and functions of myeloid-derived suppressor cells in the tumor microenvironment. Cancer Letters *380*, 253-256.

Quail, D.F., and Joyce, J.A. (2013). Microenvironmental regulation of tumor progression and metastasis. Nature Medicine *19*, 1423-1437.

Raptis, L., Marcellus, R., Corbley, M.J., Krook, A., Whitfield, J., Anderson, S.K., and Haliotis, T. (1991). Cellular ras gene activity is required for full neoplastic transformation by polyomavirus. Journal of Virology *65*, 5203-5210.

Ravera, S., Reyna-Neyra, A., Ferrandino, G., Amzel, L.M., and Carrasco, N. (2017). The Sodium/Iodide Symporter (NIS): Molecular Physiology and Preclinical and Clinical Applications. Annual Review of Physiology *79*, 261-289.

Ray, P., De, A., Min, J.J., Tsien, R.Y., and Gambhir, S.S. (2004). Imaging tri-fusion multimodality reporter gene expression in living subjects. Cancer Research *64*, 1323-1330.

Ray, P., Tsien, R., and Gambhir, S.S. (2007). Construction and validation of improved triple fusion reporter gene vectors for molecular imaging of living subjects. Cancer Research *67*, 3085-3093.

Reck, D.I. (2017). Influences of Local Lung Inflammation on the Microenvironment of Primary Tumors, the Pre-Metastatic Niche, and Metastasis. In Werner Siemens Imaging Center, Department of Preclinical Imaging and Radiopharmacy (Tübingen: Eberhard Karls University).

Romano, E., Rufo, N., Korf, H., Mathieu, C., Garg, A.D., and Agostinis, P. (2018). BNIP3 modulates the interface between B16-F10 melanoma cells and immune cells. Oncotarget *9*, 17631-17644.

Ronen, S.M., Jackson, L.E., Beloueche, M., and Leach, M.O. (2001). Magnetic resonance detects changes in phosphocholine associated with Ras activation and inhibition in NIH 3T3 cells. British Journal of Cancer *84*, 691-696.

Rotte, A., Bhandaru, M., Zhou, Y., and McElwee, K.J. (2015). Immunotherapy of melanoma: Present options and future promises. Cancer and Metastasis Reviews *34*, 115-128.

Ruckhaberle, E., Rody, A., Engels, K., Gaetje, R., von Minckwitz, G., Schiffmann, S., Grosch, S., Geisslinger, G., Holtrich, U., Karn, T.*, et al.* (2008). Microarray analysis of altered sphingolipid metabolism reveals prognostic significance of sphingosine kinase 1 in breast cancer. Breast Cancer Research and Treatment *112*, 41-52.

Rudolph, B.M., Loquai, C., Gerwe, A., Bacher, N., Steinbrink, K., Grabbe, S., and Tuettenberg, A. (2014). Increased frequencies of $CD11b^{+}CD33^{+}CD14^{+}HLA\text{-}DR^{low}$ myeloid-derived suppressor cells are an early event in melanoma patients. Experimental Dermatology *23*, 202-204.

Sawanobori, Y., Ueha, S., Kurachi, M., Shimaoka, T., Talmadge, J.E., Abe, J., Shono, Y., Kitabatake, M., Kakimi, K., Mukaida, N.*, et al.* (2008). Chemokine-mediated rapid turnover of myeloid-derived suppressor cells in tumor-bearing mice. Blood *111*, 5457-5466.

Saxena, M., and Christofori, G. (2013). Rebuilding cancer metastasis in the mouse. Molecular Oncology *7*, 283-296.

Saxena, M., Kalathur, R.K.R., Neutzner, M., and Christofori, G. (2018). PyMT-1099, a versatile murine cell model for EMT in breast cancer. Scientific Reports *8*, 12123.

Sceneay, J., Chow, M.T., Chen, A., Halse, H.M., Wong, C.S.F., Andrews, D.M., Sloan, E.K., Parker, B.S., Bowtell, D.D., Smyth, M.J.*, et al.* (2012). Primary Tumor Hypoxia Recruits $CD11b^{+}/Ly6C^{med}/Ly6G^{+}$ Immune Suppressor Cells and Compromises NK Cell Cytotoxicity in the Premetastatic Niche. Cancer Research *72*, 3906-3911.

Sceneay, J., Griessinger, C.M., Hoffmann, S.H.L., Wen, S.W., Wong, C.S.F., Krumeich, S., Kneilling, M., Pichler, B.J., and Moller, A. (2018). Tracking the fate of adoptively transferred myeloid-derived suppressor cells in the primary breast tumor microenvironment. PloS One *13*, e0196040.

Sceneay, J., Smyth, M.J., and Moller, A. (2013). The pre-metastatic niche: finding common ground. Cancer Metastasis Reviews *32*, 449-464.

Scheel, C., and Weinberg, R.A. (2012). Cancer stem cells and epithelial–mesenchymal transition: Concepts and molecular links. Seminars in Cancer Biology *22*, 396-403.

Scherer, S.D., and Sleeman, J.P. (2017). Untitled work. Unpulished work.

Schneider, C.A., Rasband, W.S., and Eliceiri, K.W. (2012). NIH Image to ImageJ: 25 years of image analysis. Nature Methods *9*, 671-675.

Schroeder, M.A., Atherton, H.J., Ball, D.R., Cole, M.A., Heather, L.C., Griffin, J.L., Clarke, K., Radda, G.K., and Tyler, D.J. (2009). Real-time assessment of Krebs cycle metabolism using hyperpolarized ^{13}C magnetic resonance spectroscopy. FASEB Journal *23*, 2529-2538.

Schwickert, G., Walenta, S., Sundfor, K., Rofstad, E.K., and Mueller-Klieser, W. (1995). Correlation of high lactate levels in human cervical cancer with incidence of metastasis. Cancer Research *55*, 4757-4759.

Seo, J.W., Tavare, R., Mahakian, L.M., Silvestrini, M.T., Tam, S., Ingham, E.S., Salazar, F.B., Borowsky, A.D., Wu, A.M., and Ferrara, K.W. (2018). $CD8^+$ T-Cell Density Imaging with ^{64}Cu-Labeled Cys-Diabody Informs Immunotherapy Protocols. Clinical Cancer Research *24*, 4976-4987.

Shah, T., Wildes, F., Penet, M.F., Winnard, P.T., Jr., Glunde, K., Artemov, D., Ackerstaff, E., Gimi, B., Kakkad, S., Raman, V.*, et al.* (2010). Choline kinase overexpression increases invasiveness and drug resistance of human breast cancer cells. NMR in Biomedicine *23*, 633-642.

Shan, S., Lv, Q., Zhao, Y., Liu, C., Sun, Y., Xi, K., Xiao, J., and Li, C. (2015). Wnt/β-catenin pathway is required for epithelial to mesenchymal transition in CXCL12 over expressed breast cancer cells. International Journal of Clinical and Experimental Pathology *8*, 12357-12367.

Sharma, U., Baek, H.M., Su, M.Y., and Jagannathan, N.R. (2011). *In vivo* ^1H MRS in the assessment of the therapeutic response of breast cancer patients. NMR in Biomedicine *24*, 700-711.

Shi, Y., Oeh, J., Eastham-Anderson, J., Yee, S., Finkle, D., Peale, F.V., Jr., Ross, J., Hedehus, M., van Bruggen, N., Venook, R.*, et al.* (2013). Mapping *in vivo* tumor oxygenation within viable tumor by ^{19}F-MRI and multispectral analysis. Neoplasia *15*, 1241-1250.

Shida, D., Takabe, K., Kapitonov, D., Milstien, S., and Spiegel, S. (2008). Targeting SphK1 as a new strategy against cancer. Current Drug Targets *9*, 662-673.

Shokeen, M., Zheleznyak, A., Wilson, J.M., Jiang, M., Liu, R., Ferdani, R., Lam, K.S., Schwarz, J.K., and Anderson, C.J. (2012). Molecular imaging of very late antigen-4 (α4β1 integrin) in the premetastatic niche. Journal of Nuclear Medicine *53*, 779-786.

Shou, D., Wen, L., Song, Z., Yin, J., Sun, Q., and Gong, W. (2016). Suppressive role of myeloid-derived suppressor cells (MDSCs) in the microenvironment of breast cancer and targeted immunotherapies. Oncotarget *7*, 64505-64511.

Simmons, J.K., Hildreth, B.E., 3rd, Supsavhad, W., Elshafae, S.M., Hassan, B.B., Dirksen, W.P., Toribio, R.E., and Rosol, T.J. (2015). Animal Models of Bone Metastasis. Veterinary Pathology *52*, 827-841.

Simpson, K.D., Templeton, D.J., and Cross, J.V. (2012). Macrophage migration inhibitory factor promotes tumor growth and metastasis by inducing myeloid-derived suppressor cells in the tumor microenvironment. Journal of Immunology *189*, 5533-5540.

Singbartl, K., Thatte, J., Smith, M.L., Wethmar, K., Day, K., and Ley, K. (2001). A CD2-green fluorescence protein-transgenic mouse reveals very late antigen-4-dependent $CD8^+$ lymphocyte rolling in inflamed venules. Journal of Immunology *166*, 7520-7526.

Sinha, P., Clements, V.K., Fulton, A.M., and Ostrand-Rosenberg, S. (2007). Prostaglandin E2 Promotes Tumor Progression by Inducing Myeloid-Derived Suppressor Cells. Cancer Research *67*, 4507-4513.

Sleeman, J.P. (2015). The lymph node pre-metastatic niche. Journal of Molecular Medicine *93*, 1173-1184.

Smith, A.M., Mancini, M.C., and Nie, S. (2009). Second window for *in vivo* imaging. Nature Nanotechnology *4*, 710.

Solaini, G., Sgarbi, G., and Baracca, A. (2011). Oxidative phosphorylation in cancer cells. Biochimica et Biophysica Acta (BBA) - Bioenergetics *1807*, 534-542.

Solito, S., Falisi, E., Diaz-Montero, C.M., Doni, A., Pinton, L., Rosato, A., Francescato, S., Basso, G., Zanovello, P., Onicescu, G.*, et al.* (2011). A human promyelocytic-like population is responsible for the immune suppression mediated by myeloid-derived suppressor cells. Blood *118*, 2254-2265.

Solovjov, D.A., Pluskota, E., and Plow, E.F. (2005). Distinct roles for the α and β subunits in the functions of integrin $\alpha_M\beta_2$. The Journal of Biological Chemistry *280*, 1336-1345.

Soria, G., and Ben-Baruch, A. (2008). The inflammatory chemokines CCL2 and CCL5 in breast cancer. Cancer Letters *267*, 271-285.

Sotgia, F., Whitaker-Menezes, D., Martinez-Outschoorn, U.E., Flomenberg, N., Birbe, R., Witkiewicz, A.K., Howell, A., Philp, N.J., Pestell, R.G., and Lisanti, M.P. (2012). Mitochondrial metabolism in cancer metastasis. Cell Cycle *11*, 1445-1454.

Speigl, L., Burow, H., Bailur, J.K., Janssen, N., Walter, C.-B., Pawelec, G., and Shipp, C. (2018). $CD14^{+}HLA\text{-}DR^{-/low}$ MDSCs are elevated in the periphery of early-stage breast cancer patients and suppress autologous T cell proliferation. Breast Cancer Research and Treatment *168*, 401-411.

Srinivas, M., Aarntzen, E.H.J.G., Bulte, J.W.M., Oyen, W.J., Heerschap, A., de Vries, I.J.M., and Figdor, C.G. (2010). Imaging of cellular therapies. Advanced Drug Delivery Reviews *62*, 1080-1093.

Sutton, E.J., Henning, T.D., Pichler, B.J., Bremer, C., and Daldrup-Link, H.E. (2008). Cell tracking with optical imaging. European Radiology *18*, 2021-2032.

Takai, Y., Irie, K., Shimizu, K., Sakisaka, T., and Ikeda, W. (2003). Nectins and nectin-like molecules: roles in cell adhesion, migration, and polarization. Cancer Science *94*, 655-667.

Takai, Y., and Nakanishi, H. (2003). Nectin and afadin: novel organizers of intercellular junctions. Journal of Cell Science *116*, 17-27.

Talmadge, J.E., and Gabrilovich, D.I. (2013). History of myeloid-derived suppressor cells. Nature Reviews Cancer *13*, 739-752.

Tan, An S., Baty, James W., Dong, L.-F., Bezawork-Geleta, A., Endaya, B., Goodwin, J., Bajzikova, M., Kovarova, J., Peterka, M., Yan, B.*, et al.* (2015). Mitochondrial Genome Acquisition Restores Respiratory Function and Tumorigenic Potential of Cancer Cells without Mitochondrial DNA. Cell Metabolism *21*, 81-94.

Tavare, R., Escuin-Ordinas, H., Mok, S., McCracken, M.N., Zettlitz, K.A., Salazar, F.B., Witte, O.N., Ribas, A., and Wu, A.M. (2016). An Effective Immuno-PET Imaging Method to Monitor CD8-Dependent Responses to Immunotherapy. Cancer Research *76*, 73-82.

Tavare, R., McCracken, M.N., Zettlitz, K.A., Salazar, F.B., Olafsen, T., Witte, O.N., and Wu, A.M. (2015). Immuno-PET of Murine T Cell Reconstitution Postadoptive Stem Cell Transplantation Using Anti-CD4 and Anti-CD8 Cys-Diabodies. Journal of Nuclear Medicine *56*, 1258-1264.

Tee, A.R. (2018). The Target of Rapamycin and Mechanisms of Cell Growth. International Journal of Molecular Sciences *19*.

Telang, S., Lane, A.N., Nelson, K.K., Arumugam, S., and Chesney, J. (2007). The oncoprotein H-Ras(V12) increases mitochondrial metabolism. Molecular Cancer *6*, 77-77.

Ter-Pogossian, M.M., Phelps, M.E., Hoffman, E.J., and Mullani, N.A. (1975). A positron-emission transaxial tomograph for nuclear imaging (PETT). Radiology *114*, 89-98.

Thiery, J.P., Acloque, H., Huang, R.Y.J., and Nieto, M.A. (2009). Epithelial-Mesenchymal Transitions in Development and Disease. Cell *139*, 871-890.

Thijssen, V.L., Heusschen, R., Caers, J., and Griffioen, A.W. (2015). Galectin expression in cancer diagnosis and prognosis: A systematic review. Biochimica et Biophysica Acta - Reviews on Cancer *1855*, 235-247.

Thunemann, M., Schörg, B.F., Feil, S., Lin, Y., Voelkl, J., Golla, M., Vachaviolos, A., Kohlhofer, U., Quintanilla-Martinez, L., Olbrich, M*., et al.* (2017). Cre/lox-assisted non-invasive *in vivo* tracking of specific cell populations by positron emission tomography. Nature Communications *8*, 444.

Tiwari, N., Gheldof, A., Tatari, M., and Christofori, G. (2012). EMT as the ultimate survival mechanism of cancer cells. Seminars in Cancer Biology *22*, 194-207.

Tobin, R.P., Jordan, K.R., Robinson, W.A., Davis, D., Borges, V.F., Gonzalez, R., Lewis, K.D., and McCarter, M.D. (2018). Targeting myeloid-derived suppressor cells using all-trans retinoic acid in melanoma patients treated with Ipilimumab. International Immunopharmacology *63*, 282-291.

Tremblay, M.L., Davis, C., Bowen, C.V., Stanley, O., Parsons, C., Weir, G., Karkada, M., Stanford, M.M., and Brewer, K.D. (2018). Using MRI cell tracking to monitor immune cell recruitment in response to a peptide-based cancer vaccine. Magnetic Resonance in Medicine *80*, 304-316.

Tyanova, S., Temu, T., and Cox, J. (2016a). The MaxQuant computational platform for mass spectrometry-based shotgun proteomics. Nature Protocols *11*, 2301-2319.

Tyanova, S., Temu, T., Sinitcyn, P., Carlson, A., Hein, M.Y., Geiger, T., Mann, M., and Cox, J. (2016b). The Perseus computational platform for comprehensive analysis of (prote)omics data. Nature Methods *13*, 731-740.

Ugel, S., Delpozzo, F., Desantis, G., Papalini, F., Simonato, F., Sonda, N., Zilio, S., and Bronte, V. (2009). Therapeutic targeting of myeloid-derived suppressor cells. Current Opinion in Pharmacology *9*, 470-481.

Umansky, V., and Sevko, A. (2013). Tumor microenvironment and myeloid-derived suppressor cells. Cancer Microenvironment *6*, 169-177.

Uniprot Consortium (2017). UniProt: the universal protein knowledgebase. Nucleic Acids Research *45*, D158-d169.

Vander Heiden, M.G., and DeBerardinis, R.J. (2017). Understanding the Intersections between Metabolism and Cancer Biology. Cell *168*, 657-669.

Veglia, F., Perego, M., and Gabrilovich, D. (2018). Myeloid-derived suppressor cells coming of age. Nature Immunology *19*, 108-119.

Venneti, S., Dunphy, M.P., Zhang, H., Pitter, K.L., Zanzonico, P., Campos, C., Carlin, S.D., La Rocca, G., Lyashchenko, S., Ploessl, K.*, et al.* (2015). Glutamine-based PET imaging facilitates enhanced metabolic evaluation of gliomas *in vivo*. Science Translational Medicine *7*, 274ra217.

Verbeek, B.S., Vroom, T.M., Adriaansen-Slot, S.S., Ottenhoff-Kalff, A.E., Geertzema, J.G., Hennipman, A., and Rijksen, G. (1996). c-Src protein expression is increased in human breast cancer. An immunohistochemical and biochemical analysis. The Journal of Pathology *180*, 383-388.

Vetsika, E.K., Koinis, F., Gioulbasani, M., Aggouraki, D., Koutoulaki, A., Skalidaki, E., Mavroudis, D., Georgoulias, V., and Kotsakis, A. (2014). A circulating subpopulation of monocytic myeloid-derived suppressor cells as an independent prognostic/predictive factor in untreated non-small lung cancer patients. Journal of Immunology Research *2014*, 659294.

Vincent, J., Mignot, G., Chalmin, F., Ladoire, S., Bruchard, M., Chevriaux, A., Martin, F., Apetoh, L., Rébé, C., and Ghiringhelli, F. (2010). 5-Fluorouracil Selectively Kills Tumor-Associated Myeloid-Derived Suppressor Cells Resulting in Enhanced T Cell–Dependent Antitumor Immunity. Cancer Research *70*, 3052-3061.

Vuk-Pavlovic, S., Bulur, P.A., Lin, Y., Qin, R., Szumlanski, C.L., Zhao, X., and Dietz, A.B. (2010). Immunosuppressive $CD14^{+}HLA\text{-}DR^{low/-}$ monocytes in prostate cancer. The Prostate *70*, 443-455.

Warburg, O. (1956). On the Origin of Cancer Cells. Science *123*, 309-314.

Warrier, S., Tapia, G., Goltsman, D., and Beith, J. (2016). An update in breast cancer screening and management. Women's Health *12*, 229-239.

Weber, C.E., and Kuo, P.C. (2012). The tumor microenvironment. Surgical Oncology *21*, 172-177.

Wegner, K.D., and Hildebrandt, N. (2015). Quantum dots: bright and versatile *in vitro* and *in vivo* fluorescence imaging biosensors. Chemical Society Reviews *44*, 4792-4834.

Weidle, H.U., Birzele, F., Kollmorgen, G., and Rüger, R. (2017). The Multiple Roles of Exosomes in Metastasis. Cancer Genomics & Proteomics *14*, 1-16.

Weinberg, F., Hamanaka, R., Wheaton, W.W., Weinberg, S., Joseph, J., Lopez, M., Kalyanaraman, B., Mutlu, G.M., Budinger, G.R.S., and Chandel, N.S. (2010). Mitochondrial metabolism and ROS generation are essential for Kras-mediated tumorigenicity. Proceedings of the National Academy of Sciences *107*, 8788-8793.

Wen, S.W., Sceneay, J., Lima, L.G., Wong, C.S.F., Becker, M., Krumeich, S., Lobb, R.J., Castillo, V., Wong, K.N., Ellis, S.*, et al.* (2016). The Biodistribution and Immune Suppressive Effects of Breast Cancer–Derived Exosomes. Cancer Research *76*, 6816-6827.

Whittington, N.C., and Wray, S. (2017). Suppression of Red Blood Cell Autofluorescence for Immunocytochemistry on Fixed Embryonic Mouse Tissue. Current Protocols in Neuroscience *81*, 2.28.21-22.28.12.

Wong, C.S.F., Sceneay, J., House, C.M., Halse, H.M., Liu, M.C.P., George, J., Hunnam, T.C.U.P., Parker, B.S., Haviv, I., Ronai, Z.e.*, et al.* (2012). Vascular Normalization by Loss of Siah2 Results in Increased Chemotherapeutic Efficacy. Cancer Research *72*, 1694-1704.

Wood, L.D., Parsons, D.W., Jones, S., Lin, J., Sjoblom, T., Leary, R.J., Shen, D., Boca, S.M., Barber, T., Ptak, J.*, et al.* (2007). The genomic landscapes of human breast and colorectal cancers. Science *318*, 1108-1113.

Wu, A.M. (2014). Engineered antibodies for molecular imaging of cancer. Methods *65*, 139-147.

Wu, A.M., and Olafsen, T. (2008). Antibodies for molecular imaging of cancer. Cancer Journal *14*, 191-197.

Yang, M., Baranov, E., Jiang, P., Sun, F.-X., Li, X.-M., Li, L., Hasegawa, S., Bouvet, M., Al-Tuwaijri, M., Chishima, T.*, et al.* (2000). Whole-body optical imaging of green fluorescent protein-expressing tumors and metastases. Proceedings of the National Academy of Sciences *97*, 1206-1211.

Yokota, H., Guo, J., Matoba, M., Higashi, K., Tonami, H., and Nagao, Y. (2007). Lactate, choline, and creatine levels measured by vitro ^{1}H-MRS as prognostic parameters in patients with non-small-cell lung cancer. Journal of Magnetic Resonance Imaging *25*, 992-999.

Youn, J.-I., Nagaraj, S., Collazo, M., and Gabrilovich, D.I. (2008). Subsets of Myeloid-Derived Suppressor Cells in Tumor Bearing Mice. Journal of Immunology *181*, 5791-5802.

Youn, J.I., Kumar, V., Collazo, M., Nefedova, Y., Condamine, T., Cheng, P., Villagra, A., Antonia, S., McCaffrey, J.C., Fishman, M.*, et al.* (2013). Epigenetic silencing of retinoblastoma gene regulates pathologic differentiation of myeloid cells in cancer. Nature Immunology *14*, 211-220.

Yousefi, M., Nosrati, R., Salmaninejad, A., Dehghani, S., Shahryari, A., and Saberi, A. (2018). Organ-specific metastasis of breast cancer: molecular and cellular mechanisms underlying lung metastasis. Cellular Oncology *41*, 123-140.

Yu, J., Du, W., Yan, F., Wang, Y., Li, H., Cao, S., Yu, W., Shen, C., Liu, J., and Ren, X. (2013). Myeloid-derived suppressor cells suppress antitumor immune responses through IDO expression and correlate with lymph node metastasis in patients with breast cancer. Journal of Immunology *190*, 3783-3797.

Zanzonico, P. (2004). Positron emission tomography: a review of basic principles, scanner design and performance, and current systems. Seminars in Nuclear Medicine *34*, 87-111.

Zelmer, A., and Ward, T.H. (2013). Noninvasive fluorescence imaging of small animals. Journal of Microscopy *252*, 8-15.

Zhang, L. (1999). The $\alpha_M\beta_2$ integrin and its role in neutrophil function. Cell Research *9*, 171.

Zhao, Z., Lu, P., Zhang, H., Xu, H., Gao, N., Li, M., and Liu, C. (2014). Nestin positively regulates the Wnt/β-catenin pathway and the proliferation, survival and invasiveness of breast cancer stem cells. Breast Cancer Research *16*, 408.

Zhu, A., and Shim, H. (2011). Current molecular imaging positron emitting radiotracers in oncology. Nuclear Medicine and Molecular Imaging *45*, 1-14.

10 APPENDIX

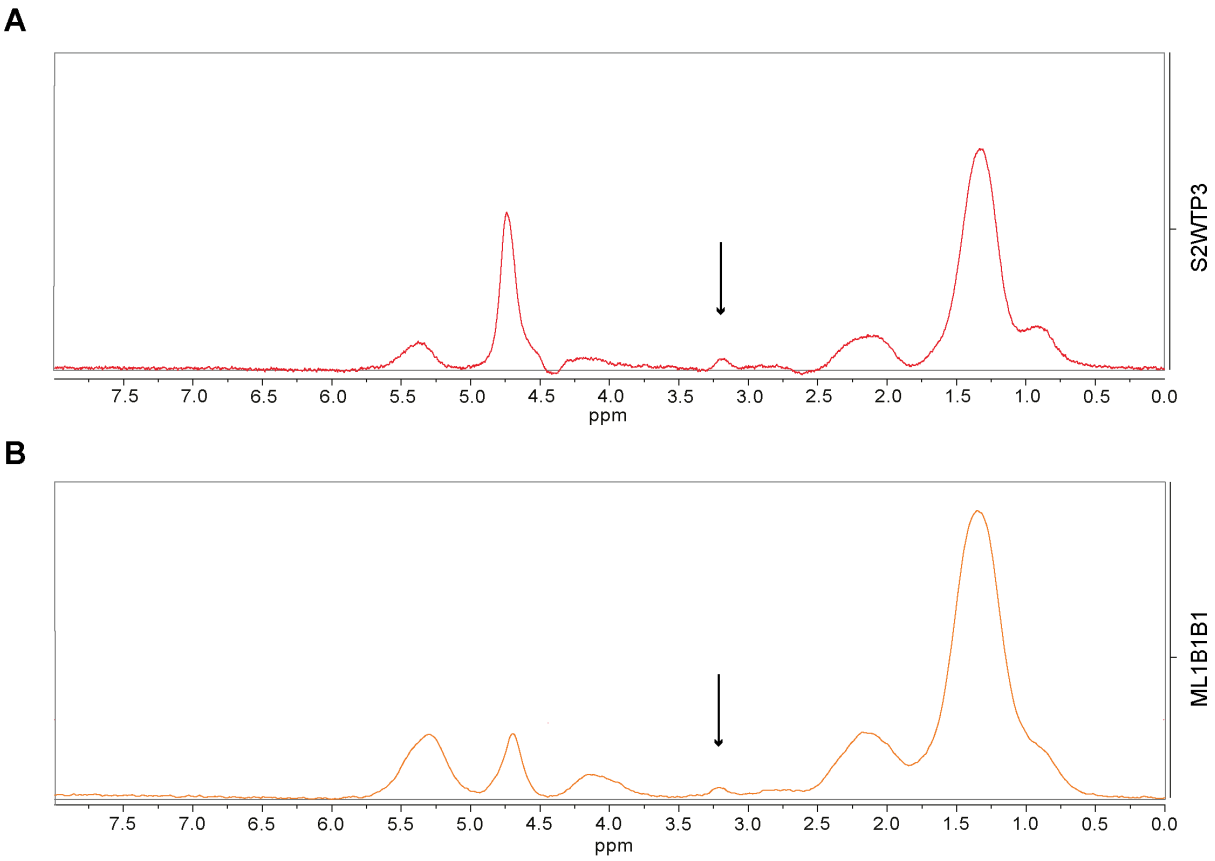

Figure 102: *In vivo* ^{1}H magnetic resonance spectra of S2WTP3 and ML1B1B1 allografts.
In vivo ^{1}H magnetic resonance spectroscopy allowed for detection of total choline peaks at 3.2 ppm (black arrows) in both S2WTP3 (**A**) and ML1B1B1 (**B**) allografts (n=5 for S2WTP3, n=5 for ML1B1B1).

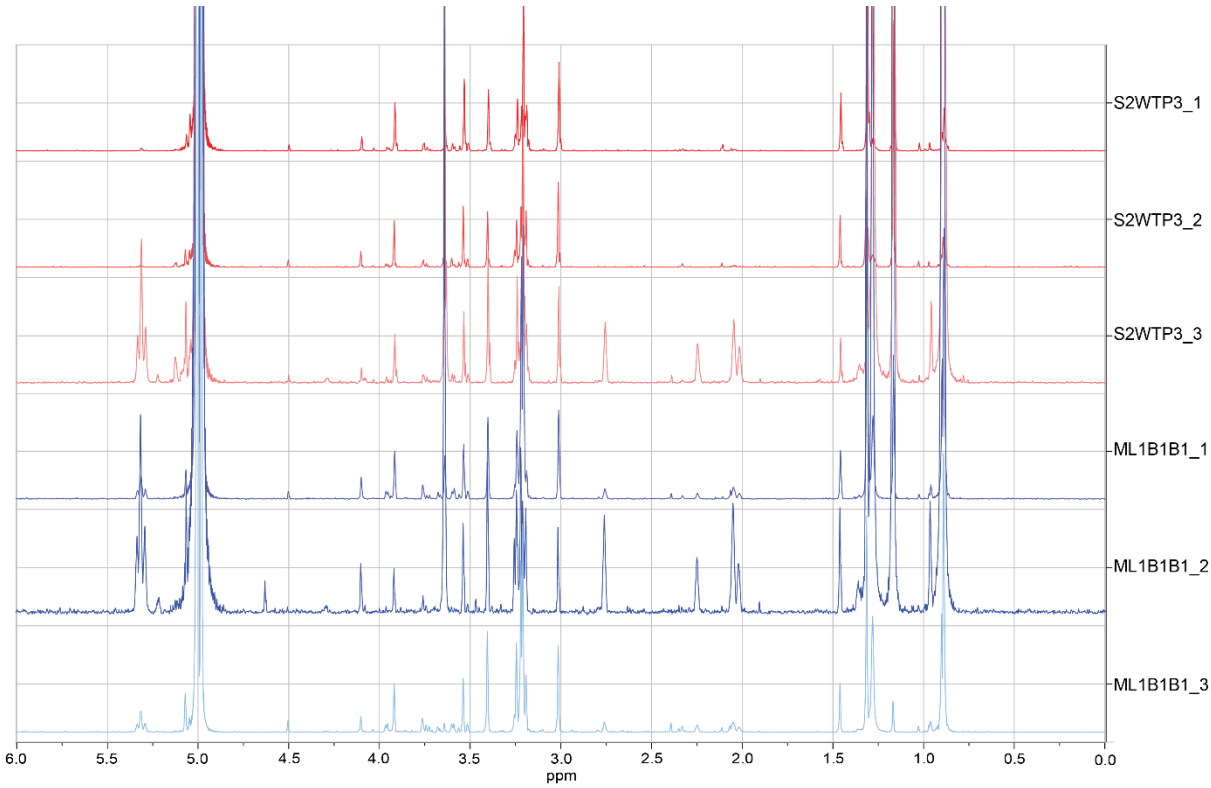

Figure 103: *Ex vivo* HR-MAS ^{1}H spectra of S2WTP3 and ML1B1B1 allografts.
In the *ex vivo* ^{1}H NMR spectra of S2WTP3 (red spectra, upper panel) and ML1B1B1 (blue spectra, lower panel) tumor allograft samples, 12 different metabolites including choline and the choline species phosphocholine and glycerophosphocholine were detected (n=3 for S2WTP3, n=3 for ML1B1B1).

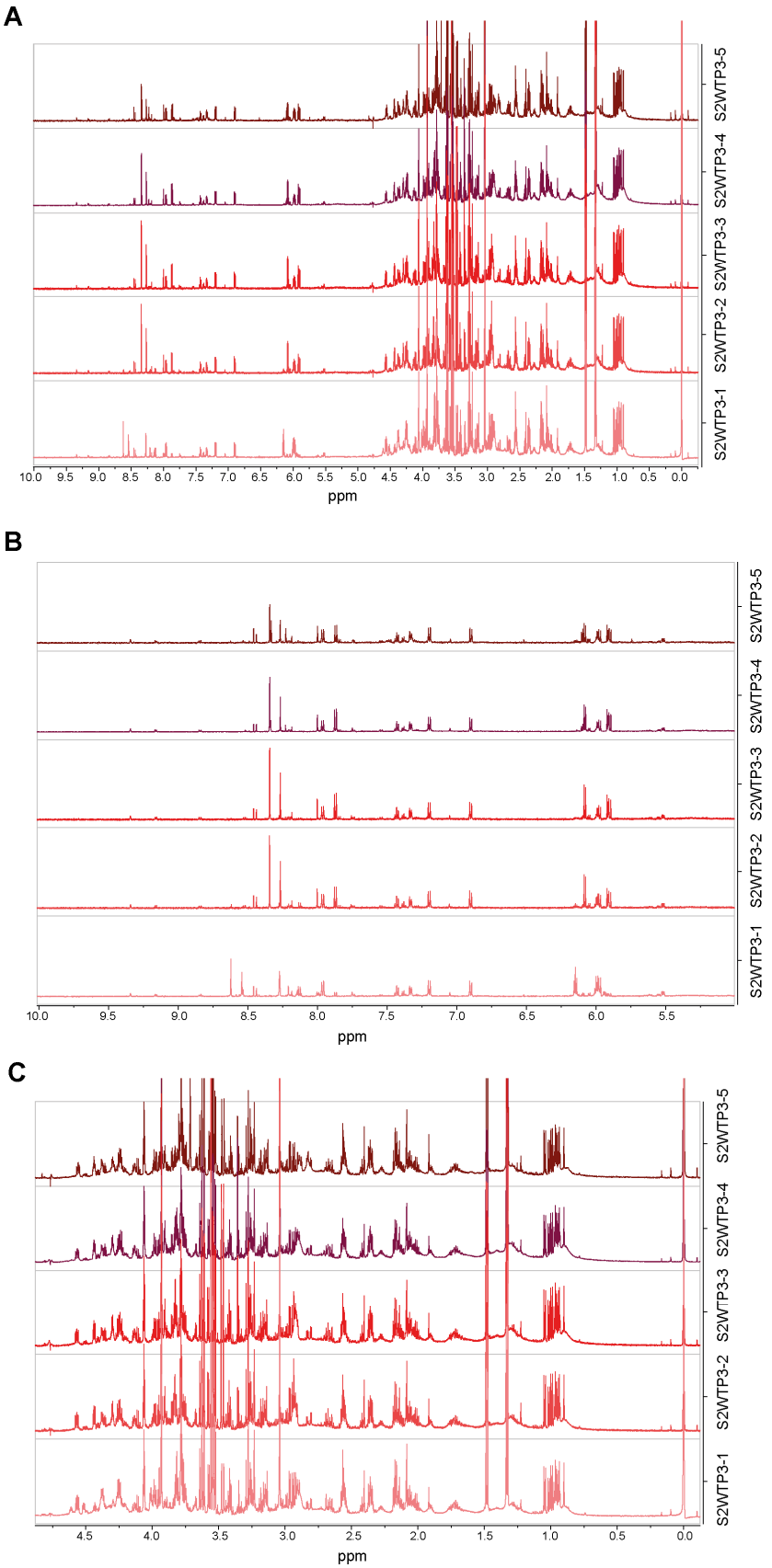

Figure 104: ^{1}H magnetic resonance spectra of S2WTP3 cell extracts.

^{1}H spectra of S2WTP3 cell extracts (**A**) and zoom on the aromatic (**B**) and aliphatic (**C**) region on the spectra revealed high reproducibility between the five replicates (S2WTP3_1 to S2WTP3_5). For visualization, the spectra are scaled to the tyrosine doublets at 7.2 ppm and 6.9 ppm.

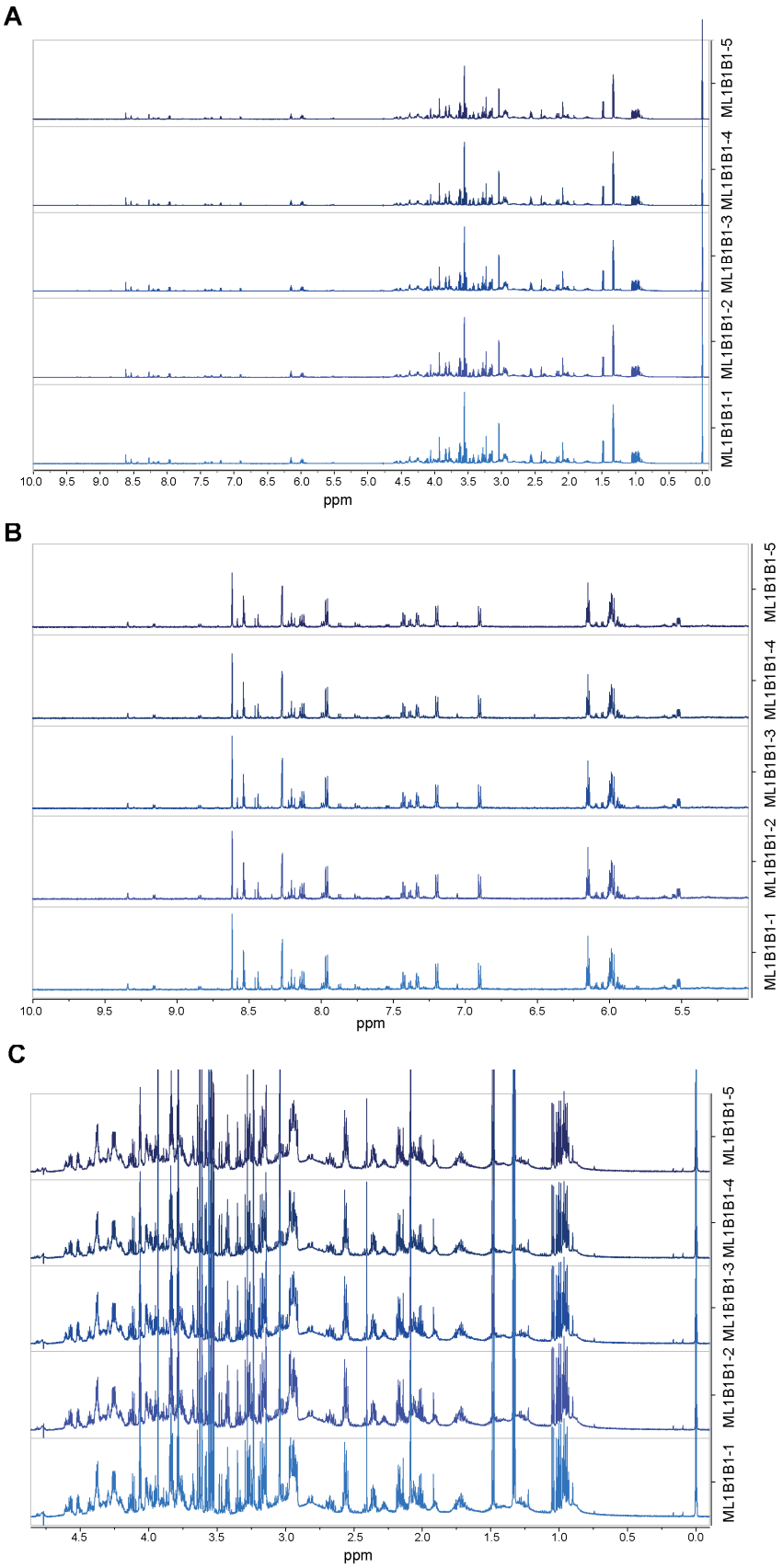

Figure 105: ^{1}H magnetic resonance spectra of ML1B1B1 cell extracts.

^{1}H spectra of ML1B1B1 cell extracts (**A**) and zoom on the aromatic (**B**) and aliphatic (**C**) region on the spectra revealed high reproducibility between the five replicates (ML1B1B1_1 to ML1B1B1_5). For visualization, the spectra are scaled to the tyrosine doublets at 7.2 ppm and 6.9 ppm.